

Investigation of the
physical properties of
Dirac materials

Thesis by
Chien-Chang Chen

In Partial Fulfillment of the Requirements for
the degree of
Ph.D of Physics

The logo for the California Institute of Technology (Caltech), featuring the word "Caltech" in a bold, orange, sans-serif font.

CALIFORNIA INSTITUTE OF TECHNOLOGY
Pasadena, California

2020
(Defended July 3, 2020)

© 2020

Chien-Chang Chen

ORCID: [0000-0003-0959-5584](https://orcid.org/0000-0003-0959-5584)

ACKNOWLEDGEMENTS

I would like to thank the many people who gave me help or support during my research life. First, I would like to thank my advisor, Nai-Chang Yeh, who gave me a fellowship in my first year and always worked hard to get funding for us. Her experience is invaluable and gave me much guidance in the research direction. I thank her for the weeks of time she spent proofreading my thesis even though time is the hardest thing for her to squeeze out.

I feel sorry but also thankful for Hao, who passed the STM to me and left the lab. This gave me a chance to be involved in a real project and work on instrumentation.

Every summer, I was always fortunate to get my second pair of hands from my SURF students and high school teacher. Many SURF students are more capable than me and helped me finish something I could not do on my own. Thanks for Adrian Po for coding and helping with experiment. Thanks to Cassidy Yang for the intense experiment schedule. Thanks to Ankit Kumar for drawing new STM stage design, writing interface code for PPMS, and developing some analysis code. Thanks to Wentao for the experiment and data analysis. Thanks to James for providing the Molecule Dynamics simulation code before he joined our group again.

Besides the SURF student, I also got help from high school teacher Erin. Thanks to visiting scholar Prof Feng, who grew the cuprate superconductor sample for me. Those extra hands are really helpful and share lots of my burdens away.

Thanks to Professor Wang's group at UCLA to grow the topological insulator samples for us. Specifically, thanks to Liang He, Koichi Murata, Lei Pan, and Peng Zhang for growing samples and etching samples to make the Hall bar device for us.

Thanks to Nils, who made many devices for us before he retired. Thanks to Michael in the instrument shop at the Chemistry department, who often helped me drill the tools without charge.

Thanks to Bill Goddard for the license of VASP and supercomputers. Thanks to Anqi for help on DFT simulation on graphene. Thanks to I-Te Lu for advice about DFT simulation.

Thanks to the interviewer from TSMC North America for giving a simple suggestion on FFT and solving my problems of several years. Thanks to the former TA Shu-Ping Lee for theory advice. They are more useful than Google.

Thanks to Renee for passing her STM skills to me before she graduated. Thanks to Adrian for giving me much practical help and suggestions on repairing and operating STM. Thanks to Marcus for helping with troubleshooting and low-temperature measurement. Thanks to all my groupmates Chen-Chih Hsu, Steve Lu, Chia Shuo Li, Wei-Hsiang Lin, Deepan Kishore Kumar, Wei-Shiuan(Vincent) Tseng, Jiaqing Wang, Duxing (Jason) Hao, Yen-Chun Chen, Akiyoshi Park, Jacob Bagley, and Jing Shi for their help on my projects and advice.

Thanks to Avery house, which let me stay there for 2 years. It let me have a full taste of undergraduate life and enjoy many undergraduate traditions other graduates can't enjoy. Thanks to my UCC Sandra and Caroline for taking care of Alley 2. Thanks to Dai Wei, Jessica, Stacy, Debbie Yu, Ray, Lisa, Chien-Yi Chang, Maggie, and many more people in Avery house to make my life colorful. I won't forget the times I did scavenger hunts, Big I, the inter-house party, ditch day, midnight madness, and make-a-difference day with you guys.

I'm thankful to the Caltech Y and graduate housing at Catalina for holding so many fun activities. I was able to backpack, hike, and garden; go golfing, horse-riding, and bouldering; do archery; go to museums, NBA games, baseball games, and hockey games; watch movies, and volunteer. These activities broadened my mind and let me have more fun. They also let me make lots of new friends, like Carol, Betty, Danny, Greg, and more. I got to be part of Make A Difference Day (MAD Day), which is a very meaningful activity. Being a supervisor for the Science Olympia reminded me of my time in high school.

I'm thankful to all the dance clubs at Caltech that taught me many dances, like the lindy-hop, west coast swing, tango, salsa, quick step, cha-cha, waltz, and much more. It's made my life colorful and less stressful. It also gave me a chance to invite many friends to dance and also let me make many new friends.

Thanks to the people at the Bridges at Caltech club. They are like my family. We ate dinner together every Friday and shared, prayed, and played together. It is a good spiritual support.

Thanks to my friends who play basketball with me every week. Basketball is really fun, and it enhances my body shape a lot.

My thanks to the International Student Program (ISP), especially Daniels and Laura, for helping me with basically everything whenever I need to go abroad. International Student Discussion provides a very delicious lunch and was something I didn't want to miss.

Thanks to Caltech for providing so many interesting seminars. I can't believe I've been able to see Bill Gates and Steve Hawkins with my own eyes. I got to see many new Nobel Laureates and listen to their talks. Also many seminars provided free food, which save me a lot of money and time spent cooking.

I'm thankful that Pasadena and South California are located in a very nice place, with lots of tall mountains and national parks around. The interesting Mediterranean climate makes summer dry and winter rainy. You can see snow in winter, flower blossoming in spring, and beautiful yellow-leafed trees in fall. This has been a wonderful place for me to explore. It's also let me make lots of new friends. This is also a very convenient place to live even without a car, so I can simply survive with a bike only.

Thanks to my hundreds of hiking friends. I don't have a car, and without you guys I couldn't have hiked even a single mountain. But now I've hiked Mt Whitney (14,505 feet /4,421 m)

two times, 3,000 m/10,000 ft mountains probably twenty times, and famous 6-packs in Southern California several times over. You guys made me one of the best hikers in Southern California. I really like snow. It makes me so happy every time I can see snow during the hike. This is probably what I will miss most when I'm back in Taiwan.

Thanks to lots of my adventure friends. Although I only saw many of them once, we have the memories of the road trip to Zion, Bryce Canyon, the Grand Canyon, Yosemite, Joshua Tree, the Channel Islands, Yellowstone, the Grand Tetons, and Denali National Park that we can't forget. The fall leaves in autumn is also something I will never forget. They are just so beautiful that I visited Bishop twice a year. Thanks to Grace for bringing me to Alaska, inside the Arctic Circle, to see polar lights and hot springs in the snow, and to fly over Mount Denali, the highest peak in North America. Thanks to Ester for bringing me to Banff in Canada. It was the coldest place in the world at -30C. This is the coldest birthday I have experienced.

Last, I am really grateful to the TSMC HR Ji-Wei. Without him, I probably would have never gotten offers from. And I probably will have no idea what I should do now.

Acknowledgement for the software:

[K. Momma and F. Izumi, "VESTA 3 for three-dimensional visualization of crystal, volumetric and morphology data," *J. Appl. Crystallogr.*, 44, 1272-1276 \(2011\).](#)

[Matlab 2011b~2020a](#)

[Mathematica 8~12.1](#)

[Solidwork 2011~2017](#)

[Labview](#)

[Gwyddion](#)

[Teamviewer](#)

[Endnote](#)

[Nanonis V4, V5](#)

[OriginLab 8](#)

[VASP - Vienna Ab initio Simulation Package](#)

I couldn't have finished the experiments, data analysis, and even the plots in this thesis without the above softwares, and am really thankful for their help.

ABSTRACT

This thesis focuses on the investigation of two types of Dirac materials: topological insulators (TI) and graphene. Both materials have received much attention and stimulated intense research activities over the last decade. Although massless Dirac electrons are wonderful, there will be more industrial applications if we can open the gap and make Dirac electrons massive. For topological insulators, we focus on studies of the TI/Magnetic TI (MTI) bilayer structures to induce a gap on the surface state. For graphene, the author focuses on the Moiré pattern and interlayer interaction.

For bilayer TI/MTI samples, they were investigated with scanning tunneling microscopy and spectroscopy (STM/STS), and with electrical transport measurements by means of a Physical Property Measurement System (PPMS). Details of the experimental setups for this research and their upgrades were described. For the current STM system, both the tube scanner and sample stage in the STM head had been redesigned and rebuilt, which led to better XYZ fine approach control, improved wire protection, and enhanced noise shielding. A new back gate capability was added to the sample stage. A customized commercial STM system has been commissioned, which is expected to provide a better sample holder with improved vacuum seals and easier temperature control, as well as more convenient approaches to loading samples and switching STM or AFM (atomic force microscope) tips. For PPMS, an optical probe had been designed and constructed, which enabled light-induced effects on the electrical transport properties of TIs. A new custom-made glove box has been installed, which provides a computer-controlled and self-circulating gas environment to minimize the concentration of air while reducing the waste of argon. The glove box is also easy to use. This upgrade helps expand our abilities to conduct research more efficiently.

STM/STS studies of both the binary and ternary types of magnetic topological insulators (MTIs) are presented. For both binary and ternary bilayer TI/MTI systems, the majority of the density of states (DOS) spectra evolved with the temperature. At room temperature, all samples showed massless Dirac spectra. However, for temperatures below 200 K, all bilayer samples with the top pure TI layer thinner than 5QL revealed opening of a surface gap.

Generally, binary TI/MTI samples exhibited smaller gapped domains, which was consistent with the finding of nearly negligible hysteretic behavior for Hall resistance *vs.* magnetic field sweeps at low temperatures. In contrast, ternary TI/MTI samples exhibited larger gapped domains, which implied longer range ferromagnetic order and was indeed corroborated by the apparent hysteretic behavior in the electrical transport measurements at low temperatures. Additionally, the application of *c*-axis magnetic fields led to slightly larger surface gaps and more uniform gap distributions, which further confirmed the physical origin of the surface gap as magnetic in nature. Besides the U or V-shaped DOS spectra, double-peak or single peak impurity resonances were also observed. These spatially localized minority spectra were found to mostly appear along the boundaries of gapped and gapless domains. Moreover, the number of impurities was found to reach a maximum around 240 K, which corresponded to the onset temperature of localized surface gaps.

Detailed studies of the electrical transport properties of both the binary and ternary MTIs by the PPMS provided a comparison between the macroscopic information thus obtained with the microscopic information derived from STS studies. Binary TI/MTI showed an anomalous Hall effect (AHE) at 25 K while ternary TI/MTI showed AHE around 20 K. Binary TI/MTI systems exhibited weak localization (WL) behavior in the longitudinal resistance *vs.* magnetic field data at 2 K. The binary TI/MTI samples with a thinner top pure TI layer revealed sharper and stronger WL behavior. In contrast, for the 3QL-TI/6QL-MTI ternary sample, weak antilocalization (WAL) behavior was present for all temperatures, while WL also showed up below 13 K. The Hall resistance *vs.* magnetic field data for all samples of ternary TI/MTI bilayers and ternary MTI monolayer samples revealed strong hysteresis at low temperatures, in contrast to the negligible hysteretic behavior in all binary TI/MTI samples. Finally, circularly polarized light was found to enhance the AHE of the bilayer ternary TI/MTI sample while weakening that of the monolayer ternary MTI. These experimental phenomena may be mostly attributed to the different band structures and Fermi levels among the binary and ternary TI/MTI samples. In particular, we note that the observation of quantum anomalous Hall effect (QAHE) only in ternary MTI monolayers at extremely low temperatures (at $T \leq 30$ mK $\ll T_c^{bulk} \sim 30$ K) may be attributed to the finite contributions of bulk carriers to excess conduction unless $T \rightarrow 0$.

Simulations have been carried out to account for the Moiré patterns of graphene on Cu (111), graphene on Cu (100), twisted bilayer graphene, and Cr-doped topological insulators. The physical origin for empirically observed structural superlubricity between graphene layers has also been modeled by simulations based on the density functional theory (DFT).

Finally, the key findings of this thesis work and the suggested future research directions are summarized.

PUBLISHED CONTENT AND CONTRIBUTIONS

Y.-C. Chen, W.-H. Lin, W.-S. Tseng, **C.-C. Chen**, G.R. Rossman, C.-D. Chen, Y.-S. Wu, N.-C. Yeh, "Direct growth of mm-size twisted bilayer graphene by plasma-enhanced chemical vapor deposition," *Carbon*, 156, pp.212-224 (2019)

DOI: [10.1016/j.carbon.2019.09.052](https://doi.org/10.1016/j.carbon.2019.09.052)

C.-C. C. measured Scanning Tunneling Spectroscopies (STS) on twisted bilayer graphene samples grown by Y.-C. C. The angles of twisted bilayer graphenes are calculated through the atomic resolution topography of the Morie Pattern. **C.-C. C.** also simulated the Morie Patterns generated by twisted bilayer graphenes and compare them with experimental results

N.-C. Yeh, C.-C. Hsu, M. L. Teague, J.-Q. Wang, D. A. Boyd, W.-H. Lin, **C.-C. Chen**, (invited paper), "Nanoscale strain engineering of graphene and graphene-based devices," *Acta Mechanica Sinica*, 32 (3), 497 – 509 (2016).

DOI: [10.1007/s10409-015-0548-9](https://doi.org/10.1007/s10409-015-0548-9)

C.-C. C. designed a code to produce nanostructures for graphene strain simulation used by J.-Q. Wang. **C.-C. C.** also develop a code for producing an effective magnetic field map according to different magnetic lengths.

C.-C. CHEN, M. L. TEAGUE, L. HE, X. KOU, M. LIANG, N. WOODWARD¹, W. FAN¹, K.-L. WANG and N.-C. YEH, "Magnetism-Induced Massive Dirac Spectra and Topological Defects in the Surface State of Cr-Doped Bi₂Se₃-Bilayer Topological Insulators", *New Journal of Physics*, 17(11), p.113042. (2015)

DOI: [10.1088/1367-2630/17/11/113042](https://doi.org/10.1088/1367-2630/17/11/113042)

C.-C. C. did the full STS study on different thickness of pure TI/ Cr-doped TI bilayer Bi₂Se samples. Each sample was measured for topography and STS for different temperatures, areas, and magnetic fields. It helps to reveal some interesting properties of binary TI.

D. A. Boyd, W.-H. Lin, C.-C. Hsu, M. L. Teague, **C.-C. Chen**, Y.-Y. Lo, W.-Y. Chan, W.-B. Su, T.-C. Cheng, C.-S. Chang, C.-I. Wu, N.-C. Yeh, "Single-step deposition of high mobility graphene at reduced temperatures," *Nature Communications* 6: 6620 (2015)

DOI: [10.1038/ncomms7620](https://doi.org/10.1038/ncomms7620)

C.-C. C. simulates Morie Pattern of graphene on copper (100) and copper (111) surface since graphene was successfully grown on both copper crystals. The simulation helps to compare with real STM images on the grown graphene and hence helps to justify the quality of the grown samples.

TABLE OF CONTENTS

Acknowledgements.....	iii
Abstract	vi
Published Content and Contributions.....	ix
Table of Contents.....	x
List of Illustrations and/or Tables.....	xiii
Chapter 1: Introduction.....	1
1.1 Ways to open the gap	5
1.2 Potential applications of magnetic TIs.....	7
1.3 Scope of this thesis	8
Chapter 2: Instrumentation and Methodology.....	9
2.1 Scanning tunneling microscopy (STM) system	9
2.1.1 STM theory.....	10
2.1.2 STM operation.....	15
2.1.3 STM system overview	19
2.1.4 STM probe head and upgrade	25
2.1.5 A customized STM/AFM system.....	34
2.2 Physical Property Measurement System (PPMS)	40
2.2.1 Customization of PPMS to add light to the sample chamber	42
2.3 Glove box and upgrade	43
2.3.1 Customized commercial glovebox	44
Chapter 3: STM/STS studies of Topological Insulators.....	48
3.1 Introduction of binary TI Bi_2Se_3 and ternary TI $(Bi, Sb)_2Te_3$	49
3.2 Sample choices and experimental setup	52
3.2.1 List of samples investigated in this work	53
3.2.2 Sample storage and preparation	55
3.2.3 Sample annealing procedure	55
3.2.4 Hydrofluoric Acid (HF) sample etching procedure	57
3.2.5 Summary of the sample handling before STM experiments	58
3.3 STM measurement settings.....	59
3.3.1 Compromise between the accuracy and the speed for spectroscopy.....	59
3.4 Structural characteristics from surface topographic studies of the binary TI/MTI system.....	61
3.5 Temperature evolution of the majority spectra in binary and ternary TI/MTI systems	62
3.5.1 (5+6)-10% binary TI/MTI.....	63
3.5.2 (1+6)-5%, (1+6)-10% and (3+6)-10% binary TI/MTI.....	64
3.5.3 (1+6)-10% and (3+6)-10% ternary TI/MTI.....	66
3.5.4 Summary and discussion.....	67
3.6 Evolution of the surface gap with temperature.....	68

3.6.1 Definition of the surface gap.....	70
3.6.2 (1+6)-5% binary TI/MTI surface gap evolution with temperature.....	72
3.6.3 (1+6)-10% binary TI/MTI surface gap evolution with temperature.....	74
3.6.4 (3+6)-10% binary TI/MTI surface gap evolution with temperature.....	76
3.6.5 (1+6)-10% ternary TI/MTI surface gap evolution with temperature.....	77
3.6.6 (3+6)-10% ternary TI/MTI surface gap evolution with temperature.....	78
3.6.7 Summary and discussion of the temperature evolution of the surface gap.....	79
3.7 Magnetic effect on the surface states.....	80
3.8 Impurity resonance.....	82
3.8.1 The appearance of the magnetic impurity resonance curve.....	82
3.8.2 Spatial distributions of the magnetic impurity resonance.....	83
3.8.3 The number of impurity resonance vs. temperature.....	85
3.8.4 Summary of impurity resonances.....	86
3.9 Summary and future project.....	87
Chapter 4: Electrical transport studies of Magnetic Topological Insulators.....	89
4.1 Transport studies of bilayer $Bi_2Se_3/Cr-Bi_2Se_3$	90
4.1.1 Sample characteristics and experimental setup.....	90
4.1.2 (1+6)-10% binary TI/MTI temperature sweep.....	93
4.1.3 (1+6)-10% binary TI/MTI magnetic field sweep.....	96
4.1.4 (3+6)-10% binary TI/MTI temperature sweep.....	98
4.1.5 (3+6)-10% binary TI/MTI magnetic field sweep.....	99
4.1.6 Summary for transport results of binary TI/MTI samples.....	101
4.2 Transport studies of bilayer $(Bi, Sb)_2Te_3/Cr-(Bi, Sb)_2Te_3$	102
4.2.1 Results from electrical transport measurements on (1+6)-10% ternary TI/MTI.....	103
4.2.2 Low magnetic field sweep analysis of the (3+6)-10% ternary TI/MTI sample.....	105
4.2.3 High magnetic field sweep analysis of the (3+6)-10% ternary TI/MTI sample.....	108
4.2.4 Temperature sweep studies of the (3+6)-10% ternary TI/MTI sample.....	110
4.2.5 Comparison of the field cooling curves taken on the (3+6)-10% ternary TI/MTI sample.....	116
4.3 Effects of circularly polarized light on the AHE of bilayer ternary TI/MTI.....	120
4.3.1 Effect of circularly polarized light on (3+6)-10% ternary TI/MTI.....	122

4.3.2 Effect of circularly polarized light on a monolayer (0+6)-10% MTI.....	123
4.4 Discussion and Summary	125
Chapter 5: Graphene and interlayer interaction.....	132
5.1 Introduction	133
5.1.1 The tight-binding model of monolayer graphene.....	135
5.1.2 Tight-binding model of bilayer graphene.....	139
5.1.3 Twist bilayer graphene and the corresponding Moiré pattern	142
5.2 Single-step Growth of Graphene by Plasma-enhanced Chemical Vapor Deposition.....	144
5.2.1 Single-step deposition of high-mobility graphene at reduced temperatures.....	145
5.2.2 STM imaging of PECVD grown graphene	147
5.2.3 Simulations for the topography and FFT of 2D single-crystalline graphene on copper substrates	149
5.2.4 Simulations for graphene on single crystalline copper substrate	157
5.2.5 Graphene on copper (111) surface.....	159
5.2.5 Graphene on copper (100) surface.....	165
5.2.7 Summary of PECVD graphene growth on Cu substrates	167
5.3 Direct growth of mm-size twisted bilayer graphene by plasma-enhanced chemical vapor deposition	168
5.3.1 Experimental setup and growth conditions	169
5.3.2 STM images for PECVD-grown twisted bilayer graphene	170
5.3.3 Simulations for the Moiré pattern and FFT of twist bilayer graphene	175
5.3.4 Summary.....	179
5.4 Interaction between layers of bilayer graphene by density functional theory (DFT)	180
5.4.1 Introduction of the density function theory	181
5.4.2 Optimization of graphite and bilayer graphene.....	182
5.4.3 Optimization of bilayer graphene for mixed stacking.....	183
5.4.4 Top layer moving in any direction relative to the bottom layer.....	185
5.4.5 Analysis of the free energy map	188
5.4.6 Lock-in effect for motion along the armchair direction with $\theta= 30^\circ$	190
5.4.7 Summary.....	192
Chapter 6: Conclusion and future project	194
6.1 Future project.....	196
Bibliography	198

LIST OF ILLUSTRATIONS AND/OR TABLES

<i>Number</i>	<i>Page</i>
Figure 1.1: (a-d) Surface-state electronic properties of TIs and magnetic TIs. (e-h) Real space illustration for the Quantum Hall effect (QHE) and Quantum anomalous Hall effect (QAHE) and their corresponding transport properties	3
Figure 1.2: Various methods to open a surface gap without an external magnetic field.	5
Figure 2.1: Tunneling effect of a single electron.	11
Figure 2.2: Schematic illustration of STM operation with a tip near a sample surface.	12
Figure 2.3: Energy level diagrams for the sample and tip separated by a small vacuum gap.	14
Figure 2.4: (a) Different distortion modes of piezoelectric materials. (b) Illustration of a realistic STM configuration.	15
Figure 2.5: Topology scan and its different modes of operation.	16
Figure 2.6: Schematic illustration of the spectroscopy scan.	19
Figure 2.7: STM probe and its Dewar.	21
Figure 2.8: Instruments used for the STM system.	24
Figure 2.9: Photos for the STM probe head.	26
Figure 2.10: Coarse z-motion mechanism.	27
Figure 2.11: Design of the tube scanner.	29
Figure 2.12: Designs of the STM probe head base.	33
Figure 2.13: Design of the customized commercial STM.	38
Figure 2.14: (a) Quantum Design DynaCool PPMS. (b) A puck is used to mount the sample and put into the PPMS.	41
Figure 2.15: Optical probe designed by group members Dr. Marcus Teague, Adrian Llanos, and Duxing Hao.	42

Figure 2.16: The old glove box.	43
Figure 2.17: Design of the new glovebox.	46
Figure 2.18: Real image of the new glove box.	47
Figure 3.1: Crystalline structure (side view) and Electronic band structure of a binary topological insulator Bi_2Se_3	50
Figure 3.2: (a) The lattice structure of the ternary TI $(Bi_xSb_{1-x})_2Te_3$ (b) Band structure of Bi_2Te_3 . (c) Band structure of Sb_2Te_3	50
Figure 3.3: (a) Band structures of the surface states of Bi_2Se_3 and Bi_2Te_3 for different thicknesses. (b) The surface bandgap size vs. sample thickness for Bi_2Se_3 and Bi_2Te_3	52
Table 3.1: List of binary Bi ₂ Se ₃ bilayer samples for STM and PPMS studies.	53
Table 3.2: $(Bi_xSb_y)_2Te_3/Cr-(Bi_xSb_y)_2Te_3$ sample list for STM and PPMS studies	53
Figure 3.4: Schematic structure (side view) of a bilayer TI/MTI sample and its nomenclature.	54
Figure 3.5: Annealing and sample loading procedures for preparing TIs for STM experiments.	56
Figure 3.6: Structural characteristics of MBE-grown Bi_2Se_3 bilayer samples on InP (111)	61
Figure 3.7: (a) Majority dI/dV -vs.- V spectral evolution with temperature in (5+6)-10% binary TI/MTI. (b) Comparison of different types of dI/dV -vs.- V spectra observed at 114 K. (c) Different types of curves observed at 88 K.	64
Figure 3.8: Majority spectra taken at different temperatures for (a) (1+6)-5% binary TI/MTI, (b) (1+6)-10% binary TI/MTI and (c) (3+6)-10% binary TI/MTI.	65

Figure 3.9: Majority spectra taken at different temperatures for (a) (1+6)-10% ternary TI/MTI and (b) (3+6)-10% ternary TI/MTI. (c)-(d) All point spectra taken from different areas of the (3+6)-10% ternary TI/MTI at 4.2K.....	67
Figure 3.10: Representative gapless and gapped dI/dV spectra.....	69
Figure 3.11: Definition of the gap through different methods. (a) Curve bottom wide gap (b) Zero-bottom wide gap	70
Figure 3.12: Gap value map and gap value histogram for (a) 80 K, (80 nm × 80 nm), (b) 164 K, (44.3 nm × 44.3 nm) and (c) 169 K, (44.6 nm × 44.6 nm).....	72
Figure 3.13: (1+6)-5% binary TI/MTI gap value vs. temperature.	74
Figure 3.14: (1+6)-10% binary TI/MTI gap value vs. temperature.	75
Figure 3.15: (1+6)-10% binary TI/MTI gap map at (a) 78K (b) 106K (c) 141K and (d) 195K	76
Figure 3.16: (3+6)-10% binary TI/MTI: (a) Gap map and gap histogram at 20 K and 79 K. (b) Gap value vs. temperature (T).	76
Figure 3.17: Surface gap vs. T for the (1+6)-10% ternary TI/MTI.....	77
Figure 3.18: Δ_{bw} and Δ_{zw} vs. T of the (3+6)-10% ternary TI/MTI for different sizes of the scan area.....	78
Figure 3.19: Evolution of the surface gap distribution at $T=18$ K with applied c-axis magnetic field.....	80
Figure 3.20: (3+6)-10% binary TI gap vs. magnetic field at $T = 18$ K.	81
Figure 3.21: STS of impurity resonance. (a) I vs. V (b) dI/dV vs. V	82
Figure 3.22: Spatial distributions of impurity resonances	84
Figure 3.23: (a) Explanation of the location of impurity. (b) Double peak resonance (c) Single peak resonance.....	85
Figure 3.24: The number of impurity resonance vs. temperature	86
Figure 3.25: Possible device to line up the location of impurity and control it by the back gate.....	87
Table 4.1: lists of bilayer binary samples for STM and PPMS studies.....	90

Figure 4.1: (a) Schematic illustration of a bilayer TI/MTI sample (b) An optical micrograph of a print circuit board (PCB) (c) Formulae used to calculate the longitudinal resistance R_{xx} and Hall resistance R_{xy} (d) The Hall bar geometry	92
Figure 4.2: R_{xx} vs. T measurements taken on (1+6)-10% binary TI for different magnetic fields: (a) 0 and 8T; (b) 0 and 5 T.	94
Figure 4.3: $ R_{xy} $ vs. T measurements on a (1+6)-10% binary TI sample.	96
Figure 4.4: Field sweeps of longitudinal and Hall resistance taken at $T = 2\text{K}$ on (1+6)-10% Bi_2Se_3 binary TI.....	97
Figure 4.5: Temperature sweeps of the longitudinal and Hall resistance for (3+6)-10% Bi_2Se_3 binary TI.....	99
Figure 4.6: Field sweeps of longitudinal and Hall resistance taken at $T = 2\text{K}$ on (3+6)-10% Bi_2Se_3 binary TI.....	100
Table 4.2: $(Bi_xSb_y)_2Te_3/Cr-(Bi_xSb_y)_2Te_3$ sample list for STM and PPMS.....	102
Figure 4.7: Field sweeps of resistance for the (1+6)-10% ternary TI/MTI sample.....	105
Figure 4.8: Low-field R_{xy} (thick line) and R_{xx} (thin line) vs. B data taken on the (3+6)-10% ternary TI/MTI sample at $T =$ (a) 1.75K, (b) 3K, (c) 6K, (d) 13K, (e) 20K, and (f) 27K	106
Figure 4.9: Field sweep measurements of R_{xx} and R_{xy} on the (3+6)-10% ternary TI/MTI sample at different temperatures	107
Figure 4.10: Field sweeps of longitudinal and Hall resistance at $T = 1.75\text{ K}, 3.5\text{ K}, 7\text{ K},$ and 14 K with different field ranges.....	109
Figure 4.11: R_{xy} -vs.- T and R_{xx} -vs.- T of a (3+6)-10% ternary TI/MTI sample measured in zero fields for both cooling and warming.....	110
Figure 4.12: Temperature sweeps for zero-field warming resistive measurements on the (3+6)-10% ternary TI/MTI sample after cooling in $B = 0\text{ T}, 1\text{ T},$ and $-1\text{ T}.$	112

Figure 4.13: R vs. T for 0.05 T warming after 0 T, 0.5 T, and -0.5 T cooling.....	113
Figure 4.14: R vs. T for $\square\square$ 0.05T warming after 0 T, 2 T, and -2 T field-cool.	115
Figure 4.15: (a) Field-cool R_{xy} vs. T curves and (b) Field-cool R_{xx} vs. T curves of the (3+6)-10% ternary TI/MTI sample at different magnetic fields (c) R_{xy} vs. B isotherms constructed from different field-cool R_{xy} vs. T curves. (d) R_{xx} vs. B isotherms constructed from different field-cool R_{xy} vs. T curves.....	117
Figure 4.16: $R_{xy}(B, T)$ and $R_{xx}(B, T)$ maps derived from the field-cooled R_{xy} vs. T and R_{xx} vs. T curves in different fields.....	118
Figure 4.17: (a) 2D map of $R_{xy}(B, T)$ as derived from field-cooled R_{xy} vs. T curves. (b) 2D map of $R_{xx}(B, T)$ as derived from field-cooled R_{xx} vs. T curves. (c) 2D map of $R_{xy}(B, T)$ as derived from zero-field-warming R_{xy} vs. T curves after field cooling. (d) 2D map of $R_{xx}(B, T)$ as derived from zero-field-warming R_{xx} vs. T curves after field cooling.	119
Figure 4.18: (a) R_{xy} vs. B with and without circularly polarized light. (b) Coercive field vs. T with and without circularly polarized light.....	123
Figure 4.19: Circularly polarized light effect on 6-QL 10% ternary MTI. ...	124
Table 4.3: Summary of electrical transport results for binary TI/MTI and MTI samples	125
Table 4.4: Summary of electrical transport results for ternary TI/MTI and MTI samples	126
Figure 4.20: Schematic plots for the evolution of band structures for a ternary TI (3+6)-10% at different temperature regions.	128
Figure 4.21: Schematic plots for the evolution of band structures for a ternary TI (1+6)-10% at different temperature regions.	129
Figure 4.22: Schematic plots for the evolution of band structures for a binary TI (1+6)-10% at different temperature regions.	130

Figure 5.1: (a) Graphene honeycomb crystal (b) The corresponding reciprocal lattice and Brillouin zone.	134
Figure 5.2: (a) Band structure of monolayer graphene in reciprocal space (b) Enlarged energy dispersion relation around one of the Dirac points (c) Band structure along the dashed line cut in the reciprocal space (d).	138
Figure 5.3: Anisotropic scattering of chiral electrons in graphene. (a) monolayer graphene and (b) bilayer graphene.	139
Figure 5.4: Crystalline structure of AB-stacked bilayer graphene.	140
Figure 5.5: (a) Band structure of bilayer graphene along the cut line (b) Bilayer graphene band structure near the K point	141
Figure 5.6: (a) Moiré pattern of twisted bilayer graphene. (b) The reciprocal lattice of the twisted bilayer graphene with a twist angle θ	143
Figure 5.7: (a) A schematic of the PECVD setup for the synthesis of graphene sheets without active heating. (b) False-color SEM images of graphene grown for excessive time and transferred to single-crystalline sapphire	146
Figure 5.8: Comparison of strain-induced in graphene grown by PECVD and thermal CVD methods.	147
Figure 5.9: Topographies of PECVD-graphene on copper.	148
Figure 5.10: Different methods to simulate a triangular lattice.....	150
Figure 5.11: Triangular lattices and the corresponding FFTs generated from the functions shown in Eqs. (5.28) – (5.30).	152
Figure 5.12: Illustration of the scheme to enlarge the size of atoms in a triangular lattice by making the effective lattice denser	153
Figure 5.13: Illustration of the scheme to enlarge the size of atoms in a square lattice by making the effective lattice denser.	155
Figure 5.14: Illustration of different approaches to construct a hexagonal lattice.	156
Figure 5.15: Lattice structure of Cu.	157

Figure 5.16: Moiré patterns of graphene on copper (111) with different stacking.	160
Figure 5.17: Comparison of real-space Moiré patterns and the corresponding FFT images from simulations for different twist angles, stacking, and lattice constants.	162
Figure 5.18: FFT simulation results for candidate models of graphene on Cu (111) that account for the real FFT from STM studies.....	163
Figure 5.19: Real-space Moiré patterns and the corresponding FFTs of graphene on a Cu (100) surface with a twist angle from $\theta = 0$ to 15°	165
Figure 5.20: Simulations of the FFT of graphene on Cu (100) at a twist angle of $\theta = 4^\circ$ vs. the FFT obtained from STM studies of graphene on Cu (100).	166
Table 5.1: the growth condition for monolayer, bilayer graphene, and twist bilayer graphene.....	169
Figure 5.21: Optical images of large monolayer graphene (MLG) and bilayer graphene (BLG) films transferred onto 285 nm-thick SiO ₂ /Si substrates and grown under different (PCH4/PH ₂) ratios over the same growth time	170
Figure 5.22: STM topographic images of PECVD-grown twisted bilayer graphene for different sizes of areas and spatial resolutions.....	171
Figure 5.23: (a) STM image with atomic resolution and Moiré patterns over a (10 nm × 10 nm) area. (b) FFT of the (a). (c) Real-space Moiré patterns simulated for a (10 nm × 10 nm) area with a twist angle $\theta = 10.32^\circ$. (d) FFT of the (c).....	172
Figure 5.24: Size of the Moiré superlattice vs. twist angle. The inset shows the enlarged details for twist angles around the magic angle ($\sim 1.05^\circ$)	174
Figure 5.25: Simulations of graphene topography and FFT.....	175
Figure 5.26: Simulation of twist bilayer graphene.....	176

Figure 5.27: Simulation of the Moiré pattern and its FFT near the magic-angle $\theta = 1.1^\circ$ for different sizes of areas and resolutions.....	179
Figure 5.28: Cell of graphite lattice and bilayer graphene lattice.	182
Figure 5.29: DFT simulations for graphene of different stacking without rotation.....	184
Figure 5.30: (a) Problems encountered in the DFT simulations for changing the relative orientation of the top layer (b) Moving the top layer against the bottom layer along an arbitrary direction (c) The resulting free energy vs. shift in any arbitrary direction	185
Figure 5.31: Simulation of the relative motion of two graphene layers in bilayer graphene at (a) $\theta = 0$ with speed = 100 m/s, and (b) $\theta = 30^\circ$ with speed = 200 m/s.....	186
Figure 5.32: Force field analysis for the top layer of bilayer graphene moving along the direction with $\theta = 0$	187
Figure 5.33: Top layer motion at $\theta = 0$, showing (a) the $F_{vertical}(F_v) = 0$ curves in the force field map and (b) the $F_{parallel}(F_u) = 0$ curves in the force field map.	188
Figure 5.34: $F_v = 0$ lines on the free energy map for the top layer moving along $\theta =$ (a) 5° , (b) 10° and (c) 15°	189
Figure 5.35: Force field analysis for motion direction along $\theta = 30^\circ$	190
Figure 5.36: Zoom in view of near $F_v = 0$ lines on the force field map around the vertical line region.	191
Table 6.1: Summary of studies on the bilayer topological insulators	194
Table 6.2: Summary of proposed future projects.....	197

Chapter 1

INTRODUCTION

The subjects of topological materials and graphene have received much attention and stimulated intense research activities [1-9] over the last decade, as evidenced by the awarding of Nobel Prizes in Physics to both the discovery of graphene (2010) and the theoretical development of topological physics (2016).

Graphene is a pure two-dimensional (2D) material of carbon atoms forming the honeycomb lattice with single-atom thickness. Its low energy spectrum consists of gapless Dirac cones, and each reciprocal lattice of graphene contains two valleys of Dirac cones. Therefore, there are four bands per unit cell in graphene due to both the valley and spin degeneracy.

Topological insulators (TIs) are a type of either three-dimensional (3D) or two-dimensional (2D) topological material that exhibits strong spin-orbit coupling and has a finite energy gap in the bulk and gapless modes at the boundaries. They differ from ordinary band insulators by their nontrivial integer topological invariant, which is formally known as the TKNN number or the Chern number[4]. Just like we cannot deform a cup without hole into a donut shape, the boundary between two insulators with different topological invariant must close the gap. In the case of 3D topological insulators, the gapless surface states are 2D in nature and form a Dirac cone as well, as illustrated in Figure 1.1 (a).

Due to the strong spin-orbital coupling, the surface carriers are spin-locked with their momentum. This spin-momentum locking obeys time-reversal symmetry (TRS). TRS makes the surface carriers robust against non-TRS-broken impurities because direct (180 degrees) backscattering is prohibited. Graphene has similar properties with pseudospin-momentum locking. Therefore, both graphene and the surface of TIs are excellent conductors against impurities and are promising for applications. Their massive carriers are expected to exhibit

anti-weak localization (AWL)[10-12] behavior because non-magnetic impurities do not contribute to localizing the electron wave functions.

However, even though direct backscattering is prohibited, scattering to other directions is still allowed. Therefore, neither the surface state of topological insulators nor graphene is a perfect conductor. If a strong magnetic field is applied to the sample, the surface-state electrons will form a cyclic motion and become like an insulator. In other words, a gap is open on the Dirac cone (Figure 1.1 (c)). Only electrons along the edge can keep going without any backscattering. This phenomenon is known as the Quantum Hall effect (QHE) (Figure 1.1 (e)). Thus, the surface state under a strong magnetic field like a 2D topological insulator with a 1D boundary state. Since 1D only has back and forth direction, with the prohibition of direct backscattering, the edge state must be dissipationless.

Despite the attractive properties associated with the edge state of QHE, the realization of this state requires a strong magnetic field, typically more than 10 T, which makes most technological applications impractical. The question is, can we create QHE-like edge states without the need for an external magnetic field?

In the presence of low magnetic fields, most conducting materials exhibit the ordinary Hall effect. For ferromagnetic materials, a finite Hall effect can appear without an external magnetic field, which is known as the anomalous Hall effect (AHE). The appearance of the AHE relies on a finite intrinsic magnetization to provide an effective magnetic field. In theory, if the internal magnetization is strong enough, the quantum version of AHE should show up, which is known as the quantum anomalous Hall effect (QAHE) (Figures 1.1 (d), 1.1 (g)). A gap is open on the surface states while a new chiral edge mode appears (Figure 1.1 (d)).

Although graphene has demonstrated perfect QHE phenomena, it is not magnetic, and so intrinsic graphene cannot exhibit AHE. In contrast, it is conceivable to dope the bulk state of 3D TIs with magnetic elements to induce ferromagnetism so that AHE can be realized with the presence of intrinsic magnetization in magnetic TIs below the Curie temperature.

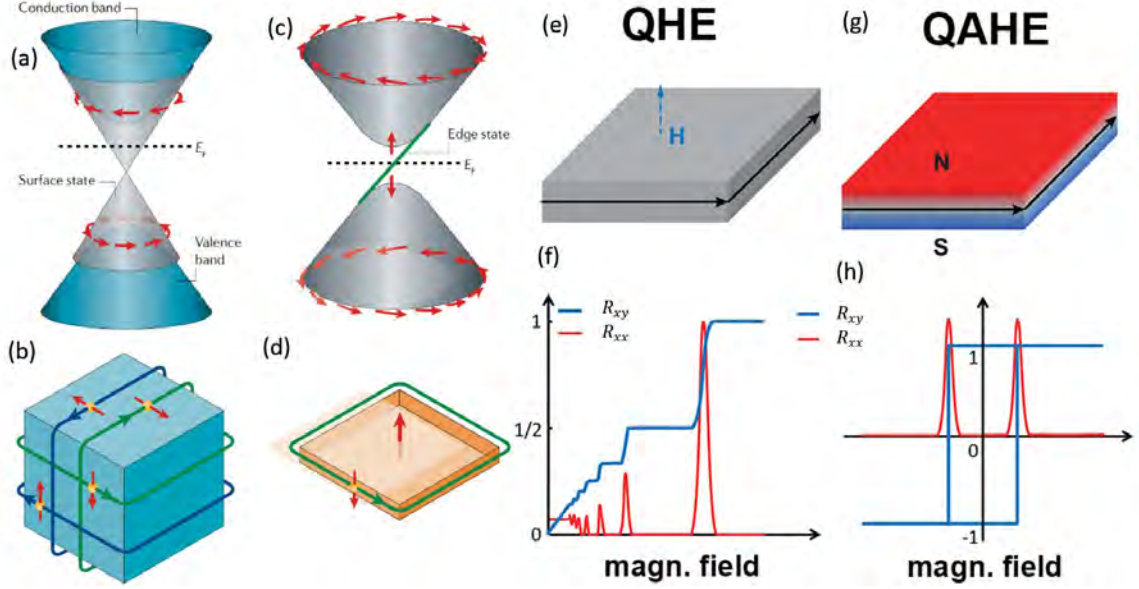


Figure 1.1: (a-d) Surface-state electronic properties of TIs and magnetic TIs. (a) Massless Dirac-like dispersion relation for the 2D surface states of TI. The spins of surface carriers lock with their momenta, and the surface-state conduction and valence bands meet at the Dirac point. (b) Real space illustration of a 3D TI with conductive surfaces and spin-momentum lock-in of the surface carriers. (c) Surface-state bandstructure of a magnetic TI, showing a gapped 2D Dirac cone and new 1D edge states. (d) A chiral edge mode appears when the Fermi energy is within the gap of the gapped Dirac cone. The edge electrons conduct electricity without dissipation in one direction along the edge of the magnetic TI. (e) Real space illustration for the Quantum Hall effect (QHE) by applying a strong magnetic field perpendicular to a 2D sample, where edge states form around the periphery of the sample and provide dissipationless conduction. (f) Hall resistance and longitudinal resistance *vs.* magnetic field for QAH. The Hall resistance R_{xy} shows quantized value plateaus wherever the longitudinal resistance R_{xx} vanishes. (g) Quantum anomalous Hall effect (QAHE) occurs in a ferromagnetic sample without an external magnetic field. It relies on the appearance of intrinsic magnetization. (h) The R_{xy} *vs.* B curve exhibits a hysteresis loop and R_{xy} is proportional to the magnetization. (a-d) adapted from [1], (e-h) adapted from [13].

Strictly speaking, only magnetization or magnetic field vertical to the 2D surface can break the TRS and open the gap in 3D TIs. This can be demonstrated by a Hamiltonian of 2D surface states normal to the z -axis:

$$H = v_F(-k_y\sigma_x + k_x\sigma_y), \quad (1.1)$$

where v_F is the Fermi velocity from the linear dispersion of the Dirac cone, and σ_x and σ_y are the Pauli matrix. Introducing a spontaneous magnetization next to or into the surface of the TI brings about the modification of the surface electronic structure via exchange interactions.

$$H = v_F(-k_y\sigma_x + k_x\sigma_y) + m\sigma_z. \quad (1.2)$$

Since the surface is in the XY plane, a vertical magnetization breaks the TRS. A gap m opens up in the Dirac surface state, which causes the massless Dirac Fermions in the surface states to become massive. On the other hand, introducing parallel magnetization $m\sigma_x$ or $m\sigma_y$ simply shift the center of Dirac cone horizontally but still preserves the TRS. Therefore, the occurrence of spontaneous magnetization does not guarantee the opening of a surface gap unless there is a net magnetization component perpendicular to the TI surface.

For QHE, the Hall resistance is quantized (Figures 1.1 (f) and (h)) according to the formula:

$$R_{xy} = \pm \frac{h}{\nu e^2}, \quad (1.3)$$

where ν is the filling factor, \pm corresponds to hole and electrons, respectively. For graphene, $\nu = 4\left(n + \frac{1}{2}\right)$. The constant $\frac{1}{2}$ is a unique feature for Dirac dispersion. The pre-factor 4, as explained in the beginning, is from 2 valleys and 2 spins per unit cell, and n is a non-negative integer.

For topological insulators, $\nu = 2\left(0 + \frac{1}{2}\right) = 1$, where the prefactor 2 is from 2 surfaces at the top and bottom. The most significant difference from graphene is that $n = 0$, in that TIs only have one Dirac dispersion band on the surface, while graphene has infinite Dirac dispersion at their 2D bulk bands.

Before reaching the quantized value of Hall resistance, Hall resistance is proportional to the superposition of the magnetization and magnetic field (the normal Hall effect). For

ferromagnetism, the magnetization shows a hysteresis loop under the magnetic field sweep. Hence, the Hall resistance will also exhibit similar hysteretic behavior under the field sweep.

The longitudinal resistance R_{xx} , in theory, vanishes as R_{xy} reaches the quantized plateau. However, the existence of the 3D bulk bands will also contribute to the resistance. As discussed in Chapter 5, the transport measurements indeed revealed contributions from both the surface and the bulk bands.

1.1 Ways to open the gap

Despite various interesting properties associated with the gapless Dirac dispersion relation on the surface of both TIs and graphene at room temperature, opening up a gap in the Dirac spectrum or further externally controlling the open and close of a gap can provide more opportunities for applications, especially since it can be done without the need of an external magnetic field.

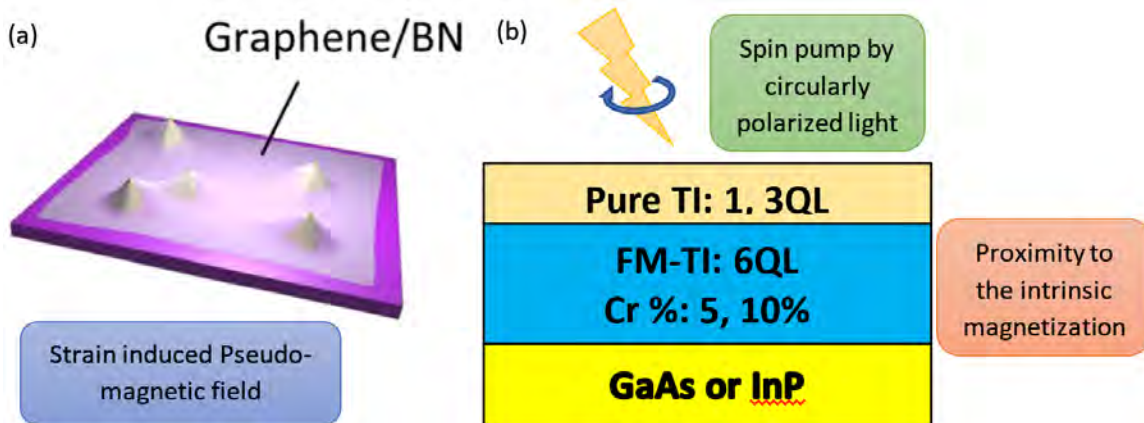


Figure 1.2: Various methods to open a surface gap without an external magnetic field. (a) Creation of giant pseudo-magnetic fields by nanoscale strain engineering of graphene [14]. (b) Schematic illustration (a side view) for the proximity of a pure TI to a magnetic TI with intrinsic magnetization, which leads to broken TRS and opening of a surface gap. The addition of circularly polarized light can further enhance the magnetization. [15]

In the case of graphene, through both theoretical simulations and experimental verifications, our group has demonstrated that non-trivial strain on graphene can induce lattice symmetry

breaking and resulting in pseudo-magnetic fields (Figure 1.2 (a)). Therefore, by placing graphene onto nanoscale architected substrates, Landau levels associated with strain-induced giant pseudo-magnetic fields have been observed by scanning tunneling spectroscopy (STS). The pseudo-magnetic fields can reach up to 800 T easily by proper design of the strain on graphene. Moreover, the pseudo-magnetic field has opposite effects on different valleys. Therefore, valley splitting can be achieved by passing electrical currents through properly designed pseudo-magnetic field patterns, leading to the observation of quantum valley Hall effect, spontaneous symmetry breaking, and quantum anomalous Hall effect. These novel phenomena associated with such “quantum straintronics” have been demonstrated in a recent publication of our group [16] and the Ph.D. thesis of our group member Chen-Chih Hsu [14].

In the case of topological insulators, doping Cr in TI can result in a ferromagnetic TI at the low temperatures. If the induced magnetization is vertical to the surface of the sample, TRS will be broken. On the other hand, the bandstructure of a Cr-doped magnetic TI (MTI) is also modified due to both electronic doping and structural distortion effects. Therefore, the effective Hamiltonian of the MTI surface state will likely deviate from that given in Eq. (1.2). To prevent complications associated with the Cr-doping, our collaborators at UCLA developed bilayer structures that consisted of a pure TI layer on top of a Cr-doped TI by means of molecular beam epitaxy (MBE). Therefore, if the surface gap of the pure TI in the TI/MTI bilayer structure becomes open, it will be the result of its proximity to a finite magnetization underneath (Figure 1.2 (b)) so that the Hamiltonian in Eq. (1.2) holds for the surface state. This thesis describes detailed investigations of such bilayer TI/MTI structures for different types of TI materials by means of both scanning tunneling spectroscopy and electrical transport measurements. Additionally, preliminary studies by introducing circularly polarized light to preferentially excite spin-polarized carriers have been carried out in an attempt to achieve better spin alignment to enhance the magnetization without an external magnetic field.

Another way to open a surface gap in TIs is through the interaction between the Dirac states on the opposite surfaces. If a 3D TI is sufficiently thin (< 5 nm), the interference between the

top and bottom surfaces will cause the gap to open. Similarly, for bilayer graphene, the interference of the electronic bands between the two layers will result in gap opening. In the case of A-B stacking, a small gap appears while the energy dispersion changes from linear to quadratic. For twist bilayer graphene at the “magic angle” ($\sim 1.1^\circ$), the electronic bands around the Fermi level become flat, leading to Mott insulating states and even superconductivity at low temperatures [17-19].

1.2 Potential applications of magnetic TIs

As discussed earlier, the appearance of QAHE is associated with the generation of chiral edge modes, which are promising for various technological applications. Although theoretically, QAHE in MTIs was expected to appear at temperatures sufficiently below the Curie temperature (typically ~ 30 K), experimentally QAHE could only be reached in certain types of MTIs and at extremely low temperatures (< 30 mK) [20, 21]. The physical origin for this extreme sensitivity of QAHE in MTIs to thermal excitations was not understood, and the requirement of ultralow temperatures for realizing QAHE essentially rendered most applications of MTIs impractical. Therefore, the motivation of our investigation was to first understand the physical origin for the lack of QAHE at intermediate temperatures below the Curie temperature and then to find proper means to mitigate the cause so that the ferromagnetism of MTIs can be enhanced to achieve QAHE at higher temperatures.

Another interesting phenomenon theoretically predicted for the TI/MTI bilayer structures is the topological magnetoelectric (TME) effect [22-26], which refers to the induction of magnetic fields by electric fields and vice versa. This effect could enable controls of magnetic domains in MTI by electric fields. Since the image charge of a point charge is a magnetic monopole under the TME effect, an STM tip could induce magnetic monopoles during the scan, thereby helping align magnetic moments along the z -axis. Such possibilities may also be explored by proper experimental designs.

The Cr-doping in the bottom MTI of the bilayer structure could also give rise to isolated magnetic impurities in the top TI layer. Our investigation of these isolated magnetic

impurities in the otherwise pure TI revealed that they were very stable as the result of topological protection and behaved like two-level systems, which may find applications in quantum memory. In particular, the STM tip may serve as the control to switch the state of an isolated magnetic impurity through the TME effect. Additionally, a circularly polarized light may be applied to switch the spin state of an isolated magnetic impurity.

1.3 Scope of this thesis

This thesis focuses on the investigation of two types of Dirac materials: topological insulators and graphene. The research methodology includes scanning tunneling microscopy and spectroscopy (STM/STS), electrical transport measurements using a Physical Property Measurement System (PPMS), and simulations.

The remaining parts of this thesis are structured as follows. Chapter 2 describes the details of the experimental setup for the research. In Chapter 3, STM/STS studies of both the binary and ternary types of magnetic topological insulators (MTIs), as well as the physical implications of our experimental findings, are discussed. Chapter 4 describes detailed studies of the electrical transport properties of both the binary and ternary MTIs by the PPMS and provides comparisons between the macroscopic information thus obtained with the microscopic information derived from STS studies. In Chapter 5, simulations carried out to account for the Moiré patterns, and structural superlubricity observed empirically are detailed. Finally, the primary results derived in this thesis and suggestions for future research directions are summarized in Chapter 6.

Chapter 2

INSTRUMENTATION AND METHODOLOGY

The electronic structure of graphene involves 2D bulk states with 4 Dirac cones, while that of 3D topological insulators (TIs) consists of 2D surface states with 1 Dirac cone in addition to the 3D bulk state. Among many experimental techniques employed to investigate the properties of these Dirac materials, in this work we focus on imaging and studying the local electronic density of states by a homemade scanning tunneling microscope (STM), and on measuring the macroscopic electrical transport properties by a commercial Physical Property Measurement System (PPMS).

For the investigation of TIs, it is generally desirable to have the Fermi level located within the bulk gap and close to the Dirac point to ensure dominant contributions from the topological surface states. This objective may be achieved by either using a back gate or optimally doping the TI during the growth to tune the Fermi level. The TI thin films and heterostructures studied in this work were fabricated by molecular beam epitaxy (MBE) techniques[2, 27-31] and were provided to us by our collaborators in Professor Kang-Long Wang's group at UCLA. These samples had been optimally tuned during the growth process so that the Fermi level of each sample was sufficiently close to the Dirac point. Since the TIs are air-sensitive and degrade with time, the surface of most samples provided to us was covered by a protective capping layer. Therefore, we had to remove the capping layer in a vacuum or inert gas environment prior to our experiments.

2.1 Scanning tunneling microscopy (STM) system

Scanning tunneling microscopy (STM) combines the distance-sensitive quantum tunneling effect and piezoelectric control to explore the local electronic density of states (DOS) of sample surfaces with high spatial and energy resolutions. Therefore, it provides a potent technique to perform noncontact, atomically resolved imaging, and spectroscopic

measurements. Because the tunneling current exponentially decays with distance, the surface states of the sample contribute most. Since both topological insulators and graphene have 2D Dirac surface states, STM is an ideal tool for investigating their characteristics.

To achieve the highest resolution in an STM image, an atomically sharp STM tip and low noise conditions (both mechanically and electronically) are required. In the following, we will first briefly review the theory of STM and its operation principles, and then describe the current setup of our homemade STM. Some upgrades to the STM system have been made by the author and/or other group members to reduce the noise level and to introduce new capabilities (such as a back gate and photo excitations). With the added capabilities, more versatile experiments can be carried out in the future.

2.1.1 STM theory

Scanning Tunneling Microscopy is based on quantum tunneling. The simplest way to understand its operation is to consider a single electron passing through a potential barrier (Figure 2.1). Even if the electron energy is lower than the potential barrier, there is still a finite probability for the electron to appear on the other side of the barrier. However, the probability of tunneling attenuates exponentially with the barrier thickness s , which makes it a very sensitive method to detect the barrier thickness. Mathematically, the transmission coefficient can be expressed as T:

$$T \sim e^{-2\chi s} \quad (2.1)$$

with the decay rate

$$\chi = [2m(V_0 - E)]^{1/2} / \hbar.$$

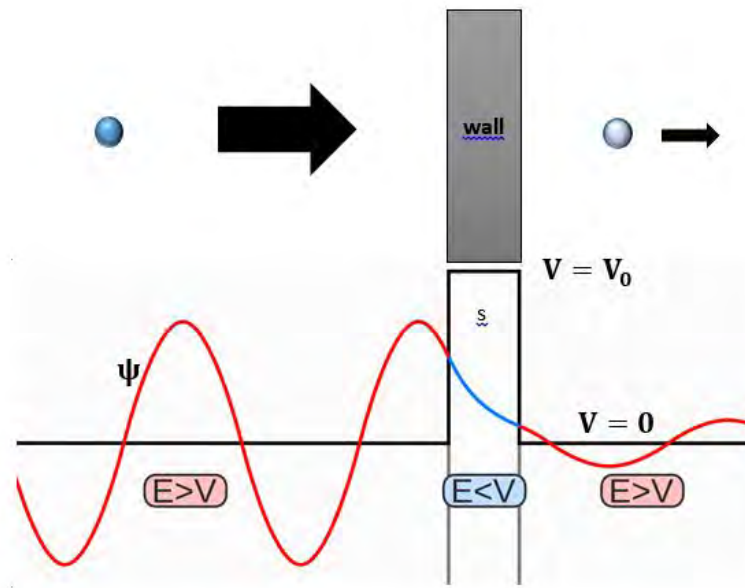


Figure 2.1: Tunneling effect of a single electron. When an electron of energy E moving from the left encounters a barrier of potential energy $V_0 > E$ and thickness s , there is a finite probability for the electron to tunnel through the potential barrier, and the transmission probability to the right will depend on V_0 , E and s .

For realistic conditions, though, electrons are bound inside the materials, which may be conductors, semiconductors, or insulators. Vast amounts of electrons inside crystalline materials form electronic band structures with valence bands and conduction bands. Given that electrons are fermions, they follow the Fermi-Dirac distribution so that no two electrons can occupy the same state. Therefore, we define the Fermi level as the energy level below which all the electrons occupy the lowest possible energy states in the band structure. In the case of metals, the motion of conducting electrons are free-electron like in bulk. However, to leave the bulk of a metal, electrons must overcome a work function, which naturally serves as a potential barrier.

For STM measurements, we move a tip very close to the sample surface (Figure 2.2). The tip is usually made of tungsten (W) or Pt/Ir and is thus metallic. We can approximate the density of states (DOS) of the STM tip as the constant around its Fermi level. Since the tunneling current (I) is proportional to the density of states of both the sample and the tip, the

current is expected to be proportional to the DOS of the sample when the DOS of the tip is constant.

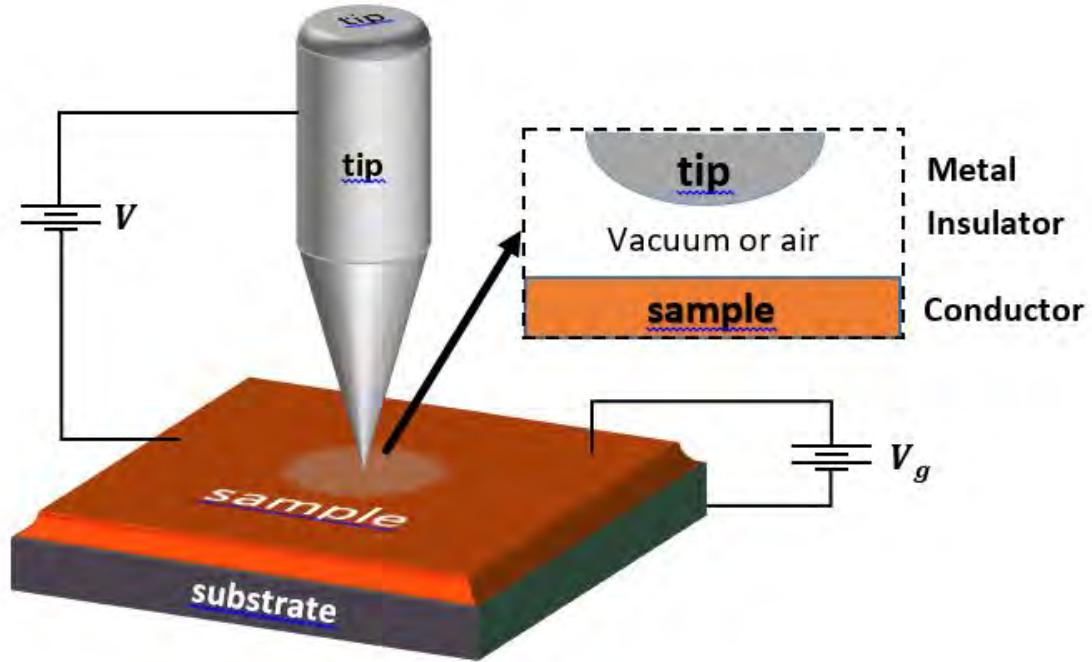


Figure 2.2: Schematic illustration of STM operation with a tip near a sample surface. The work functions of the tip and sample form potential barriers. The effective barrier thickness is the distance between the tip and the sample. When a bias V is added between the tip and the sample, a tunneling current will cross between the tip and the sample, with the direction determined by the sign of the bias voltage. If a back gate voltage is added between the sample and the substrate, we can further tune the Fermi level of the sample so that the density of states of the sample may be studied as a function of the Fermi level.

If the sample is metal, we may consider the tip, vacuum, and sample as a metal-insulator-metal tunneling junction. Following Bardeen's approach [32], the current can be evaluated in the first-order time-dependent perturbation theory, which yields the following expression:

$$I = \frac{4\pi e}{\hbar} \int_{-\infty}^{+\infty} [f(E_f - eV + \epsilon) - f(E_f + \epsilon)] \rho_s(E_f - eV + \epsilon) \rho_T(E_f + \epsilon) |M|^2 d\epsilon. \quad (2.2)$$

Here the Fermi-Dirac distribution function is given by $f(E) = \frac{1}{e^{(E-E_f)/(k_B T)} + 1}$, ρ_S and ρ_T are the DOS of the sample and the tip, respectively, E_f is the Fermi level, and M is the tunneling matrix defined by

$$M_{ST} = \frac{\hbar^2}{2m} \int d\mathbf{S} \cdot (\psi_S^* \nabla \psi_T - \psi_T \nabla \psi_S^*), \quad (2.3)$$

where ψ_S and ψ_T are the wave functions for the sample and the tip, respectively. The surface integral is over the closed surface wrapping around the region between the tip and the sample. The rate for electron transfer is determined by the Fermi's Golden Rule.

Equation (2.2) can be further simplified if we approximate the Fermi-Dirac function as a step function. Since $k_B T = 0.025 eV$ for $T = 298K$, this is a valid assumption if our bias voltage sweep range is much larger than the thermal energy. Thus, Eq. (2.2) becomes

$$I = \frac{4\pi e}{\hbar} \int_0^{+eV} \rho_S(E_f - eV + \epsilon) \rho_T(E_f + \epsilon) |M|^2 d\epsilon. \quad (2.4)$$

This equation can be easily understood by considering Figure 2.3: In the absence of any bias, the Fermi level from the tip and the sample reach equilibrium so that there is no net current. When there is positive sample bias, the electrons tunnel from the filled DOS of the tip to the empty DOS of the sample. When there is a negative bias, the electrons tunnel from the filled DOS of the sample to the empty DOS of the tip.

If we use a metallic tip (*e.g.*, W, Pt/Ir), we may assume $\rho_T(E_f + \epsilon)$ is a constant. Therefore, we can calculate the differential conductance as follows:

$$\begin{aligned} \frac{dI}{dV}(V) &\propto \rho_S(E_f + eV) \rho_T(E_f) M^2(eV, eV) \\ &+ \int_0^{+eV} \rho_S(E_f - eV + \epsilon) \rho_T(E_f + \epsilon) \frac{d|M|^2}{dV} d\epsilon. \end{aligned} \quad (2.5)$$

Since the transmission coefficient M^2 is smooth and monotonic, the last term in the equation (2.5) can be ignored. Therefore, we obtain the relation:

$$\frac{dI}{dV}(V) \propto \rho_s(E_f + eV). \quad (2.6)$$

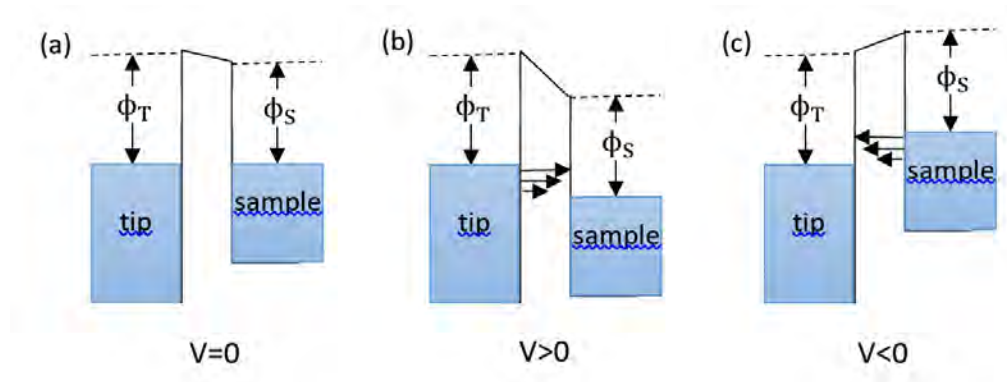


Figure 2.3: Energy level diagrams for the sample and tip separated by a small vacuum gap. **(a)** No bias. Sample and tip are in equilibrium. No net current. **(b)** Positive sample bias; electrons tunnel from tip to the sample. **(c)** Negative sample bias; electrons tunnel from sample to tip.

Consequently, we can extract information about the DOS of a sample if we use a metallic STM tip under a small bias voltage and evaluate the tunneling conductance dI/dV . For all STM measurements described in this thesis, we have always used Pt/Ir for the tip. In principle, if the STM tip is replaced by a ferromagnetic metal (*e.g.*, Ni) or coated with a ferromagnetic thin film (*e.g.*, Cr), the tunneling currents will have preferred spin polarization so that the spin-polarized STM (SP-STM) can be used to study the spin-dependent DOS of a sample.

Even though we know how to extract the DOS information from the tunneling effect, STM would not be viable unless we know how to control the tip position. Piezoelectric materials make precision control possible. When we apply a voltage across a piezoelectric material, it will deform and become shortened, lengthened, or exhibit sheer motion (Figure 2.4 (a)). Despite generally small deformation associated with piezoelectric materials, it is more than enough for atomic-scale studies by STM. By applying different biases to piezoelectric

materials, we can control their deformation and, therefore, the tip that is connected to these materials. Through the bias applied to the piezoelectric material, we can also obtain information about the location of the tip and control the tip to scan over areas of the sample surface on demand. With the introduction of the feedback loop, we can even maintain the distance between the tip and the sample during the scan. Combining the information acquired from the tip-sample distance as a function of the tip location in the XY-plane, we can obtain a topologic image of the sample surface, as illustrated in Figure 2.4 (b).

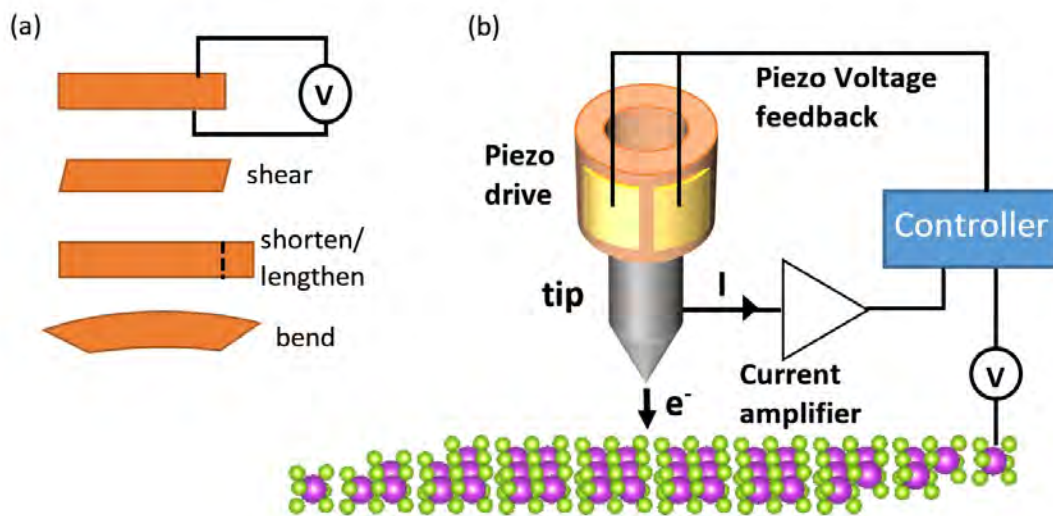


Figure 2.4: (a) Different distortion modes of piezoelectric materials. When a voltage is applied to both sides of the piezoelectric, it could deform into shear motion, contraction/expansion, and bend. We can use different types of deformations to design the proper piezo drive for the STM tube scanner and the sample stage. (b) Illustration of a realistic STM configuration. Here a piezo drive is used to move the tip in x , y , z directions. When a bias voltage is applied across the tip and sample, a tunneling current is induced. The controller provides the feedback and selects the desirable STM operational mode for measurements.

2.1.2 STM operation

To perform STM measurements, we first need to bring the tip close to the sample surface. The distance between the tip and the sample can be controlled by the tunneling junction resistance $R_{\text{junction}} = V_{\text{bias}}/I$, which is typically about $1\text{G}\Omega$ with bias on the order of 1V and a tunneling current on the order of 1nA . Once the distance is set, we can do a scan with one of the scan modes: topography or spectroscopy scan.

Topography scan

For a quick topography scan, the bias voltage between the tip and sample is fixed. The tip is moved along the surface of the sample to obtain tunneling current or height information. Since the data is continuously taken, we can get a high-resolution image within a short time. We can also let tip stop by at each pixel to take spectroscopy and get the density of the states to form the topography map later. Depending on the mode we use, we can derive different information. (Figure 2.5)

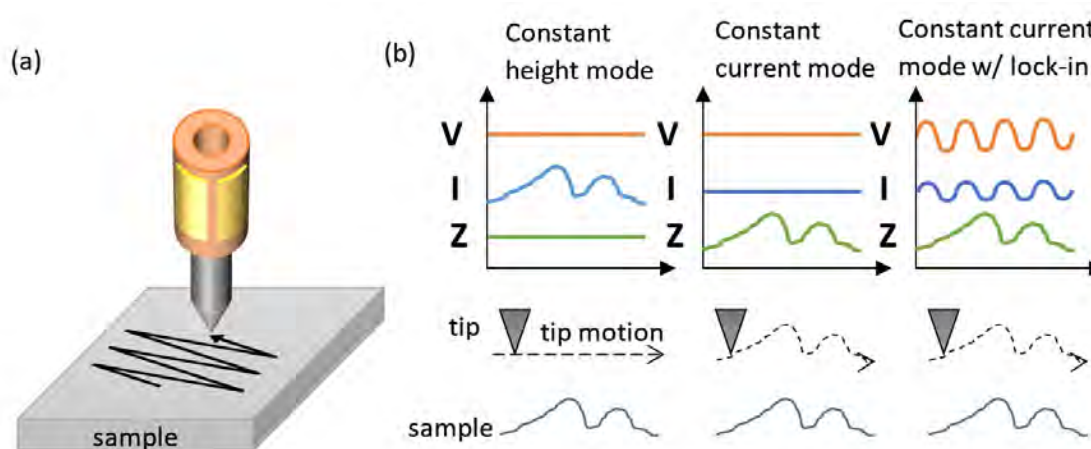


Figure 2.5: Topology scan and its different modes of operation. **(a)** For the topography scan, we use a piezoelectric drive to move the tip and scan the sample surface line by line. **(b) left and middle:** Different modes for topology scan. *Constant height mode* turns off the feedback for z position and keeps the bias voltage constant; the resulting tunneling current, therefore, correlates with the surface topology of the sample. *Constant current mode* uses a feedback loop to adjust the z position and to keep the current constant. The topography profile can be recorded during the scan, and thus we obtain the topographic images directly. **(b) right:** If we add a small AC bias and use lock-in techniques to extract the AC response, we can measure the DOS at the same time with a topology scan.

Constant height mode: In this case, as shown in figure 2.5 (b) left, the feedback for the z -direction is turned off, and the STM tip scans the surface of the sample at a constant tip height and a constant bias voltage and then measures the current. If the surface is relatively flat, the current would be positively correlated to the sample topography. Nevertheless, the topography can only be determined qualitatively not quantitatively, because when the

sample-tip distance changes, the transmission coefficient $|M|^2$ changes too. Also, this is a very dangerous mode because it is impossible to ensure atomic flatness over the scan areas of the sample, and so the fast constant-height scan could risk crashing the tip onto possible protrusion from the sample surface. A more practical way is to reduce the speed of feedback so that the tip only responds to large scale features. Then the large scale features can be seen on the topography map while small scale features can be seen on the current map.

Constant current mode: In this case, as shown in figure 2.5 (b) middle, the feedback of the z -direction is used to maintain the current constant during the scan on the surface of the sample. Since we know the z height along with the scan, the z height is usually proportional to the topography (strictly speaking DOS). For this mode, the feedback needs to be fast enough to maintain the constant current. However, it should not be too fast; otherwise, it could falsely respond to the noise in the current. In the spectroscopy scan, the tip would stop at each pixel and hold onto the same tunneling junction resistance as initialization. This setup is virtually a constant current mode at a much slower pace, and therefore, we can also obtain topographic images while doing spectroscopy scan. The image we derive from this constant current mode is not a simple topography of the surface. Rather, it is a topography of constant DOS. Therefore, by applying different biases, we can explore the DOS map at different energy of the band. Since different orbitals or spin states have different energy levels, we may even explore the DOS map for different bonding or spin states of the sample.

Spectroscopy scan (Scanning Tunneling Spectroscopy or STS)

In this mode, we want to acquire the current-voltage characteristics (I-vs.-V curve) for each point so that we can calculate the tunneling conductance (dI/dV) to obtain the tunneling conductance map (and thus the DOS map) for different bias voltages. For the spectroscopy scan, the tip stops at each pixel (Figure 2.6), where the tip holds its height with a set R_{junction} . Then the bias voltage is swept through a range we set, and the tunneling current is measured and recorded. In this way, we can obtain the I-vs.-V curve at each pixel. Since we hold the same R_{junction} value at each point as an initial condition, we can also derive height information and thus the topography from the spectroscopy scan. With an I-vs.-V plot for

each point, we can calculate the corresponding (dI/dV) -vs.- V for each pixel and obtain the conductance map at different bias voltages. To reduce the noise and errors, a typical approach is to measure a backward sweep and then average it with the forward sweep to remove systematic errors. The sweeps are taken several times at the same pixel point to remove random noises.

Spectroscopy scan with a lock-in amplifier

The calculation of dI/dV from I -vs.- V involves differentiation, which could introduce lots of noise for the raw data. Therefore, measuring dI/dV directly would be a better approach.

To measure dI/dV directly, we add a small sinusoidal bias voltage $\Delta V \cos(\omega t)$ onto the DC bias voltage and measure the response sinusoidal current $\Delta I \cos(\omega t)$ through a lock-in amplifier. We know that

$$\Delta I(V_{DC} = V_{bias}, I = I_{set}) = \frac{\Delta I}{\Delta V} \Delta V (V_{DC} = V_{bias}, I = I_{set}). \quad (2.7)$$

Because $\Delta I \ll I_{set}$ and $\Delta V = \text{constant} \ll V_{bias}$, $\frac{\Delta I}{\Delta V} \approx \frac{dI}{dV} (V_{DC} = V_{bias}, I = I_{set})$. We get

$$\Delta I \propto \frac{dI}{dV} (V_{DC} = V_{bias}, I = I_{set}). \quad (2.8)$$

Thus, through a lock-in amplifier, we can get $\Delta I (V)$ which is proportional to $\frac{dI}{dV} (V)$. To make the lock-in method work, ω^{-1} needs to be much less than the feedback response time, so that the tunneling junction resistance is maintained based on the DC bias and current. The lock-in takes time to recognize a sinusoidal output. When the controller sweeps through the range of bias, it needs to wait at each value of bias for a much longer time. (figure 2.6 (b) right)

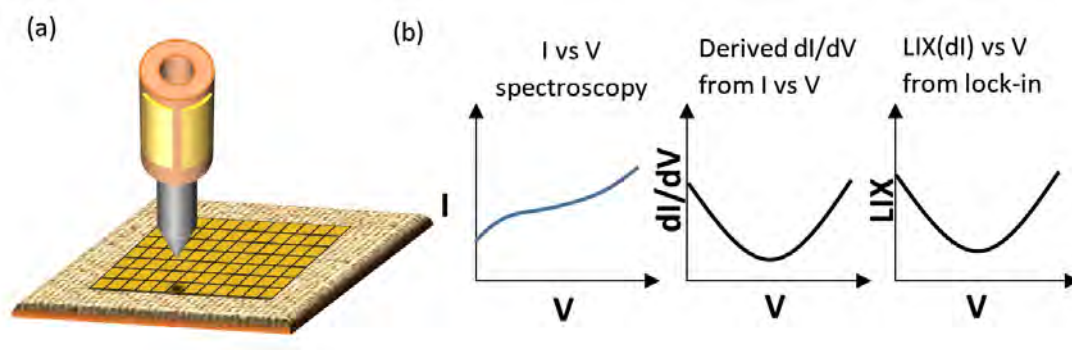


Figure 2.6: Schematic illustration of the spectroscopy scan. (a) Measurement is taken on each pixel point of the grid over the area we would like to scan. Whenever the tip moves to the new pixel point, the tip height is initialized to the set tunneling junction resistance and hold its position before sweeping the voltage. (b) Two modes that we can use to obtain DOS-vs.-V spectrum. One is to measure I-vs.-V and then calculate dI/dV -vs.-V from it. The other is to use the lock-in technique to derive signal LIX, which is proportional to (dI/dV) so that dI/dV -vs.-V can be measured directly.

Although, in theory, the lock-in technique is a better way to obtain the conductance map data, this method could take up to several days to complete a scan so that the average location of the tip relative to the sample may have drifted significantly. Additionally, for low-temperature measurements, time is more limited because of a finite evaporation rate of liquid helium. The presence of AC noises from electrical cables could also introduce excess noises to the lock-in response and make the measured response unstable. Therefore, for most experiments, we only measured I-vs.-V for STS. On the other hand, our controller provides a built-in lock-in function module that can be used for direct (dI/dV) -vs.-V measurements so that we can choose the lock-in option when needed.

2.1.3 STM system overview

From the introduction above, we know that to build a successful STM system, we need at least a tip, a piezo drive, a feedback system for controlling the piezo drive from tunneling current, a bias voltage system, and a pre-amplifier to amplify the weak tunneling current. However, to maintain the distance between the tip and sample at the angstrom scale, a noise-free environment is necessary. Any mechanical vibration from the ground, building, or sound in the environment can easily cause several nanometers (nm) vibrations. The tunneling

current we measure can be as small as a few pico-amperes (pA) and hence require a current amplifier to amplify the signal to be detectable. Any environmental electromagnetic radiation can readily introduce substantial noise currents. Therefore, it is essential to optimize the shielding of electromagnetic noises so that the feedback can respond to the real signal.

The microscope used in this thesis was previously designed and built by Ching-Tzu Chen and Nils Asplund[33]. It was subsequently modified by Andrew Beyer [34] and Marcus Teague [35]. Additional modifications to the STM head were made by the author and will be described in detail later. Here, we introduce the overall STM setup first.

The main body of the STM probe is a stainless steel stick with several partitions to block thermal radiations and with several copper cold fingers to enhance the thermal conduction to the STM can (Figure 2.7 (a)). The STM can is a metal tube that provides protection and vacuum seal to the STM probe. The STM can be separated into the top part and bottom part. The top part is made of stainless steel, while the bottom part is made of copper.

For cryogenic experiments, good thermal isolation between the top and bottom parts of the STM probe and the STM can is essential. Stainless steel has low thermal conduction at low temperatures and is a solid material with sufficient mechanical strength. Therefore, both the top part of the STM probe and STM can are made of stainless steel to prevent heat load from top to bottom.

The bottom part of the STM probe is the STM head. More details about the STM head will be given in the next subsection. The STM can is separable so we can load the sample directly inside the glove box in an argon environment. This design is crucial when handling air-sensitive samples. We insert the STM probe into the STM can and then move it to the glovebox. The glove box is filled with argon gas so that it is safe to expose the air-sensitive sample in argon after it has been annealed or etched and then loaded into the STM head. After the sample is loaded, an indium wire is used as a gasket between the top and bottom parts of the STM can. Finally, both parts are tightened together with a set of screws.

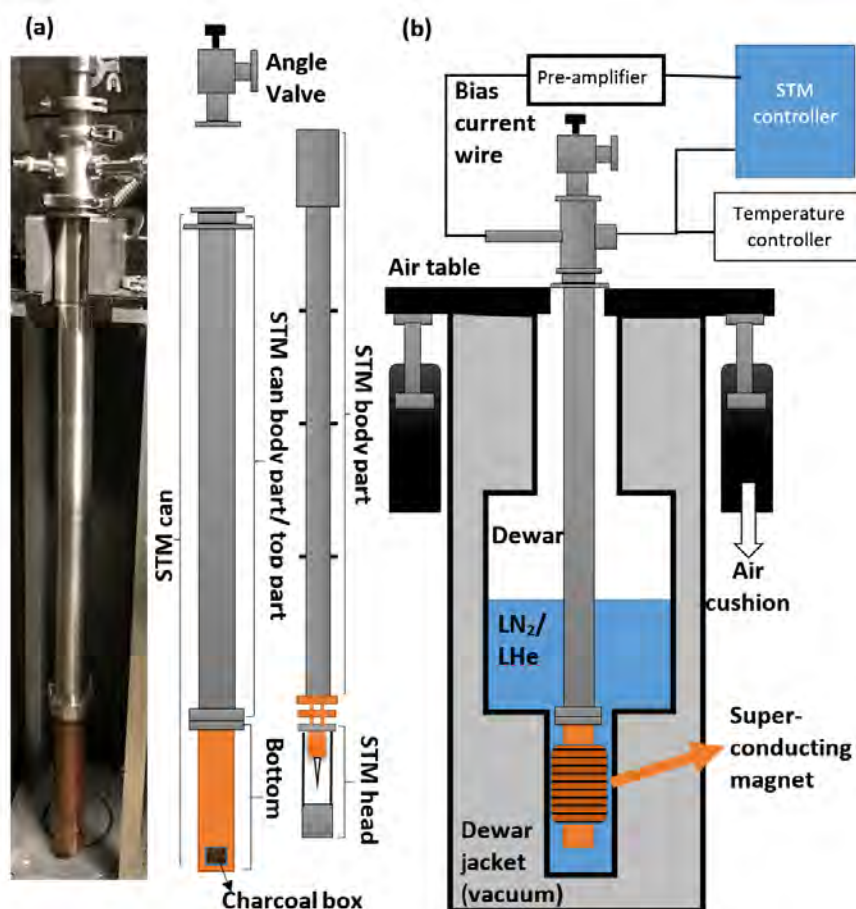


Figure 2.7: STM probe and its Dewar. **(a)** The STM probe consists of a probe body and a probe head. The STM head includes a tube scanner, piezo drives, and sample stage. The entire STM probe is protected by the STM can, which can be separated to the top part and the bottom part. The bottom part is made of copper for better thermal conduction in liquid helium. The charcoal box is placed at the bottom of the bottom can as a cryogenic pump to enhance the vacuum more. The top part is made of stainless steel to reduce the thermal load from room temperature. The angle valve is used to seal the STM probe so that we can vacuum it. **(b)** The STM probe is placed inside the STM Dewar. The Dewar is installed on an air table to reduce mechanical vibration. Dewar jacket needs to be vacuumed to enhance thermal isolations. The Dewar can be filled with different cryogens like liquid nitrogen (LN₂) or liquid helium (LHe) to lower the temperature of the Dewar and STM probe. A 7-T superconducting magnet is installed at the bottom of the STM Dewar. It can only be used when it is fully immersed into liquid helium and cooled below the superconducting transition temperature. Several wires connect the STM head to the feedthrough at the top of the probe. The bias current signal is sent through the pre-amplifier first before it enters the STM controller. The temperature sensor and heater are controlled by a temperature controller.

The STM probe with the outer can is capped by an angle valve so we can evacuate the argon gas inside the STM can by first using a roughing pump and then a turbopump. Even though a high vacuum is not necessary for an air-stable sample like graphite or gold, keeping the STM probe in a high vacuum environment is still a good measure to prevent potential contamination and keep the STM system under a premier condition. Additionally, the voltage required for activating the piezo drives can be as high as 400 V, which could cause discharge and damage the piezo drive in the absence of a high vacuum. Finally, for measurements at cryogenic temperatures, it is essential to evacuate residual air from the STM system to prevent the liquification of air at liquid nitrogen temperature (77K) and ice formation of air at liquid helium temperature, which could cause damage to the STM head. Moreover, an ultrahigh vacuum is particularly crucial for cryogenic measurements because even a very thin layer of liquefied air or ice on the sample surface could complicate or even nullify STM studies of the sample.

With a turbopump, the pressure at room temperature can reach $\sim 10^{-6}$ torr if the STM probe was baked before the insertion of a sample. A small copper box full of charcoal is placed at the bottom of the STM can, which can be activated at low temperatures as a cryogenic pump. The final pressure reaches as low as $\sim 10^{-10}$ torr at liquid helium temperature. After pumped down to a vacuum level of $\sim 10^{-6}$ torr, the STM probe is inserted into a steel vacuum jacket mounted in an Oxford cryogenic Dewar. The Oxford Dewar is set on a three-inch-thick aluminum plate mounted on four air-damped pneumatic legs to reduce mechanical vibrations.

We can transfer cryogen such as liquid nitrogen (LN2) or liquid helium (LHe) into the STM dewar to cool down the STM probe. The dewar jacket needs to be vacuumed before transferring cryogen; otherwise, the air inside the dewar jacket will be frozen and cause damages. As we warm up the Dewar, evaporated cryogen will build up pressure inside the vacuum-sealed dewar jacket quickly. A pressure release valve is used to release the excess pressure and to prevent the potential risk of explosion.

There is a superconducting magnet at the bottom of the STM dewar. The magnet consists of a solenoid of superconducting wires with a superconducting transition temperature significantly higher than liquid helium temperature. Hence, after liquid helium transfer and immersing the entire solenoid in liquid helium, the solenoid becomes superconducting, which can hold a very high current in the persistent current mode without dissipating any energy, as long as the current stays below the critical current of the material. The superconducting magnet is an exceedingly power-efficient way to generate a strong magnetic field for a long time. Our superconducting magnet can hold currents up to 90 A and a maximum field of 7 T with controller shown in figure 2.8(d).

To ensure sufficient cooling power to the sample, we use copper as the material for the bottom part of the STM can. The material of the STM head consists of molybdenum, Macor, sapphire, and aluminum, all non-magnetic to avoid unwanted interferences with the applied magnetic field.

Conducting wires for various purposes connect the STM head to the top of the STM probe. The bias voltage, bias current, piezo drives are controlled by the STM controller (Figure 2.8 (b)). We use the Nanonis controller as our STM controller, which includes HVS4 (high voltage supply), HVA4 (fine approach control), PMD4 (coarse approach control), SC4 (8 output and 8 input ports), and RC4 (the brain of all controllers and connect to the computer). The output signals include the bias voltage and back gate of the STM, and HVA 4 for fine approach control. The input signal is the bias current from the pre-amplifier. The controller connects to the white power or power conditioner in our lab to minimize electrical noises from other facilities in the building. Bias current ground also connects to the white power ground, while bias voltage ground shares the same ground with the controller.

A current pre-amplifier, Femto DLPCA-200 Variable Gain Low Noise Current Amplifier (figure 2.8 (a)), is used to amplify the current before inputting into the controller. This amplifier has a Low Noise (LN) mode and High Speed (HS) mode. The Low Noise mode can amplify current with a gain from 10^3 to 10^9 and the High Speed mode can amplify current with a gain from 10^5 to 10^{11} . Generally, a smaller gain has a higher level of

background noise, which can be even higher than our bias current setpoint. Therefore, we choose as high gain as possible most of the time.

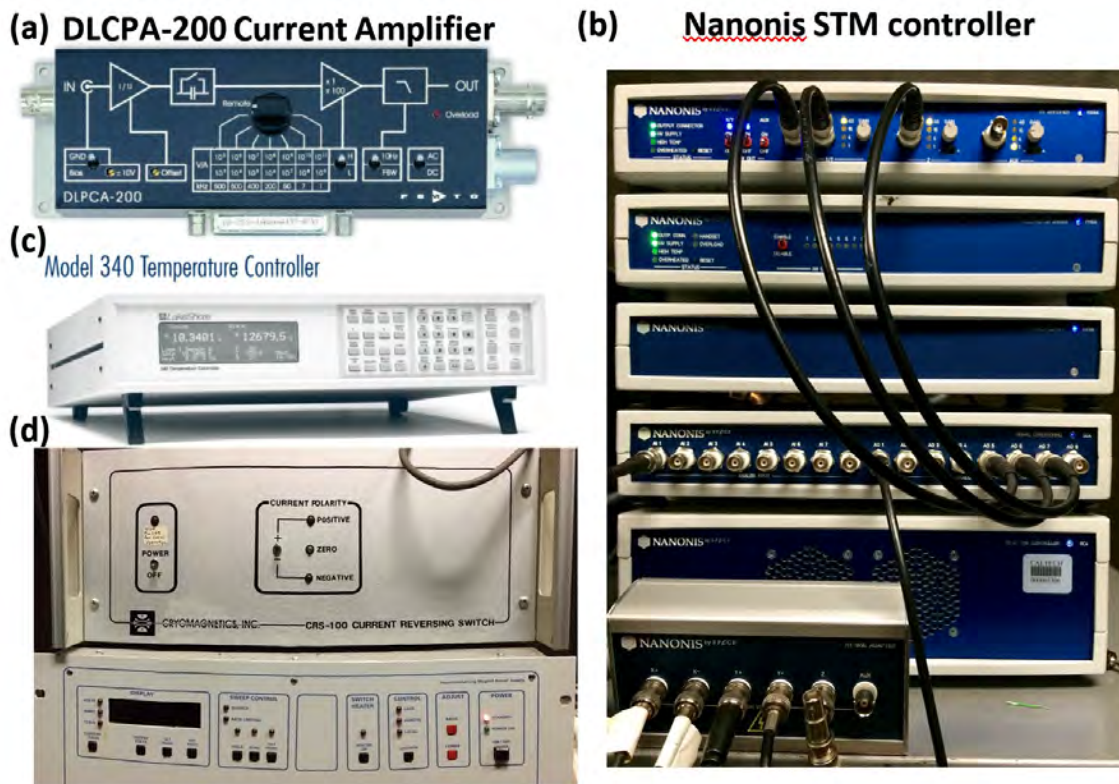


Figure 2.8: Instruments used for the STM system. (a) DLCP-200 Variable Gain Low Noise Current Amplifier (picture adapted from manual). (b) Nanonis STM controller sets. The instruments from top to bottom are HVA4, PMD4, HVS4, SC4, and RC4. (c) LakeShore Model 340 Temperature controller. (d) Superconducting magnet controller and current reversing switch.

The conducting wires from the temperature sensor and heater at STM head go to a LakeShore Model 340 Temperature Controller (figure 2.8 (c)). The temperature sensor is CX-1050-SD-4L Cernox Resistor, with a working range from 4K to 325K. The Cernox resistive temperature sensor is chosen for its low-temperature compatibility and negligible sensitivity to the magnetic field.

Our STM lab is at the subbasement of the building. Sound absorbing sponges are attached to all interior walls of the lab. Outside the lab, we cover the wall with sound-reflecting curtains.

Additionally, the air table, together with the STM dewar in the lab, is enclosed by a wooden box with sound-absorbing sponges on both the interior and exterior surfaces. Outside the wooden box, we put four pieces of aluminum walls with sound-absorbing sponges attached to both sides of each wall to surround the wooden box. Here the metallic walls are used to shield electromagnetic radiation. Several heavy bricks are placed on the air table to enhance the total mass of the system, thereby reducing the vibrational amplitude induced by mechanical noise. Lastly, the most significant noise is the 60 Hz noise from the power lines. Therefore, we turn the light off during all STM experiments. Additionally, low noise BNC cables are used for all electrical connections. Despite all the efforts, the ultimate noise level is often determined by other activities (such as the operation of a nearby elevator, running of large vacuum pumps in other research groups, *etc.*) outside the STM lab, which are unfortunately beyond our control. This situation can be mitigated by concentrating more measurements during the evenings and weekends when external activities are much reduced.

2.1.4 STM probe head and upgrade

The STM probe head contains 3 parts: the STM head body, a spacer, and the STM head base (Figure 2.9 (a)). Most components of the STM head are made of Molybdenum (Mb) for conductors and Macor for insulators due to their similar thermal expansion coefficient. The STM head body uses three pairs of piezo stacks to hold a tube scanner and to provide coarse Z motion for the tube scanner to move the tip in big steps continuously. The tube scanner holds the tip and receives a bias current. It contains a piezo tube to move the tip in x, y, z directions and provides finite but more precise motion for the tip.

The STM head base has three pairs of piezo to provide coarse X and Y motion for the sample stage that is made of sapphire (old version) or alumina (new version). On top of the sample stage is the sample holder. After recent upgrades, the STM head base can not only hold the sample but also provide back gate voltages to the sample.

STM head spacer is used to enhance the connection between the head body and head base.

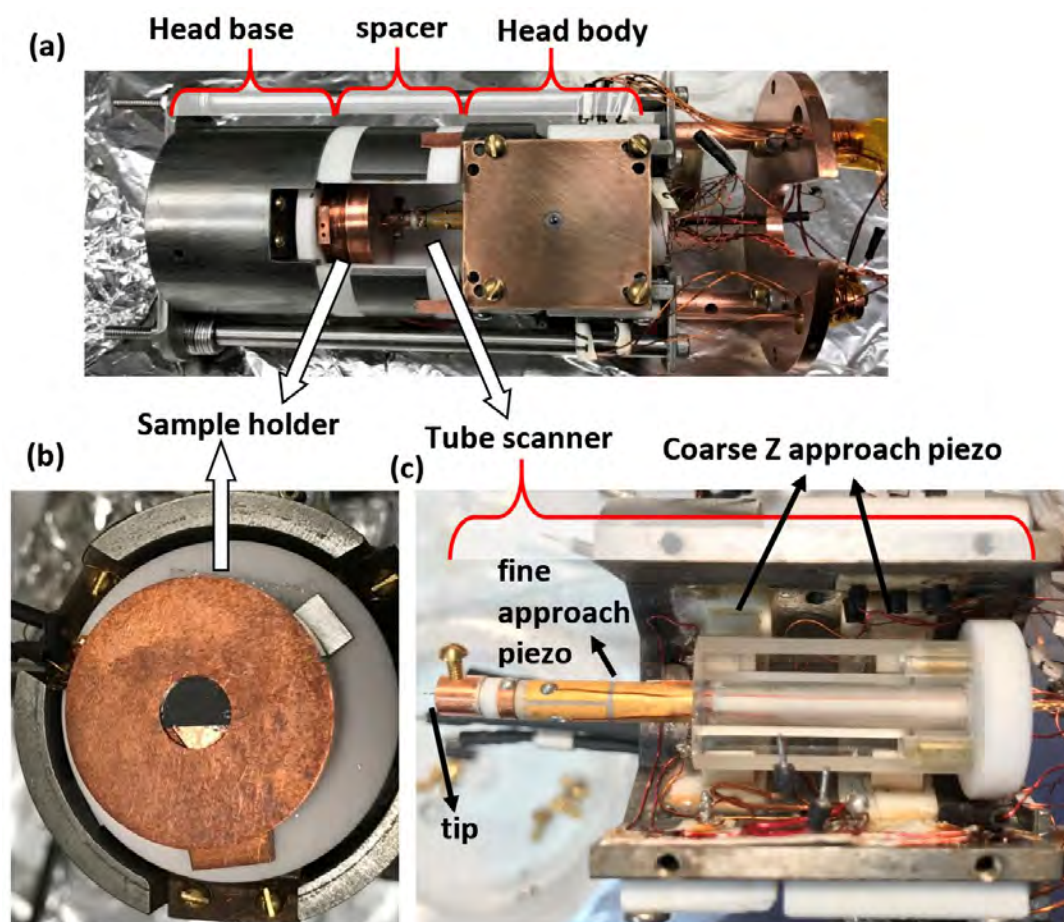


Figure 2.9: Photos for the STM probe head. (a) Assembly of the entire STM probe head. It includes the head body, head spacer, and head base. (b) STM head base holds a sample holder onto the sample stage. It also includes piezo stacks for coarse XY motion to move the sample stage around. (c) STM head body includes tube scanner and coarse Z piezo stack to move the tube scanner up and down. The tube scanner contains a piezo tube to provide fine motion on the tip. It also has a tip holder to hold the tip.

The biggest challenge for STM is to move the tip close to the sample and then form a stable tunneling junction. The separation between the tip and sample surface for STM measurements is only a few nanometers. To enable the tip to find the sample surface successfully without crashing into it, we design the coarse motion and fine motion for the STM tip. Coarse Z motion moves the tube scanner up and down. Without physical limitation of the length of the tube scanner, it can take infinite steps and move the tube scanner by an

infinite distance. Coarse XY motion moves the sample stage around relative to the tip position.

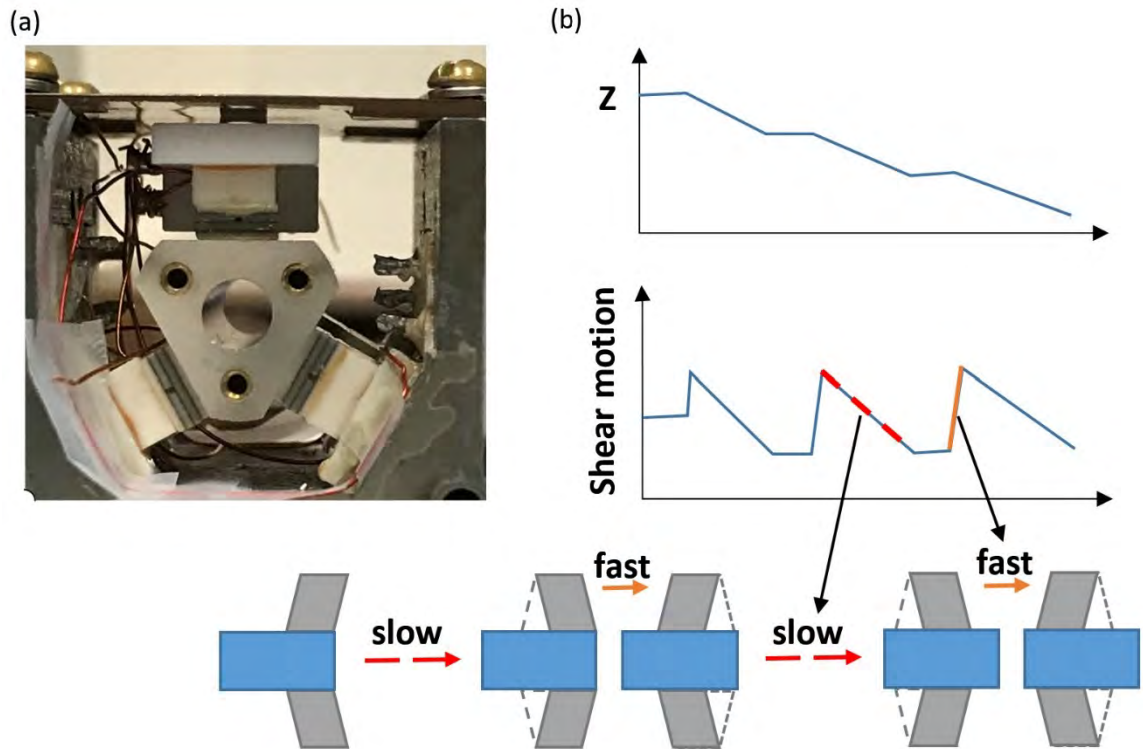


Figure 2.10: Coarse z-motion mechanism. (a) Top view of the tube scanner sapphire crystal inside the Mo head body. In order to keep the sapphire crystal attached to the piezo stack tightly, a triangular cylindrical crystal is required. The copper plate at the top of this image presses the piezo stack onto the sapphire crystal to make the crystal in tight contact with the piezo stacks. (b) The coarse approach is achieved through a sequential fast and slow shear motion of the piezo stack. If the shear motion of the piezo stack is slow enough, the crystal it holds will move with it. On the other hand, if the piezo stack has quick shear motion, the stack will slide through the crystal and make the position of the crystal unchanged. By repeating these steps, the crystal can keep moving until it is out of range.

The coarse motion of the tip is achieved by shear piezo stacks. The mechanism is shown in Figure 2.10. We use 3 pairs of piezo stacks to hold the sapphire crystal of the tube scanner tightly. Then by applying voltages to the piezo stacks, shear motion takes place on the stacks. If the shear motion is sufficiently slow, the sapphire crystal will move with the shear motion of the piezo stacks together. However, if the shear motion is fast enough, the sapphire crystal will stay in the same place. This stick-slip motion is similar to the case of placing a cloth on

a table and putting a bottle on top of the cloth. If we pull the cloth very quickly, the bottle will stay in the same place on the table. On the other hand, if we pull the cloth very slowly, the bottle will move with the cloth. If we keep repeating the stick-slip approach, the sapphire crystal can keep moving until it is either out of range or blocked by some obstacles.

The primary challenge here is to ensure that the piezo stacks attached to the sapphire crystal tightly. Therefore, the sapphire crystal needs to be triangular pillars, so we have the flexibility to clamp the crystal by different tightness we want. The interface between a sapphire crystal and the piezo stack must be smooth so that the sapphire crystal will not be dragged by the shear motion of piezo independent of the speed.

In the past, we calibrated raw piezo stacks and combined those stacks with similar shear strength together. However, the shear strength of piezo stacks diminished with time and thermal cycles. The coarse approaching mechanism no longer worked at low temperatures after several years. We used commercial shear piezo stacks P-121.01T from PI ceramic as our coarse approach piezo drive, where P-121.01T was made of PZT with very high Curie temperature. The piezo material was compatible with the ultra-high vacuum (UHV) environment, and its operating temperature range was from 4 K to 358 K, entirely within our experimental parameter space.

STM tube scanner and its upgrade

The STM tube scanner is the core of the STM operation. It controls the fine motion of the STM tip, decides the scan range of the STM for topography, and collects the tunneling current from the tip. The tube scanner has three parts: Macor pillar and top, piezo tube, and tip holder (Figure 2.11).

The Macor pillar and top provide the support and holds against the triangular cylindrical sapphire crystal. By moving the sapphire crystal via the coarse Z piezo drive, the entire tube scanner moves with it. The Macor pillar has several grooves for electrical wires to run

through from the piezo tube. It protects and physically separates the wires to prevent cross-talks of the electrical signals.

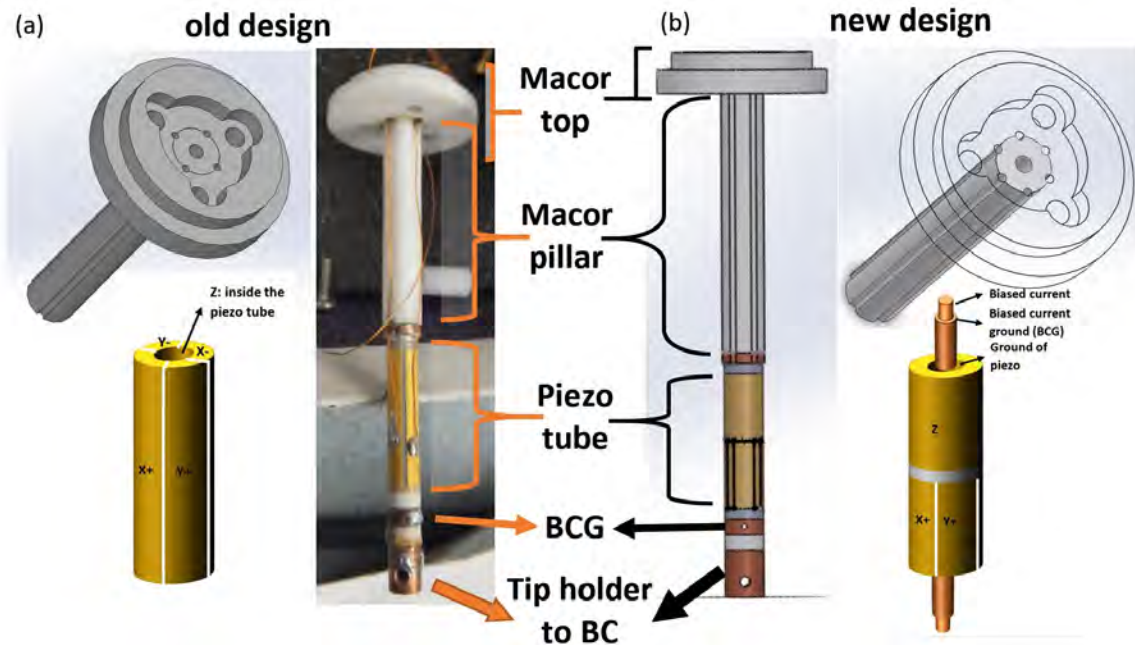


Figure 2.11: Design of the tube scanner. The tube scanner contains Macor top, Macor pillar, piezo tube, copper ring for bias current ground (BCG), tip holder for bias current (BC). The three big holes on the Macor top are for the screws that lock the sapphire crystal. Coarse Z piezo stacks then control the position of sapphire crystal. The design of the tube scanner has been changed due to some problems in the old design. **(a)** The old design of the tube scanner. The piezo tube only had four quadrants to serve as fine X, Y, and Z motion. The Z voltage was applied in the inner side of the piezo tube and used the average voltages of X+, X-, Y+, and Y- as reference ground. Even though there were five wires for X+, X-, Y+, Y- and Z, the Macor pillar only had four grooves while the Macor top only had four small holes. Therefore, the Z wire was forced to go outside the sapphire crystal and was exposed. It was dangerous when the tube scanner was moved by the coarse Z piezo drive with applied high voltage. The piezo tube did not have insulating rings on both ends, and so we had to add an extra Macor ring to avoid possible shorting. The bias current (BC) wire was connected to the tip holder from outside of the tube scanner. The BC wire was also exposed and so might collect excess noise. The dangling BC wire could further introduce vibration noise to the BC. **(b)** The new design of the tube scanner. Here the piezo tube uses the split design to separate fine Z from fine X and fine Y. The inner side of the piezo tube is a shared ground. The top half of the tube is used as a fine Z motion. The bottom portion of the tube is used as XY motions, like the old design. This design also reduces the coupling between fine Z and fine XY. The Macor pillar has six grooves while the Macor top has six holes. All wires from X+, X-, Y+, Y-, Z, and ground can go inside the sapphire crystal and be protected. The BC wire goes into the piezo tube. We can use a stronger coaxial cable with much better shielding as the bias current wire. Since the wire is fixed in the inner hole of the Macor pillar and piezo tube, there is no problem of wire dangling either.

In the old design (figure 2.11 (a)), the Macor pillar only had 4 grooves to accommodate 4 wires from the piezo tube, which left one wire exposed. The author changed the design of the Macor pillar to accommodate 6 grooves for all the wires from the piezo tube to the top of the STM probe. This improvement helped to prevent possible damages and shorting of the wires when the tube scanner moved by the coarse piezo drive.

The piezo tube controls fine X, Y, and Z motion of the STM tip. In the old design, it only had 4 quadrants. Each quadrant could change its length when a voltage was applied. If 4 quadrants of the piezo tube elongated differently, the piezo tube would bend in one direction. On the other hand, the average elongation of all the quadrants of the piezo tube would change the total length of the piezo tube and therefore changed the Z height of the tip. The 4 quadrants were named X+, X-, Y+, and Y- corresponding to the XY motion. The inner side of the piezo tube was called Z.

On the other hand, this weird design coupled the XY motion with the Z motion. It was difficult to be certain of the XY location according to the applied XY piezo voltage under different Z voltages. The piezo tube that we used in the old design was EBL #2 from EBL Products.

With the suggestion of an EBL engineer, we purchased the new split-design piezo tube (figure 2.11 (b)). It partitions half of the tube as fine Z motion and therefore decouples fine the Z motion from the fine XY motion. Because of this new design, the inner side of the tube can be used as a ground, which increases the stability of the circuit and can be used as shielding for the bias current coaxial cable inside the tube. The Z motion part needs to be at the top of the XY motion part so that the elongation from Z piezo is in the Z direction. An insulating ring is added to both ends of the piezo tube, which simplifies the design for the tube scanner without the need to add two extra Macor rings on both ends of the piezo tube.

The tip holder has a hole in the bottom for a tip and side holes for screws to fix the tip. In the old design, there was only one side hole for one screw. When we tightened the screw, the tip would bend. We had to straighten the tip again using a tweezer after tightening the screw,

which could introduce significant strain to the tube scanner and could even break it. To avoid this problem, in the new design, two threaded side holes and two screws are introduced, so two screws can hold the tip at the same time. The tip can, therefore, be kept straight even after screws are tightened.

All tips used for the STM studies described in this thesis use are all made from Pt/Ir wires, which contains 80% platinum and 20% iridium. Platinum is an inert metal and will not degrade or get oxidized with time. However, pure platinum is too soft to be used. Mixing platinum with 20% iridium enhances the hardness of the wire and hence the tip made from it. The tip can be made by mechanically cutting or chemical etching. We have also tried to develop spin-polarized tips by depositing the Cr thin films onto the tip, but it is difficult to justify the effectiveness of the spin-polarization without proper calibration.

For totally flat 2D materials like HOPG, cutting the Pt/Ir wire is not a bad tip-making method as there are always a few dangling atoms at the end of the tip. However, the tip shape is more irregular. Several mini-tips might form at the end of the tip. For a flat surface, we can ensure the lowest mini-tip contributes to the tunneling current. However, for uneven topography, other mini-tips might become closest to the sample. Therefore, most of our STM tips have been made by chemically etching to ensure a symmetrical cone-shaped tip and consistent quality. 1M to 1.5M Calcium Chloride dehydrate solution is used for etching the tip.

In the old design, the bias current wire was connected externally from the side of the STM head body to the tip holder of the tube scanner. The last part of the wire had to be soft and long enough to allow the tube scanner to move around. For this reason, copper wire instead of coaxial cable was used in the last part. This external copper wire had no shielding and so was prone to pick up electrical noises. It was also dangling between the side of the STM head body and the tube scanner. The dangling could produce some vibration and/or introduce extra strain on the tube scanner.

In the new design, the bias current coaxial cable goes through the central inner hole of the tube scanner and piezo tube to reach the tip holder. The coaxial cable and the ground of the

piezo tube provide the shielding to the bias current signal. The coaxial cable is held tightly by the tube scanner and so prevents any dangling vibration. This improvement indeed helps us obtain atomic resolution more easily.

STM sample stage, sample holder and Macor spacer

The STM head base includes the coarse XY piezo drive, sample stage, and sample holder. The sample holder is installed on the sample stage by G-varnish, and the sample stage is clamped by 3 pairs of the piezo drive for the XY motion. (Figure 2.12)

The Macor spacer fixes the distance between the STM head body and the STM head base to keep the head base from vibration. In the old design (Figure 2.12 (a)), the wall of the Macor spacer was thick, with only one opening on one side. This design restricted the size of the sample holder and squeezed all electrical wires out of the same opening. It could cause wires to entangle, making it difficult to connect wires to the connection pins at the top of the STM head or even leading to breakage of the wires. In particular, whenever we had to install the STM head base inside the glove box, squeezing all wires through the single opening of Macor would be challenging.

The sample holder was also very simple. It consisted of a pure bulk copper stand plus a screw and a small copper plate. The small copper plate with a screw was used as a clamp and also the top gate. This design made the top of the sample short with the bottom, which made back-gating the sample impossible. A heater was attached to the bottom of the copper stand while a temperature sensor was attached to the side of the copper stand. The clamp only pressed against the edges of the sample to avoid blocking the tip landing area. However, to hold the sample in place, we had to tighten the screw, and the stress often caused the sample to tilt with one side of the sample hanging in the air. Such tilting would introduce a colossal slope background in topography, which could reduce the resolution of height seriously and could also induce vibration. The sample could also be damaged due to the intense point contact stress.

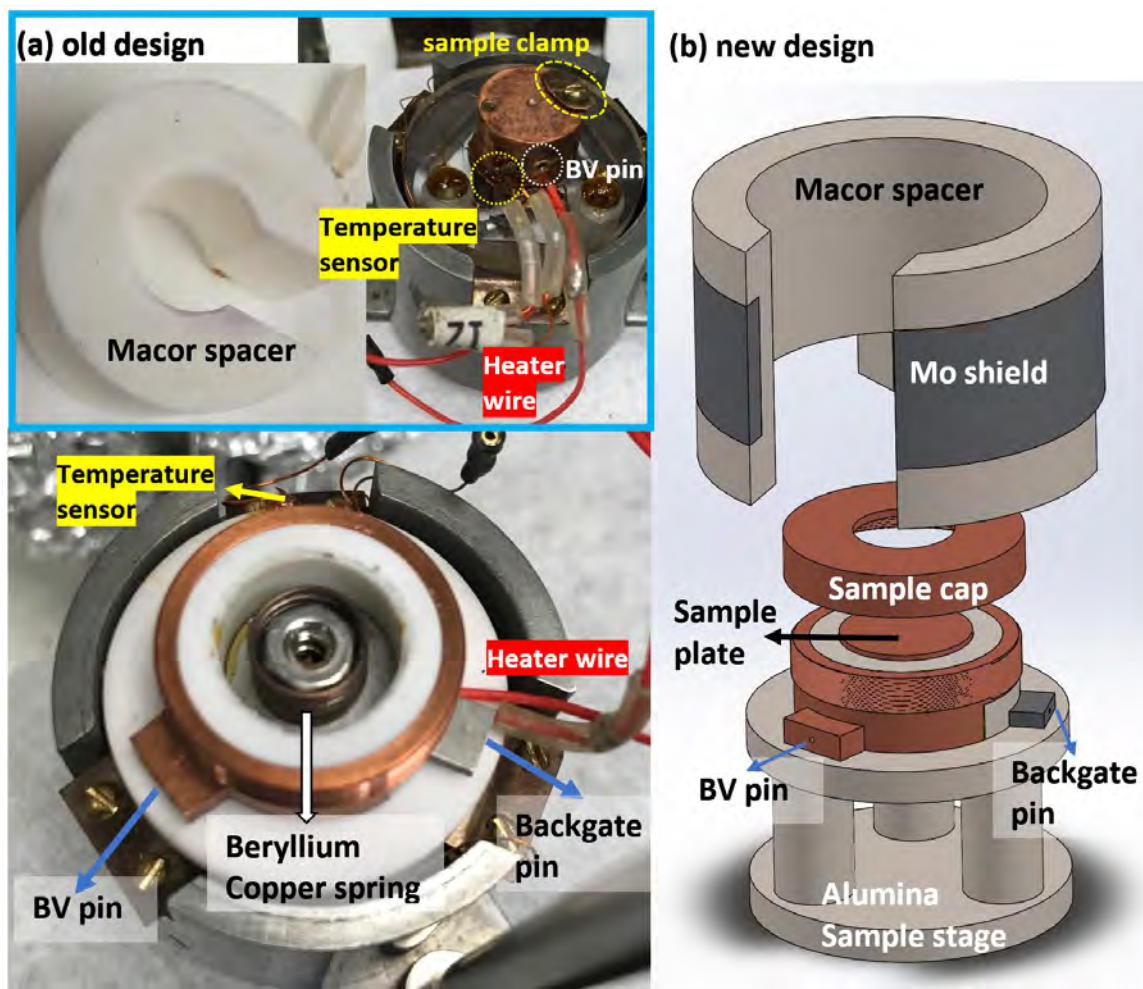


Figure 2.12: Designs of the STM probe head base. **(a)** The old design of the head base and Macor spacer. The sample holder was only a copper stand with a small copper plate tighten by a screw as a sample clamp. A heater was placed under the copper stand. A temperature sensor was attached to the side of the copper stand. The Macor spacer had a thick wall with only one opening on one the side, so that all wires, including temperature sensor wires, heater wires, and bias voltage wire, must come out of the sample opening. Space was narrow and difficult to operate. The clamp only added pressure to the edge of the sample, and so would make sample tilt relative to the STM tip. Also, there was no way to apply a back gate voltage to the sample as the clamp shorted to the copper stand directly. **(b)** The new design of the STM sample holder and Macor spacer. The wall of the Macor spacer is thinner with 3 openings to allow electrical wires to get through. The Mo shield is installed on the side of the spacer to provide radiation shielding. The sample holder includes a Mo base for the back gate, a Macor ring for insulating separation between the back gate and top gate, a big copper ring to attach the temperature sensor and bias current wires, a copper sample plate for placing the sample, a beryllium copper spring to push the sample plate up, and a copper cap to screw into the copper ring to hold the sample and provide the top gate function. The temperature sensor wires, heater wires, back gate wire, and BV wire are arranged to run out from 3 different corners to reduce the wire density.

Because of the aforementioned drawbacks, the author came up with a new design to address all these issues (Figure 2.12b). The new Macor spacer has a thinner wall and provides more space for the sample holder. It has three openings to spread the distribution of electrical wires. A molybdenum shield is added to the side of the spacer and short to the STM probe head to provide radiation shielding.

The new sample holder is much bigger with several parts. A molybdenum base, a beryllium copper spring, and a copper sample plate are used for the back gate connection. An outer copper ring and a copper cap are used for the top gate connection. A Macor ring is used as insulation between the top gate and the back gate. The sample is installed onto the sample plate with the spring pushing the plate up. The copper cap can be screwed down to the outer copper ring to hold the sample. This design ensures the flatness of the sample.

The temperature sensor is attached to the side of the outer copper ring. The wires from the temperature sensor, bias voltage, and back gate are distributed to come through from 3 different openings of the new Macor spacer. This design makes wires better organized and easier to repair.

2.1.5 A customized STM/AFM system

Limitation of our current STM system

Even though we try to make several modifications to enhance the capabilities of our current STM and make it easier to operate and repair, most of the STM system is more than 20 years old. It is a homemade system, and the design is old. Several limitations make it difficult to experiment with our STM system.

The new sample holder still has some shortcomings. First, screwing down the copper sample cap is not easy, and it might damage the sample during the process. A tweezer is used to push the sample stage down against the beryllium copper spring in order to keep the sample from touching the copper cap during the process of tightening the copper cap. This task is even harder to do inside the glove box. Additionally, beryllium copper spring would lose its

strength and elasticity at the helium temperature to push the sample plate up. A better approach to hold the sample in place while allowing the application of the back gate is needed.

The wires and other components cannot survive many thermal cycles and will need repairs after multiple low-temperature measurements. We have connected wires from the probe head to the top of the probe body feedthrough with pin sockets. The pin sockets can become loose or short with the STM body easily. The feedthrough we used on the STM probe is an old type and cannot find the replacement any more. This problem implies that we must maintain the old components and hope that they remain working indefinitely. A new STM system with modern vacuum components and electronic components will not only enhance its function but also makes it easy to repair and maintain.

Loading air-sensitive samples requires us to detach the STM can and reapply the indium wires as the gasket after the loading process. The whole STM probe has to be moved to the glove box. We need to etch the sample, load the sample onto the sample holder, and install the STM head base back to the head body all inside the glove box. Even if we can succeed, we need to check if the tip is right above the sample so the tip can approach. Finally, we need to install the bottom can back to the STM can body and hope that there are no leaks on the can, and that all electrical contacts are still reasonable on the STM probe. Then we need to pump on the STM probe to achieve a good vacuum, approach the tip, transfer liquid nitrogen and helium, and finally, if liquid helium is enough, we can turn on the magnetic field. There are so many required steps, but the failure rates are high. A more durable and reliable commercial system is, therefore, desirable.

Even though we can measure the temperature and turn on the heater by the temperature controller, we cannot connect the controller to the computer and use the computer to read the temperature and switch on the heater. The controller is too old to add this function. We need to record the temperature by hand and match them to the data we took. Therefore, it is impossible to control the temperature with the heater provided through some feedback system. The software for the STM controller cannot be upgraded for free, so the OS of the

computer has to stick to Windows XP. A new STM system with a new controller compatible with the latest Windows 10 system will be beneficial for faster and easier data acquisition.

Limitation on STM itself

Although STM itself is a powerful technique, it has several limitations. First, the STM scan range is small. Even though we can do the area scan as large as few microns, the scan itself is very time-consuming due to the speed of feedback. Most of the time, we limit our scan size to hundreds of nanometer. We cannot predict where the tip would land on the sample. It is also challenging to study specific small features on the sample due to the small field of view associated with the STM unless the interesting features can be found everywhere. Therefore, we tried to develop the SEM/STM system to solve this problem. With SEM, we can image a larger area of the sample and then zoom in to study the interesting regions with a higher spatial resolution by STM.

Second, the STM can only study conductors and semiconductors. From Equation (2.6), we know that the tunneling current depends on the DOS on both the sample and the tip. If the DOS of the sample vanishes, the tip cannot detect a tunneling current and, therefore, will crash to the sample surface. The topological insulators we studied are actually small-gap semiconductors, so that the STM is still useful. On the other hand, if we have materials that exhibit a phase transition between an insulating state and a conducting or superconducting state, STM techniques would appear to be difficult for use in investigating the spatial evolution of DOS near such phase transitions due to the inability of STM to probe non-conducting materials.

Even though we can get useful data from STS, simultaneous in-situ measurements with other complementary techniques such as atomic force microscopy (AFM) will provide more information on the samples.

Customized commercial solution for STM

All in all, with the advance of the technology, commercial STM systems have become more capable, multi-functional, and robust compared to typical homemade systems. The author began to look for a company willing to provide a customized commercial system which can fit out need.

After contacting several companies, Nanomagnetics Instruments company is the only company willing to make customization while keeping the price much lower than all the competitors. We discussed with them about all the problems that we would like to solve, and they agreed to provide us with commercial solutions.

Their products are featured by the modular design of the probe head. The probe body is compatible with several probe heads with different features like STM, Atomic Force Microscope (AFM), Magnetic Force Microscope (MFM), Kelvin Probe Force Microscopy (KPFM), and Piezo Response Force Microscope (PRFM). This design provides us with the flexibilities to switch among different functions for our probe. A further upgrade to conductive Atomic Force Microscope (c-AFM) is requested, and it can provide us with the ability to do simultaneous STM/AFM scans. The data acquired from STM and AFM can compare with each other for verification. This STM system will be a considerable upgrade for us.

Our new customized commercial is under construction, but its design shows that it is promising to solve several major problems in our current system.

The new design makes the STM probe head detachable. The bottom part of the probe is called the STM shuttle, which contains a tube scanner and sample stage. The shuttle itself can be opened and taken off the bottom cover to expose the STM head. We can install samples easily with a new sample stage design that contains a top PCB (printed circuit board) and a bottom PCB. The top PCB acts as a top gate. Four screws are used to lock the top PCB

onto the bottom PCB while holding the sample. Bottom PCB contains a back gate electrode, temperature sensor, and heater.

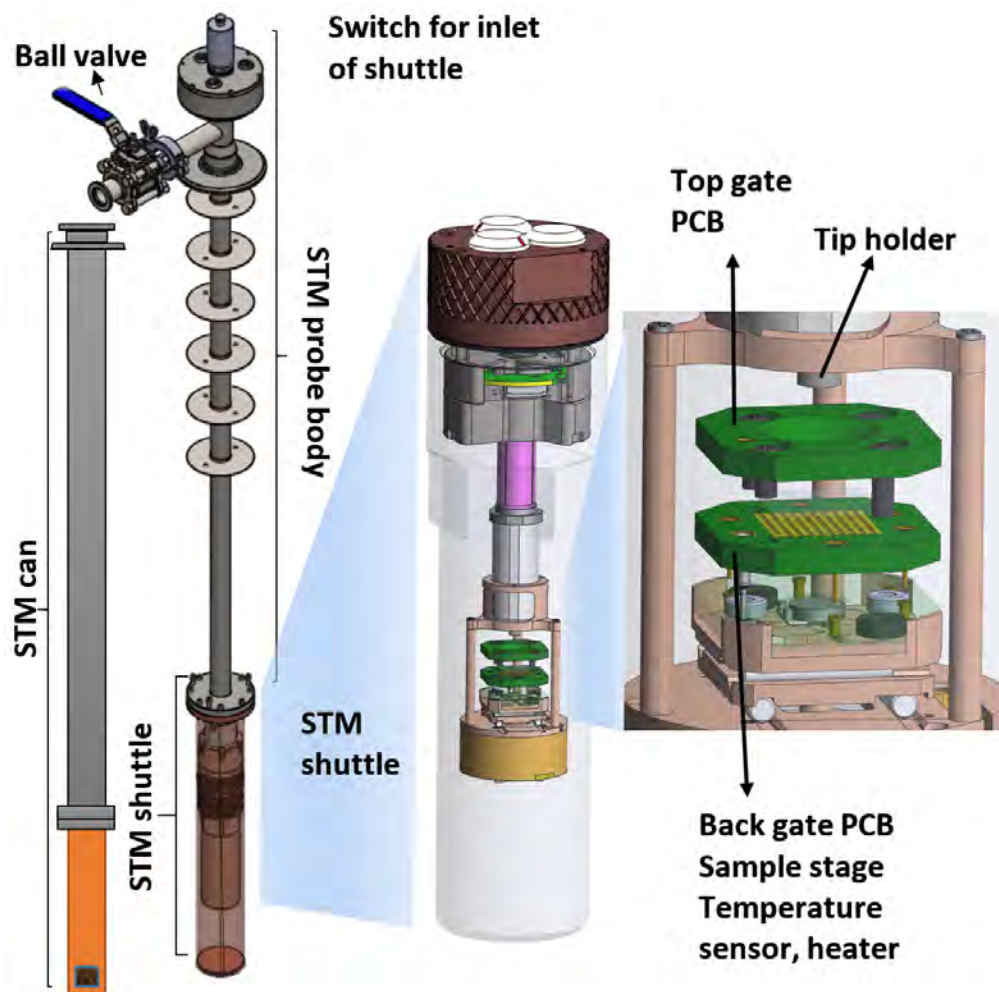


Figure 2.13: Design of the customized commercial STM. The STM probe is detachable with the STM shuttle at the bottom. The switch at the top of the probe can control the valve of the shuttle to vacuum seal it or open it. The sample can be loaded into the STM shuttle first inside the glovebox. Then attach the STM shuttle onto the STM probe. Finally, insert the STM probe into the STM can and pump it. In this design, the STM can will never need to be detached. The STM probe body can be pumped first before we open the vacuum seal of the STM shuttle to pump the STM shuttle. The sample is easier to load with the top PCB as top gate and screws. Back gate, temperature sensor, and heaters are built in the bottom PCB.

Once the sample is loaded, we can put the bottom cover back to the STM shuttle and make the STM shuttle vacuum sealed. The STM shuttle is small enough to put inside the glove box. We can load our sample in the argon-filled environment and close the shuttle to make it vacuum-sealed in the glove box. Then we can attach the shuttle back to the STM probe body and put the whole probe into the STM can to pump it down. The space between the shuttle and the STM can be pumped first. When the pressure is low enough, we can open the valve of the STM shuttle through the switch at the top of the STM probe to pump the STM shuttle too.

This design significantly simplifies the procedure of loading air-sensitive samples. It also avoids the need to detach the STM can bottom part and to reapply indium wire as a gasket, and therefore reduces one possible failure point. Originally the STM can is designed to be a single piece of metal with no detachable part, but then we realized we need to apply the magnetic field, so the design is switched back to similar to the old design with the copper bottom part.

The most significant advantage of the new design is that there are no exposed wires. The probe body looks clean and straightforward. It also helps reduce the outgassing problem. The number of flanges reduces to one. A ball valve replaces the angle valve in the current system and provides lower leaking rates. The vacuum of the STM is expected to improve significantly.

The wires are integrated into the components like PCB or inner tube. The thermal anchoring of the wires is expected to be better. The probe head should have enough cooling power to reach close to the liquid helium temperature. Since there is no exposed wire, the system is expected to be much robust against experimental operations. It will be easy to maintain.

A new STM controller comes with the new STM system. A new computer will also be provided with the latest OS Windows 10 and the latest STM software with many built-in functions for quick data analysis. The computer can read and even control the temperature directly with a heater. We can monitor the exact temperature for each scan taken. This feature

is essential when we try to do temperature-dependent measurements on the sample like topological insulators.

All in all, the new customized commercial STM will be a major upgrade to our current system and will increase the productivities for our STM experiments. This STM is much easier to operate, more robust, can reach lower temperatures, and provides more flexibility for future upgrades. With the coming of the new STM, the old STM can still run in parallel. We will have more capabilities to do several experiments at the same time.

2.2 Physical Property Measurement System (PPMS)

The PPMS (Figure 2.14) is a versatile measurement platform providing turn-key and customizable capabilities to measure a wide range of material and device properties as a function of temperature and magnetic field.

The Rosenbaum Lab acquired a Quantum Design DynaCool PPMS with joint funding from the Institute for Quantum Information and Matter (IQIM) at Caltech and made it accessible to other labs. The PPMS DynaCool is a completely redesigned instrument that provides all the capabilities of the PPMS without the need for any liquid cryogenics. The system uses a single two-stage pulse tube cooler to cool both the superconducting magnet and the temperature control system, providing a low vibration environment for sample measurements.

Comparing to the expensive low-temperature measurements using our STM system, the PPMS provides quick and reliable low-temperature and high magnetic-field measurements at little cost. The system can maintain stable temperatures from 1.9 K to 300 K and maintain the field up to ± 9 T. We rely on it to do the electrical transport measurements on our samples of topological insulators, graphene, and other materials. With a little modification, we have been even able to add light excitations inside the PPMS during the transport measurements.

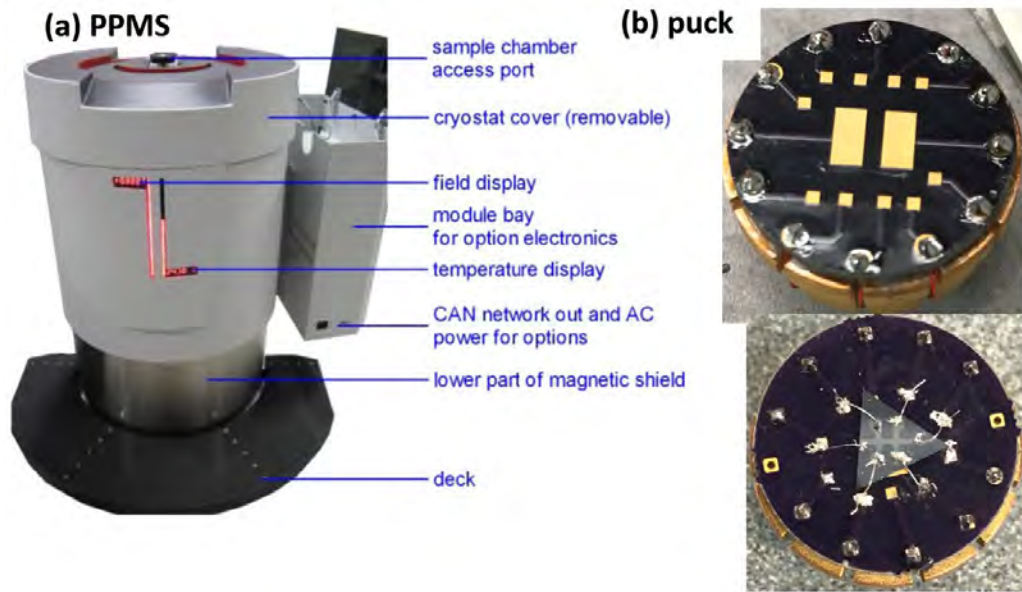


Figure 2.14: (a) Quantum Design DynaCool PPMS, a powerful system for conducting electrical transport measurements of samples as a function of temperature and magnetic field at relative ease and low cost. (b) A puck is used to mount the sample and put at the sample chamber at the bottom of the PPMS. The puck has 12-pin sockets at the bottom for making connections to pins at the bottom of the PPMS and to the outside. We can connect the wires to any pin for our measurement.

There is a sample chamber at the bottom side of the PPMS. We can insert the “puck” (Figure 2.14b) to the sample chamber with the puck inserting tool. The puck has 12 sockets at the bottom, which connects to the outbox of the PPMS when the puck is installed. We can mount the sample on top of the puck. A more practical way is to design the PCB to have 12 pins to connect to the sockets at the bottom of the puck through the wires. The design of the PCB is shown in Figure 2.14(b). Two of the 12 pins connect to the central rectangular pad as a back gate. The other 10 pins connect to the side pin pad around the back gate pad. We glue our sample onto the center of the PCB and then solder the Al wires from the side pin pad to the pin pad on the sample with indium as the solder. For a smaller sample, wire bonding or deposition of gold will be necessary because indium has a low melting point and is very sticky so that it is not suitable for delicate soldering to very small samples.

2.2.1 Customization of PPMS to add light to the sample chamber

PPMS DynaCool is customizable with the inserting tool as long as it is compatible with the sample access point. We are interested in studying the effect of circularly polarized light on the transport properties of TIs. Therefore, we customize an optical probe to send light to the sample chamber.

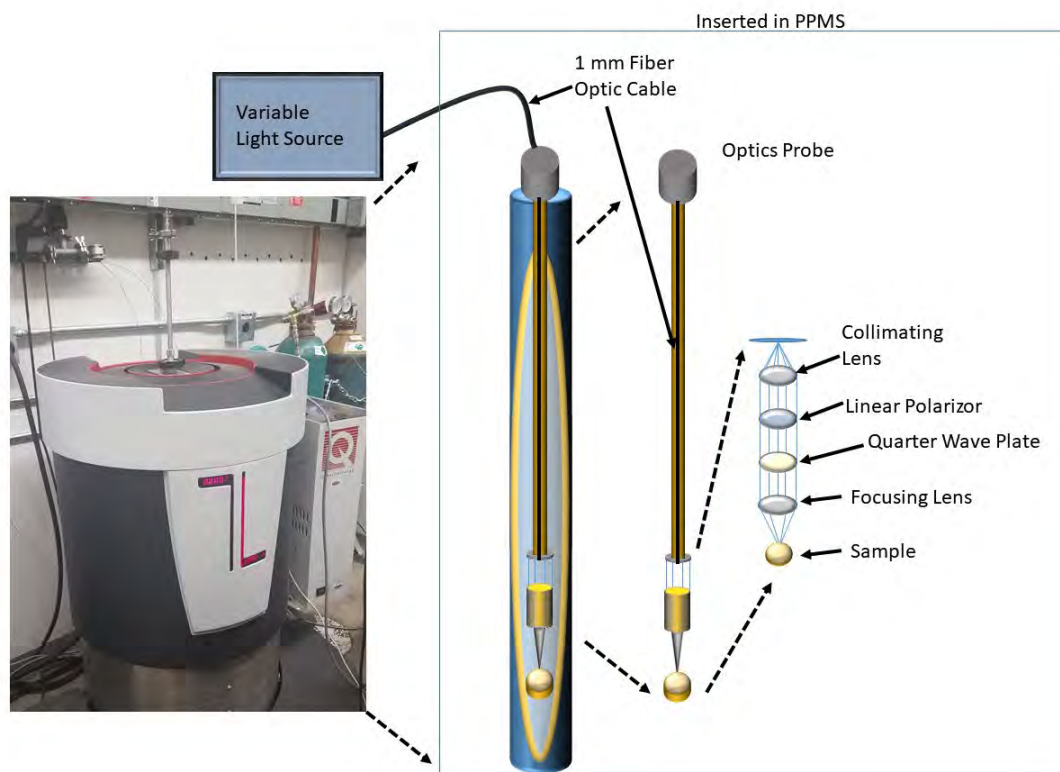


Figure 2.15: Optical probe designed by group members Dr. Marcus Teague, Adrian Llanos, and Duxing Hao. It includes a quarter-wave plate so we can produce the circularly polarized light from a light source to the sample surface.

This optical system (Figure 2.15) contains a light source, optical fibers, and several lenses to polarize the light and focus it. Marcus and Adrian made the initial design, and Duxing improved it further. This optical system is further introduced to another STM so that we can even perform STM studies with light.

2.3 Glove box and upgrade

The use of a glovebox or a glove bag can provide us with an inert-gas-filled environment for handling air-sensitive samples. The most common use of a glove box is to load air-sensitive samples into the STM stage.

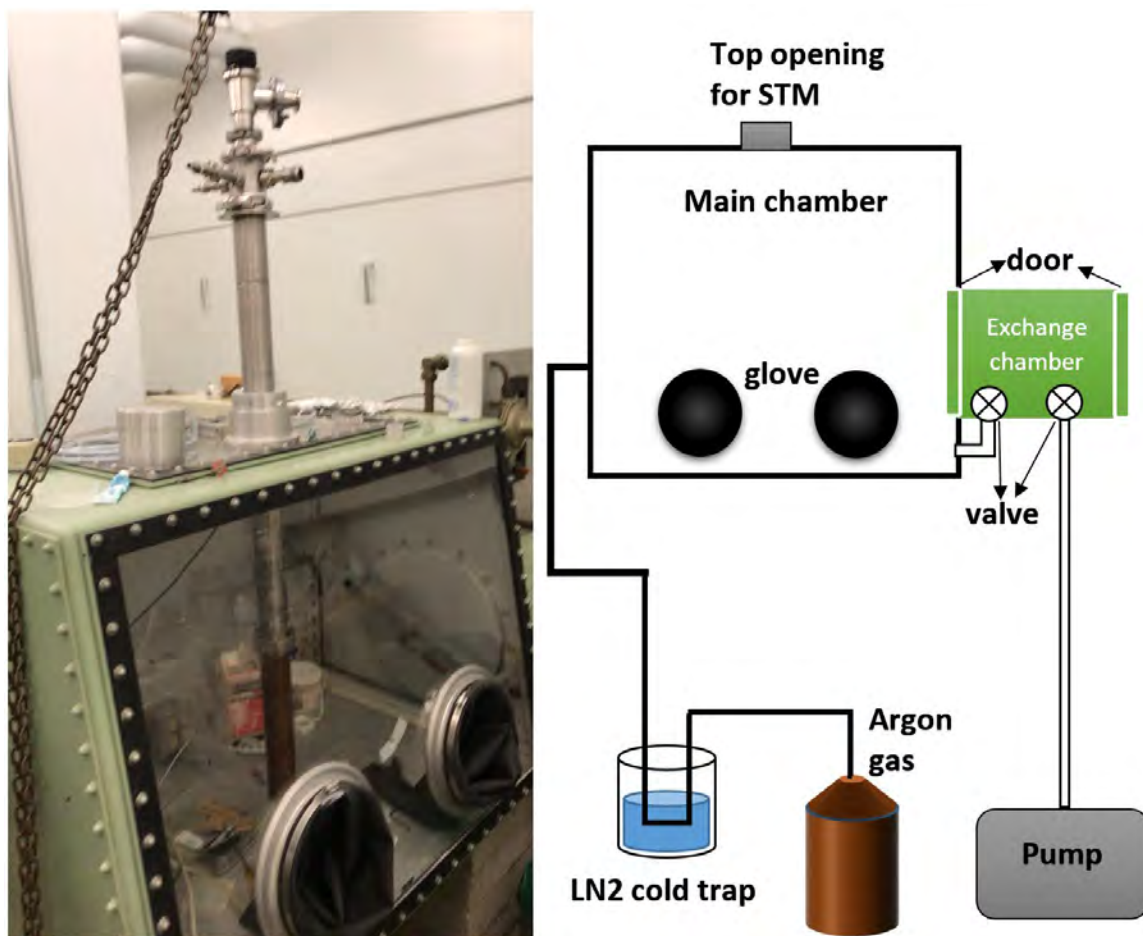


Figure 2.16: The old glove box. The left side shows a real photo with STM inserted. The right side provides the diagram of the glovebox. The glovebox has two chambers: the main chamber and the exchange chamber. Two chambers are separated by a door. The main chamber has two gloves and an opening at the top for inserting the STM. We refresh the glovebox by filling with Argon gas and then pumping it. The Argon gas needs to go through the liquid nitrogen cold trap to remove the water and other impurities. All stuff is sent into the main chamber through the exchange chamber.

Our old glove box was very primitive, basically consisting of just two chambers (Figure 2.16). The main chamber included two gloves attached to the glass and an opening at the top for inserting the STM probe. It also connected to a pipeline for external gas, usually an inert gas like argon. The argon gas had to pass through a liquid nitrogen cold trap to remove moisture and impurities inside the gas. The exchange chamber was used to load the necessary tools and chemicals for sample preparation into the main chamber. It had two doors on both sides. One controlled access to the outside, and the other controlled access to the main chamber. Another pipeline controlled by a valve connected both chambers to control the pressure of the main chamber. The exchange chamber was also directly connected to a vacuum pump directly.

To load air-sensitive samples, we had to fill the glove box with an inert gas like argon. We first flushed the main chamber several times with argon gas to reduce the partial pressure of air as much as possible. The process included first pumping on the main chamber to let glove expanded towards the inner side. Since we could not make glove swell like a balloon, the pressure level inside the glove box had to be kept finite, and so it was far from a good vacuum. Then argon gas was filled into the main chamber to push the glove outward. Again, we hope the glove does not swell like a balloon, so it limited the pressure inside the main chamber. Each flushing process helped dilute air concentration by about 80%. Therefore, if the process was repeated 10 times, only 10% of gas inside the chamber was air. It helps a little, but it is far from perfect.

Keep flushing the chamber with argon gas was quite wasteful and still could not completely eliminate the residual air. Obviously, this very old glovebox could not meet our needs despite our efforts to mitigate problems.

2.3.1 Customized commercial glovebox

We started looking for a commercial glovebox with customization. Vacuum Technology Inc. (VTI) was willing to customize its commercial product to accommodate our needs. The following are the features of the new glovebox.

Closed Loop Gas Circulation – Inert gas in a closed loop. The gas is circulated by the blower and purifier, H₂O, O₂ can be removed continuously.

Auto Purging – The replacement of the atmosphere inside the glove box can be achieved automatically by the purging valves.

Automatic Regeneration – H₂O and O₂ removal material can be regenerated. The regeneration process can be program-controlled.

Pressure Control in the Glove Box – The pressure in the glove box is controlled automatically by the Programmable Logic Controller (PLC). Working pressure can be set between +10 mbar and -10 mbar. If the pressure goes over ± 12 mbar, the system will be protected automatically.

Automatic Vacuum Pump Control – The vacuum pump will be activated automatically when necessary and will turn off after a period of idle time.

ECO Mode - The vacuum pump will be activated automatically when necessary, and will turn off after a period of idle time. Blower frequency will be switched to 25 Hz when moisture and oxygen level reaches to less than 1 ppm

Closed-loop gas circulation and purification ensure that the main chamber is always water-free and oxygen-free. All the argon gas is recycled and no need to refill. There are analyzers for moisture and oxygen levels, so we can notice any problems quickly. The main chamber is so clean that we can even store our samples inside.

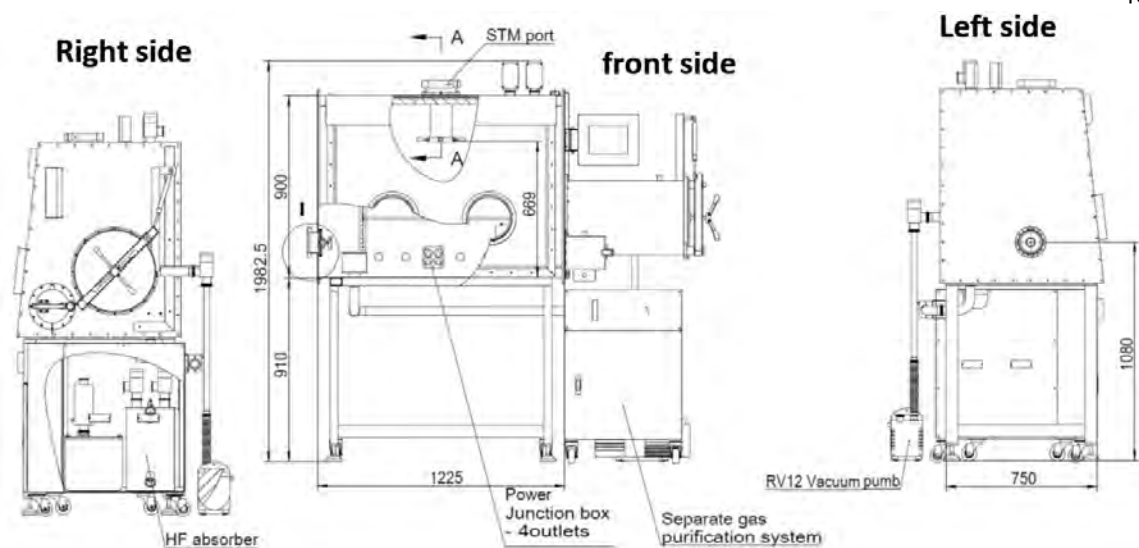


Figure 2.17: Design of the new glovebox. It utilizes closed-loop gas circulation and keeps the main chamber water-free and oxygen-free all the time. It has an HF absorber and an STM port to fit out needs. All components include the Main Chamber, Large Antechamber, Small Antechamber, Gas Purification, System Control, Vacuum Pump, Moisture Analyzer, Oxygen Analyzer, Electrical Feedthrough, and External Solvent Absorber/HF Absorber.

Due to our needs to do HF etching and load the sample into the STM, an HF absorber and an STM port are included. It also provides a power outlet and light inside. Five electrical feedthroughs at the backside of the main chamber can be used to add more features like a gas gun, USB cables, or BNC cables.

There are one small antechamber and one large antechamber as an exchange chamber. The small one can be used to send small stuff inside quickly. The auto-purge system lets us operate these antechambers without thinking about pumping and purging.

All in all, the new customized glovebox is expected to be helpful for us to do air-sensitive operations. It saves us much time in the preparation of the chamber. The gas inside the chamber is much cleaner than what we can have in the old glovebox. We can not only etch and load air-sensitive samples but also perform measurements inside the glovebox. The glovebox has been set up recently and will be a big boost to our experiments.



Figure 2.18 Real image of the new glove box. With the latest design, operation inside the glovebox is much more convenient than that inside the old glovebox.

Chapter 3

STM/STS STUDIES OF TOPOLOGICAL INSULATORS

Three dimensional (3D) topological insulators (such as Bi_2Se_3 , Bi_2Te_3 , and Sb_2Te_3) have 2D gapless surface states with a relatively small bulk bandgap (ranging from 0.1 ~ 0.3 eV) [36-40]. STM is a potent tool to study the surface states locally. Earlier studies of TIs had mostly focused on their macroscopic properties from electrical transport measurements [41-50] and angle-resolved photoemission spectroscopy (ARPES) [51-57]. The observation of quantum anomalous Hall effect (QAHE) [20, 21] implies global time reversal symmetry breaking in the sample. However, the absence of QAHE in magnetically doped TIs until extremely low temperatures (< 30 mK, well below the Curie temperature ~ 30 K) suggests that spatially inhomogeneous magnetization is likely throughout the sample. The implication of inhomogeneity cannot be easily verified by macroscopic tools. Similarly, strongly localized phenomena such as impurity resonances [58, 59] or Majorana modes [60-70] in TIs cannot be directly detected by macroscopic experiments such as electrical transport measurements and ARPES. A scanning probe technique (such as STM) with high spatial resolution will be necessary to reveal the strongly localized phenomena in the surface state of TIs.

In the case of transport measurements, the signal generally includes contributions from both the bulk states and the surface states. On the other hand, the exponential decay of tunneling current with distance in STM studies implies that signals taken by STM are primarily from the surface states of TIs unless the surface states open up an energy gap greater than that of the bulk. This means that STM is an ideal tool to investigate the local density of states of TIs on the surface.

This chapter focuses on our detailed STM studies of the bilayer TI/magnetic-TI structures, where the TIs include the binary TI, Bi_2Se_3 , and the ternary TI, $(\text{Bi}, \text{Sb})_2\text{Te}_3$.

3.1 Introduction of binary TI Bi_2Se_3 and ternary TI $(\text{Bi}, \text{Sb})_2\text{Te}_3$

Bismuth selenide is the simplest topological insulator with a clean bulk bandgap and a single surface Dirac cone. Although it is a 3D TI, it consists of 5-atom layers called quintuple layers (Figure 3.1). Within a quintuple layer, the constituent atoms are chemically bonded. However, the chalcogenide atoms (Se and Te) and transition-metal atoms (Bi, Sb, and Cr) form separate atomic planes so that they do not intermix in the same atomic plane, as shown in Figure 3.1. Between the quintuple layers, the interlayer coupling is the van der Waals interaction, just like that in graphite. Additionally, the TI sample needs to be thicker than a characteristic length to avoid the interferences between the surface states of the top and bottom layers; otherwise, the interferences would lead to a surface gap opening [71, 72], with the gap size increasing with decreasing thickness.

Figure 3.1 (right) shows the band structure of bismuth selenide (Bi_2Se_3) [38, 72, 73]. A clear single Dirac dispersion surface state is between the bulk valence and conduction bands, where the Dirac point appears between the bottom of the bulk conduction band and the top of the bulk valence band.

For ternary TI bismuth-antimony telluride $(\text{Bi}_x\text{Sb}_{1-x})_2\text{Te}_3$, the location of the original Se atom is replaced by Te, while the Sb substitutes some of the Bi. It is still the same quintuple layer structure. Given that the Sb-substituted Bi_2Te_3 samples do not form specific chemical compounds, the substitutions of Bi by Sb are mostly random. Interestingly, for studies of Cr-doped magnetic TIs (MTIs), it is more beneficial to study ternary TIs with partial Sb substitution for Bi, because the similar sizes of Cr and Sb will lead to less structural strain in Cr-doped ternary TIs than in Cr-doped binary TIs (such as Bi_2Se_3 and Bi_2Te_3), the latter involving Cr substitution for much larger Bi atoms. Figure 3.2 (a) shows a lattice structure of ternary TI $(\text{Bi}_x\text{Sb}_{1-x})_2\text{Te}_3$, where Sb and Bi share the same lattice plane.

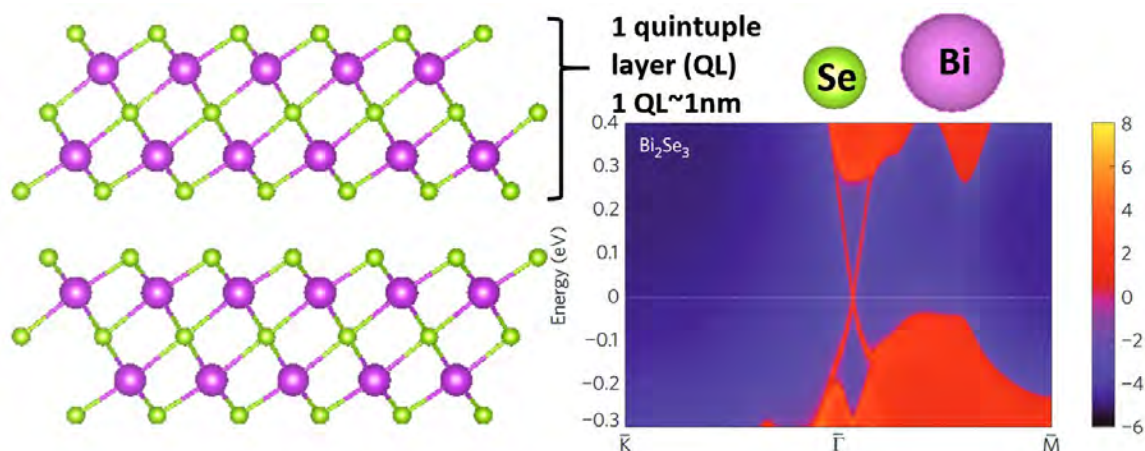


Figure 3.1: (left) Crystalline structure (side view) of a binary topological insulator Bi_2Se_3 . For ternary TIs $(Bi,Sb)_2Te_3$, the same structure holds if we replace the location of Se by Te and some of Bi by Sb. (right) Electronic band structure of Bi_2Se_3 , adapted from [74].

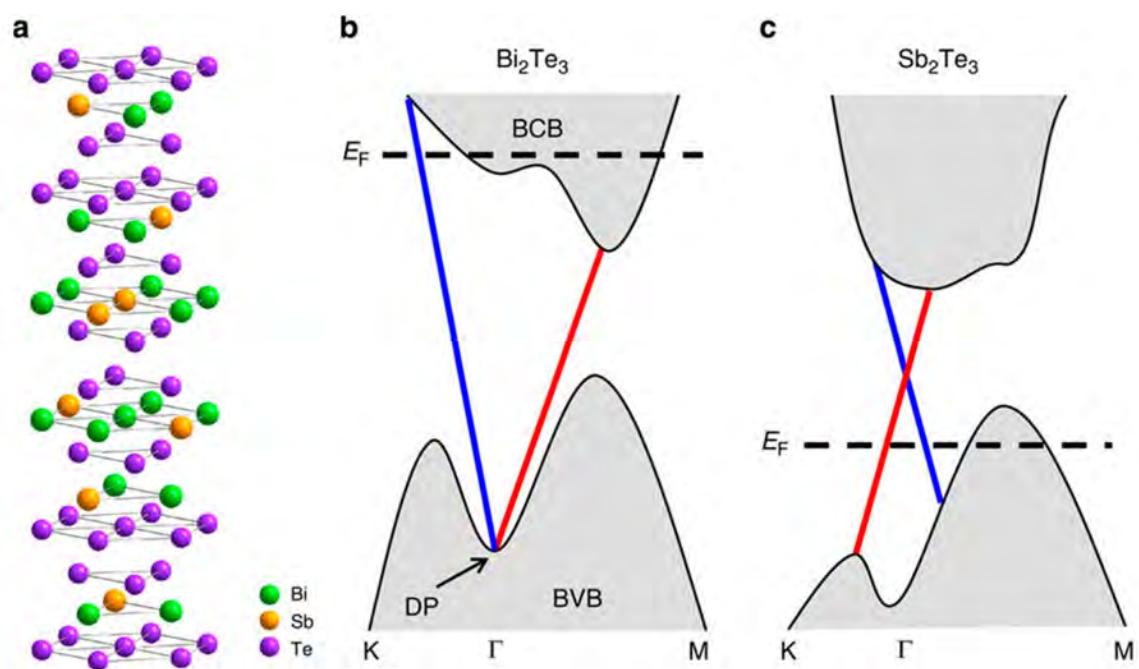


Figure 3.2: (a) The lattice structure of the ternary TI $(Bi_xSb_{1-x})_2Te_3$. The electronic band structures shown on the right are for the extreme cases of the binary compounds. (b) Band structure of Bi_2Te_3 . (c) Band structure of Sb_2Te_3 . Here the blue and red lines represent the surface states. The plot is adapted from [75].

One thing notable about the ternary TIs is their tunable ratio between Bi and Sb. Besides the aforementioned issue about strain in MTIs, are there other good reasons to investigate the ternary TIs instead of simply studying their binary forms of Bi_2Te_3 and Sb_2Te_3 ?

To answer this question, let us consider the band structures of binary TI Bi_2Te_3 in Figure 3.2 (b) [37, 38] and Sb_2Te_3 in Figure 3.2 (c) [76], respectively. Although both of them have surface states, their bulk bands and Fermi energies appear quite different.

For the band structure of Bi_2Te_3 , the Dirac point is low in energy and hide inside the bulk valence band (BVB) [37, 38, 74, 77]. The Fermi level is across the bulk conduction band (BCB), which indicates significant electron doping and, therefore, considerable contributions of the bulk carriers on electrical conduction. Even if we can gate it and tune the Fermi level in the middle of the bulk bandgap, it is still far from the Dirac point where the resistance is the largest, and the onset point for gap opening occurs. Noting that the QAHE can only show up when the Fermi level is inside the surface bandgap, it is unlikely to observe the QAHE in binary Bi_2Te_3 .

Sb_2Te_3 , on the other hand, is on the other side of the spectrum. Its Dirac point locates nicely in the middle of the bulk bandgap, while the Fermi level is inside the BVB and below the Dirac point. The majority carriers are holes from both the bulk and surface states.

The totally opposite situations for Bi_2Te_3 and Sb_2Te_3 suggest that mixing the two spectra could lead to something better [78]. With a proper ratio between Bi and Sb, the Fermi level can match the Dirac point perfectly without even any back gating, and the temperature for the onset of QAHE will be the highest when the Fermi level coincides with the Dirac point. Therefore, for the purpose of optimizing the QAHE in MTIs, tuning the chemical compositions of ternary TIs to achieve the best match of the Fermi energy and Dirac point without back gating would be the objective for exploration.

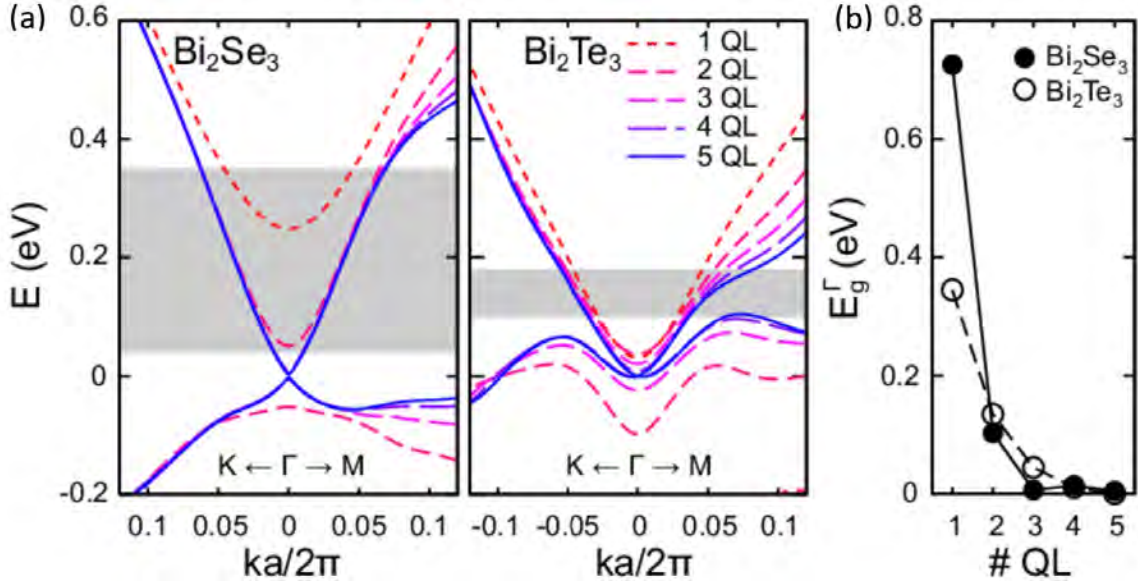


Figure 3.3: (a) Band structures of the surface states of Bi_2Se_3 and Bi_2Te_3 for different thicknesses. (b) The surface bandgap size vs. sample thickness for Bi_2Se_3 and Bi_2Te_3 . Adapted from [38].

The thickness of TIs also influences their band structures. As shown in Figure 3.3, in the 2D limit, the interference between the top and bottom surface states leads to a surface gap opening for both Bi_2Se_3 and Bi_2Te_3 . However, with thickness above the 4QL, both TIs recover the band structures in the 3D limit by theory. These theoretical predictions have subsequently been verified experimentally [72].

3.2 Sample choices and experimental setup

We have been collaborating with Professor Wang's group at UCLA on our studies of topological insulators. Professor Wang's group synthesizes various types of TIs and their heterostructures on different substrates by molecular beam epitaxy (MBE). Our previous group member began to explore pure Bi_2Se_3 on Si with STM for 60-QL and 7-QL samples and found strong Fermi-level dependent impurity resonances in the surface states as the result of topological protection [58]. However, as introduced in Chapter 1, the opening of a surface gap by TRS breaking in the TIs is expected to bring about better applications. Therefore, in this thesis work, we focus our studies on magnetically doped TIs.

To break TRS on TIs, intrinsic magnetization is needed. Most research groups chose to dope the entire sample with Cr to introduce ferromagnetism at low temperatures. However, direct doping of Cr to TIs will lead to changes to the bulk band structures as well as shifts in the Fermi level in addition to breaking TRS. Ideally, we would like to find means to simply break the TRS in TIs without modifying the bulk band structure.

By putting a pure TI layer on top of a magnetic TI (MTI), we can make sure that the surface states of the pure TI remain intact for temperatures above the Curie temperature of the MTI. If anything changes on the surface with decreasing temperature, we can attribute them to the result of proximity to the MTI underneath.

3.2.1 List of samples investigated in this work

Table 3.1 List of binary Bi_2Se_3 bilayer samples for STM and PPMS studies.

sample ID(UCLA)	Top layer# Bi_2Se_3	bottom layer# $Cr-Bi_2Se_3$	Cr %	capping	substrate	Grower
LH 997	1QL	6QL	10%	Se	InP	Liang He
LH 999	3QL	6QL	10%	Se	InP	Liang He
LH 1001	5QL	6QL	10%	Se	InP	Liang He
LH 1002	7QL	6QL	10%	Se	InP	Liang He
LH 1183	1QL	6QL	5%	Se	InP	Liang He
KM 1870	1QL	6QL	10%	Se	InP	Koichi Murata
KM 2785	3QL	6QL	10%	Al	GaAs	Koichi Murata
KM 2786	1QL	6QL	10%	Al	GaAs	Koichi Murata

Table 3.2 $(Bi_xSb_y)_2Te_3/Cr-(Bi_xSb_y)_2Te_3$ sample list for STM and PPMS studies

sample ID(UCLA)	Top layer # $(BiSb)_2Te_3$	bottom layer # $Cr-(BiSb)_2Te_3$	Cr %	capping	Grower	x:y
LH 1182	1QL	6QL	10%	Al	Liang He	1:1
LP 2788	1QL	6QL	10%	Al	Lei Pan	1:1.3
PZ 3267	3QL	6QL	10%	Al 2nm	Peng Zhang	0.3:0.7
PZ 3268	1QL	6QL	10%	Al 1nm	Peng Zhang	0.3:0.7

Note: the substrate is GaAs for all the ternary samples.



Figure 3.4: Schematic structure (side view) of a bilayer TI/MTI sample and its nomenclature.

Table 3.1 and Table 3.2 list all the samples grown by our UCLA collaborators in Professor Wang's group in chronological order. The author especially thanks them for accommodating our requirements for the sample structure, Cr doping, and capping. They also etched Hall bars on some of the samples for us to conduct the PPMS measurements.

Our samples all have the TI/MTI bilayer structure on semiconducting substrates, and each is protected by a capping layer, as shown in Figure 3.4. We use (# of top QL+# of bottom QL)-Cr concentration % as our nomenclature for all samples, such as (1+6)-10%, for example.

For binary bilayer TIs, earlier samples were grown on the indium phosphate (InP) substrate. We used these samples to investigate the influence of the top layer thickness and Cr-doping concentration on the resulting properties. These samples helped us conclude the effectiveness of the proximity effect from magnetic TIs.

Later on, the UCLA group changed the substrates from InP to gallium arsenide (GaAs) to enhance the sample quality. For ternary TIs, all samples were grown on GaAs only. The ratio of Bi to Sb was changed to tune the Fermi level. The latest samples with a 3:7 ratio were shown to exhibit the highest onset temperature for QAHE, with the Fermi level right at the Dirac point.

3.2.2 Sample storage and preparation

ALL MBE samples came with a capping layer to protect them from oxidization or deterioration with time. They were stored either in a nitrogen-flow desiccator or an airtight desiccator to reduce contact with water/air.

Different capping layers require different procedures to remove them. For Se capping, it required annealing to evaporate all Se atoms. For Al capping, assuming it was oxidized quickly after deposition, we used dilute HF in pure ethanol to etch away the capping layer and then rinsed the sample in pure ethanol.

3.2.3 Sample annealing procedure

Figure 3.5 shows the annealing procedure for Se-capped samples. The Se capping layer can evaporate between 160 ~ 200 °C while keeping the underlying TI sample intact. The most challenging part is to keep the sample in a vacuum while loading it onto the STM sample stage.

Annealing was carried out inside a small vacuum chamber. Inside the chamber, there was a stage to hold the sample, a heater right above the stage, and a thermocouple next to the stage to monitor the temperature. The vacuum chamber had a big side gate, which allowed us to take out the sample easily with a big tweezer.

The annealing procedure is as follows. To begin with, we opened the chamber and thoroughly cleaned the interior with ethanol. After ethanol cleansing, the chamber was further baked by heating tape under ultra-high vacuum. This procedure was to ensure the thorough removal of water and ethanol inside the chamber.

Next, we inserted the sample into the chamber, clamped it onto the sample stage, and adjusted the heater and thermocouple positions before we closed the chamber and started pumping on it. Optional flushing the chamber several times with argon gas to further dilute the oxygen levels could be carried out when pumping the chamber with a roughing pump before turning

on the turbo pump. It would not be practical to combine flushing the vacuum chamber with the usage of the turbo pump because it would take more than 20 minutes to spin down a turbo pump. Once the chamber was sufficiently clean, we turned on the turbo pump to reach ultra-high vacuum ($< 10^{-7}$ torr) in the chamber.

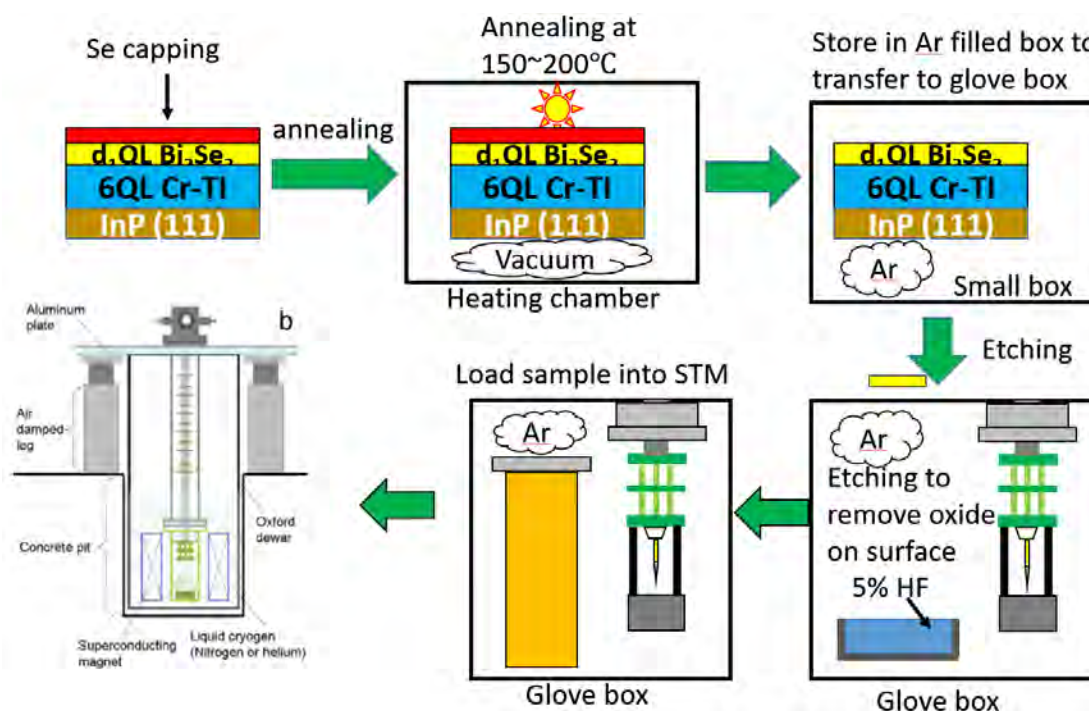


Figure 3.5: Annealing and sample loading procedures for preparing TIs for STM experiments.

To anneal the TI sample, we turned on the heater and monitored the sample temperature. The heater did not make direct contact to the sample. Instead, it heated the sample surface through radiation. A temperature gradient existed between the sample surface and the heater. This gradient ensured that the top of the sample, which was capped, was exposed to the highest temperature, which helped avoid overheating the underlying TI sample.

Reaching a stable annealing temperature would take a while. In general, annealing the sample at a lower temperature range over a longer time was safer than annealing at a higher temperature. The typical annealing time was more than 30 mins between 160 to 200 °C. Once

the annealing was completed, we turned off the heater, closed the valve between the chamber and the pump, and then turned off the pump by spinning down the turbopump.

Since the annealing chamber was small enough, it could be placed inside a glove bag, which was filled with argon. The sample was taken out of the annealing chamber, transferred into a small stainless steel box, and then sealed off the stainless steel box inside the glove bag. The small stainless steel box that contained the sample and full of argon gas was placed inside the glovebox. Finally, the sample was taken out of the stainless steel box and loaded onto the STM sample stage, as shown in Figure 3.5.

3.2.4 Hydrofluoric Acid (HF) sample etching procedure

Hydrofluoric (HF) acid is useful for removing any oxides. For aluminum capping on the TI samples, aluminum will become oxidized to aluminum oxide within a short time. This oxide layer can be removed easily by HF acid.

If a sample had been measured once, it would have been exposed to air afterward the experiment. We sometimes re-etched the sample with HF acid in order to carry out additional measurements on the same sample.

We performed HF etching of TI samples inside the glovebox, which was filled with argon gas during the process. 50% HF was diluted to 5% HF with 100% ethanol. Then the sample was rinsed in the HF solution for about 5 to 15 seconds, depending on its oxidation level.

Although HF was generally dangerous to deal with, we used to consider HF etching a more straightforward procedure for cap removal than annealing. However, TI samples after HF etching often exhibited a surface gap even at the room temperature, which could be due to either incomplete cap removal or HF-induced damages to the sample surface. In this context, whether it is necessary to remove the surface cap is in question.

3.2.5 Summary of the sample handling before STM experiments

Removal of the capping layer on TIs is challenging and time-consuming. Moreover, the quality of the sample surface after cap removal was often questionable because the expected gapless Dirac spectrum on the surface at high temperatures did not always show up. Since the vacuum of STM was only 10^{-6} torr at room temperature and would only reach $< 10^{-9}$ torr at helium temperature when the charcoal pump became activated, the vacuum level was not usually not good enough to keep the sample from deterioration after a month-long of measurements.

Although in principle we could regenerate a TI sample after it degraded by repeating the HF etching, the sample surface typically became rougher after etching and the tunneling spectra would still not show the expected gapless Dirac spectrum everywhere at 300 K.

On the other hand, for transport measurements, we never removed the thin capping layer on the TI samples, and we found that the experimental results were always reproducible with the same parameters within the same measurement cycle. Moreover, the same sample could be reused for transport measurement again and again at a later time.

In principle, for sufficiently thin oxide layers on top of a TI sample, we may consider the combination of the surface aluminum oxide and the vacuum gap as one effective tunneling barrier for STM measurements. Indeed, when we performed STM studies directly on the Al capped TI samples, we found that the gapless Dirac spectra appeared everywhere at the room temperature as expected, and the results were similar to the best case of a similar TI sample with the cap removed.

For Se-capped TI samples, we might be concerned with the possibility of the tip occasionally picking up a surface Se atom and therefore changed the tunneling characteristics. Additionally, pure Se has a smaller bandgap than those of most TIs, which definitely will definitely contribute to the total STS. In contrast, the bandgap of aluminum oxide is much larger than those of all TIs, so that the bandstructure of aluminum oxide will not contribute

to the total STS of the capped TI sample as long as the oxide layer is very thin (~ 1 nm). Therefore, it seems that the cap removal for Al-capped TI samples is unnecessary for both STM and electrical transport measurements. Moreover, keeping the Al-cap has the benefit of preserving the quality of the underlying TI sample for an extended period of time. Such capped TI samples are also expected to be more practical for industrial applications than the uncapped air-sensitive TI samples.

3.3 STM measurement settings

We used our homemade STM system (detailed in Chapter 2) to study spatially resolve topography and spectroscopy of TIs. The tunneling resistance (bias to set point tunneling current) was set to $1\text{ G}\Omega$.

In our earlier STM/STS studies of the TIs, the bias was set around 1 V to prevent possible tip-crushing. However, such high voltages would overemphasize contributions from the bulk bands. Additionally, in the case of spectroscopy scans on TI/MTI heterostructures, high bias voltages could induce effective magnetic fields through the topological magnetoelectric (TME) effect, which could increase the size of the surface gap. Therefore, when comparing earlier STM/STS studies with transport measurements, it would be more suitable to consider field-cooled data rather than zero field cooled data.

3.3.1 Compromise between the accuracy and the speed for spectroscopy

Ideally, to acquire high-quality spectroscopic data, we may take as many I-vs.-V curves as possible at the same location and then average them to reduce random noise. We may also use a big time constant to average out noises for each tunneling current point at each bias. Once I-vs.-V curves are obtained, we can then calculate dI/dV to obtain the density of the states (DOS). Another approach is to measure signals directly proportional to dI/dV using the lock-in technique, as discussed in Chapter 2. However, this approach requires enough span in the time domain, which means a much larger time constant.

Therefore, all methods for low-noise data acquisition generally take a long time. It also implies that fewer data can be collected for statistical analysis of spatially inhomogeneous materials. On the other hand, a longer *I-vs.-V* sweep time tends to introduce more noise to the data because STM is highly sensitive to any environmental changes.

Our cryogenic STM is a wet system, which means the cryogen in the Dewars controls the temperature of the STM. At constant temperatures such as the ambient, liquid nitrogen, or liquid helium temperature, we can take much higher resolution spectral scans with less noise. Nonetheless, for measurements at liquid helium temperatures, the STM system could only last for 2-3 days without more liquid helium transfer, and so the measurement time is also constrained.

For temperature-dependent STS maps, we often acquired such data during the warmup of the STM. The temperature could change up to 5K/hr, and so the spectral scan over a spatial area must be completed as fast as possible to prevent significant temperature variations during the scan. Typically, the spectroscopy had to be completed within one hour when the temperature is changing. Therefore, we would reduce the pixel size to (32×32) and the number of sweeps per pixel to 1 or 2. The speed of voltage sweep was also faster than that for measurements at constant temperatures. In contrast, at either room temperature or liquid nitrogen temperatures, much more generous settings may be used for higher resolution data over wider areas.

For most of the STS described in this chapter, we have chosen the faster scan settings. Each *I-vs.-V* curve was smoothed and normalized afterward. To verify the reliability of the measurements, we monitored the difference between the less noisy setting and optimized setting regularly throughout the experiments to make sure that the results from these settings were consistent.

In this following subsections, detailed studies of the binary TI/MTI system (TI: Bi_2Se_3 , MTI: Cr-doped Bi_2Se_3) are presented, which are complemented by some comparative studies of the ternary TI/MTI system (TI: $(\text{Bi,Sb})_2\text{Te}_3$, MTI: Cr-doped $(\text{Bi,Sb})_2\text{Te}_3$).

3.4 Structural characteristics from surface topographic studies of the binary TI/MTI system

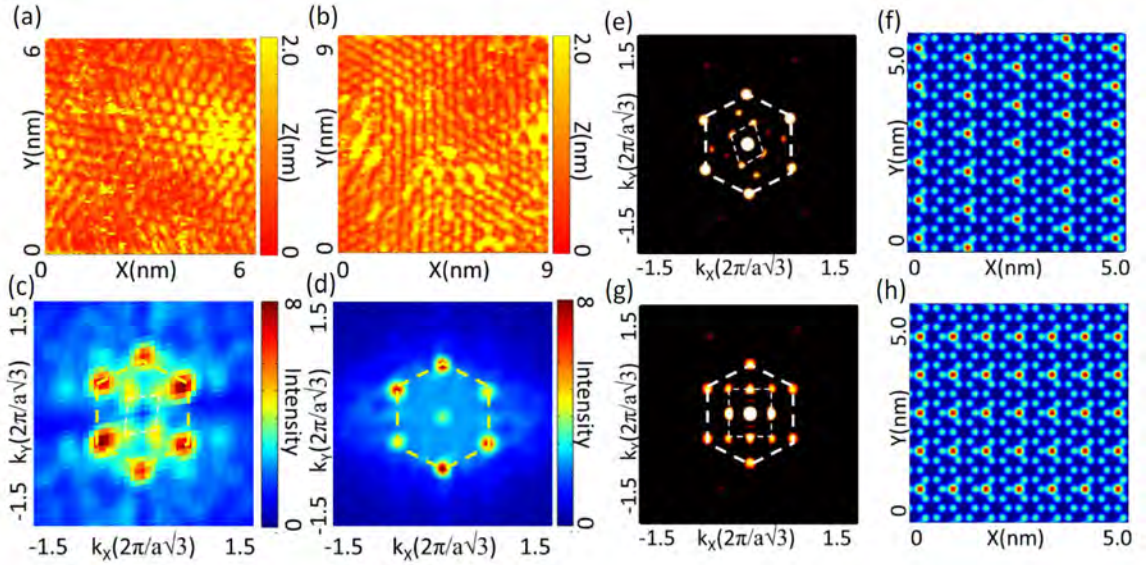


Figure 3.6: Structural characteristics of MBE-grown Bi_2Se_3 bilayer samples on InP (111): **(a)** Surface topography of a (1+6)-10% sample over an area of $(6 \times 6) \text{ nm}^2$, showing a triangular lattice structure. **(b)** Surface topography of a (5+6)-10% sample over an area of $(6 \times 6) \text{ nm}^2$, showing a triangular lattice. **(c)** Fourier transformation (FT) of the surface topography in a (1+6)-10% sample, revealing a dominant hexagonal reciprocal lattice structure and a secondary superlattice of a much weaker intensity, probably coming from the underlying Cr-doped Bi_2Se_3 layer. Here “a” in the reciprocal space scale ($2\pi/a\sqrt{3}$) refers to the in-plane nearest neighbor distance between Bi (Se) and Bi (Se). **(d)** FT of the surface topography on a (5+6)-10% sample, showing a purely hexagonal reciprocal lattice. **(e)** Simulated FT of the 1/12 Cr-substituted Bi layer illustrated in **(f)**, showing an FT similar to the data in **(c)**. Here the blue dots represent Bi atoms, and the red dots represent Cr substitutions. **(g)** Simulated FT of the 1/8 Cr-substituted Bi layer illustrated in **(h)**, showing an FT also similar to the data in **(c)** within experimental errors. [15]

The surface topography on large scales of all MBE-grown TIs generally revealed pyramid-like terraces with steps corresponding to single atomic layers, as detailed by our UCLA collaborators [2, 79]. For an averaged, nominal top layer thickness d_1 -QL (where d_1 represents the average integer number of the top TI layer in units of QLs), the local thickness of the top layer could vary up to 1-QL. In our STM/STS studies of the binary TI/MTI system, atomically resolved topographic images exhibited triangular lattice patterns that were always

consistent with that of pure Bi_2Se_3 , as exemplified in Figure 3.6 (a) and Figure 3.6 (b) for (1+6)-10% and (5+6)-10% samples, respectively. On the other hand, the Fourier transformation (FT) of the surface topography appeared to be dependent on d_1 . We found that FT of the (1+6)-10% topography showed an expected hexagonal Bragg diffraction pattern for Bi_2Se_3 plus an additional, faint superlattice structure (Figure 3.6 (c)), which may be attributed to the underlying Cr-doped Bi_2Se_3 . For instance, a periodic substitution of Cr for Bi, as exemplified in Figure 3.6 (f) for a two-dimensional projection of the two Bi-layers within one-QL, yields an FT pattern (Figure 3.6 (e)) similar to that in Figure 3.6 (c). This superlattice structure corresponds to a local Cr concentration of $1/12$. Another similar structure with a local Cr concentration of $1/8$ (Figure 3.6 (h)) is also feasible within experimental uncertainties of the superlattice constant and its angle relative to the Bi lattice (Figure 3.6 (g)). In contrast, the FT in Figure 3.6 (d) for the surface topography of a (5+6)-10% sample only revealed the hexagonal diffraction pattern of pure Bi_2Se_3 due to the relatively thick d_1 layer. Interestingly, we note that the FT topography of the (1+6)-5% samples also agreed with Figure 3.6 (d), suggesting random Cr substitutions of Bi for a smaller Cr concentration, which is consistent with the randomly distributed Cr clusters found with STM studies directly on 2% Cr-doped Bi_2Se_3 [80]

3.5 Temperature evolution of the majority spectra in binary and ternary TI/MTI systems

Bias spectroscopy scan (I -vs.- V , or tunneling current vs. bias) was the main tool for our study of the microscopic properties of TIs. As introduced in Chapter 2, dI/dV is proportional to the density of states (DOS) of the sample surface. For pure TIs, previous studies by members of our group have shown that the tunneling spectra were largely spatially homogenous with V-shaped dI/dV -vs.- V spectra consistent with the Dirac dispersion relation for massless Dirac fermions. Occasional non-magnetic impurity resonances were also observed, which exhibited strong Fermi-energy dependence and were highly localized spatially due to topological protection [58]. In contrast, as we shall demonstrate below, the tunneling spectra associated with the TI/MTI bilayer system appear to be much more inhomogeneous than

those taken on pure TIs, which may be attributed to the Cr-doping in the MTI layer that introduced inhomogeneous distributions of strain, magnetic moments and charge.

Despite the spatial variations in the tunneling spectra, the temperature evolution of all dI/dV -vs.- V spectra appeared to follow a consistent trend statistically. This observation gave us the confidence to discuss the spectral evolution by inspecting the majority spectra of each TI/MTI sample. Similar to the findings in pure TIs, we also found interesting minority spectra associated with the binary TI/MTI system, which may be attributed to magnetic impurity resonances and will be discussed later in this chapter.

We first examine how the majority spectra evolve with temperatures for all TI/MTI samples.

3.5.1 (5+6)-10% binary TI/MTI

For (5+6)-10% binary TI/MTI, the temperature evolution of the majority dI/dV -vs.- V spectra is shown in Figure 3.7 (a), where we selected several representative spectra taken at different temperatures, with each spectrum obtained by averaging a number of similar spectra taken in different regions. We note that for $T \geq 88$ K, all majority spectra looked alike with only subtle differences at all temperatures. For example, the spectrum at $T = 114$ K revealed a sharper V-shape curve near the Dirac point than those spectra taken at other temperatures. Overall, 100 ~ 150 K is an interesting temperature range for comparison with other samples of different thicknesses, which we shall elaborate later.

On the other hand, we may examine spatially varying spectra taken at a constant temperature. For instance, besides the majority spectrum taken at 114 K as shown in Figure 3.7 (a), there were three other types of minority spectra (Figure 3.7 (b)). One of them appeared to be a gapped spectrum, whereas the rest appeared to be gapless, and the spectrum shown in black seemed to be consistent with an impurity resonance.

At 88 K, the types of spectra were simpler, showing either gapless behavior (majority) or gapped U-shaped behavior (minority). This observation may indicate the onset of surface gap opening at this temperature.

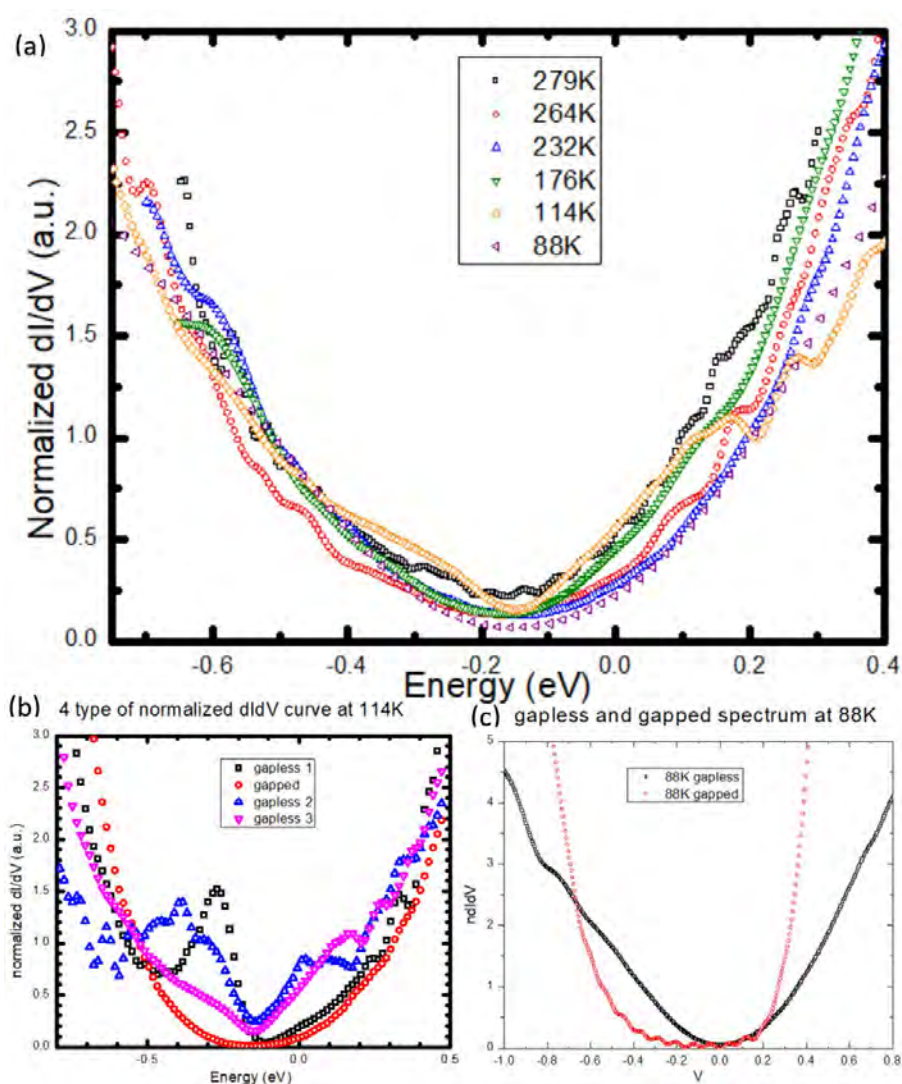


Figure 3.7: (a) Majority dI/dV -vs.- V spectral evolution with temperature in (5+6)-10% binary TI/MTI. (b) Comparison of different types of dI/dV -vs.- V spectra observed at 114 K. (c) Different types of curves observed at 88 K.

3.5.2 (1+6)-5%, (1+6)-10% and (3+6)-10% binary TI/MTI

For binary TI/MTI samples with a thinner ($d_1 < 6$) top pure TI, the majority spectra exhibited much more interesting temperature evolution (Figure 3.8).

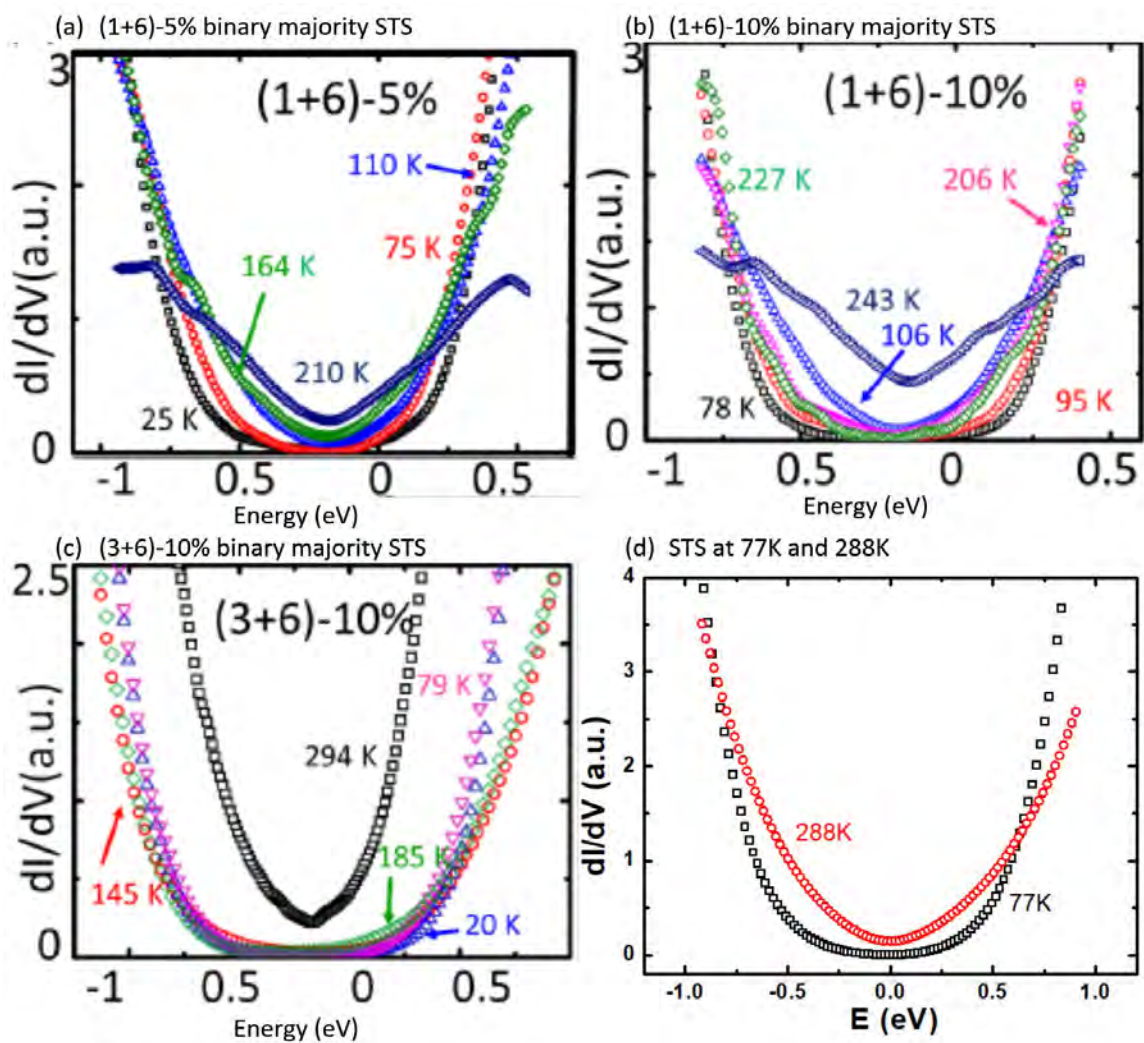


Figure 3.8: Majority spectra taken at different temperatures for (a) (1+6)-5% binary TI/MTI, (b) (1+6)-10% binary TI/MTI and (c) (3+6)-10% binary TI/MTI. (d) Comparison between the gapless spectrum at 300 K and the gapped spectrum at 77 K for (1+6)-10% binary TI/MTI under the same sweep range and normalization. [15]

Figure 3.8 (a)-(c) shows the temperature evolution of the majority spectra for (1+6)-5%, (1+6)-10%, and (3+6)-10% binary TI/MTI samples. A better comparison of the spectral evolution from 300 K to 77 K with the same bias ranges for the (1+6)-10% sample is shown in Figure 3.8 (d), which reveals apparent gapless behavior at 300 K and gapped behavior at 77 K.

From Figure 3.8, it is clear that the majority spectra for all three samples evolved from more V-shaped curvature to U-shaped curve with decreasing temperature. The spectra eventually exhibited a nearly-flat bottom at sufficiently low temperatures, which implied the appearance of a surface gap.

3.5.3 (1+6)-10% and (3+6)-10% ternary TI/MTI

Figure 3.9 shows the temperature evolution of the majority spectra for (1+6)-10% ternary TI/MTI and (3+6)-10% ternary TI/MTI samples. Similar to the trend found in binary TI/MTI samples with $d_1 < 5$, the majority spectra of (1+6)-10% ternary TI/MTI follow the trend of binary TI samples; a gap began to open and then increased with decreasing temperature. In contrast, the majority spectra of (3+6)-10% ternary TI/MTI were quite conductive at room temperature. It shows not only Dirac-dispersion like curve but also large minimum conductance. With decreasing temperature, no apparent gap appeared down to 78.3K, where the majority spectrum exhibited a standard Dirac dispersion with almost zero minimum conductance. Recent studies by group member Adrian Llanos at 4.2 K revealed only a very small gap (ranging from 20 to 40 meV) at 4.2K (Figures 3.9 (c)-(d)).

Our transport measurements on the (3+6)-10% ternary TI/MTI sample (to be elaborated in Chapter 4) also revealed results that suggested an interesting position of the Fermi level relative to the Dirac point and the bulk bands so that the peak-like feature at ~ 100 meV (Figures 3.9 (c)-(d)) may be attributed to the excess density of states from the bulk valence band near its maximum, as shown in Figure 4.19. The highly conducting spectra and the absence of any discernible energy gap until very low temperature from STS studies is also consistent with the temperature evolution of the band structures shown in Figure 4.19. That is, despite the opening of a direct surface gap below the Curie temperature, no energy gap could be detected until very low temperatures when an indirect gap much smaller than the direct surface gap opened up due to the position of the Fermi level. Please refer to Chapter 4 for more details. Overall we found a consistent physical picture between the microscopic STS results and the macroscopic transport measurements.

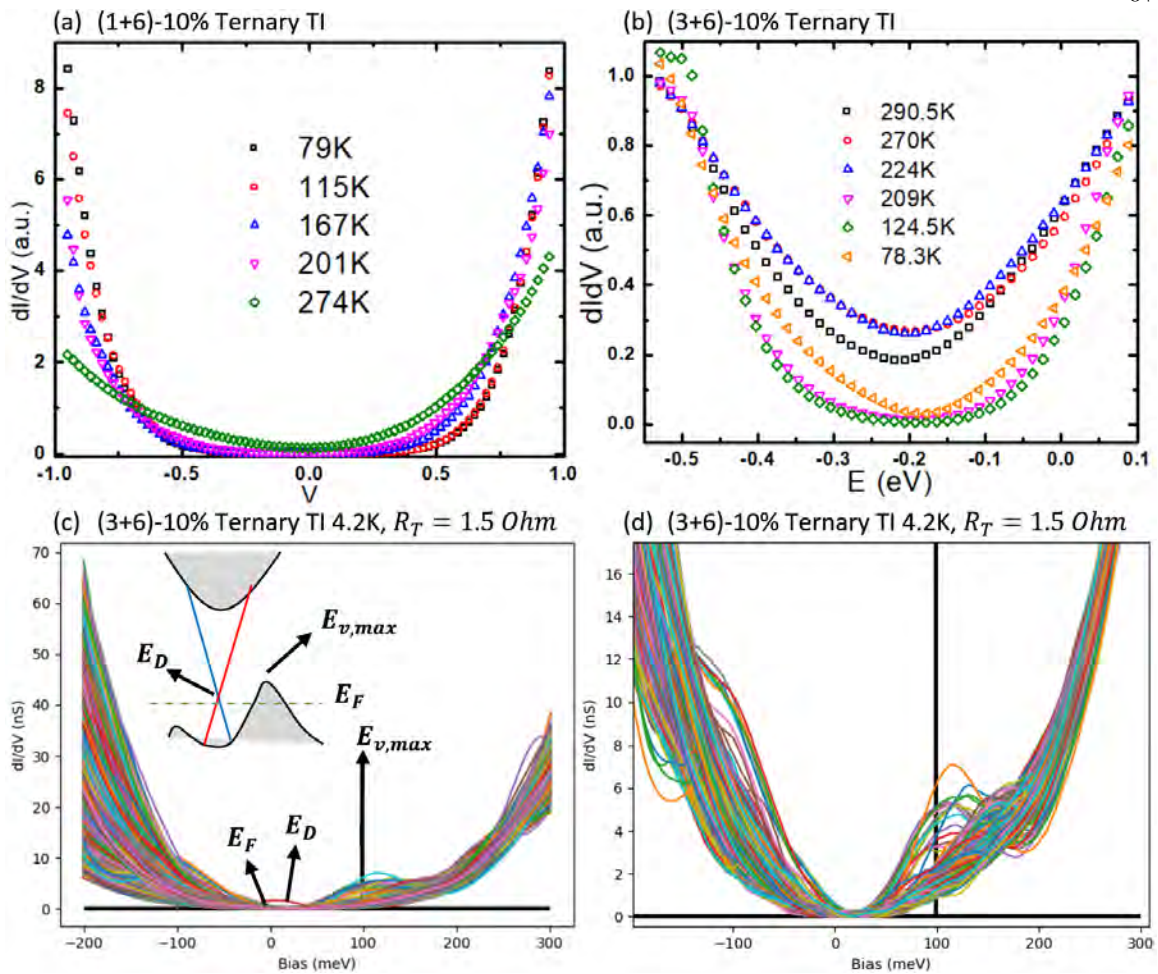


Figure 3.9: Majority spectra taken at different temperatures for **(a)** (1+6)-10% ternary TI/MTI and **(b)** (3+6)-10% ternary TI/MTI. **(c)-(d)** All point spectra taken from different areas of the (3+6)-10% ternary TI/MTI at 4.2K, showing the opening of a relatively small gap ranging from 20 meV to 40 meV. The Fermi energy, Dirac energy and valence band maximum energy can be identified from the dI/dV curves.

3.5.4 Summary and discussion

The average of majority dI/dV -vs.- V spectra taken at different temperatures indeed revealed meaningful temperature evolution for all binary and ternary TI/MTI samples. However, detailed studies indicated different degrees of spatial inhomogeneity for different types of samples, which is in contrast to the much more homogeneous spectra found in pure TI samples. The spatial inhomogeneity in the surface density of the states (DOS) may be attributed to different surface termination, attachment of oxygen atom [81], Cr-doping

induced effects such as lattice strain, excess charge, and magnetism. The tunneling spectra are also influenced by STM settings such as the bias, bias sweep range, bias current, tunneling conductance, and sweep speed. The phase change of the tip or an atom picked up by the tip could also suddenly change the dI/dV curves.

The majority spectra of the (5+6)-10% binary TI/MTI sample revealed similar gapless dI/dV for all temperatures, whereas those of (1+6)-10% and (3+6)-10% binary TI/MTI samples exhibited gap opening at low temperatures. These findings suggested that the proximity effect of binary MTI was limited to a distance $< 5\text{-QL}$, which is consistent with other studies [82, 83].

For (1+6)-10% and (3+6)-10% binary TI/MTI, a surface gap opened up below ~ 200 K, which increased with decreasing temperature initially and then exhibited a non-monotonic dip near 100 K before increased again with further decreasing temperature.

For ternary TI/MTI samples, the (1+6)-10% ternary TI/MTI also exhibited a consistent trend of surface gap opening and increasing with decreasing temperature, although the spectral evolution with temperature was more monotonous, probably due to the fact the Fermi level of the sample intersects the bulk band, as shown in Figure 4.20.

In the case of (3+6)-10% ternary TI/MTI, we found gapless spectra for most temperatures except a small surface gap opening (20 \sim 40 meV) at the lowest temperature of 4.2 K, and the excess DOS around the energy $E \sim 100$ meV relative to the Dirac point. These results could be consistently explained by the band structure and the Fermi level of the ternary MTI, as shown in Figure 4.19, and were further corroborated by the electrical transport measurements detailed in Chapter 4.

3.6 Evolution of the surface gap with temperature

Given the vast amount of STS data (on the order of millions of spectra) taken for this thesis work, it is necessary to develop a more quantitative way to analyze our data in order to extract meaningful information.

To investigate how dI/dV spectra evolved with temperature, two types of representative spectra are noteworthy (Figure 3.8(d) or Figure 3.10). One is a V-shaped gapless spectrum. The other is a U-shaped gapped spectrum.

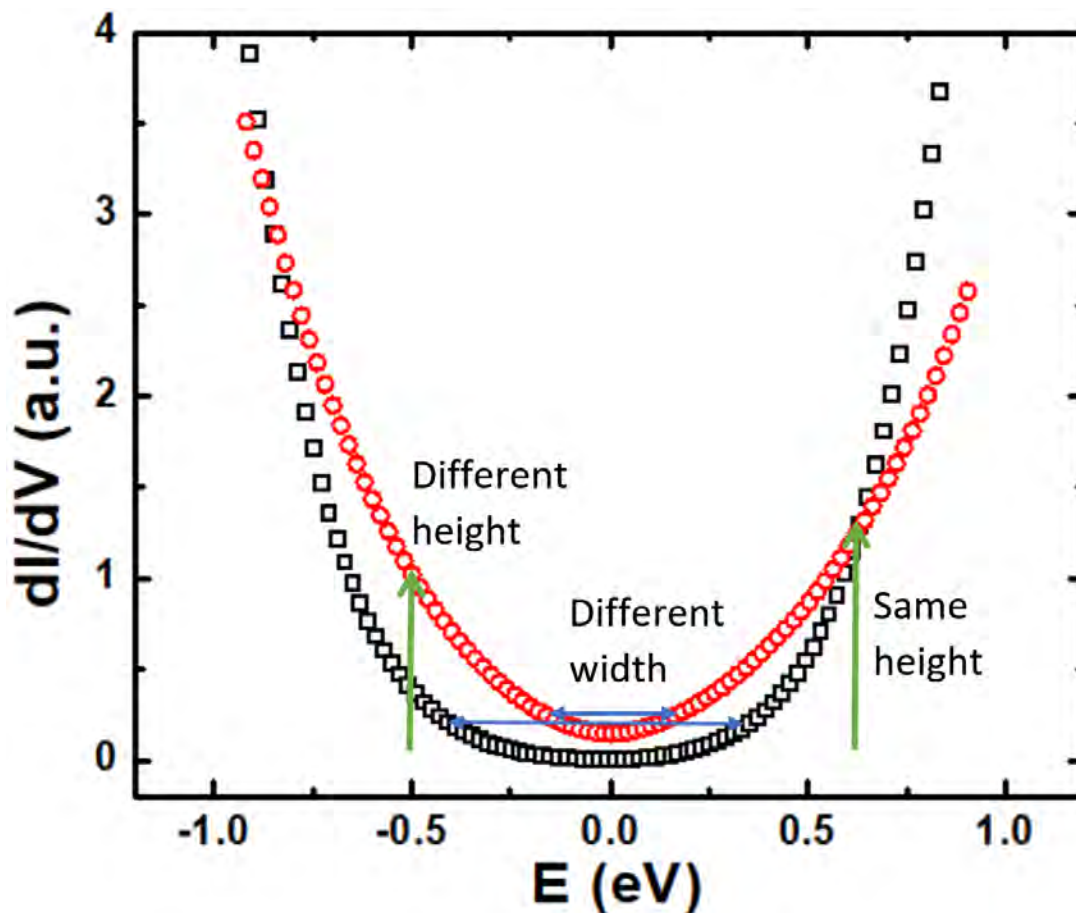


Figure 3.10: Representative gapless and gapped dI/dV spectra.

Although these two spectra are visually very different, telling them apart by writing computer code is challenging. We may consider the conductance map at a constant bias. For example, the left green arrow at $-0.5V$ in Figure 3.10 shows the maximum difference in conductance between the gapless and gapped spectra. Therefore, we would expect to observe an unambiguously gapped region and a gapless region in the conductance map at $-0.5V$.

There are two problems. First, we cannot guarantee that the conductance at some bias can always differentiate the gapped and gapless curve, as shown by the right green arrow in Figure 3.10. Second, we cannot derive the size of the gap through the conductance map. Nevertheless, the conductance map is still a very powerful tool to identify extremely localized DOS in energy scale, like impurity resonance.

3.6.1 Definition of the surface gap

The best way to differentiate gapped and gapless spectra is through the comparison of their spectral width at zero conductance. However, there are several challenges to derive the correct gap values: First, thermal smearing of the spectra caused by thermal excitation of electrons must be corrected. Second, noises caused by thermal excitation and differentiation of I-vs.-V often make the should-be-flat bottom of the spectra noisy and uneven. Third, if the surface gap is larger than the bulk gap or overlap with the ungapped DOS of the bulk states, then the bulk states will contribute to the tunneling current directly. It also causes the unevenness of the bottom of the curve.

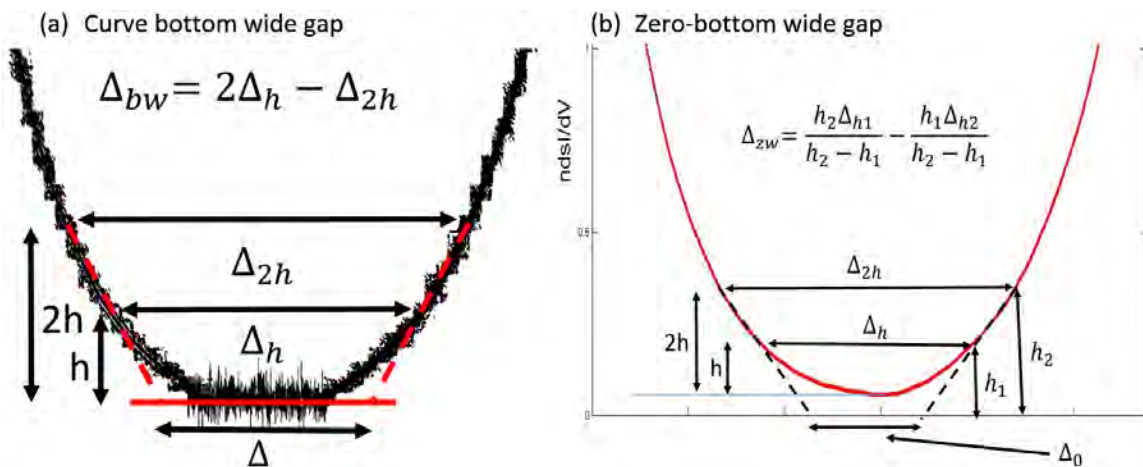


Figure 3.11: Definition of the gap through different methods. **(a)** Curve bottom wide gap determines the gap value at the bottom of the curve. **(b)** Zero-bottom wide gap determines the gap at 0 conductance rather than at the bottom of the curve.

The aforementioned issues would not have been big problems if we only had to do measurements at 4.2 K, because the low-temperature spectra should exhibit a flat bottom,

and the thermal smearing effect would have been minimized [84]. However, to study the temperature-dependence of the DOS, we must figure out a justifiable way to define the gap.

Figure 3.11 shows how we define a gap. The threshold height h from the bottom of the curve is needed to bypass the noise level at the bottom. The bottom value of the curve is determined by the average around the minimum region to remove the noise effect. We can obtain a gap size Δ_h according to the threshold height h . However, Δ_h definitely overestimates the size of the gap. What we can do is get another gap Δ_{h_2} with higher threshold height h_2 and use linear extrapolation back to derive $\Delta_{h=0}$:

$$\Delta_0 = \Delta_{h=0} = \frac{h_2 \Delta_{h_1}}{h_2 - h_1} - \frac{h_1 \Delta_{h_2}}{h_2 - h_1}. \quad (3.1)$$

In the most convenient case, choose $h_2 = 2h_1 = 2h$ so that $\Delta_0 = 2\Delta_h - \Delta_{2h}$. The idea of linear extrapolation is from the linear dispersion of the Dirac spectrum. However, as we can see from Figure 3.11, there is no real linear dispersion region around the gap. One choice is to choose 3 threshold height h_1, h_2, h_3 to do quadratic extrapolation. Another choice is to choose the h as small as possible and let h_2 as close as to h_1 as possible.

For extrapolation, we can extrapolate the gap back to the bottom (minimum in idea situation) of the curve. I called this the curve bottom wide (bw) gap Δ_{bw} . Another choice is to extrapolate the gap back to the 0 conductance, which I called zero bottom wide (zw) gap Δ_{zw} .

From the plot in Figure 3.11, both bw and zw gap overestimate the real gap size. However, this overestimation is nearly constant. Therefore, if we expect the gap at room temperature (RT) is 0. We may define our bw or zw gap here as thermal smearing gap:

$$\Delta_{smear} = \Delta_{bw}(RT) - \Delta_{2D}(RT) = \Delta_{bw}(RT) \quad (3.2)$$

$$\Delta_{2D}(T) = \Delta_{bw}(T) - \Delta_{smear}. \quad (3.3)$$

Despite this correction, $\Delta_{2D}(T, h)$ inevitably depends on h and still overestimates the real surface gap value. Therefore, we should not take the absolute value of the gap too seriously and compare it with DOS. For us, the most important thing is to have the metric to differentiate different shapes of dI/dV curves. As we will show soon, our results are quite fruitful.

We will present most of our results in Δ_{bw} . No further correction will be made to avoid confusion. Δ_{bw} is preferred because often, a phase change of the STM tip will introduce the constant conductance background while the overall shape of the dI/dV is still the same. Δ_{bw} is better to track the shape change of the spectra. Different measurements for different samples might use a different threshold to optimize for the noise level. In general, we try to use as small threshold h as possible. Δ_{bw} is definitely positively correlated to the real surface gap Δ_{2D} so it should give us a good idea about how the gap evolved with the temperature.

3.6.2 (1+6)-5% binary TI/MTI surface gap evolution with temperature

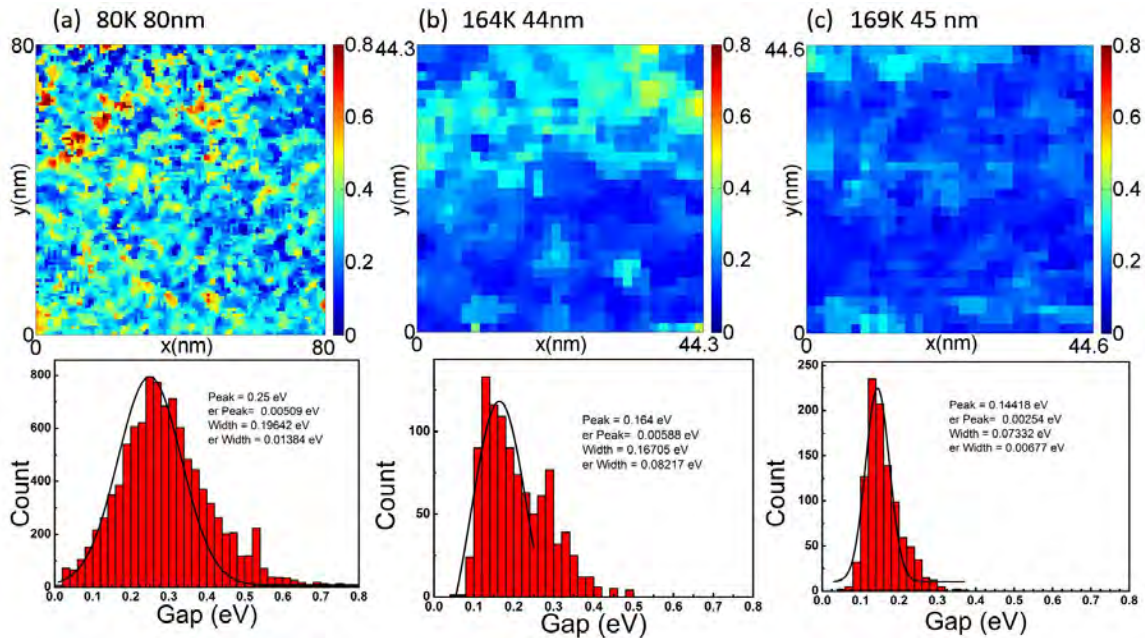


Figure 3.12 Gap value map and gap value histogram for (a) 80 K, (80 nm \times 80 nm), (b) 164 K, (44.3 nm \times 44.3 nm) and (c) 169 K, (44.6 nm \times 44.6 nm).

Figure 3.12 shows the gap value maps (gapmap) and gap value histograms (gaphist) for (1+6)-5% at 80 K, 164 K, and 169 K for (80 nm \times 80 nm), (44.3 nm \times 44.3 nm), and (44.6 nm \times 44.6 nm), respectively. The gapmap demonstrated the validity of our gap definition as the gapped domain-like feature in 164 K. Two main peaks show up in its histogram. One peak is for the gapless region, and another is for the gapped region. On the other hand, at a similar temperature of 169 K, the most area is gapless.

The peak of gapless gap distribution is around 0.15 eV for both 164 K and 169 K. In this case, we can assume $\Delta_{bw} = \Delta_{smear}$. The peak of the gapped region in 164 K is about 0.27 eV. The appearance of two peaks rather than a single peak also tells us something.

First, it implies that the opening of the gap was discontinuous around ~ 164 K, which is reasonable because the gap is proportional to the underlying magnetization M .

Second, at sufficiently low temperatures (*e.g.*, 80 K), most regions became gapped, although there were still many gapless regions. The peak of the histogram was around 0.25 eV, which is similar to what we obtained from the gapped peak in 164 K. However, the gap distribution became much broader. The gapped regions were still not well connected so that no anomalous Hall effect (AHE) could be observed at this temperature, as shown in Chapter 4.

We did the peak fitting for all the gaphist at all temperatures so we could estimate get peak value and error bar. Figure 3.13 shows the gap value *vs.* temperature for (1+6)-5%. If we consider the high-temperature averaged gap value (~ 0.15 eV) derived from the definition outlined earlier as the baseline, we notice a small jump in the averaged gap value between 240 and 260 K. From the gap maps, this was the temperature range where some gapped region began to appear. We can define the onset temperature as 2D Curie temperature T_{2D} . However, this transition is not very obvious. A more significant sudden jump of gap value occurs around 100 K.

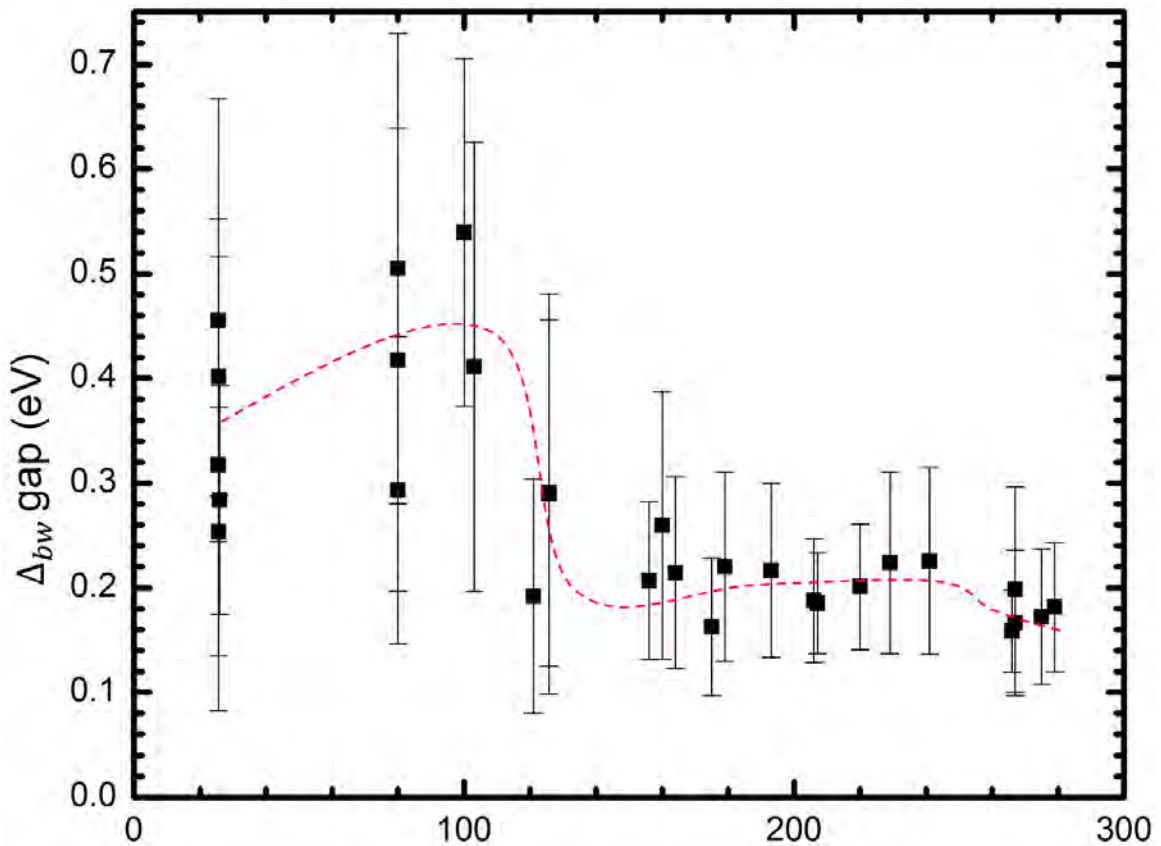


Figure 3.13: (1+6)-5% binary TI/MTI gap value vs. temperature. The gap value and error bar are from fitting the peak in the gap value histogram.

3.6.3 (1+6)-10% binary TI/MTI surface gap evolution with temperature

The (1+6)-10% sample has a higher Cr concentration, so the magnetic effect should be more substantial. However, the overall qualitative behavior should be similar to that of the (1+6)-5% sample. Figure 3.14 shows the corresponding gap value vs. temperature. Here we see a more significant jump at around 240 K. The onset of the surface gap is more evident than (1+6)-5% binary TI. The gap seems to appear between 130 K and 220 K. However, we need to more careful as the gap we used is a curve-bottom-wide gap Δ_{bw} , which simply determines the gap by purely the shape of the curve. However, if the curve has a very high minimum conductance, it is definitely conductive even if it is not a gapless Dirac spectrum but metal like DOS.

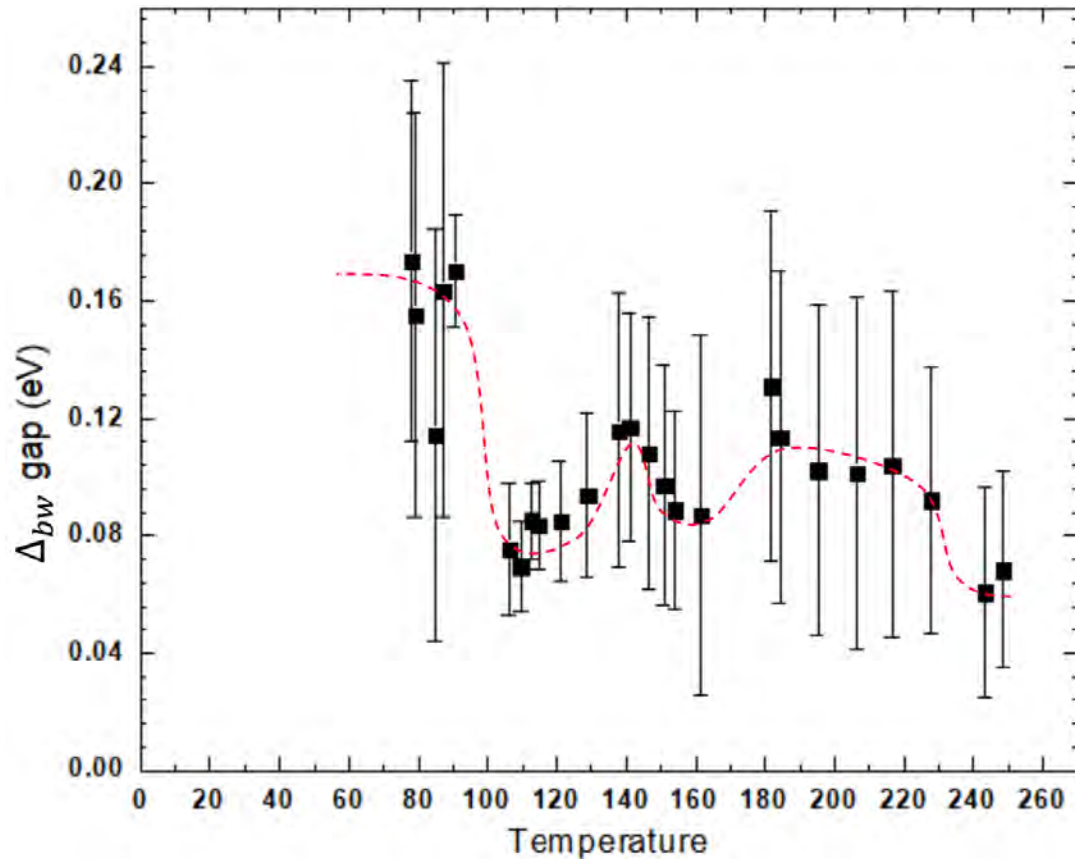


Figure 3.14: (1+6)-10% binary TI/MTI gap value vs. temperature. The gap value and error bar are from fitting the peak in the gap value histogram.

Figure 3.15 shows the gap maps at 78K, 106K, 141K, and 195K. The gap size is indeed corresponding to the values in Figure 3.14. The gap map at 78 K has smaller gapless regions compared to that of (1+6)-5% binary TI. The spectra became gapless around 100 K. This is quite interesting and may be related to the phase transition of the Cr.

Also, we note that long-range ferromagnetism does not always lead to a surface gap if the ferromagnetism is primarily aligned in the xy plane, as discussed in Chapter 1. We conjecture that the mixture of gapless and gapped regions between 141 K and 195 K was largely due to different magnetic domain alignment, which would explain why no AHE was observed at such high temperatures in the binary samples due to lack of long-range magnetization. This

notion could be further corroborated by studying the gap maps under a strong magnetic field applied perpendicular to the sample.

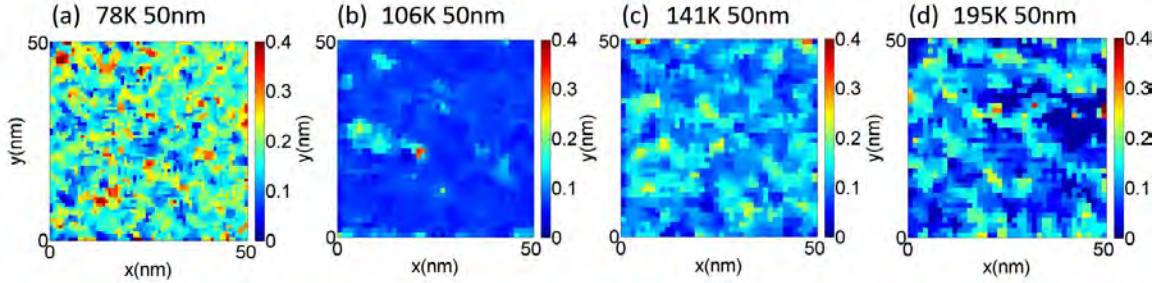


Figure 3.15: (1+6)-10% binary TI/MTI gap map at (a) 78K (b) 106K (c) 141K and (d) 195K

3.6.4 (3+6)-10% binary TI/MTI surface gap evolution with temperature

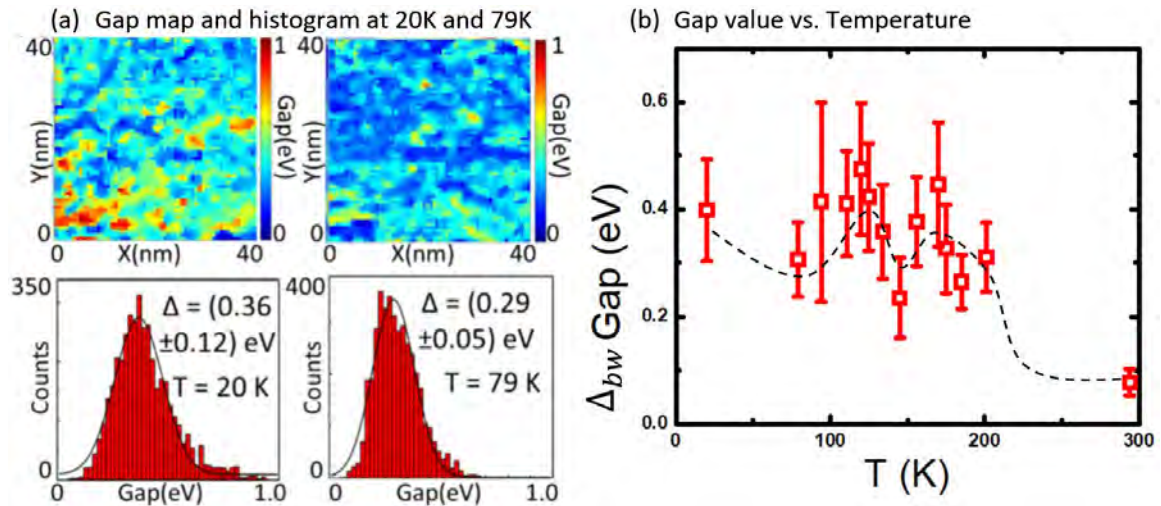


Figure 3.16: (3+6)-10% binary TI/MTI: (a) Gap map and gap histogram at 20 K and 79 K. (b) Gap value vs. temperature (T). [15]

For the (3+6)-10% binary TI/MTI, the result was very similar to those found in the (1+6)-10% sample with the onset of the gap above 200 K. There was also non-monotonic temperature evolution between 80 K and 200 K. The gap distribution on the gap map was also similar to the (1+6)-10% sample.

3.6.5 (1+6)-10% ternary TI/MTI surface gap evolution with temperature

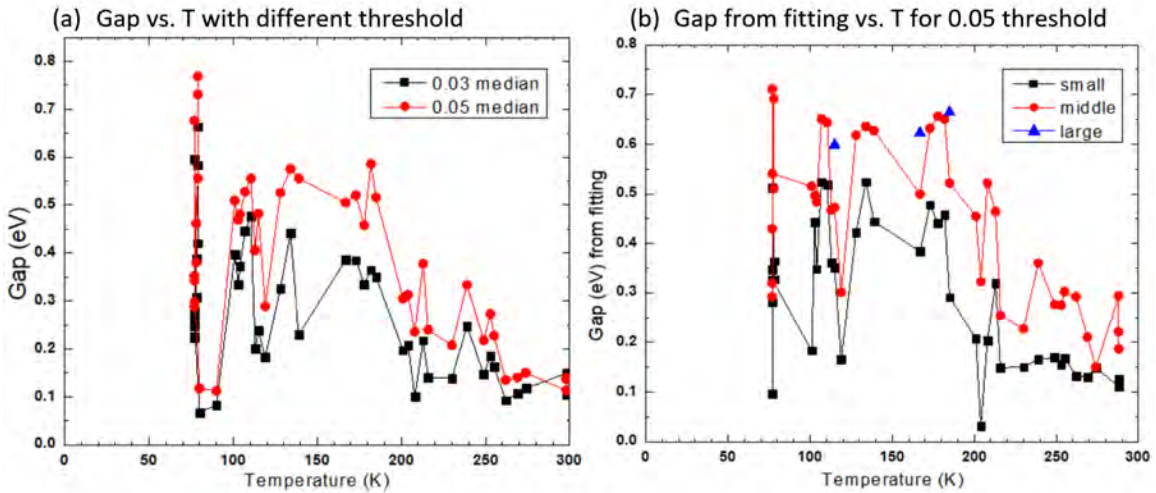


Figure 3.17: Surface gap vs. T for the (1+6)-10% ternary TI/MTI. **(a)** Gap derived from two different thresholds 0.03 and 0.05 (for the normalized dI/dV). **(b)** Gap derived from multi-peak fitting on gap histogram of threshold 0.05.

For the (1+6)-10% ternary TI/MTI sample, we explored different ways to better estimate the gap value. Figure 3.17 (a) we compare the gap vs. temperature plot with different thresholds h . As expected, the estimated gap value depends on the threshold. However, two curves are almost parallel to each other, which means the qualitative phenomenon we observed from the plot was reliable and representative of the temperature evolution of the tunneling spectra, no matter the threshold we chose as long as the threshold was above the noise level.

For the binary sample, we always used the single peak fit on the gap histogram to derive the gap and error bar. However, a single peak fitting could not match the histogram perfectly, so we explored the use of multi-peak fitting to fit the histogram better, as shown in Figure 3.17 (b). Multi-peak fitting worked best for the high-temperature part as the peak associated with the gapless curve is almost the same, while in Figure 3.17 (a), it shows fluctuation due to the onset of the gapped region. The 2D transition temperature was around 200 K and can be recognized easily in Figure 3.17 (b).

Between 100 and 250 K, both gapped and gapless domains coexisted. If we happened to scan the gapped or gapless domain, the result would differ a lot. The multi-peak fitting can solve this problem.

3.6.6 (3+6)-10% ternary TI/MTI surface gap evolution with temperature

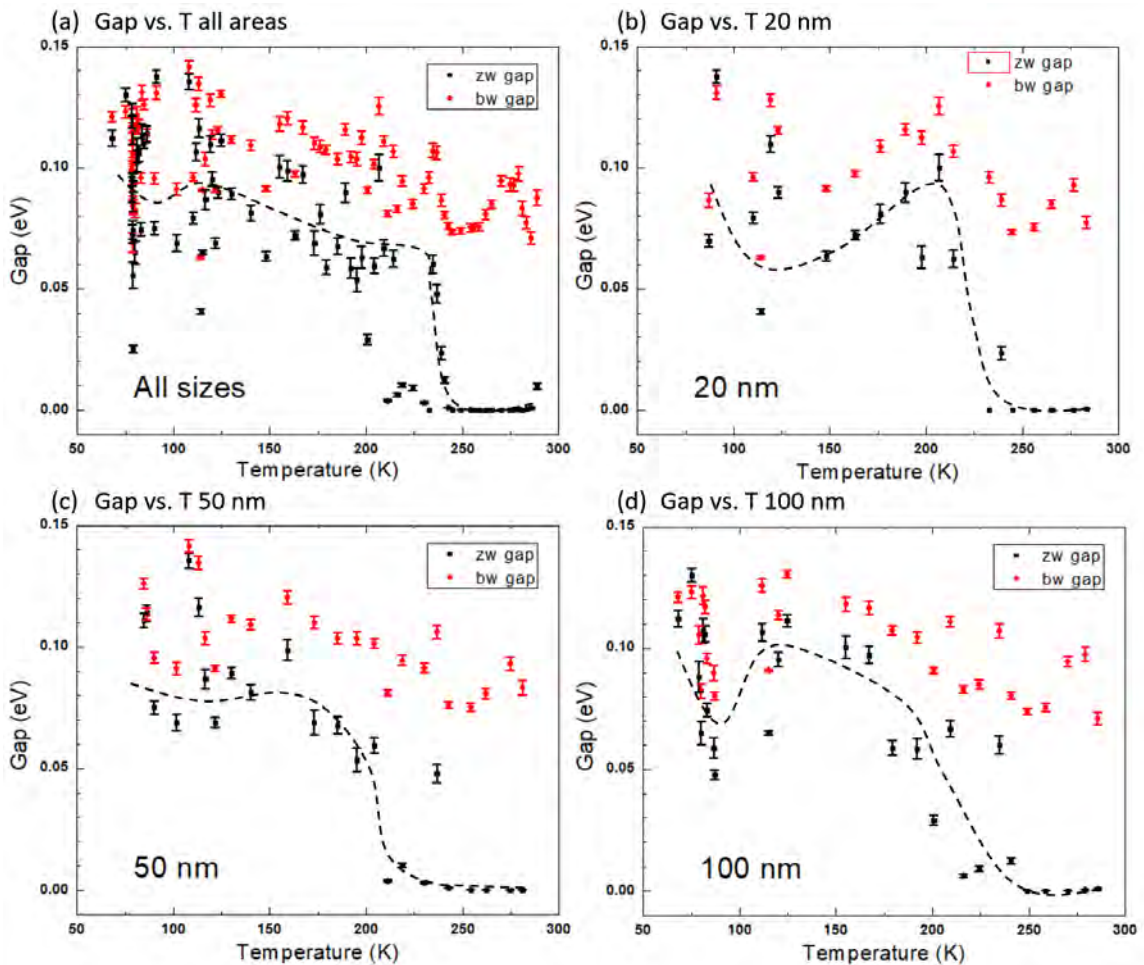


Figure 3.18: Δ_{bw} and Δ_{zw} vs. T of the (3+6)-10% ternary TI/MTI for different sizes of the scan area. **(a)** All sizes (including 20×20 , 50×50 , 100×100 , 200×200 , 500×500 , 1000×1000 nm²); **(b)** (20 nm \times 20 nm); **(c)** (50 nm \times 50 nm); **(d)** (100 nm \times 100 nm).

For the (3+6)-10% ternary TI/MTI sample, we considered two other factors that might influence the estimate for the gap value. One is the comparison between Δ_{zw} and Δ_{bw} . The other is the STS scan size of the area.

Δ_{bw} is related to the shape of the curves rather than their height while $\Delta_{zw} = 0$ for a more metallic curve. In Figure 3.18, both Δ_{zw} and Δ_{bw} are shown. A huge difference appeared above 200 K as big minimum conductance began to appear. The transition temperature is easier to recognize in Δ_{zw} vs. T plot. Overall, it appeared that Δ_{zw} was a better representation of surface gap. From the Δ_{zw} vs. T data, we also found that the overall surface gap distribution in the ternary TI/MTI appeared to be more homogeneous than that in the binary TI/MTI system, which is consistent with the finding of hysteretic behavior in electrical transport measurements only in the ternary TI/MTI samples, as discussed in Chapter 4.

If gapped domains began to form below the 2D Curie temperature, the gap value for a larger area scan should fluctuate more as shown in Figure 3.18 that both curves taken over (50 nm \times 50 nm) and (100 nm \times 100 nm) areas indeed appeared to fluctuate more near the 2D Curie temperature, while the curve taken over (20 nm \times 20 nm) exhibited smoother transition near the 2D Curie temperature.

3.6.7 Summary and discussion of the temperature evolution of the surface gap

For both binary and ternary TI/MTI samples, small gapped regions began to show up around 200 K. However, the size of the gap did not increase monotonically with decreasing temperature in the binary TI/MTI samples. Instead, the majority spectra became nearly gapless again around 100 K and then reopened and increased with decreasing temperature again for $T < 100$ K. In contrast, the averaged surface gap in ternary TI/MTI samples appeared to be mostly monotonically increasing with decreasing temperature except a slight decrease near 100 K, and the spatial distributions of the gap value more also more homogeneous. These findings from microscopic STS studies are consistent with the macroscopic electrical transport measurements detailed in Chapter 4, where resistive hysteresis associated with long-range ferromagnetism was only observed in the ternary TI/MTI samples

3.7 Magnetic effect on the surface states

As discussed in Chapter 1, finite out-of-the-plane magnetization is responsible for the surface gap opening in the TIs. In this context, we may apply an out-of-plane magnetic field to better align magnetic moments, which could lead to more homogeneous gap distributions and also enhance the averaged gap values.

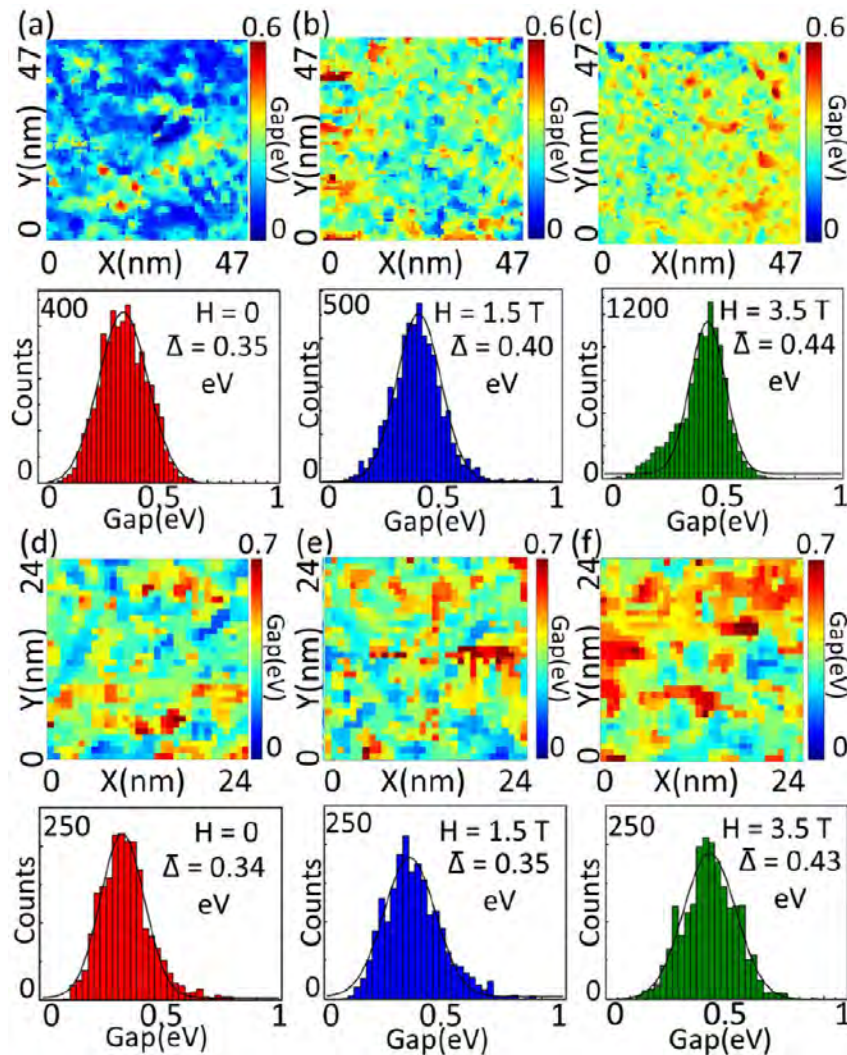


Figure 3.19 Evolution of the surface gap distribution at $T=18$ K with applied c-axis magnetic field: (a)–(c) gap maps (upper panels) and the corresponding gap histograms (lower panels) of a (1+6)-5% sample taken at $H=0$, 1.5 T and 3.5 T over the same (47×47) nm² area. (d)–(f) Gap maps (upper panels) and the corresponding gap histograms (lower panels) of a (3+6)-10% sample taken at $H=0$, 1.5 T, and 3.5 T over the same (24×24) nm² area. [15]

Figure 3.19 shows the gap map and the corresponding histogram under different magnetic fields for (1+6)-5% and (3+6)-10% binary TI/MTI samples at $T = 18$ K. The external magnetic field appeared to help enhance the gap value slightly. However, the effect was relatively small at $T = 18$ K, as shown in Figure 3.20. More importantly, however, the gap distribution appeared to be much more homogeneous.

These results were not surprising when we compare the STS data with the electrical transport measurement for binary TI/MTI in Chapter 4. It was found that the magnetic field did not have any effect on the macroscopic transport properties until below 8 K.

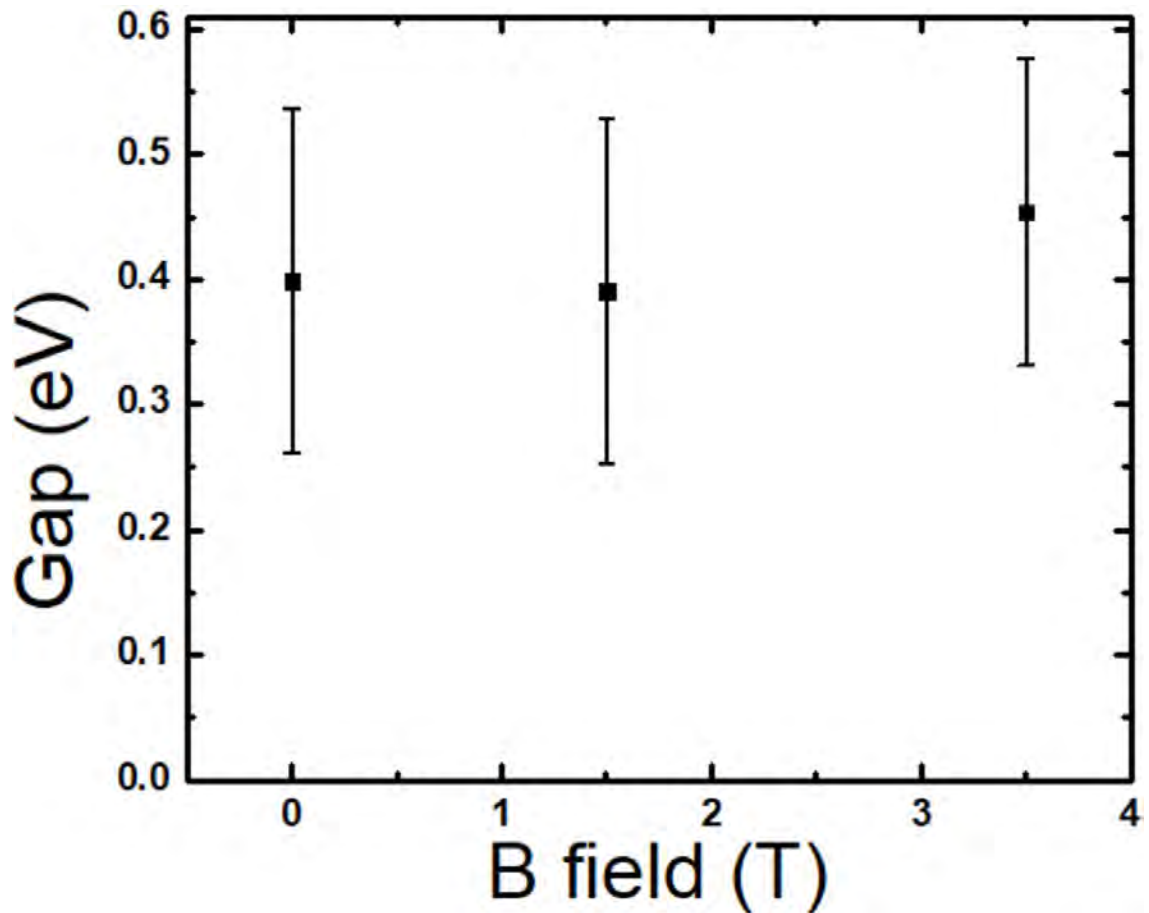


Figure 3.20: (3+6)-10% binary TI gap vs. magnetic field at $T = 18$ K.

We also did some measurements on ternary TI/MTI with a magnetic field. However, the measurements were incomplete due to the lockdown, and so I cannot draw any conclusions. However, ternary TI/MTI is expected to exhibit novel responses to magnetic fields from electrical transport measurements. Future field-dependent STS measurements at low temperatures on the ternary TI/MTI samples would be useful to understand better the microscopic origin of novel field-dependence in the electrical transport measurements.

3.8 Impurity resonance

As we mentioned before, although the majority dI/dV -vs.- V spectra look like either V-shaped gapless spectra or U-shape gapped spectra, there were occasionally reproducible minority spectra that were distinctly different from the characteristics of majority spectra. The impurity resonance spectra is one of them. We can think of impurity resonance as a single discrete state in DOS. Hence, the DOS curve looks like a delta function or a single peak.

3.8.1 the appearance of the magnetic impurity resonance curve

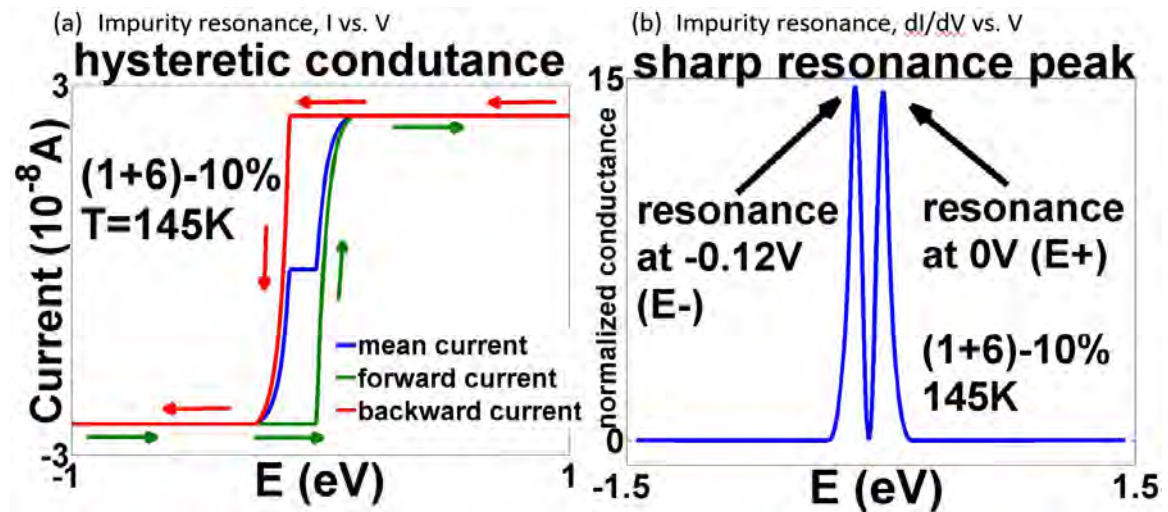


Figure 3.21 STS of impurity resonance. (a) I vs. V (b) dI/dV vs. V

In our STS of binary TI/MTI samples, some sharp double peaks showed up. Their I -vs.- V spectra exhibited hysteresis, which indicated their magnetic origin. Therefore, the spectra

appeared as double peaks in the dI/dV - v_s - V . We note that the I - v_s - V spectrum looks like the R_{xy} v_s - B data and the dI/dV - v_s - V spectrum looks like the R_{xx} v_s - B data (Chapter 4). It might also be related to the topological magnetoelectric (TME) effect. On the other hand, non-magnetic impurity is the only single peak with its energy right in the middle of double peak magnetic impurity. Interestingly, we also observed some single peak magnetic impurities with their peak position the same as one of the double peaks.

Another notable thing is that the energy between the double peaks of impurity is almost the same no matter the location or even the temperature. These seemingly puzzling results are investigated further in the following.

3.8.2 Spatial distributions of the magnetic impurity resonance

The location of each impurity resonance can be determined easily through the conductance map at one of its peak energy, as shown in Figure 3.22 (b). The locations of double-peak and single-peak resonances can be recognized easily by comparing the conductance map at both peak energy. Those impurities are extremely localized (within 0.1 ~ 0.2 nm range), as shown in the 3D conductance map in Figure 3.22 (c) and dI/dV along the line cut cross the impurity at Figure 3.22 (d).

This extreme localization of magnetic impurity resonances in binary TI/MTI may be attributed to the topological protection of the surface state. In contrast, no impurity resonances were observed in the ternary TI/MTI samples. As elaborated in Chapter 4, the Fermi level in the ternary TI/MTI samples that we studied always involved bulk carriers so that the surface states were not dominant as in the case of binary TI/MTI systems. We conjecture that the significant contributions of bulk bands at all temperatures in the ternary TI/MTI system weakened the topological protection of the surface state, hence the absence of any localized magnetic resonances in the ternary TI/MTI system.

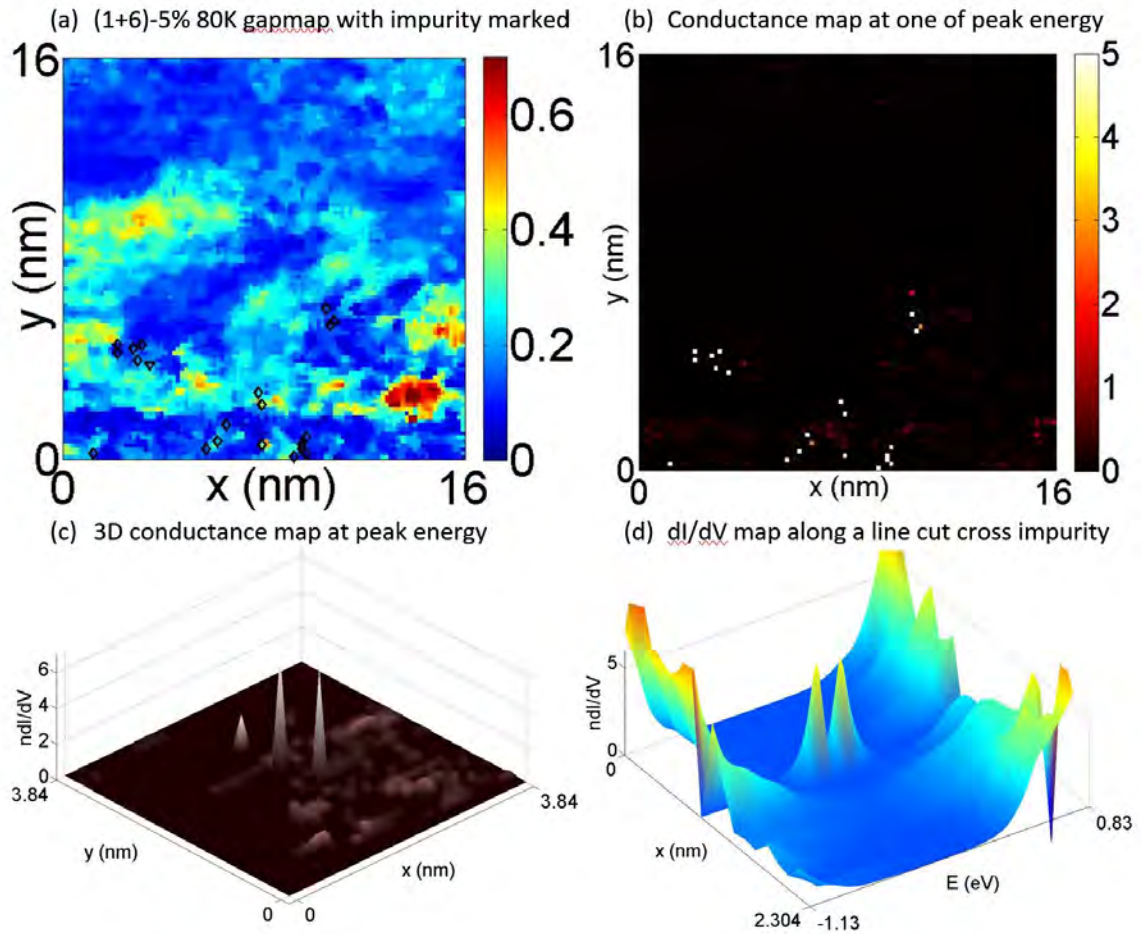


Figure 3.22 (a) Spatial distributions of impurity resonances on the gap map for the (1+6)-5% binary TI/MTI sample. The up triangle is for a single peak at higher energy. The down triangle is for a single peak at the lower energy. The diamond shape is for a double peak. (b) Conductance map at one of the impurity peak energy -0.28V (c) 3D conductance map near the impurity resonance. (d) dI/dV along the line cut cross the impurity resonance.

Interestingly, when we overlapped the location of the impurities onto the gap map, we found that the impurity mostly appeared at the boundary of the gapped and gapless domains. This finding is reasonable because isolated spins along the domain boundaries were not tightly aligned to the magnetization of the domain, and so could respond to the TME effect exerted from the STM tip. For isolated spin aligned in the in-plane direction, sweeping the voltage could create an effective magnetic field to move the spin along either $+z$ or $-z$ direction, hence the double-peak feature (Figure 3.21(b) and Figure 3.23(b)). On the other hand, for an isolated spin along either $+z$ or $-z$ direction, the TME effect from the STM tip would simply

determine the sign of effective energy associated with the isolated spin, hence a single peak resonance (Figure 3.23(c)).

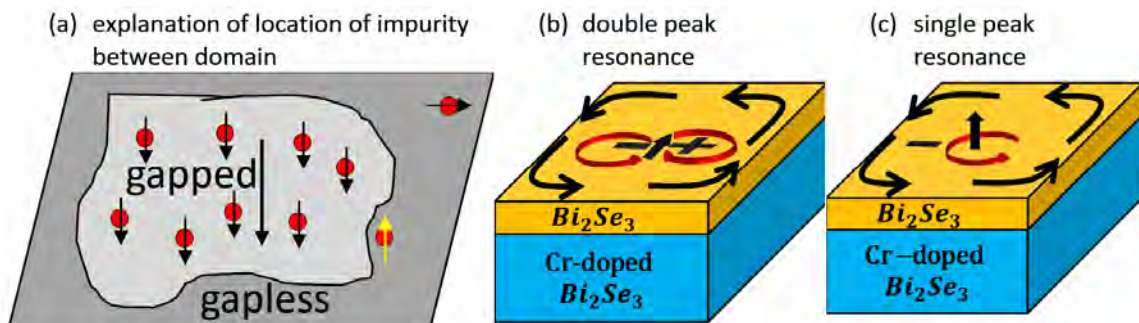


Figure 3.23 (a) Explanation of the location of impurity. (b) Double peak resonance might be caused by in-plane spin impurity (c) Single peak might be caused by out of plane spin impurity

3.8.3 The number of impurity resonance vs. temperature

In our investigation of a Se-capped (1+6)-10% binary TI/MTI, we found that the tunneling conductance spectroscopic studies revealed a large gap almost everywhere with spotty gapless regions. In this particular sample, many domain boundaries were present, which were accompanied by the frequent appearance of the impurity resonances.

To verify whether our observed impurity resonances were indeed associated with isolated spins along domain boundaries, we analyzed the number of impurity resonance vs. temperature, as shown in Figure 3.24. At low temperatures, the number of impurity resonances was low small. As the temperature increased, the number of impurities went up sharply near 250 K, which was approximately the 2D Curie temperature we observed. A sudden drop occurs, and then the impurity gradually went up again.

The temperature dependence of the number of impurity resonances is consistent with the finding of isolated spins along the gapped and gapless boundaries because strong thermal fluctuations could allow more spins along the domain boundaries to freely respond to the TME effect of the STM tip, hence a strong increase in the number of impurity resonances near the 2D Curie temperature.

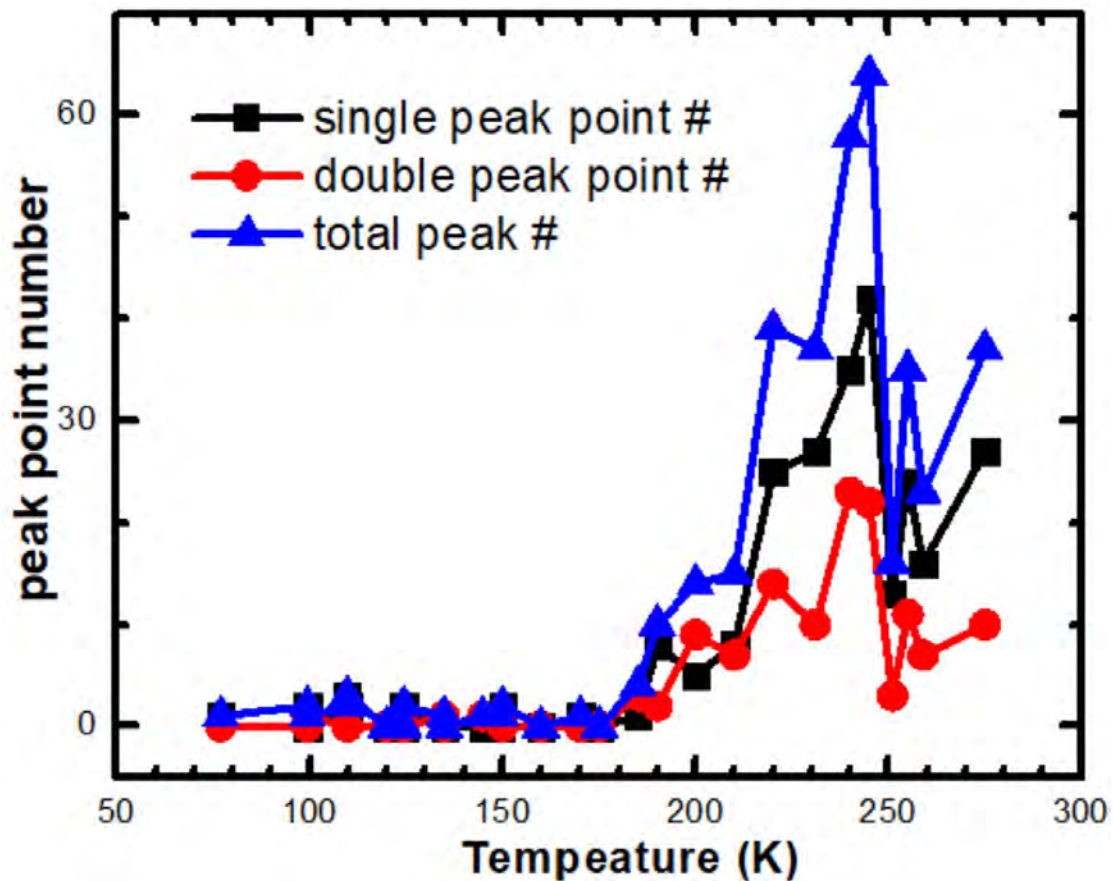


Figure 3.24 The number of impurity resonance vs. temperature

On the other hand, the specific influence of Se-cap is still unknown. It might introduce more gap regions on the sample. Future investigations of Al-capped binary TI to Se-capped binary TI/MTI samples could shed light on the relevance of the Se-capping.

3.8.4 Summary of impurity resonances

Magnetic impurity resonances due to isolated spins only appeared in binary bilayer TI/MTI samples, which may be attributed to the lack of long-range ferromagnetism and the dominance of the surface state for better topological protection. Impurity resonances only appeared between gapped and gapless domain boundaries and were found to be very localized and robust. Therefore, these interesting features may be considered as “topological bits” for potential applications to quantum memory. We may take advantage of the finite

range of magnetic proximity effect in the binary TI/MTI system to design a device with different thicknesses of the top TI-layer to create a controlled gap and gapless regions, which could confine magnetic impurities to the designed boundaries as shown in Figure 3.25. The interaction among the impurities may be tuned by the Fermi level, which is controlled by the back gate.

Ternary TI, on the other hand, lacks any impurity resonance. The transport measurement also demonstrates that weak anti-localization exists above 13K. Below 13K, weak localization appears under the weak magnetic field (<0.5 T). We might be able to see something interesting below this temperature.

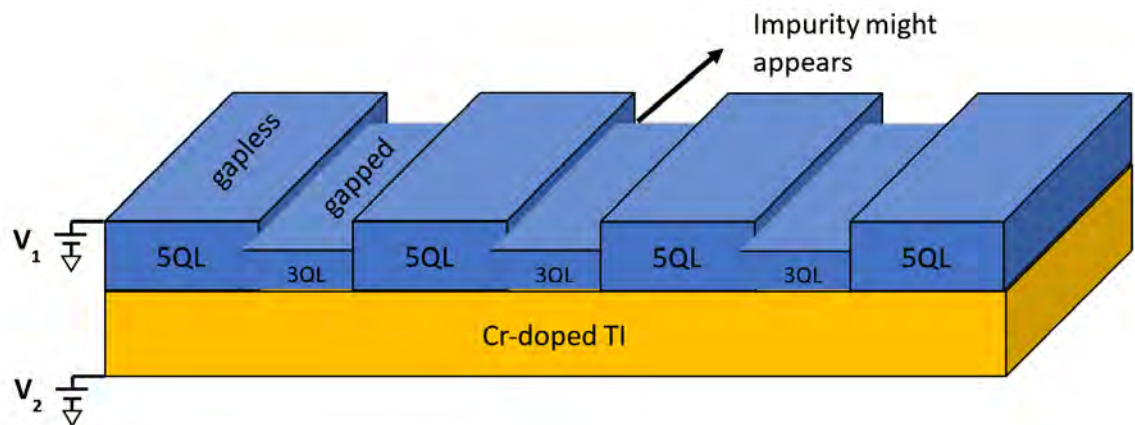


Figure 3.25 Possible device to line up the location of impurity and control it by the back gate.

3.9 Summary and future project

We have shown that a surface gap in the top TI layer of both binary and ternary TI/MTI structures can open through the proximity effect to the underlying MTI. Although our definition of gap tends to overestimate the real gap value a lot, qualitatively, we still get many useful results, including the identification of a 2D Curie temperature, the observation of more significant spatial gap inhomogeneity in the binary TI/MTI system, and the estimate of the range of magnetic proximity effect along the c-axis. Many findings in the STS studies are consistent with the electrical transport measurements, such as the lack of hysteresis in binary

TI/MTI samples and the absence of impurities resonances in ternary TI/MTI. The contrasts between the binary and ternary TI/MTI samples may be primarily due to the differences in their band structures and Fermi level, particularly the persistent presence of bulk band contributions to the tunneling spectra in the ternary TI/MTI system differs significantly from the dominant surface state contributions in the binary TI/MTI system.

The external magnetic field seemed to have relatively small effects on the gap size of binary TI/MTI at $T = 18$ K, although the gap homogeneity could be significantly improved. Lower temperature studies of the magnetic field effect, as well as employing spin-polarized STM or magnetic force microscopy (MFM) in our new STM/AFM system, may help shed light on the effect of the magnetic field.

Ternary TI/MTI samples at the low temperatures may show very interesting results as a function of the magnetic field. We also have a bilayer TI/antiferromagnetic sample that exhibits a much higher bulk Curie temperature, which may reveal very different gap distributions as a function of temperature and magnetic field.

Electrical transport measurements on ternary TI/MTI samples have shown the interesting influence of circularly polarized light on the anomalous Hall effect. It will be interesting to investigate how circularly polarized light may affect the tunneling spectra of ternary TI/MTI samples and compare the findings with transport measurements.

The upcoming new customized commercial STM/AFM system is exciting as it will enable us to do the experiment faster and easier. It has both AFM and STM function and MFM tip. It can also help us have more discoveries on the topological insulators.

Chapter 4

ELECTRICAL TRANSPORT STUDIES OF MAGNETIC TOPOLOGICAL INSULATORS

STM is a powerful tool to investigate the surface states of topological insulators (TIs). Earlier studies of TIs were mostly carried out by angle-resolved photoemission spectroscopy (ARPES) and electrical transport measurements. Both techniques provided the macroscopic behaviors of TIs. Although the global properties of TIs may be considered as the collective behavior of microscopic properties, our STM studies of magnetic TIs (MTIs) have revealed significant deviations of the microscopic, 2D magnetic transition temperature from the macroscopic, 3D magnetic transition temperature, as discussed in Chapter 3. To understand how the microscopic properties of MTIs influence their macroscopic properties, it is essential to investigate the global behavior of MTIs systematically. Thus, the combined studies of spatially resolved magnetic orders by STM and of the global magnetic properties by electrical transport measurements can help construct a more complete picture for the properties of MTIs.

The acquisition of a Physical Property Measurement System (PPMS) at Caltech provides us with a cost-effective and powerful experimental tool to control the sample environment for electrical transport studies. With its helium cycling system, no liquid helium is required for the cryogenic experiments. Unlike our STM system, the temperature and magnetic field of PPMS on the sample can be adjusted easily and quickly. The temperature range for the PPMS is from 300 K to ~ 1.8 K, and the magnetic field range is from 0 to 9 T. The relative ease of PPMS operation enables in-depth studies of the transport properties of TIs and MTIs.

In this chapter, I will first describe the electrical transport studies of binary bilayer Bi_2Se_3 /Cr-doped Bi_2Se_3 structures, which will be followed by the transport studies of ternary bilayer $(BiSb)_2Te_3$ /Cr-doped $(BiSb)_2Te_3$ structures.

4.1 Transport studies of bilayer Bi_2Se_3 / Cr- Bi_2Se_3

4.1.1 Sample characteristics and experimental setup

The binary TIs we studied by PPMS is similar to what we studied by STM except for the different capping layers and the substrates. Table 4.1 lists all the binary samples we used for STM and PPMS studies. All these samples consist of a bilayer structure of TI/ Cr-doped TI, with the TI being Bi_2Se_3 , which has the simplest bandstructure and the largest bulk gap among all TIs. While most researchers studied Cr-doped TIs directly, as explained in Chapter 3, in our studies of magnetic effects on TIs, we would like to prevent the complications associated with Cr-doping induced structural changes. The bilayer structure with a pure TI on top of a Cr-doped TI enables surface gap opening in the pure TI layer without structural changes through its proximity to ferromagnetism when the underlying Cr-doped TI becomes ferromagnetic below the Curie temperature.

Table 4.1 lists of bilayer binary samples for STM and PPMS studies.

sample ID(UCLA)	Top layer# Bi_2Se_3	bottom layer# $Cr-Bi_2Se_3$	Cr %	capping	substrate	Grower
LH 997	1QL	6QL	10%	Se	InP	Liang He
LH 999	3QL	6QL	10%	Se	InP	Liang He
LH 1001	5QL	6QL	10%	Se	InP	Liang He
LH 1002	7QL	6QL	10%	Se	InP	Liang He
LH 1183	1QL	6QL	5%	Se	InP	Liang He
KM 1870	1QL	6QL	10%	Se	InP	Koichi Murata
KM 2785	3QL	6QL	10%	Al	GaAs	Koichi Murata
KM 2786	1QL	6QL	10%	Al	GaAs	Koichi Murata

From the STM studies in Chapter 3, we found that a surface gap could be detected on a bilayer binary TI/MTI structure if the thickness of the top TI layer was less than 5 QL. Therefore, we chose (1+6)-10% and (3+6)-10% binary TI/MTI structures for the electrical transport studies. In principle, (5+6)-10% samples should have been studied as well for comparison. However, due to the limited availability of the shared PPMS and a large number

of samples we would like to explore, we only chose the most interesting samples for this investigation.

A collection of the bilayer binary TI/MTI samples are summarized in Table 4.1. These samples were grown by molecules beam epitaxy (MBE) on semiconducting substrates at UCLA by Professor Kang-Long Wang's group. Empirically it was found that the choice of GaAs substrates yielded better TI samples than InP substrates and that the use of aluminum (Al) to form aluminum oxide as the capping layer provided better protection than Se to prevent the TI samples from degradation. Therefore, for electrical transport studies of the binary bilayer TI/MTI compounds, we focused on the investigation of KM 2785 (3+6)-10% and KM2786 (1+6)-10% samples. We further note that for the transport measurements, it was not necessary to remove the capping layer before placing the electrodes on the sample because the capping layer was very thin ($< 3\text{nm}$) so that electrical currents from electrodes placed above the capping layer could tunnel easily into the sample. Therefore, electrical connections to the samples could be made by directly soldering electrodes onto the surface of the sample.

For the preparation of transport measurements, the sample was etched into the 6-contact Hall bar geometry, as shown in Figures 4.1(b) and 4.1(d). The etching was done by Advanced Oxide Etcher (AOE) with a metal mask and the etching gas CHF_3 . The sample was then attached to the print circuit board (PCB) with either adhesive tapes or GE varnish if no back gate was required, or with silver paste if a back gate was required. Aluminum wires are soldered to the electrical contacts on the sample Hall bar and also to the pins on the inner ring of the PCB (Figure 4.1 (b)). The solder was indium because of its softness, stickiness, and low melting temperature that prevented overheating the sample. The pins of the PCB were then soldered to the puck, while the PCB must be electrically isolated from the puck by an insulating insertion layer. The puck was subsequently loaded into the PPMS for electrical transport measurements as a function of temperature and magnetic field. More details about the PPMS setup have been given in Chapter 2.

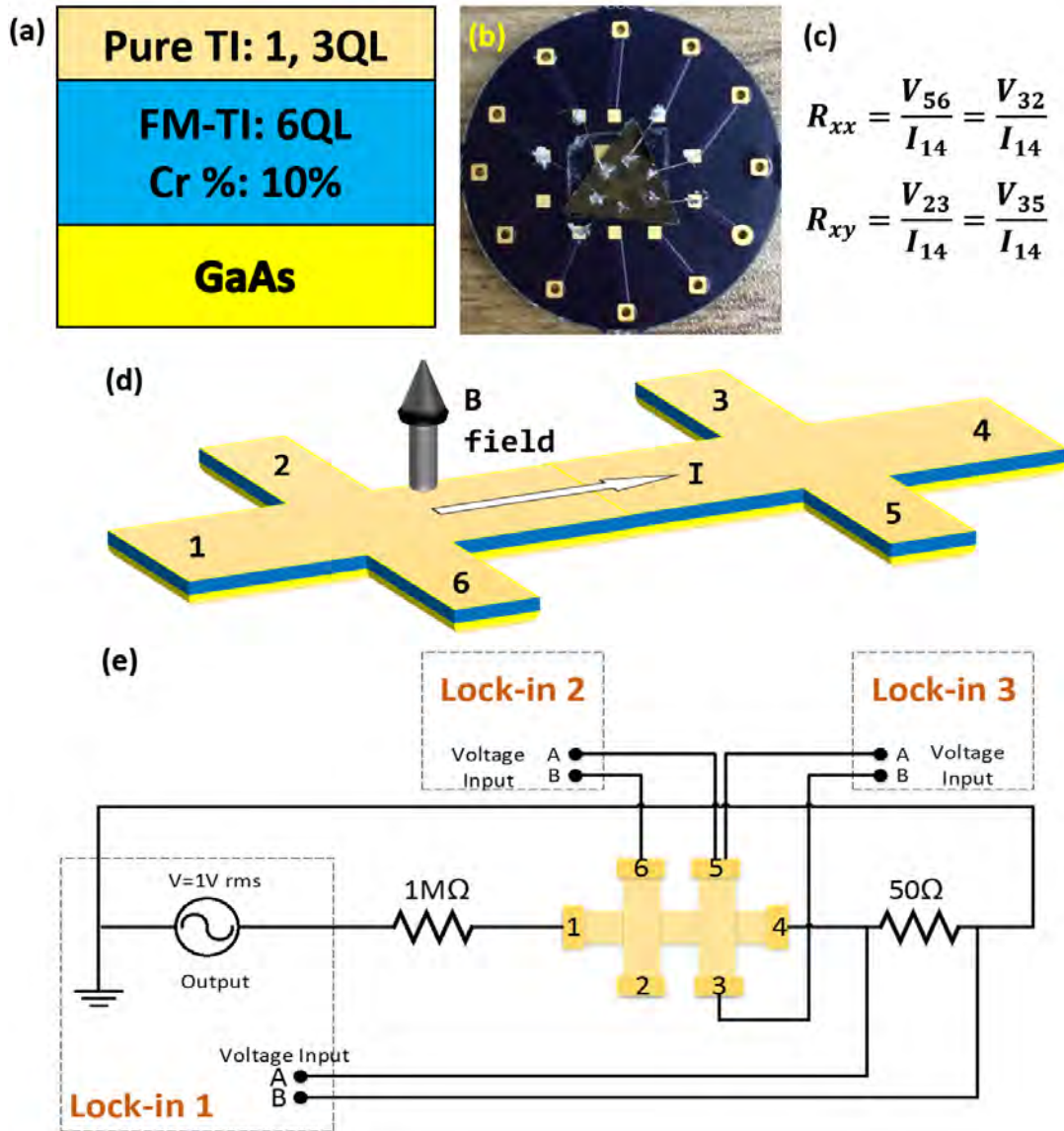


Figure 4.1: (a) Schematic illustration of the side view of a representative bilayer TI/MTI sample, showing a pure TI layer with 3-QL thickness on top of a ferromagnetic (FM), 10% Cr-doped TI layer with 6-QL thickness. The nomenclature for this bilayer TI/MTI is thus given by (3+6)-10%. (b) An optical micrograph of a print circuit board (PCB), showing electrical connections to the Hall bar structure patterned on a sample (triangular shape) in the center of the PCB. (c) Formulae used to calculate the longitudinal resistance R_{xx} and Hall resistance R_{xy} through measurements of the voltages and current defined in (d). (d) The Hall bar geometry and definitions of the electrical contacts 1~6 on the Hall bar. The external magnetic field is applied perpendicular to the Hall bar plane. (e) Electrical circuit setup for the Hall bar measurements. 3 Lock-in amplifiers are used for detecting the signals: Lock-in 1 determines the electrical current, Lock-in 2 measures R_{xx} , and Lock-in 3 measures R_{xy} .

The primary objective of the transport measurements is to determine the longitudinal resistance R_{xx} and Hall resistance R_{xy} (Figure 4.1 (c)). Although such measurements may be carried out with a DC approach, we employed three lock-in amplifiers to measure the voltage responses and current responses in order to enhance the signal-to-noise ratio. One of the lock-ins was also used as a voltage source to supply the electrical current. The frequency of the source was set to a value between 5 ~ 15 Hz, which was near the DC limit. Therefore, to ensure that we had stable and accurate measurements, the time constant was set to approximately 10 times the period of the source, yielding 1 ~ 3 seconds. Instead of detecting the current directly, we measured the voltage across a precision resistor placed in series with the rest of the circuit for higher precision and less systematic errors in the resulting current reading.

The software interface based on Labview was jointly developed by my SURF student Ankit Kumar, my groupmate Adrian Llanos, and his SURF student **Bannhat Phat**. For measurement settings, "temperature sweep" took voltage signals continuously at different temperatures under a constant magnetic field, whereas "field sweep" took data in changing magnetic fields while at a fixed temperature. Although one may naively assume that the same 3D map of signals vs. the magnetic field (B) and temperature (T) could be obtained by either temperature sweeps or field sweeps if measurements were taken with a sufficiently large number of temperature and field values, for ferromagnetic samples caution must be taken because the measured signals would be history-dependent.

4.1.2 (1+6)-10% binary TI/MTI temperature sweep

For temperature sweep measurements, we could choose either cooling or warming sweeps at specific magnetic fields. To identify the onset temperature for the anomalous Hall effect (AHE), we performed zero-field-cool (ZFC) measurements. On the other hand, a magnetic field was applied during the warm-up temperature sweep.

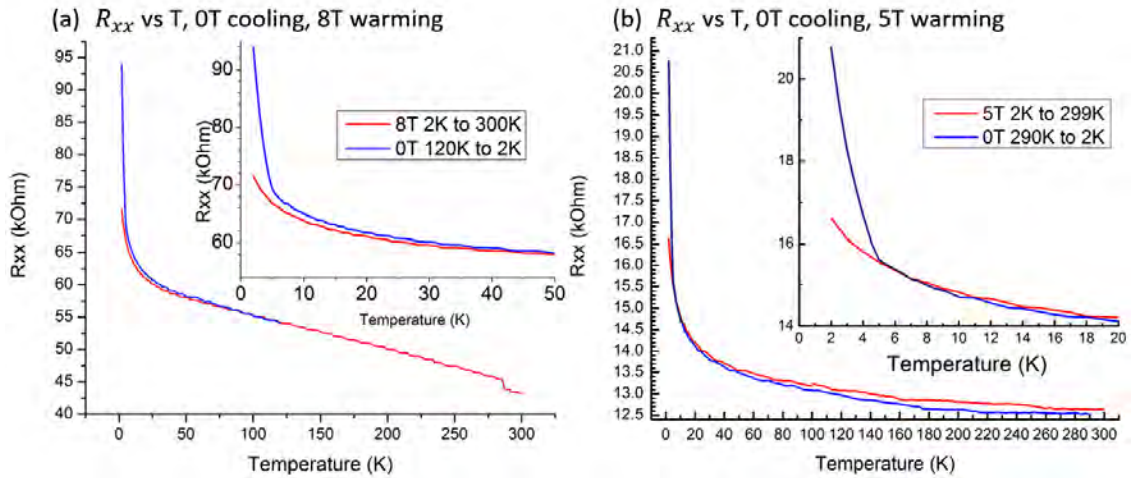


Figure 4.2: R_{xx} vs. T measurements taken on (1+6)-10% binary TI for different magnetic fields: **(a)** 0 and 8T; **(b)** 0 and 5 T. The blue curve denotes the ZFC sweep, and the red curve represents the warm-up sweep in a constant magnetic field. The resistance differs between different samples due to different contact resistance and soldering location.

Figure 4.2 shows the results from two separate measurements. In general, R_{xx} increased monotonically with decreasing temperature. This trend could be understood by considering two different contributions to the conductivity of TIs: One was from the bulk carriers, and the other from the surface state. The bulk carriers followed the thermally activated conduction behavior of an insulator with a bulk energy gap of ~ 0.3 eV for Bi_2Se_3 . On the other hand, for pure TIs the surface state of Dirac fermions would exhibit metallic behavior at high temperatures and weak anti-localization (AWL) behavior at low temperatures [10, 85, 86], whereas for MTIs the surface state Dirac fermions would exhibit both thermally activated behavior at low temperatures due to the opening of a ferromagnetism-induced surface gap and weak localization (WL) behavior due to broken time-reversal symmetry. Given that the bulk gap of Bi_2Se_3 is independent of temperature, whereas the ferromagnetism-induced surface gap only opens below the Curie temperature, the sharp rise in R_{xx} around 5K for ZFC temperature sweep (Figure 4.2) may be attributed to the appearance of a surface gap.

In contrast to the ZFC data, the warm-up temperature sweep under a constant magnetic field revealed significant negative magnetoresistance at low temperatures ($< \sim 5$ K), as shown in

the insets of both Figures 4.2(a) and 4.2(b). However, the magnitude of negative magnetoresistance diminished rapidly above 5 K, and the magnetoresistance even became slightly positive above ~ 30 K under 5 T (Figure 4.2(b)). The presence of strong negative magnetoresistance at low temperatures was indicative of significant spin-disorder scattering of the bulk carriers and the WL behavior of the surface-state massive Dirac fermions; the former could be suppressed by a large applied magnetic field whereas the latter could be manifested in low fields, as elaborated in the next subsection.

For the Hall resistance measurements, we found that $|R_{xy}|$ taken at $B = 0$ was essentially zero at high temperatures, and then started showing a significant increase with decreasing temperature below ~ 30 K (Figure 4.3), which may be attributed to the onset of AHE where bulk ferromagnetism appeared. We may denote this temperature as the 3D Curie temperature T_C^{bulk} of the MTI. On the other hand, $|R_{xy}(5T)|$ was slightly larger than $|R_{xy}(0)|$ for most temperatures until $T < \sim 5$ K where $|R_{xy}(5T)|$ became marginally smaller than $|R_{xy}(0)|$.

To understand temperature dependence of $|R_{xy}(5T)|$ and $|R_{xy}(0)|$, we consider the Hall resistance of a ferromagnetic system, which may be expressed by the following relation (in SI units):

$$R_{xy} = R_0 B + R_s(\mu_0 M). \quad (4.1)$$

Here $R_0 = \sum_i [1/(n_i e_i)]$ is the ordinary Hall coefficient associated with the carrier density n_i of charge e_i , R_s denotes the anomalous Hall coefficient, μ_0 is the permeability, and M is the magnetization. For $T > T_C^{bulk}$, $M = 0$ so that $R_{xy} = 0$ if $B = 0$. Below T_C^{bulk} , R_{xy} is entirely determined by the sample magnetization M if $B = 0$, whereas R_{xy} is dependent on both the magnetization and the density/sign of the carriers if $B \neq 0$. For an insulator without impurities, the ordinary Hall resistance is negligible due to equal densities of thermally activated electrons and holes. On the other hand, dopants in an insulator may result in finite contributions to the ordinary Hall coefficient, particularly at sufficiently low temperatures when the thermally activated carriers associated with impurities becomes very small. Therefore, $|R_{xy}(5T)| > |R_{xy}(0)|$ for $5 \text{ K} < T < T_C^{bulk}$ may be attributed to enhanced

magnetization by the applied magnetic field. In contrast, for $T < 5$ K, the total magnetization became saturated while thermally activated electron carriers associated with dopants diminished rapidly with decreasing temperature so that $|R_{xy}(5T)| < |R_{xy}(0T)|$ according to Eq. (4.1) with $e < 0$. While the physical origin of the dopants could not be identified from our experiments, we speculate that the inhomogeneous distributions of Cr dopants in the MTI layer may be responsible. This conjecture is also consistent with the finding of strong negative magnetoresistance observed at low temperatures due to strong disorder spin scattering.

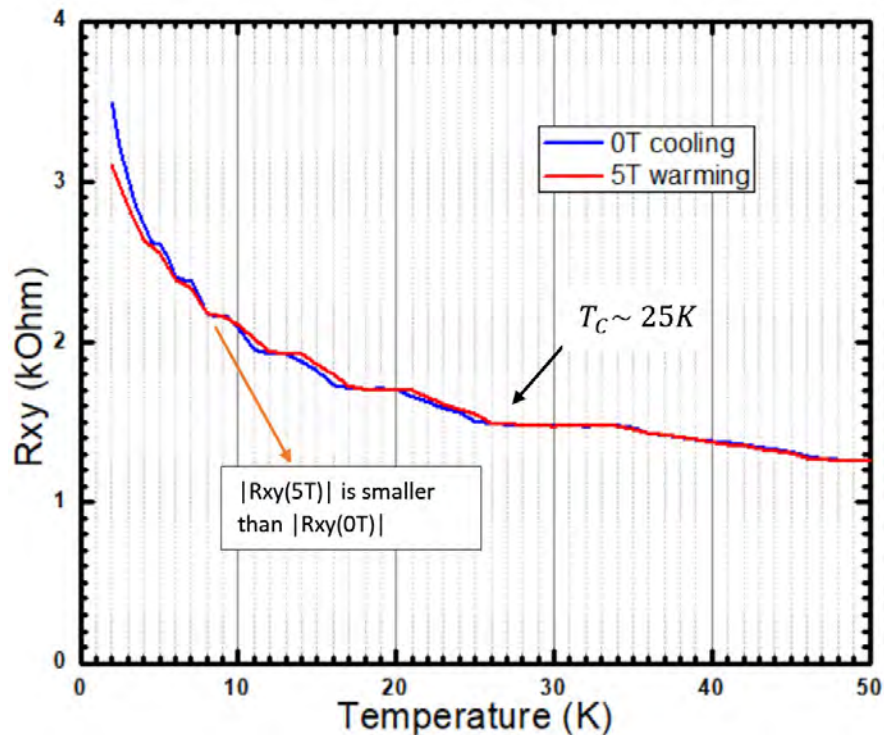


Figure 4.3: $|R_{xy}|$ vs. T measurements on a (1+6)-10% binary TI sample. (Room temperature background resistance is removed.)

4.1.3 (1+6)-10% binary TI/MTI magnetic field sweep

We carried out studies of the magnetic field sweep for (1+6)-10% binary TI at 2K (Figure 4.4). From the temperature sweeps both with and without fields in Subsection 4.1.2, we expect both magnitudes of R_{xx} and R_{xy} to decrease with increasing $|B|$, although the magnetic

field effect would be much smaller for $|R_{xy}|$. This was indeed the case in our studies of field sweeps, as shown in Figure 4.4. The field sweeps were carried out by ramping the field first up and then down and finally back to 0. However, no apparent hysteresis loops were found in this (1+6)-10% binary TI, suggesting the absence of sizable magnetic domains and also negligible coercive fields.

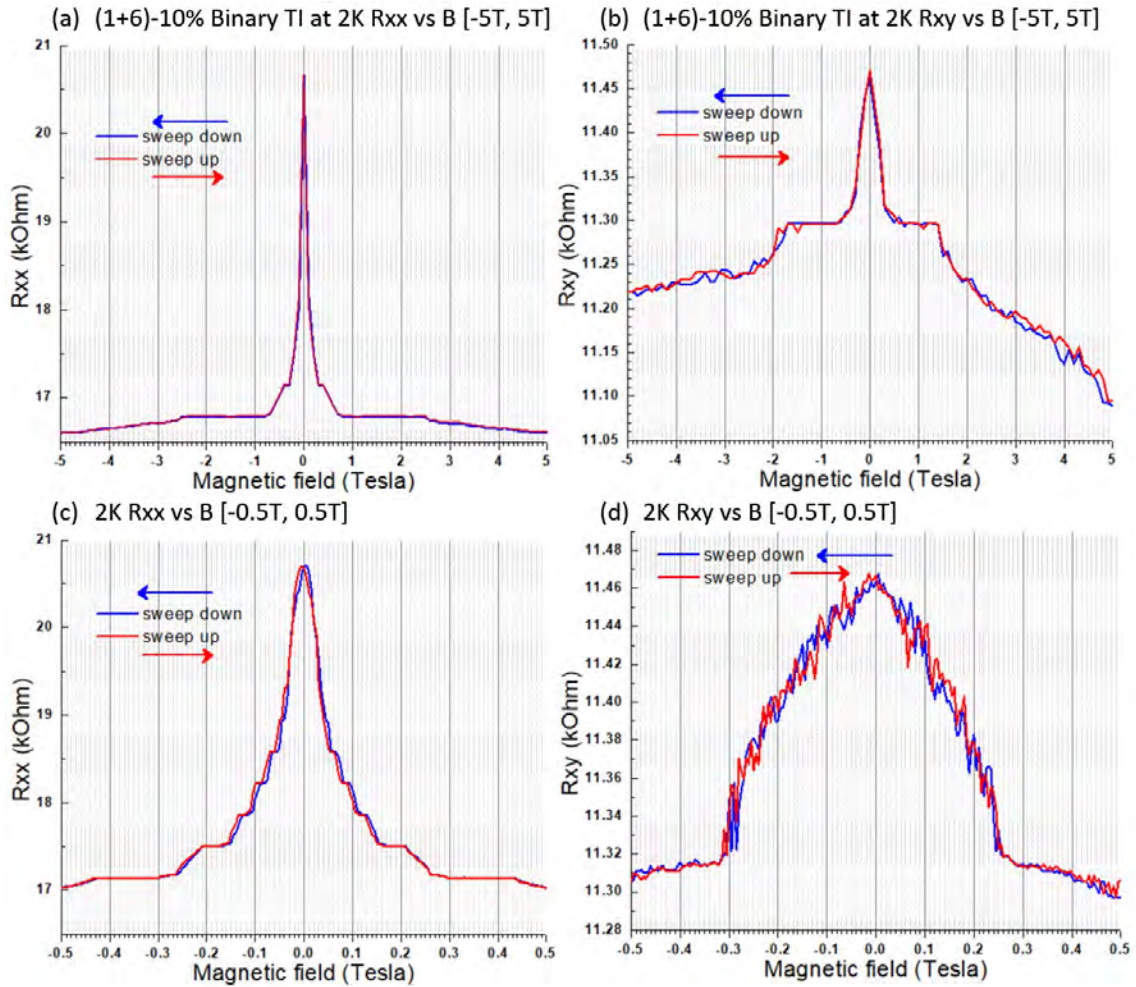


Figure 4.4: Field sweeps of longitudinal and Hall resistance taken at $T = 2\text{K}$ on (1+6)-10% Bi_2Se_3 binary TI. (a) R_{xx} vs. B between -5 to 5 Tesla. (b) R_{xy} vs. B between -5 to 5 Tesla. (c) R_{xx} vs. B between -0.5 to 0.5 Tesla. (d) R_{xy} vs. B between -0.5 to 0.5 Tesla.

From Figures 4.4(a) and 4.4(c), we note that R_{xx} for low fields behaves quite differently from that for high fields: In the low field regime, R_{xx} decreased precipitously with increasing $|B|$

up to ~ 0.25 T. With further increase of $|B|$, R_{xx} became nearly flattened and only exhibited very gradual decrease for $|B| > 0.25$ T. We attribute the low-field R_{xx} behavior to the quantum phenomenon of WL of the surface massive Dirac fermions, and the high-field R_{xx} behavior to the classical negative magnetoresistance due to the suppression of disorder-spin scattering by magnetic fields. On the other hand, the field sweeps of $|R_{xy}|$ did not show any hysteresis, suggesting a highly disordered ferromagnetic system without sizable magnetic domains. Additionally, the slight decrease of $|R_{xy}|$ with $|B|$ may be attributed to the presence of impurity carriers, as discussed in the previous subsection. The asymmetric $|R_{xy}|$ -vs.- $|B|$ curve shown in Figure 4.4(b) further corroborated the existence of an ordinary Hall component. Interestingly, we note that the sharp drop of $|R_{xy}|$ occurred for $|B| < 0.3$ T (Figure 4.4(d)), which was comparable to the magnetic field range for the observation of WL behavior in $|R_{xx}|$. Noting that the magnetic field length associated with $|B| = 0.25$ T is $l_B = \sqrt{\frac{\hbar}{eB}} \sim \frac{25.7 \text{ nm}}{\sqrt{B(\text{Tesla})}} \sim 51$ nm, our finding suggests that a doping range on the order of 51 nm determines the coherence length of WL, leading to similar low-field behavior of both $|R_{xx}|$ and $|R_{xy}|$.

4.1.4 (3+6)-10% binary TI/MTI temperature sweep

The (3+6)-10% TI/MTI sample has a thicker top TI layer, and so we expect the sample to be more conductive. Figure 4.5 shows the temperature sweep result for (3+6)-10% binary TI in linear and log temperature scales. For this set of data, we performed field cooling (FC) and zero field warming measurements, which was opposite to what we did for the (1+6)-10% binary. Given that no hysteresis was observed in the R_{xy} vs. B measurements of the (1+6)-10% sample, we believe that the cooling and warming histories in a magnetic field should not influence the temperature sweep measurements.

The resistance of (3+6)-10% binary TI/MTI sample was found to be much smaller than that of (1+6)-10% as expected and is shown in Figure 4.5. From the R_{xy} vs. T measurements shown in the upper panel of Figure 4.5(a), we identified the AHE onset temperature to be around 30K, which is similar to the value identified for the (1+6)-10% binary TI/MTI sample, suggesting that the same 6-QL MTI layer contributed to the occurrence of the AHE. Below

30 K, $R_{xy}(1T)$ was slightly larger than $R_{xy}(0)$ until 5K, and $R_{xy}(1T)$ became smaller than $R_{xy}(0)$ for $T < 5$ K, similar to the findings for the (1+6)-10% binary TI/MTI sample. Therefore, the temperature dependence of R_{xy} in different magnetic fields for this (3+6)-10% binary TI/MTI sample follows the same qualitative descriptions as those for the (1+6)-10% binary TI/MTI sample in subsection 4.1.2.

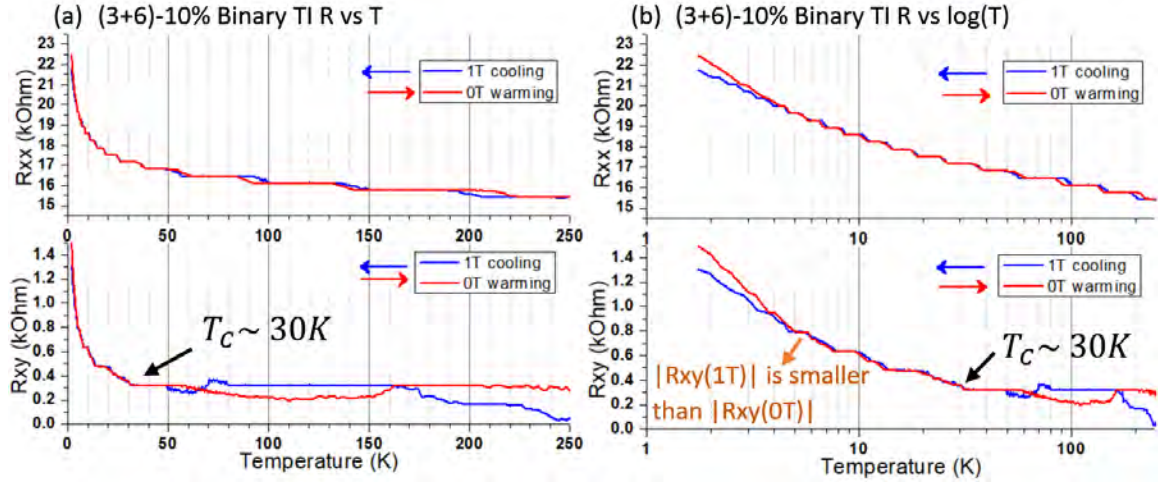


Figure 4.5: Temperature sweeps of the longitudinal and Hall resistance for (3+6)-10% Bi_2Se_3 binary TI. (a) Upper panel: R_{xx} -vs.- T . Lower panel: R_{xy} -vs.- T . (b) Upper panel: R_{xx} -vs.- $\log(T)$. Lower panel: R_{xy} -vs.- $\log(T)$.

4.1.5 (3+6)-10% binary TI/MTI magnetic field sweep

Figure 4.6 shows the field sweep data R_{xy} -vs.- B and R_{xx} -vs.- B for the (3+6)-10% binary TI/MTI sample. Similar to the findings for the (1+6)-10% sample, no hysteresis was observed for the field sweeps. Additionally, the R_{xx} -vs.- B curves also exhibited WL behavior. However, comparing the central peak of the R_{xx} -vs.- B curve for the (3+6)-10% sample with that for the (1+6)-10% sample, we found that the peak height of (3+6)-10% was smaller and broader. Specifically, the peak width of (3+6)-10% was ~ 4 T as compared with that of ~ 0.5 T for (1+6)-10%. The height ratio of the peak is about $1/20 \sim 5\%$ compared to $4/20 \sim 20\%$ for (1+6)-10%. Apparently, the WL peak for the (1+6)-10% sample was much sharper and stronger. This finding implied that the origin of WL was likely associated with the bottom MTI layer, while a thicker top layer of pure TI diluted the effect. We further note that the

coherence length associated with the WL peak of the (3+6)-10% sample was ~ 18 nm, which was nearly three times smaller than that (~ 51 nm) of the (1+6)-10% sample and appeared to corroborate with our conjecture of attributing a charge doping range to the Cr-dopants in the MTI layer.

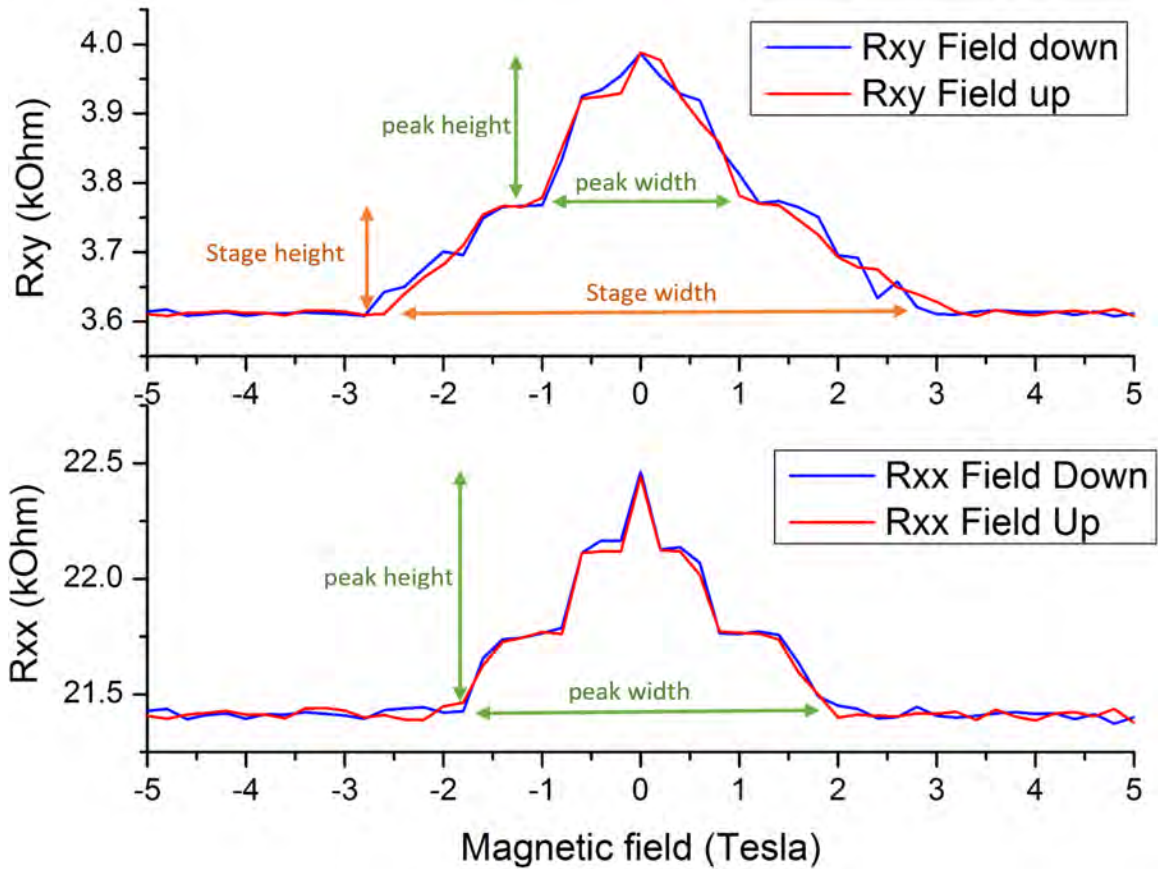


Figure 4.6: Field sweeps of longitudinal and Hall resistance taken at $T = 2$ K on (3+6)-10% Bi_2Se_3 binary TI. (a) R_{xx} vs. B between -5 to 5 Tesla. (b) R_{xy} vs. B between -5 to 5 Tesla.

The field sweeps of the Hall resistance, R_{xy} vs. B , also exhibited no hysteresis and a similar "two-stage" peak, as shown in the top panel of Figure 4.6. The full width of the bottom stage was about 6 T as compared to that of 3.5 T for the (1+6)-10% sample. The height ratio of the bottom stage was about $1.5/36 \sim 4.2\%$ as compared to that of $0.05/11.25 = 0.44\%$ for the (1+6)-10% sample. The full width of the peak was about 2 T as compared to that of 0.5 T for the (1+6)-10% sample. Moreover, this peak width of R_{xy} was consistent with that of R_{xx} . The

height ratio of the peak was $0.25/3.6 \sim 7\%$, whereas that of the (1+6)-10% sample was $0.15/11.25 \sim 1.3\%$. Overall, the R_{xy} -vs.- B peak for the (3+6)-10% sample was broader and higher than that for the (1+6)-10% sample. The broader linewidth was associated with a smaller length scale, following the same discussion for the WL peak of R_{xx} . The larger decrease of R_{xy} with increasing B may be attributed to a smaller doping electron density in the (3+6)-10% sample that led to smaller R_{xy} , according to Eq. (4.1), consistent with the notion that a thicker top layer of pure TI effectively diluted the contributions from the bottom MTI layer.

4.1.6 Summary for transport results of binary TI/MTI samples

Unlike STM studies that primarily provide information about the surface state, electrical transport measurements provide information from both the surface and bulk states. Our comparative studies of the (1+6)-10% and (3+6)-10% samples revealed that AHE appeared in both systems around $T_C^{bulk} = 30$ K. However, no hysteresis loops appeared in either the R_{xx} -vs.- B or R_{xy} -vs.- B curves for $T < T_C^{bulk}$, implying small magnetic domains and significant magnetic disorder, which is consistent with the microscopic information obtained from STM studies described in Chapter 3. At $T = 2$ K $\ll T_C^{bulk}$ and in the low-field limit, both the R_{xx} -vs.- B and R_{xy} -vs.- B curves of the (1+6)-10% and (3+6)-10% samples exhibited sharp peaks centered at $B = 0$. The linewidths of both R_{xx} -vs.- B and R_{xy} -vs.- B curves for each sample were consistent, and the linewidths for the (1+6)-10% sample were significantly narrower than those for the (3+6)-10% sample. We attribute the peak associated with the R_{xx} -vs.- B curve to WL behavior of the surface-state massive Dirac fermions, and derive the WL coherence length from the linewidth of the peak. We also found that the WL coherence length of the (1+6)-10% sample was ~ 51 nm, much longer than that (~ 18 nm) of the (3+6)-10% sample and suggesting that a thicker pure-TI layer on top of the MTI tends to dilute the contributions from the bottom MTI layer. We further conjectured that the WL coherence length might be associated with the carrier doping range in the binary TI/MTI samples, which led to an excess ordinary Hall effect in the presence of finite magnetic fields, with contributions opposite in sign to the magnetization and therefore resulting in the peak

centered at $B = 0$ in the R_{xy} -vs.- B curve. On the other hand, for $5 \text{ K} < T < 30 \text{ K}$, increasing the magnetic field helped increase R_{xy} slightly due to enhanced magnetization, and higher temperature suppressed the ordinary Hall effect due to increasing thermally activated carriers.

In contrast to the bilayer binary TI/MTI samples based on Bi_2Se_3 , electrical transport measurements of the bilayer ternary TI/MTI samples based on $(\text{Bi,Sb})_2\text{Te}_3$ revealed clear ferromagnetic signatures and better magnetic order. Therefore, we placed more emphasis on the studies of the bilayer ternary TI/MTI compounds.

4.2 Transport studies of bilayer $(\text{Bi}, \text{Sb})_2\text{Te}_3 / \text{Cr}-(\text{Bi}, \text{Sb})_2\text{Te}_3$

Chromium doped ternary TIs $(\text{Bi,Sb})_2\text{Te}_3$ have drawn considerable attention due to the discovery of the Quantum Anomalous Hall effect (QAHE) at 30 mK in such systems [20, 21]. However, the temperature where the QAHE could be reached was much lower than the theoretical prediction. The mechanism that led to rapid deviations from the QAHE with increasing temperature is still unknown and requires further investigation. In our STM study, we investigated the ternary TIs because the size of Sb is much closer to that of Cr than Bi, so that Cr-doping would cause less strain on the ternary TIs than on the binary TIs.

Instead of studying the Cr-doped magnetic ternary TIs directly, we again investigated the bilayer structure that consists of a pure ternary TI layer on top of a Cr-doped MTI layer.

Table 4.2 $(\text{Bi}_x\text{Sb}_y)_2\text{Te}_3 / \text{Cr}-(\text{Bi}_x\text{Sb}_y)_2\text{Te}_3$ sample list for STM and PPMS

sample ID(UCLA)	Top layer # $(\text{BiSb})_2\text{Te}_3$	bottom layer # $\text{Cr}-(\text{BiSb})_2\text{Te}_3$	Cr %	capping	Grower	x:y
LH 1182	1QL	6QL	10%	AL	Liang He	1:1
LP 2788	1QL	6QL	10%	Al	Lei Pan	1:1.3
PZ 3267	3QL	6QL	10%	Al 2nm	Peng Zhang	0.3:0.7
PZ 3268	1QL	6QL	10%	Al 1nm	Peng Zhang	0.3:0.7

Table 4.2 lists all the ternary TIs we used for the electrical transport and STM measurements. For $(Bi_xSb_y)_2Te_3$, there is one more variable for the ratio between bismuth and antimony. The ratio of Bi to Sb controls the Fermi level and similarity of the band structure to that of Bi_2Te_3 or Sb_2Te_3 . To maximize the temperature for achieving the QAHE, the Fermi level of the magnetic ternary TI needs to be tuned to the Dirac point either by adjusting the ratio of Bi to Sb or by gating the Fermi level. Our collaborators at UCLA in the group of Professor Kang-Long Wang can grow a very high-quality sample with an accurate ratio of Bi to Sb to tune the Fermi level very close to the Dirac point. Therefore, the gating is not necessary, which makes our electrical transport measurements simpler by reducing one more control variable.

The bilayer ternary TI/MTI samples for our studies were all grown on gallium arsenide (GaAs) substrates with aluminum capping. The procedure to prepare the Hall bar geometry was the same as that employed for the binary TI/MTIs. The pin connection was made by indium soldering the aluminum wires to the contact of the sample and pin pads on the PCB. We studied (1+6)-10% and (3+6)-10% samples, PZ3267 and PZ3268, with the PPMS.

4.2.1 Results from electrical transport measurements on (1+6)-10% ternary TI/MTI

We did some temperature sweeps with zero-field cooling and field warming. The transition temperature was found to be around 35 K from the R_{xy} -vs.- T measurements. The field sweeps at low temperature exhibited clear hysteresis loops, which implied that we need to be more careful about the operation of temperature sweeps with and without magnetic fields. For the (1+6)-10% sample to be discussed in this subsection, we focused on the field-sweep results in low fields, whereas more systematic studies of field sweeps on the (3+6)-10% sample over a broader range of magnetic fields will be discussed in subsections 4.2.2 and 4.2.3.

The field sweeps of R_{xx} and R_{xy} at 2 K exhibit apparent hysteretic behavior, as shown in Figure 4.7 (a). In particular, R_{xy} -vs.- B curves looked similar to the magnetization hysteretic loops of field sweeps for ferromagnetic materials. As discussed in subsection 4.1.2, the Hall

resistance R_{xy} of a ferromagnetic system may be expressed by the following relation (in SI units):

$$R_{xy} = R_0 B + R_S (\mu_0 M) \quad (4.1)$$

Here $R_0 = \sum_i [1/(n_i e_i)]$ is the ordinary Hall coefficient associated with the carrier density n_i of charge e_i , R_S denotes the anomalous Hall coefficient, μ_0 is the permeability, and M is the magnetization. For sufficiently low fields, $R_0 B < R_S M$, and so we expect $R_{xy} \propto M$. Additionally, R_{xx} -vs.- B also showed hysteric double peaks, with each peak centering at the corresponding $R_{xy} = 0$ point. This finding was similar to what we had observed in our studies of the binary TI/MTI samples, where R_{xx} reached a maximum near $R_{xy} = 0$. We may understand this correlation between maximum R_{xx} and minimum $|R_{xy}|$ (*i.e.*, $R_{xy} = 0$) by noting that $R_{xy} = 0$ corresponded to $M = 0$ in the low field limit, which implied that the magnetization of different magnetic domains was randomized, which resulted in the strong scattering of carriers from one domain to another and therefore maximum longitudinal resistance.

For this (1+6)-10% ternary TI/MTI sample, we did not pursue field sweeps to high fields. As we shall see in our later discussion of the (3+6)-10% ternary sample, at a high field, R_{xx} will revert to the classical magnetoresistance behavior, which was notably absent in the bilayer binary TI/MTI systems.

Figure 4.7 (b) shows R_{xy} -vs.- B hysteresis loops at different temperatures. The size of the hysteresis loop appeared to shrink rapidly with increasing temperature and became nearly paramagnetic at 10 K. We may define the up-sweep and down-sweep coercive fields as the B values where $R_{xy} = 0$ and plot the coercive field vs. T curves in Figure 4.7 (d). Interestingly, we note that the coercive field changed signs at 15 K, which was further verified in Figure 4.7 (c) for the R_{xy} -vs.- B data at 15 K.

Additionally, we note that the R_{xx} -vs.- B data at 15 K exhibited seemingly unusual features. The double peak locations were not symmetric around $B = 0$, nor did they correspond to the coercive field, which suggested that the behavior of the resistive data may not be solely

correlated with the magnetism of the magnetic layer. We shall address this issue later in our detailed studies of the (3+6)-10% sample.

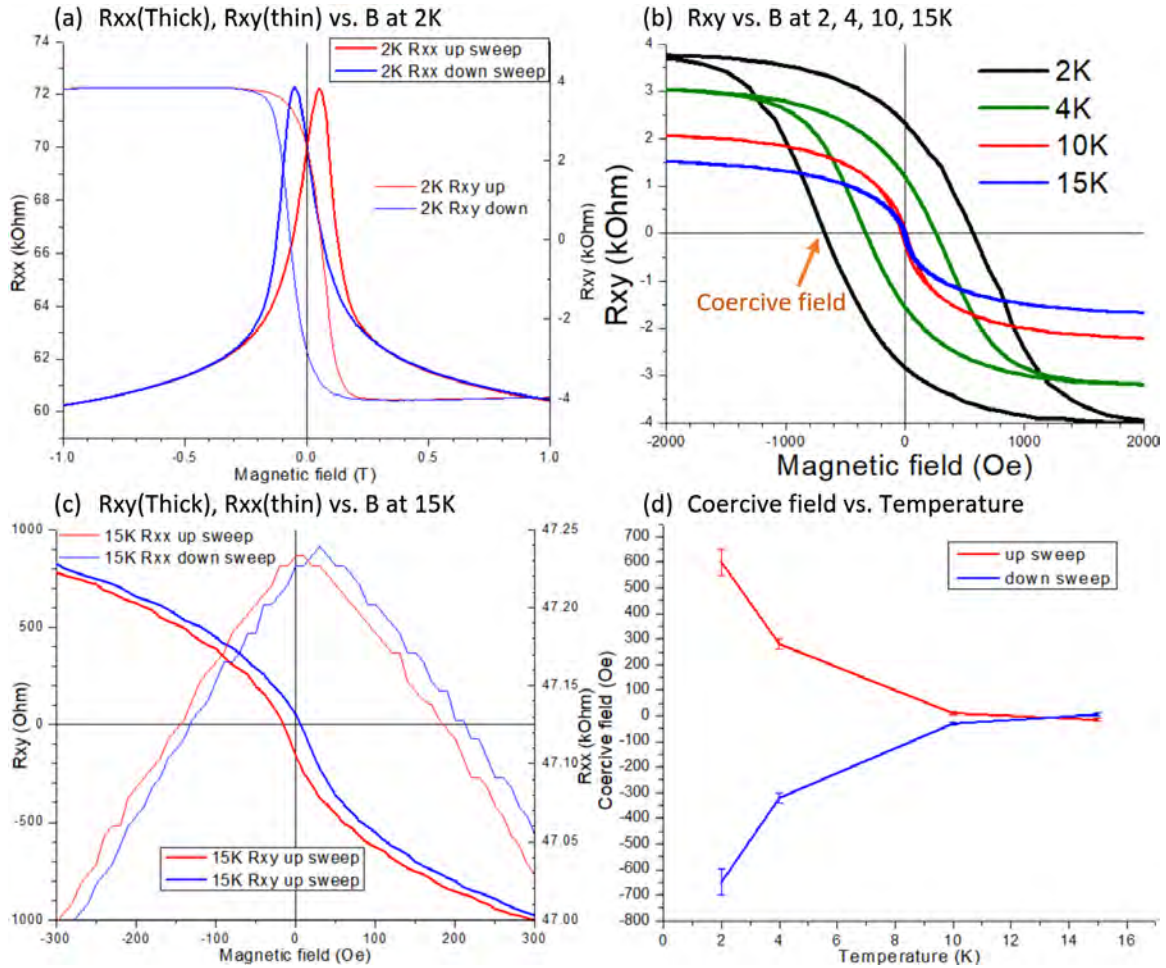


Figure 4.7: Field sweeps of resistance for the (1+6)-10% ternary TI/MTI sample. (a) R_{xx} and R_{xy} -vs.- B at $T = 2$ K. (b) R_{xy} -vs.- B curves at $T = 2, 4, 10, 15$ K (c) R_{xx} and R_{xy} -vs.- B at $T = 15$ K. (d) Coercive field vs. T .

4.2.2 Low magnetic field sweep analysis of the (3+6)-10% ternary TI/MTI sample

With the observation of R_{xy} -vs.- B hysteresis loops at low temperatures for the (1+6)-10% ternary TI/MTI sample, we proceeded with more detailed field sweep studies on the (3+6)-10% ternary TI/MTI sample. Figure 4.8 shows R_{xy} and R_{xx} vs. B curves taken at different temperatures. As the sample cooled from 27 K to 13 K, the magnitude of the coercive field

decreased with decreasing temperature and became nearly paramagnetic around 13 K. The sign of the coercive field for $13 \text{ K} \leq T \leq 27 \text{ K}$ was negative. Below 13 K, the coercive field became positive and increased rapidly with decreasing temperature. Additionally, the maximum R_{xy} or saturated R_{xy} increased monotonically with decreasing temperature. These results implied that the ferromagnetic order of the TI/MTI sample improved upon lowering the sample temperature.

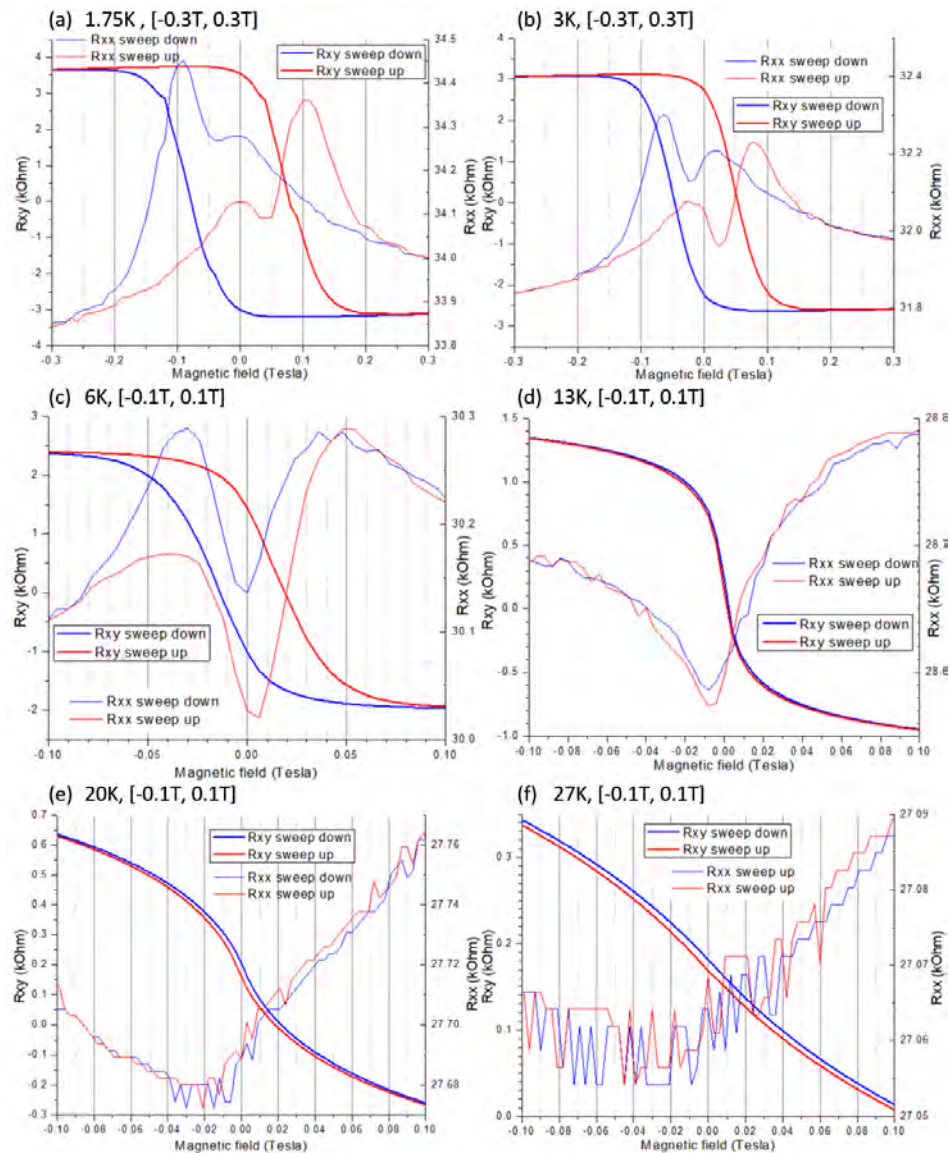


Figure 4.8: Low-field R_{xy} (thick line) and R_{xx} (thin line) vs. B data taken on the (3+6)-10% ternary TI/MTI sample at $T =$ (a) 1.75K, (b) 3K, (c) 6K, (d) 13K, (e) 20K, and (f) 27K

Interestingly, below 13 K, the R_{xx} -vs.- B curves in this (3+6)-10% ternary sample did not exhibit the double-symmetric-peak hysteresis behavior, as seen in the studies of the (1+6)-10% ternary sample. Instead, the temperature evolution of the R_{xx} -vs.- B curves became quite complicated below 13 K, showing asymmetric hysteretic curves with WL behavior near $|B| = 0$ and anti-weak-localization (AWL) behavior for larger fields. On the other hand, for $T > 13$ K, the R_{xx} -vs.- B curves appeared V-shaped without clear hysteretic behavior and were consistent with the AWL behavior. Further, we note that the B field associated with the minimum of R_{xx} -vs.- B curves above 13K was -0.02 T rather than 0.

The novel evolution of the R_{xx} -vs.- B behavior with T and B in the low field limit was suggestive of sign changes in the majority carriers with T and B . To better understand the evolution of R_{xy} and R_{xx} with B in higher fields, we showed in Figures 4.9(a) and 4.9(b) the R_{xy} -vs.- B and R_{xx} -vs.- B isotherms up to $|B| > 1$ T, respectively. We found that for $T = 1.75$ K, 3 K, and 6 K, $|R_{xy}|$ decreased with increasing $|B|$ above the saturation fields. On the other hand, for $T = 13$ K, 20 K, and 27 K, $|R_{xy}|$ increased with increasing $|B|$ in the high field regime, although the changes in $|R_{xy}|$ for $T = 13$ K were very small.

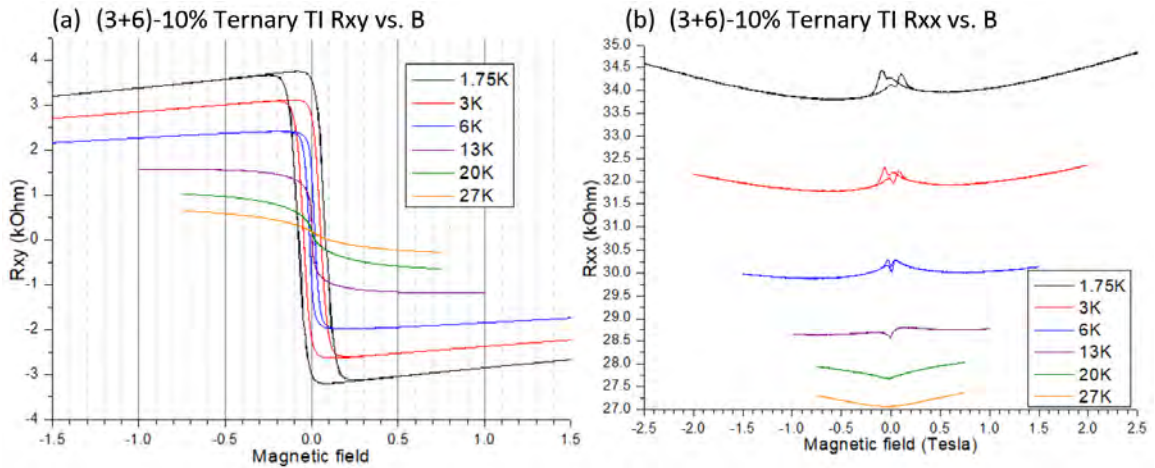


Figure 4.9: Field sweep measurements of R_{xx} and R_{xy} on the (3+6)-10% ternary TI/MTI sample at different temperatures: (a) R_{xy} -vs.- B isotherms, and (b) R_{xx} -vs.- B isotherms.

For the R_{xx} -vs.- B isotherms in Figure 4.9(b), we found that R_{xx} all increased with $|B|$ for $|B| > 1$ T except at $T = 13$ K where R_{xx} was nearly a constant in high fields. On the other hand,

in the intermediate field regime, R_{xx} -vs.- B for $T = 1.75$ K, 3 K, and 6 K exhibited WL and hysteretic behavior while R_{xx} -vs.- B for $T = 13$ K, 20 K, and 27 K shows AWL behavior.

4.2.3 High magnetic field sweep analysis of the (3+6)-10% ternary TI/MTI sample

Although R_{xy} changed fastest around in the low field limit, high magnetic field scans could provide additional useful information. For instance, the saturation of sample magnetization in high fields would render any changes in R_{xy} to changes in the ordinary Hall signals. In this context, if the majority carriers changed signs with either T or B in the high field limit, the ordinary Hall signals would reflect the sign change as well. Therefore, it is worth investigating high field sweeps at different temperatures.

In Figure 4.10, we show R_{xy} -vs.- B and R_{xx} -vs.- B isotherms up to $|B| = 8$ T at different temperatures. Surprisingly, we found that for all R_{xy} -vs.- B isotherms, $|R_{xy}|$ did not either saturate or increase with $|B|$ in the high field limit. Rather, the slope $d|R_{xy}|/d|B|$ was negative in the high $|B|$ limit. In contrast, $d|R_{xy}|/d|B|$ was positive over the field range of the hysteresis loops. From Eq. (4.1), we may attribute the positive $d|R_{xy}|/d|B|$ behavior to contributions from the sample magnetization, and the negative $d|R_{xy}|/d|B|$ in the high field limit to contributions from the majority carriers with an opposite sign to the magnetization.

For R_{xx} -vs.- B isotherms at $T < 14$ K, R_{xx} exhibited hysteretic WL behavior and decreased with $|B|$ for $|B| < 1$ T (Figures 4.10(b) and 4.10(d)), whereas the hysteretic behavior of R_{xx} nearly vanished at $T = 14$ K and R_{xx} -vs.- B first exhibited AWL behavior for $|B| < 0.1$ T, as shown in Figures 4.10(d) and 4.10(f), and then decreased slightly for 0.1 T $< |B| < 1$ T. On the other hand, for $|B| > 1$ T, R_{xx} became increasing with $|B|$ for all temperatures.

Overall, studies of the field sweeps revealed that for $T < 13$ K, both R_{xy} -vs.- B and R_{xx} -vs.- B isotherms were consistent with the presence of ferromagnetism and exhibited hysteretic behavior. Specifically, R_{xy} -vs.- B exhibited positive coercive fields while R_{xx} -vs.- B exhibited double peaks. For $T > 13$ K, the coercive field became negative, and hysteresis vanished in R_{xx} -vs.- B isotherms. The anomalous, inverse ferromagnetic hysteresis in R_{xy} -vs.- B for $T > 13$

K could not be easily understood and 'might be from some kind of over-compensating mechanism. If such a mechanism existed, it should have appeared in the temperature sweep as well, which is the next subject of our investigation.

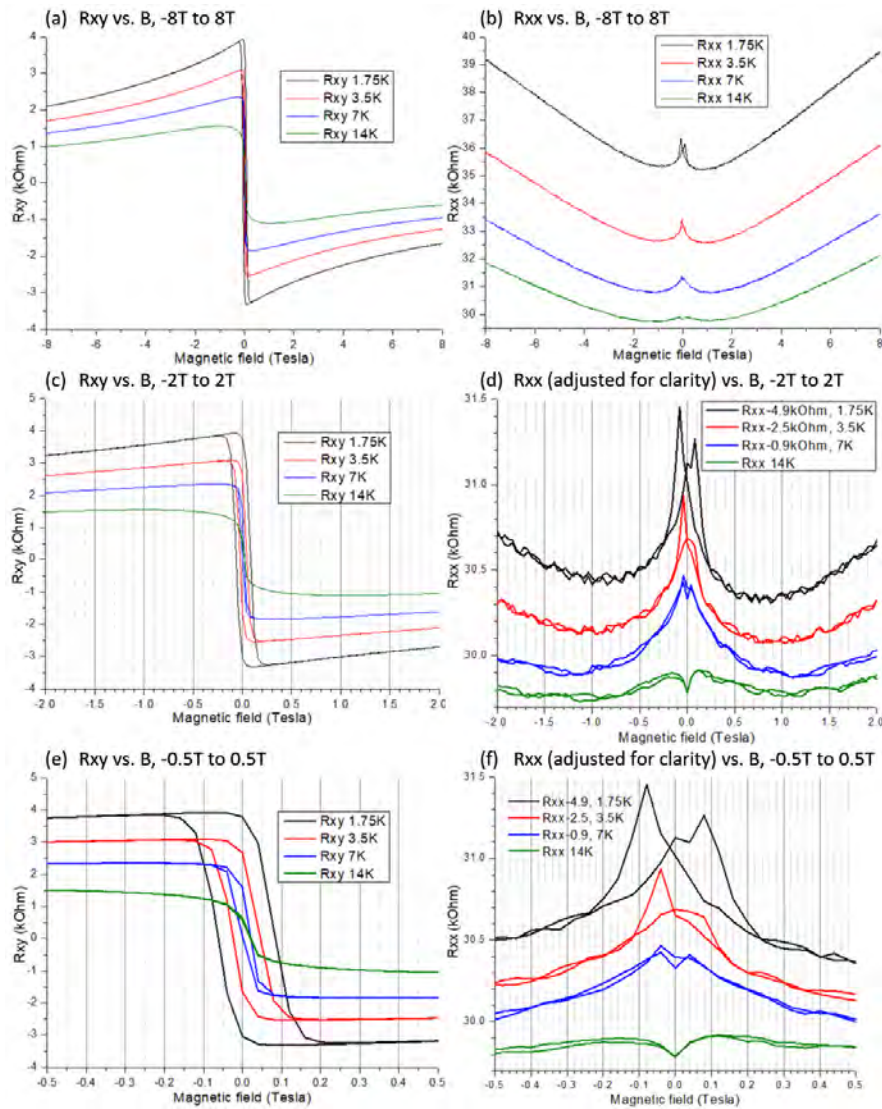


Figure 4.10: Field sweeps of longitudinal and Hall resistance at $T = 1.75$ K, 3.5 K, 7 K, and 14 K with different field ranges: (a) R_{xy} -vs.- B from -8 T to 8 T; (b) R_{xx} -vs.- B from -8 T to 8 T; (c) R_{xy} -vs.- B from -2 T to 2 T; (d) R_{xx} -vs.- B from -2 T to 2 T; (e) R_{xy} -vs.- B from -0.5 T to 0.5 T; (f) R_{xx} -vs.- B from -0.5 T to 0.5 T.

4.2.4 Temperature sweep studies of the (3+6)-10% ternary TI/MTI sample

The R_{xy} -vs.- T measurements of the (3+6)-10% ternary TI/MTI sample at $B = 0$ in Figure 4.11 revealed an onset of finite R_{xy} around $T \sim 25$ K and rapid increase in R_{xy} with decreasing temperature for $T < 25$ K, similar to the zero-field R_{xy} -vs.- T data of the (1+6)-10% ternary TI/MTI sample with an onset of R_{xy} around $T \sim 30$ K. We define this onset temperature for finite R_{xy} as T_C^{bulk} , where AHE appears due to the onset of bulk ferromagnetism with a finite total magnetization.

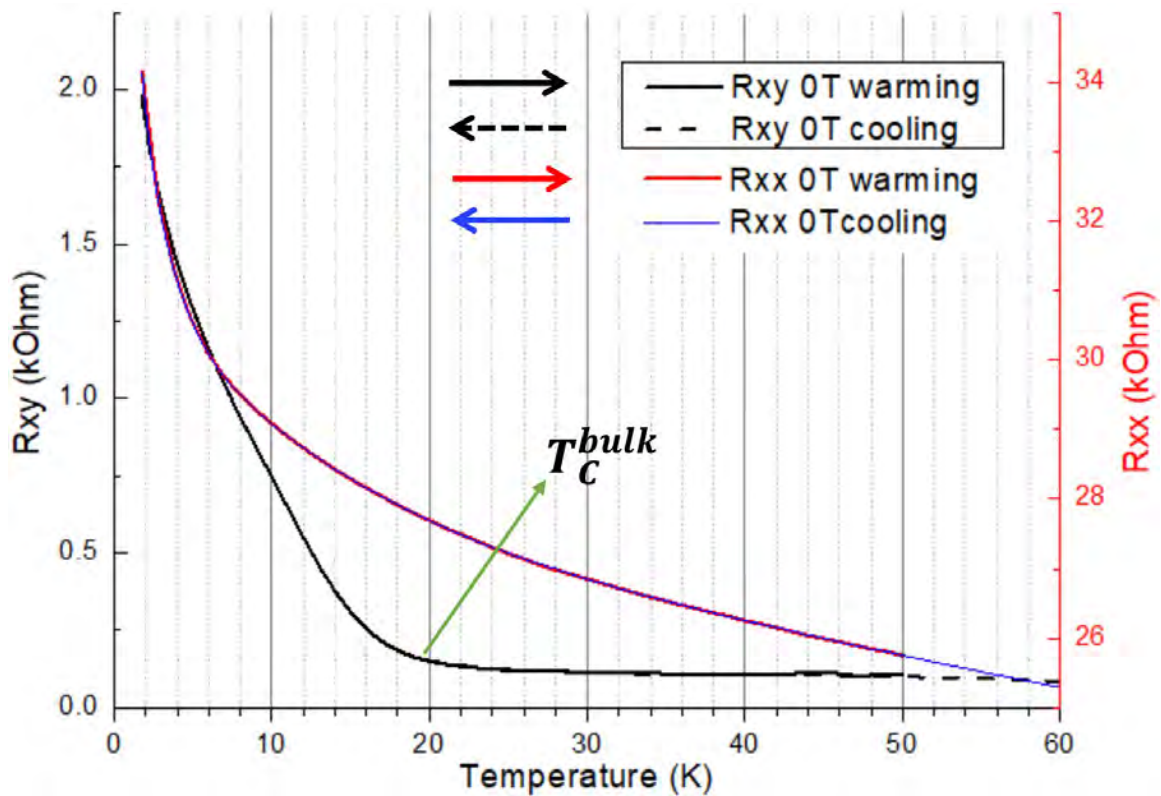


Figure 4.11: R_{xy} -vs.- T and R_{xx} -vs.- T of a (3+6)-10% ternary TI/MTI sample measured in zero fields for both cooling and warming

Next, we would like to investigate the robustness of the spontaneous magnetization by asking whether it may be influenced by the initial conditions so that we may control the magnetic state by external factors such as circularly polarized light or a small magnetic field. We would

also like to understand whether the R_{xy} -vs.- T curve is repeatable or dependent on the history of the scan.

Regarding the issue of reproducibility of the zero-field R_{xy} -vs.- T data, Figure 4.11 clearly shows both the cool-down and warm-up R_{xy} -vs.- T curves in zero fields matched each other perfectly well so did the cool-down and warm-up R_{xx} -vs.- T curves.

Next, we investigated R_{xy} -vs.- T behavior after cooling in a strong magnetic field larger than the saturation field and then measured in zero fields while warming up.

0 T warm-up after field-cool

Figure 4.12 (a) shows the R_{xy} -vs.- T curves measured under different cooling and warming conditions, where the arrows indicate the temperature sweep directions. From the perfectly matched zero-field cooling and warming curves, the spontaneous magnetization appeared negative for our experimental configuration. Cooling the sample in a negative magnetic field $B = -1$ T and then measuring the R_{xy} -vs.- T in zero fields also revealed the same negative sign of R_{xy} , although the maximum $|R_{xy}|$ value was enhanced for the field-cool data. In contrast, for field cool in $B = 1$ T, the maximum value of $|R_{xy}|$ was larger than that for field cool in $B = -1$ T. Although the physical origin for this disparity is yet to be investigated, it may be attributed to the asymmetric interfaces associated with the MTI and TI layers, leading to Rashba-like splitting in these strong spin-orbit-coupled materials.

R_{xy} (after 1 T field-cooled) curve merges with ZFC R_{xy} curve at around 16 K, while R_{xy} (after -1 T field-cooled) curve merges with ZFC R_{xy} curve at around 24 K, which is about T_C^{bulk} . This disparity implied that negative fields were preferred to positive fields so that it required higher temperatures to randomize magnetic order. Both R_{xy} (after 1 T field-cooled) and R_{xy} (after -1 T field-cooled) change the sign between 10K and 24K, which corresponds to the appearance of the negative coercive field.

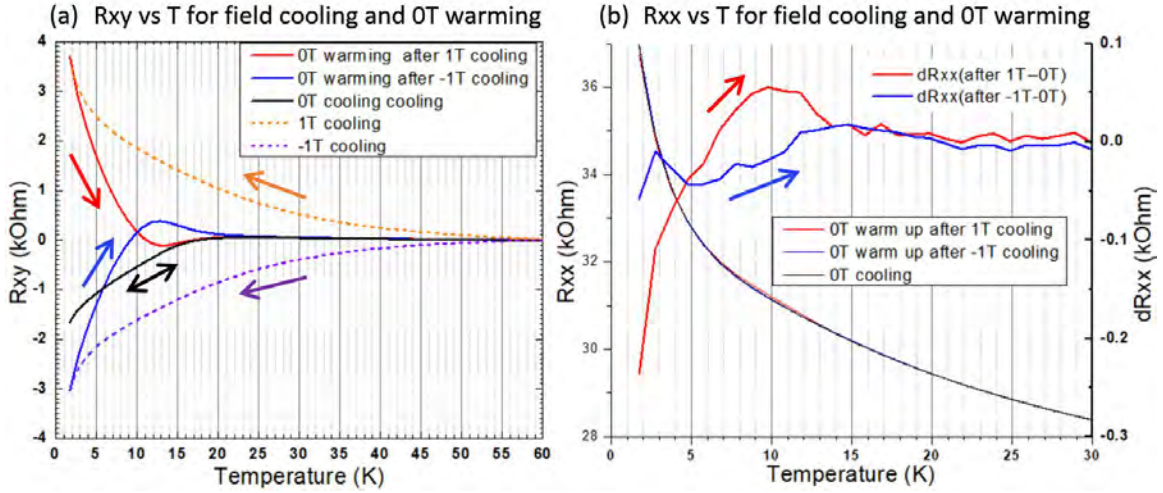


Figure 4.12: Temperature sweeps for zero-field warming resistive measurements on the (3+6)-10% ternary TI/MTI sample after cooling in $B = 0$ T, 1 T, and -1 T. **(a)** R_{xy} -vs.- T curves. The arrows indicate the sweep direction. **(b)** R_{xx} -vs.- T and $[R_{xx}(B) - R_{xx}(0)]$ -vs.- T curves.

Similarly, R_{xx} vs. T also exhibited differences for different field-cool curves, although the magnitudes of the changes were much smaller than those found in R_{xy} vs. T curves, as shown in Figure 4.12 (b), where the difference between R_{xx} (after 1 T) and R_{xx} (after 0 T) was illustrated in red as dR_{xx} (1 T) and that between R_{xx} (after -1 T) and R_{xx} (after 0 T) was illustrated in blue as dR_{xx} (-1 T). The behavior for R_{xx} vs. T at low temperatures was more complicated because of the competition between WL and AWL in R_{xx} vs. B isotherms (Figure 4.9(b), Figure 4.10(f)). Overall, we found that R_{xx} vs. B was symmetric around 0 T above 13.5 K. In contrast, R_{xx} (after 1 T) was greater than R_{xx} (after -1 T) between 4.5 K and 13.5 K, with the maximum difference occurred around $T = 10$ K, whereas R_{xx} (after 1 T) became smaller than R_{xx} (after -1 T) below 4.5 K.

0.05 T warm-up after field-cool

After studying the zero-field warm-up responses, we investigated 0.05 T warm-up responses after field-cooled in 0.5, 0, and -0.5 T (Figure 4.13). The motivation for studies of the warm-up curves in 0.05 T was because 0.05 T was a sufficiently weak positive field opposite to the

spontaneous magnetization of AHE, which may give rise to differences between the 0.05 T warm-up $|R_{xy}|$ -vs.- T curve after -0.5 T field-cool and that after ZFC at low temperatures.

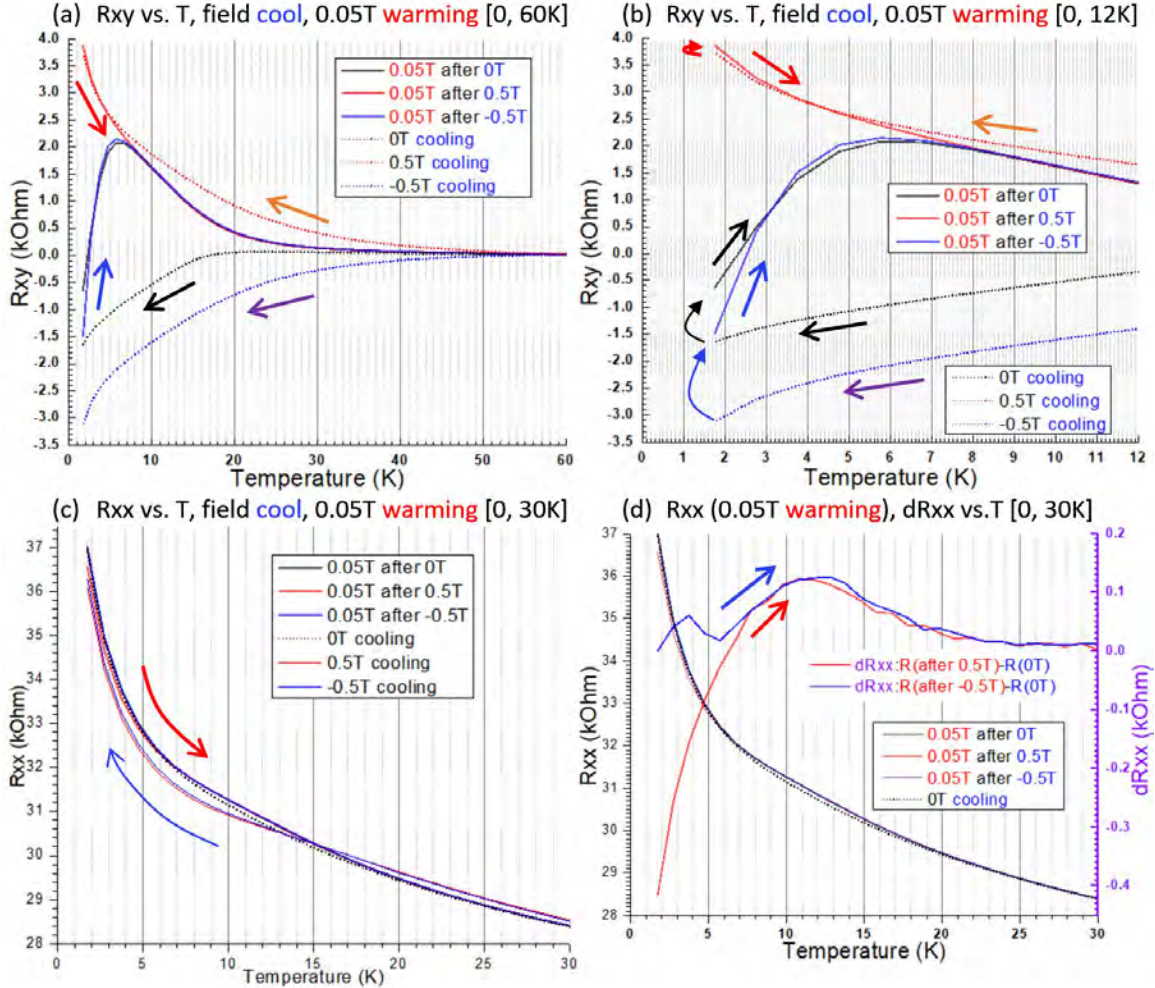


Figure 4.13: R vs. T for 0.05 T warming after 0 T, 0.5 T, and -0.5 T cooling. **(a)** R_{xy} vs. T for $0 < T < 60$ K. **(b)** R_{xy} vs. T for $0 < T < 12$ K. **(c)** R_{xx} vs. T for $0 < T < 30$ K. **(d)** R_{xx} vs. T and dR_{xx} vs. T for $0 < T < 30$ K, where $dR_{xx} \equiv R_{xx}(\text{after field-cool}) - R_{xx}(\text{after ZFC})$.

Surprisingly, we found that after field-cooled in -0.5 T, the negative R_{xy} value quickly switched sign to positive values upon warmed up in 0.05 T, as shown in Figures 4.13(a) and 4.13(b). All 0.05 T warm-up R_{xy} curves (after 0.5, 0, -0.5 T cooling) merges at 8 K, which indicated that 0.05 T might correspond to the saturation field at 8 K. On the other hand, no negative coercive field was found for the 0.05 T warm-up curve as in the case of the zero-

field warm-up curve, suggesting that 0.05 T was probably already too large to preserve the anomalous negative coercive field.

The behavior of R_{xx} vs. T curves generally depends on the magnitude of the applied field. We found that R_{xx} (ZFC) and R_{xx} (0.05 T warming) curves were similar, while R_{xx} (0.5 T cooling) was similar to R_{xx} (-0.5 T cooling), as shown in Figures 4.13(c) and 4.13(d). Interestingly, R_{xx} (± 0.5 T cooling) intersected with R_{xx} (0.05 T warming) around 14K, which was around the charge neutrality temperature (Figure 4.13 (c)). Below 14 K, the R_{xx} vs. B isotherms showed WL in low fields while above 14 K, the R_{xx} vs. B isotherms exhibited AWL behavior in low fields, as shown in Figure 4.10(f).

Comparing the 0.05 T warm-up R_{xx} vs. T curves after ± 0.5 T field-cooled, (Figure 4.13 (d)), several findings are noteworthy: First, the 0.05 T warm-up R_{xx} vs. T curve after 0.5 T field-cool matched the 0.05 T warm-up R_{xx} vs. T curve after -0.5 T field-cool near 8 K, suggesting that 0.05 T may correspond to be saturation field at 8 K, consistent with the findings from the R_{xy} vs. T curves. Second, the 0.05 T warm-up R_{xx} (after ± 0.5 T field-cool) curves deviated from R_{xx} (ZFC) around $25 \text{ K} \sim T_C^{bulk}$. The deviation reached a maximum at $T = 12 \sim 13 \text{ K}$, near the charge neutral point. Moreover, the 0.05 T warm-up R_{xx} (after 0.5 T field-cool) curve deviated substantially from the R_{xx} (ZFC) curve a lot below 8 K, while the 0.05 T warm-up R_{xx} (after -0.5 T field-cool) curve was closer to R_{xx} (ZFC) below 8 K, as shown in Figures 4.13(d).

– 0.05 T warm-up after field-cool

We also investigated -0.05 T warm-up R_{xy} vs. T curves after field-cool, and we expected the results to be similar to those found from the 0.05 T warm-up R_{xy} vs. T curves after field-cool except with an opposite sign. Figures 4.14 (a) and 4.14 (b) show the R_{xy} vs. T curve after 2 T field-cool merges with the R_{xy} vs. T curve after -2 T field-cool at around 8 K, similar to the results found from the 0.05 T warm-up R_{xy} vs. T curves after ± 0.5 T field-cool.

In contrast, for R_{xx} -vs.- T , we expect the result to be different at low temperatures due to the asymmetry of the R_{xx} -vs.- B isotherms at low temperatures near 0 T.

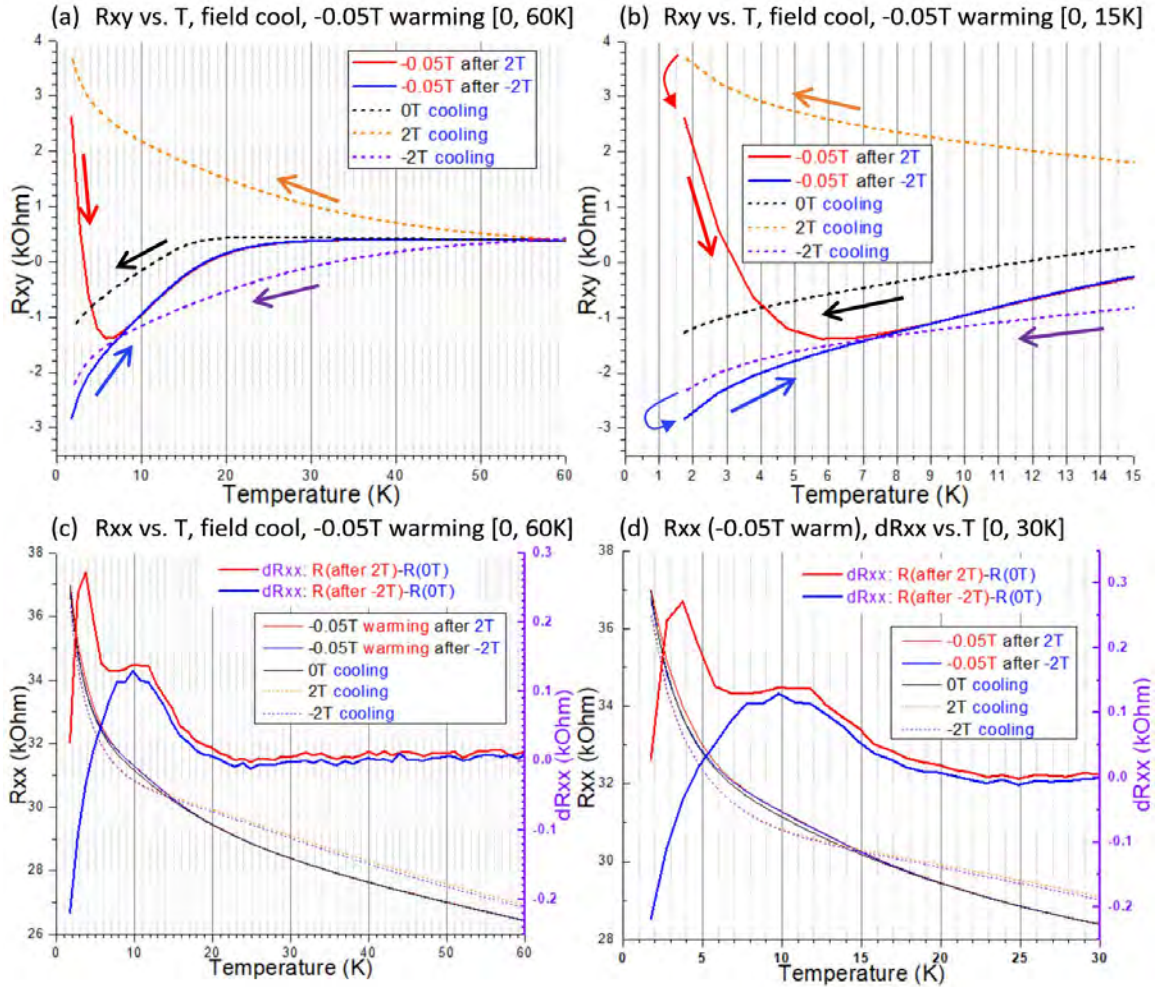


Figure 4.14: R vs. T for $-0.05T$ warming after 0 T, 2 T, and -2 T field-cool. (a) R_{xy} vs. T for $0 < T < 60$ K. (b) R_{xy} vs. T for $0 < T < 15$ K. (c) R_{xx} vs. T for $0 < T < 60$ K. (d) R_{xx} vs. T and dR_{xx} vs. T for $0 < T < 30$ K, where $dR_{xx} \equiv R_{xx}(\text{after field-cool}) - R_{xx}(\text{after ZFC})$.

Figures 4.14(c) and 4.14(d) reveal that the -0.05 T warm-up R_{xx} -vs.- T curves after 2 T field-cool matched the R_{xx} -vs.- T curves after -2 T field-cool at around 8 K. Additionally, the R_{xx} values after 2 T field-cool were consistently larger than the ZFC R_{xx} values below 25 K so that $dR_{xx} > 0$ for $T < 25$ K and a small peak of dR_{xx} appeared at 4 K. Although a similar peak

dR_{xx} was also seen in the 0.05 T warm-up R_{xx} curve after -0.5 T field-cool, as shown in Figure 4.13(d), the latter was less significant in the peak height.

4.2.5 Comparison of the field cooling curves taken on the (3+6)-10% ternary TI/MTI sample

Since taking R vs. B data at different temperatures, in general, is time-consuming, taking R vs. T at different magnetic fields can be an alternative approach that provides us with lower-resolution R -vs.- B information. To ensure the feasibility of this approach, we compared the R -vs.- B isotherms constructed from the high-field R -vs.- T curves with those obtained directly from the field-sweep measurements.

From Figure 4.15 (a), we note that the field-cool R_{xy} vs. T curves at different magnetic fields deviated from the ZFC R_{xy} vs. T curve at $T \sim 60$ K, and that the field-cooled R_{xy} vs. T curves at B field and $-B$ field were symmetric with respect to the ZFC R_{xy} vs. T curve for $T > T_C^{bulk} \sim 20$ K. Additionally, within either positive or negative field cooling curves, there was another crossing point around $T = 12 \sim 13$ K. This crossing corresponds to the flatness of the R_{xy} vs. B isotherm in the high field limit at $T = 13$ K, as shown in Figure 4.10(f).

Using the R vs. T curves taken at multiple magnetic fields as shown in Figures 4.15(a) and 4.15(b), we can construct low field-resolution R vs. B isotherms with much higher temperature resolution, as shown in Figures 14.15(c) and 14.15(d) for R_{xy} vs. B and R_{xx} vs. B , respectively. The only problem with this method is that the hysteresis could not be resolved. On the other hand, if we were only interested in the high-field behavior, this method could provide useful information about how the majority carriers evolve with temperature.

For R_{xx} vs. T , the crossing point for curves of different fields occurred around $14 \sim 15$ K. This temperature was slightly different from the crossing point at $T = 12 \sim 13$ K found in the R_{xy} vs. T . From the R_{xx} vs. T curves at various magnetic fields, we constructed low-resolution R_{xx} vs. B curves at different temperatures in Figure 14.15(d). At 14.8 K, the R_{xx} vs. B curve was nearly flat. Below 14.8 K, the low-resolution R_{xx} vs. B curves revealed largely WL behavior

for $|B| < 0.5$ T and then turned into classical magnetoresistance for $|B| > 0.5$ T. Above 14.8 K, R_{xx} increased with $|B|$ and showing AWL behavior for all fields. Comparing Figure 14.15(d) with the high-resolution R_{xx} vs. B curve at $T = 14$ K in Figure 4.10(d), we note that the curve was actually not flat and showing AWL behavior for $|B| < 0.1$ T. Our findings of predominantly AWL behavior for $T > 14$ K and WL behavior for $T \leq 14$ K suggest that there were competing mechanisms that determined the electrical transport properties of the (3+6)-10% ternary TI/MTI sample.

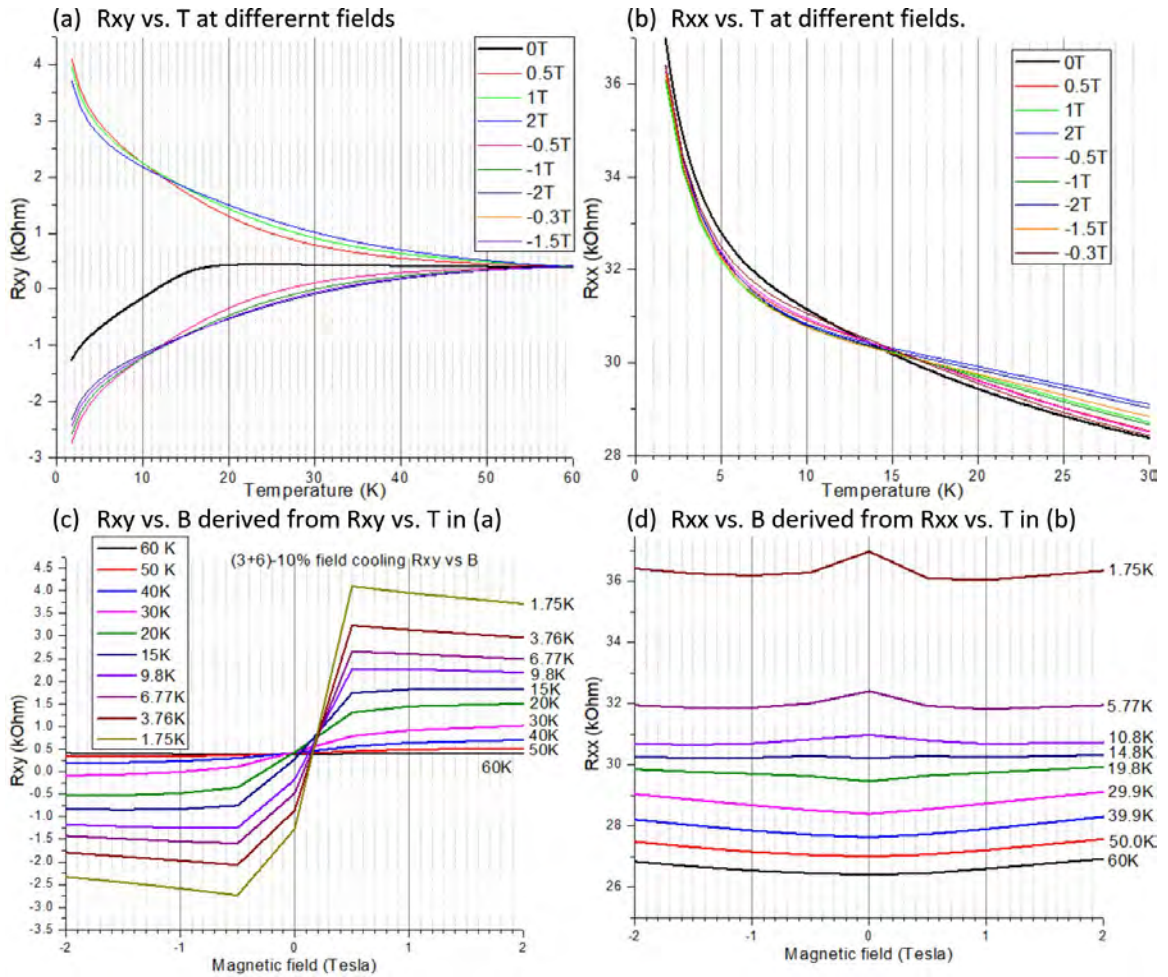


Figure 4.15: (a) Field-cool R_{xy} vs. T curves of the (3+6)-10% ternary TI/MTI sample at different magnetic fields. (b) Field-cool R_{xx} vs. T curves of the same sample at different magnetic fields. (c) R_{xy} vs. B isotherms constructed from different field-cool R_{xy} vs. T curves. (d) R_{xx} vs. B isotherms constructed from different field-cool R_{xy} vs. T curves.

To better understand the temperature evolution of R vs. B curves and the magnetic field evolution of R vs. T curves, we constructed the 3D plots of R_{xy} and R_{xx} as a function of B and T , as shown in Figure 4.16. From the $R_{xy}(B, T)$ data shown in Figures 4.16(a) and 4.16(c), it is clear that the color maps were not symmetrical relative to $B = 0$. Due to AHE, spontaneous magnetization is along the negative field direction. Taking the light blue color line (corresponding to $R_{xy} = 0$) as the onset of the AHE for negative fields and the yellow color line as the onset of the AHE for positive fields, we found that the onset of AHE with a negative applied field appeared at a higher temperature than that with a positive field.

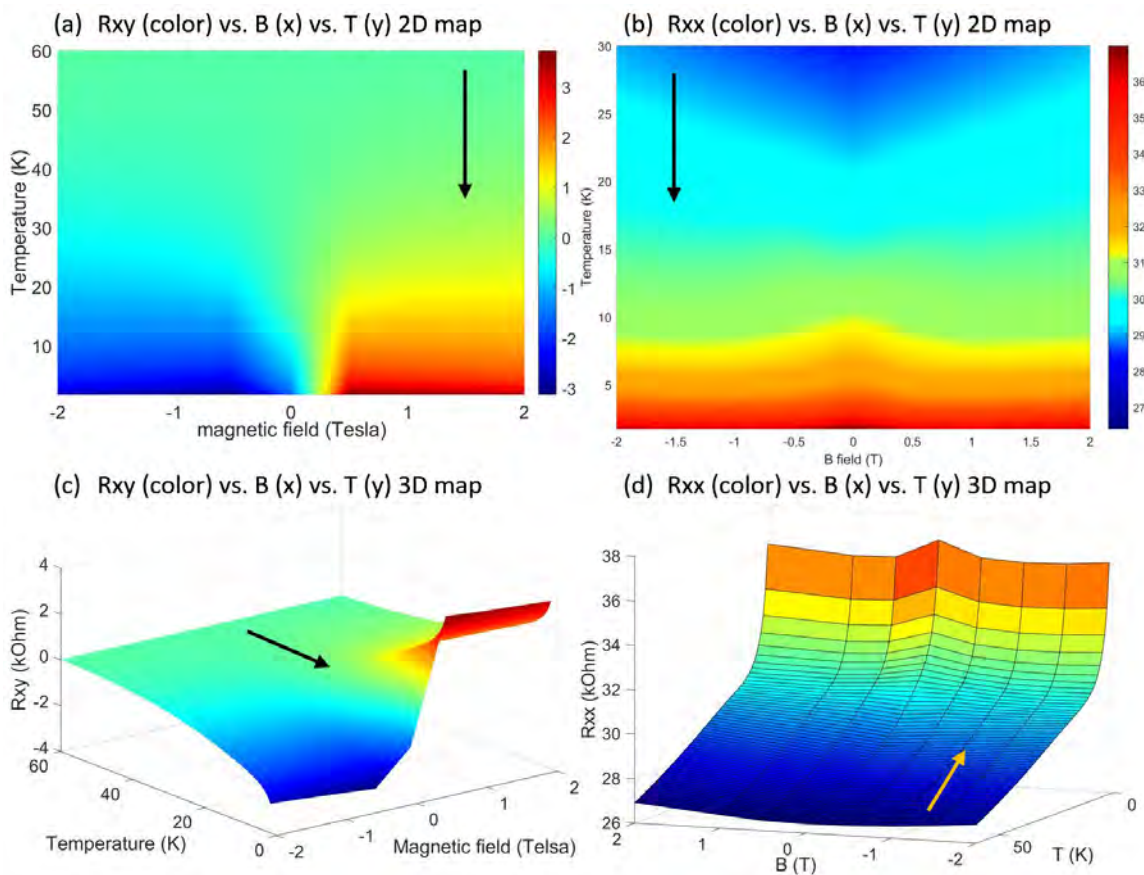


Figure 4.16: $R_{xy}(B, T)$ and $R_{xx}(B, T)$ maps derived from the field-cooled R_{xy} vs. T and R_{xx} vs. T curves in different fields. **(a)** 2D map of $R_{xy}(B, T)$, where the color bar represents the magnitude of R_{xy} in units of $k\Omega$. **(b)** 2D map of $R_{xx}(B, T)$, where the color bar represents the magnitude of R_{xx} in units of $k\Omega$. **(c)** 3D map of $R_{xy}(B, T)$. **(d)** 3D map of $R_{xx}(B, T)$.

For the evolution of R_{xy} with B and T , it is as we described before. Nevertheless, the transition from weak anti-localization to weak localization is quite smooth without any apparent transition. This again implies the ratios of both contributions from somewhere cause the transition of the curve.

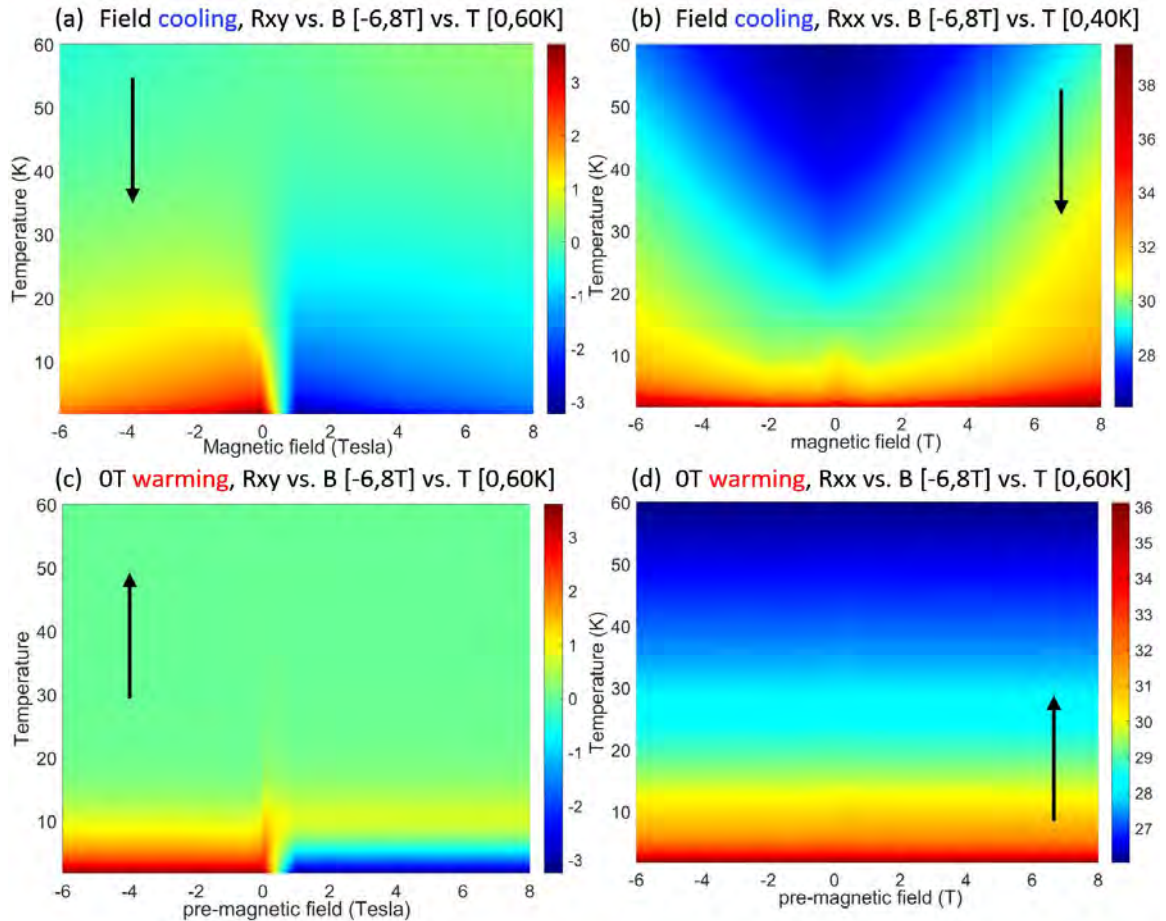


Figure 4.17: (a) 2D map of $R_{xy}(B, T)$ as derived from field-cooled R_{xy} vs. T curves. (b) 2D map of $R_{xx}(B, T)$ as derived from field-cooled R_{xx} vs. T curves. (c) 2D map of $R_{xy}(B, T)$ as derived from zero-field-warming R_{xy} vs. T curves after field cooling. Here B represents the field applied before zero-field warming. (d) 2D map of $R_{xx}(B, T)$ as derived from zero-field-warming R_{xx} vs. T curves after field cooling. Here B represents the field applied before zero-field warming.

To obtain a more complete picture, we conducted resistive measurements using temperature sweeps again by first cooling the sample in a much stronger magnetic field up to 8T and then measuring the resistance while warming up in zero fields, as shown in Figure 4.17. For field

cooling, the value of $|R_{xy}|$ decreased with increasing fields in the large field limit, as shown in Figure 4.17(a), which is consistent with what we had observed before. Similar studies of the $R_{xx}(B, T)$ data is shown in Figure 4.17 (b), which revealed how the $R_{xx}(B, T)$ curve transitioned from a W-shape at low temperatures to a V-shape at high temperatures by considering horizontal cuts in Figure 4.17 (b).

It is interesting to note that the zero-field warming R_{xy} map (after field cooling) shown in Figure 4.17(c), the $|R_{xy}|$ value became independent of the applied magnetic field for $B > 1$ T in the positive field response and for $|B| > 0.5$ T in the negative field response, which implies the saturation of the magnetization.

For the positive field response shown in Figure 4.17(c), R_{xy} evolved from negative to positive values between $T = 7$ K to 15 K, which corresponded to negative coercive fields, consistent with what we had observed from the hysteretic R_{xy} vs. B isotherms over this temperature range. In the case of negative field response, $|R_{xy}|$ decreased monotonously with increasing temperature. However, the R_{xy} value after cooled in negative fields was found to be smaller than that after cooled in the positive fields for $10 \text{ K} < T < 15 \text{ K}$. The asymmetric dependence of the AHE and spontaneous magnetization on positive and negative field responses is interesting, which may be associated with the asymmetric interfaces of both the TI and MTI layers, leading to Rashba-like splitting[87].

In the case of the $R_{xx}(B, T)$ map shown in Figure 4.17(d), R_{xx} vs. B was independent of the pre-applied field for $B > 0.1$ T. This is not surprising because after field-cooled by sufficiently high magnetic fields, a saturation of magnetization completely suppressed disorder spin scattering and so R_{xx} obtained under zero-field warming would be only dependent on the temperature and would be independent of -the magnetic fields applied during field-cooling.

4.3 Effects of circularly polarized light on the AHE of bilayer ternary TI/MTI and monolayer ternary MTI

Increasing the onset temperature of AHE in ferromagnetic materials is highly desirable for realistic spintronic applications. Given that the appearance of AHE requires long-range ferromagnetic order, increasing its onset temperature implies achieving long-range coupling of magnetic moments at a higher temperature. In the TI/MTI compounds of our study, the magnetic moments are associated with the Cr-dopants, and the onset temperature of AHE in these samples is always around 30 K, which we identified as the bulk Curie temperature T_C^{bulk} of the material. On the other hand, our STM studies revealed local surface gap opening at temperatures as high as ~ 200 K, suggesting that short-range ferromagnetic order could appear well above T_C^{bulk} . Additionally, our collaborators at UCLA had successfully fabricated AFM/MTI/AFM (AFM: antiferromagnet) heterostructures by MBE and demonstrated enhancement of T_C^{bulk} up to 100 K by multilayers of AFM/MTI/AFM sandwich [88]. The mechanism for this enhancement is the result of exchange coupling between Dirac Fermions and the A-type AFM layer, which helps align the spins of Cr-dopants in the MTI. These results suggest that the relatively low T_C^{bulk} in the ternary MTIs was due to disordered spins and so T_C^{bulk} could be much enhanced by better spin alignments. Indeed, our electrical transport studies of the ternary TI/MTI samples also revealed that with the help of an external magnetic field, the onset of AHE could appear at a temperature as high as 60 K, as shown in Figure 4.15(a), which further corroborated the notion that the onset temperature of AHE could be enhanced by whatever means feasible to align the spins of the Cr dopants.

Besides the application of high magnetic fields or the introduction of exchange coupling, it would be interesting to explore possible non-contact and non-destructive methods to enhance the alignment of spins of Cr-dopants in the MTIs. One such possibility could be the application of circularly polarized light.

Light-matter interaction can induce many interesting effects on the material surface, including the generation of photocurrents and quantum excitations that satisfy optical selection rules. For sufficiently high photon energy, the photon can excite an electron from the valence band to the conduction band. For 3D TIs, circularly polarized light can be shown

to generate a directional helicity-dependent photocurrent (HDPC) [89-91]. This photo-induced DC current is found to be dependent on the circular polarization of the light. Due to the spin-momentum lock-in on the TI surface states, when electrons are excited from the surface states to the conduction band, they still retain their spin helicity. Therefore, it is worth investigating whether we may populate one spin texture more than the other, thereby enhancing the overall spin alignment of Cr-dopants.

As described in Chapter 2, we constructed an optical probe for the PPMS system to conduct photo-assisted transport measurements. Given that we employed lock-in technique for the resistive measurements, the light-induced DC photocurrent may not be directly detected in our AC measurements. However, we may be able to observe changes in the R_{xy} signal because of its dependence on the sample magnetization, which motivated our investigations of the electrical transport properties under the excitations of circularly polarized light. Adding light to the transport measurements requires substantial optical alignments and light source tuning to send light to the bottom of the PPMS successfully. Our homemade optical probe was designed, constructed, and calibrated by several groupmates, including Marcus Teague, Duxing Hao, and Adrian Llanos.

For the optical experiments, our broadband light source was a tunable lamp for wavelengths $\lambda = 200$ to 2200 nm. The maximum available power for the light source was 10 mW. For our preliminary experiments, we used a wavelength $\lambda = 1750$ nm (~ 0.7 eV), which corresponded to more than twice the bandgap of the ternary TI, and therefore it might also induce excitations of bulk electrons in addition to surface-state electrons.

4.3.1 Effect of circularly polarized light on (3+6)-10% ternary TI/MTI

We carried out R_{xy} vs. B measurements between $B = -0.1$ T and $B = 0.1$ T for $T = 2, 4, 7, 10, 12$ and 14 K both with and without circularly polarized light, and the results for $T = 2$ K are shown in Figure 4.18(a). Circularly polarized light appeared to have enhanced the magnetization in one direction ($B < 0$) while nearly no effect in the other direction ($B > 0$), as shown from the coercive field of decreasing field sweep in Figure 4.18(a). This

asymmetric behavior is again consistent with what we have observed in the measurements of $R_{xy}(T, B)$, which we attribute to possible Rashba effects. Additionally, from the coercive field vs. T measurements both with and without circularly polarized light, we found that R_{xy} with and without light deviates from each other below 7 K, as shown in Figure 4.17(b), which also corroborated the effect of circularly polarized light on the AHE.

Based on these promising preliminary measurements, we expect more interesting effects on the AHE of the bilayer ternary TI/MTI samples by the application of circularly polarized light with different wavelengths and power densities. It is a pity that we could not conduct more photo-assisted transport measurements due to the lockdown of the labs in the past few months. Future in-depth studies of these phenomena should yield very interesting results.

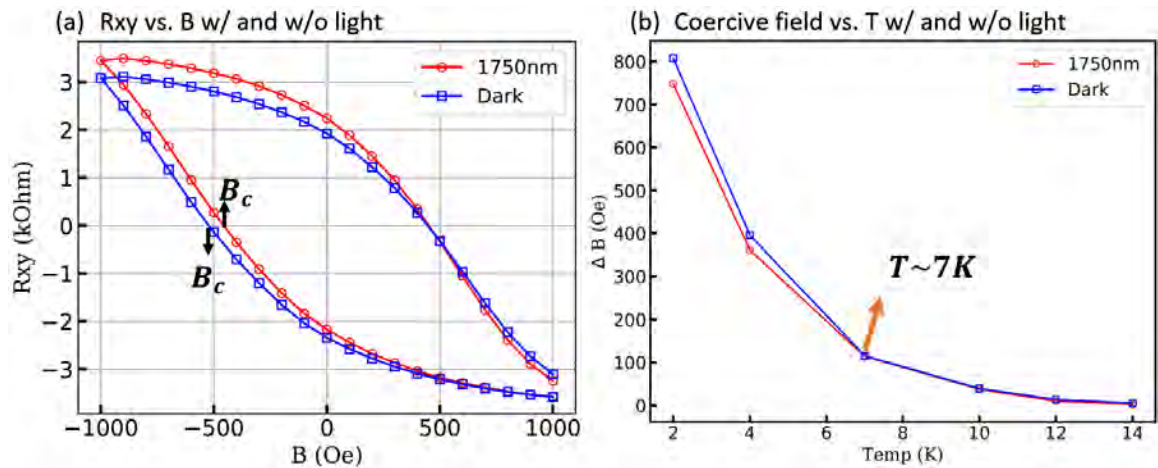


Figure 4.18: (a) R_{xy} vs. B with and without circularly polarized light. (b) Coercive field vs. T with and without circularly polarized light.

4.3.2 Effect of circularly polarized light on a monolayer (0+6)-10% MTI

We did the field sweep measurement on monolayer 6QL-10% ternary MTI at 2 K and 10 K. At 2 K, R_{xx} vs. B shows a strong weak localization, which is consistent with (1+6)-10% ternary TI/MTI. R_{xy} vs. B also shows a strong hysteresis loop. At 10 K, hysteresis nearly disappears for both R_{xx} and R_{xy} vs. B . However, it shows a very strong weak localization. In contrast, at charge neutrality point 13 K for (3+6)-10% ternary TI/MTI, R_{xx} vs. B shows weak

antilocalization. Further studies of field sweeps of (0+6)-10% MTI and (1+6)-10% TI/MTI at higher temperatures to see if the hysteresis is indeed closed or only due to the charge neutrality. It is also interesting to see if weak antilocalization will show up at higher temperatures.

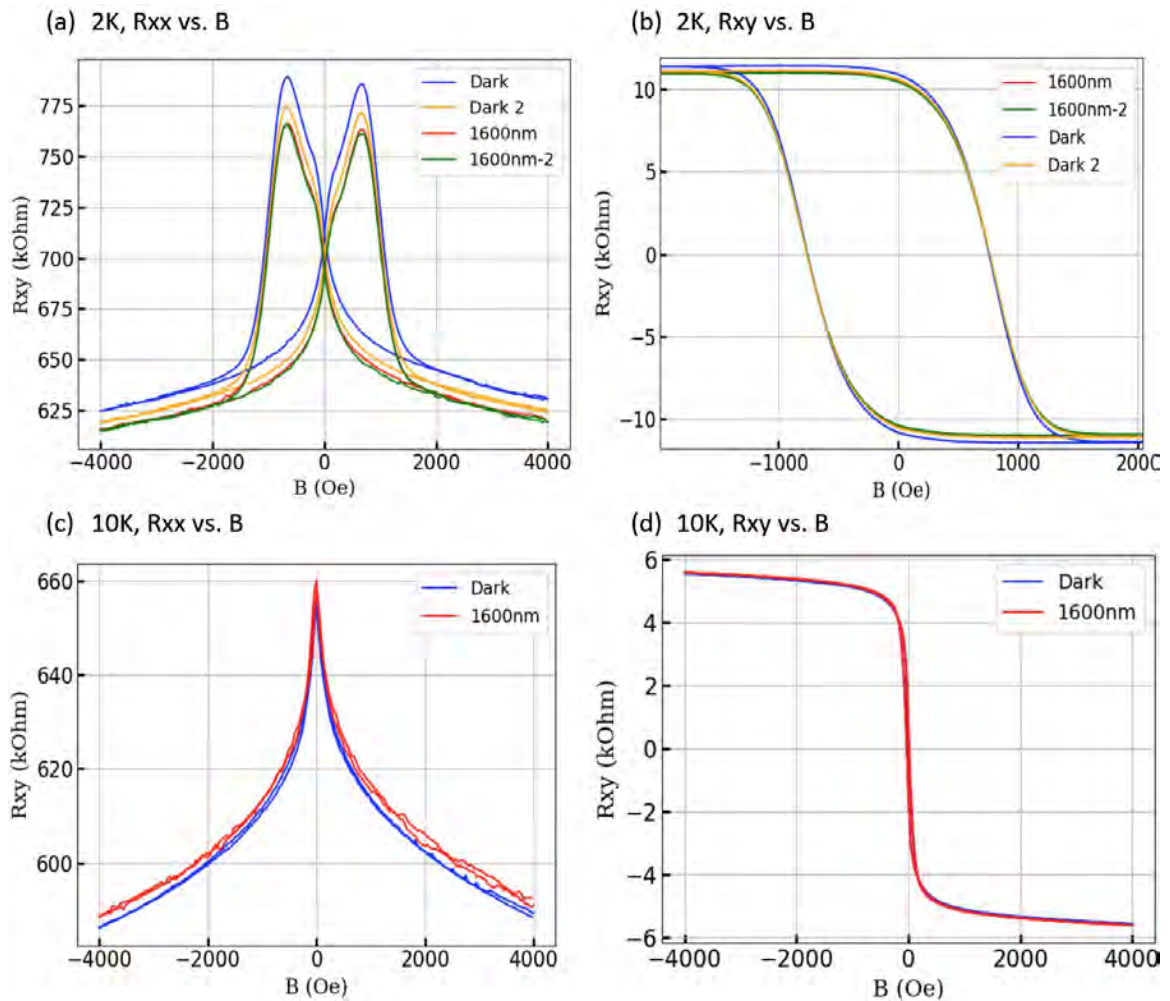


Figure 4.19 Circularly polarized light effect on 6-QL 10% ternary MTI. (a) R_{xx} vs. B at 2 K. (b) R_{xy} vs. B at 2 K. (c) R_{xx} vs. B at 10 K. (d) R_{xy} vs. B at 10 K

Unlike (3+6)-10% ternary TI/MTI, circularly polarized light seems to have a negative effect on a monolayer (0+6)-10% MTI at $T = 2$ K. Both R_{xx} and $|R_{xy}|$ decrease when the circularly polarized light is applied. At 10 K, though, the light seems to enhance the R_{xx} vs. B a little. The low-temperature decrease in R_{xx} under light may be attributed to light-induced excess

photo-carriers in the MTI, which were theoretically predicted to cause structural distortions that suppressed the FM coupling between neighboring Cr ions, leading to suppression in $|R_{xy}|$ as observed experimentally. However, detailed studies of field sweeps at different temperatures both with and without light will be necessary to fully understand the interplay of photo-induced carrier densities and spin alignment by circularly polarized light.

4.4 Discussion and Summary

Unlike STM, transport measurements study the global contributions from the band structure of the sample. In this chapter, we employed PPMS to investigate the longitudinal and Hall resistance of bilayer TI/MTI structures based on binary TI Bi_2Se_3 and ternary TI $(Bi,Sb)_2Te_3$.

Table 4.3 Summary of electrical transport results for binary TI/MTI and MTI samples

sample	(1+6)-10% Binary bilayer TI/MTI	(3+6)-10% Binary bilayer TI/MTI	(7+0)-10% Binary monolayer TI
R_{xy} vs B	<ul style="list-style-type: none"> ○ Negligible hysteresis ○ Decrease with field 	<ul style="list-style-type: none"> ○ Negligible hysteresis ○ Decrease with field 	No data
R_{xx} vs B	<ul style="list-style-type: none"> • Sharp and strong WL peak 	<ul style="list-style-type: none"> • Broader and shallow WL peak 	<ul style="list-style-type: none"> • WAL for all temperature
T_C^{bulk}	<ul style="list-style-type: none"> • 25K 	<ul style="list-style-type: none"> • 30K 	none

Note: (7+0)-10% Binary TI result is from our collaborator in UCLA [92]

Table 4.3 summarizes the transport results for binary TI/MTI samples. Binary TI/MTI bilayer samples revealed the onset of AHE around 30 K from zero-field R_{xy} vs. T sweep, while for ternary TI/MTI samples, the onset of AHE was around 20 K. However, binary TI/MTI samples only revealed decreasing $|R_{xy}|$ with increasing $|B|$ from R_{xy} vs. B measurements; no hysteretic behavior was seen in either R_{xx} vs. B or R_{xy} vs. B isotherms. Additionally, R_{xx} vs. B exhibited WL behavior, which may be attributed to the presence of

massive Dirac fermions of MTIs, in contrast to the WAL behavior of massless Dirac fermions in the surface state of pure TIs [92]. Both (0+6)-10% and (5+6)-10% binary TI can be studied in the future to confirm the origin of the weak anti-localization and weak localization on binary TI.

Table 4.4 Summary of electrical transport results for ternary TI/MTI and MTI samples

sample	(1+6)-10% Ternary TI/MTI	(3+6)-10% Ternary TI/MTI	(0+6)-10% Ternary MTI
R_{xy} vs B	<ul style="list-style-type: none"> ○ Hysteresis ○ Negative coercive field at $T \geq 15K$ 	<ul style="list-style-type: none"> ○ Hysteresis ○ Negative coercive field at $T > 13K$ 	<ul style="list-style-type: none"> ○ hysteresis
R_{xx} vs B	<ul style="list-style-type: none"> • WL at $T \leq 15K$, even with negative coercive field 	<ul style="list-style-type: none"> • WAL at $T > 13 K$ • Competition between WL and WAL at $T < 13 K$ 	<ul style="list-style-type: none"> • WL at $T \leq 10 K$
T_C^{bulk}	□ 20K	□ 20K	□ 20K
Light effect	No data	<ul style="list-style-type: none"> • Enhance R_{xy} (due to better spin alignment) at $T < 7K$ 	<ul style="list-style-type: none"> • Reduce R_{xx}, R_{xy} at 2 K • Slight enhance R_{xx} at 10 K

Note: Measurements of the (0+6)-10% ternary MTI and (3+6)-10% ternary TI/MTI under circularly polarized light were made by Adrian Llanos.

On the other hand, ternary TI/MTI bilayer samples exhibited ferromagnetic hysteresis loops with negative coercive fields in the R_{xy} vs. B isotherms for $13 K < T < 25 K$, whereas no hysteresis loops were found in the R_{xx} vs. B isotherms over this temperature range. Below 13 K, both R_{xy} vs. B and R_{xx} vs. B isotherms revealed standard ferromagnetic hysteresis loops. Additionally, we found that the slope of dR_{xy}/dB in the R_{xy} vs. B isotherms changed signs around 13 K in the high-field limit where magnetization saturated, implying sign-change in the majority carriers around $T = 13 K$ for (3+6)-10% ternary TI/MTI.

For bilayer (1+6)-10% ternary TI/MTI, R_{xx} vs. B only exhibited weak localization (WL) behavior, similar to the monolayer (0+6)-10% ternary MTI. Interestingly, WL of 6-QL monolayer ternary MTI was stronger than the WL behavior of (1+6)-10% ternary TI/MTI, consistent with the dominating bulk contributions from the gapped ternary MTI. In contrast, for (3+6)-10% ternary TI/MTI, the feature of WAL appeared at all temperatures while below 13 K, the WL feature showed up, implying the competition between WL and WAL behavior. Further studies of the field sweeps for (1+6)-10% ternary TI/MTI at higher temperatures to see if WAL may appear when the surface gap closes will help correlate the physical origin of the WL/WAL competition to the surface/bulk states contributions.

The appearance of spontaneous magnetization with a preferred direction in zero fields implied broken symmetry between a positive and a negative magnetic field of the same magnitude below T_C^{bulk} . This asymmetry was also observed when circularly polarized light was applied to the sample. We conjectured that the appearance of a preferred magnetization direction might be attributed to the asymmetric interfaces of the TI and MTI layers, leading to Rashba-like effects in these strong spin-orbit coupled materials.

One noteworthy point was that our transport measurements on different pieces of bilayer ternary TI/MTI samples often revealed slight differences. We attribute these slight differences found in the transport properties to slight variations in either the Fermi level or the electronic band structures of the ternary TIs. Specifically, we consider the evolution of the surface and bulk band structures of the ternary TIs as a function of temperature, as schematically shown in Figure 4.20 for the (3+6)-10% ternary TI/MTI bilayer sample, and in Figure 4.21 for the (1+6)-10% ternary TI/MTI bilayer sample.

The schematic band structures of $(Bi, Sb)_2Te_3$ shown in both Figure 4.20 and Figure 4.21 are based on the assumption that the bandstructure is between that of Bi_2Te_3 and Sb_2Te_3 . If we further assume that for the (3+6)-10% ternary TI/MTI sample the Fermi level E_F is located above the Dirac point and slightly below the bulk valance band (Figure 4.20), and that for the (1+6)-10% ternary TI/MTI sample the Fermi level E_F is located below both the

surface state Dirac point and the bulk valance band (Figure 4.21), we are able to consistently account for all phenomena seen in our experiments.

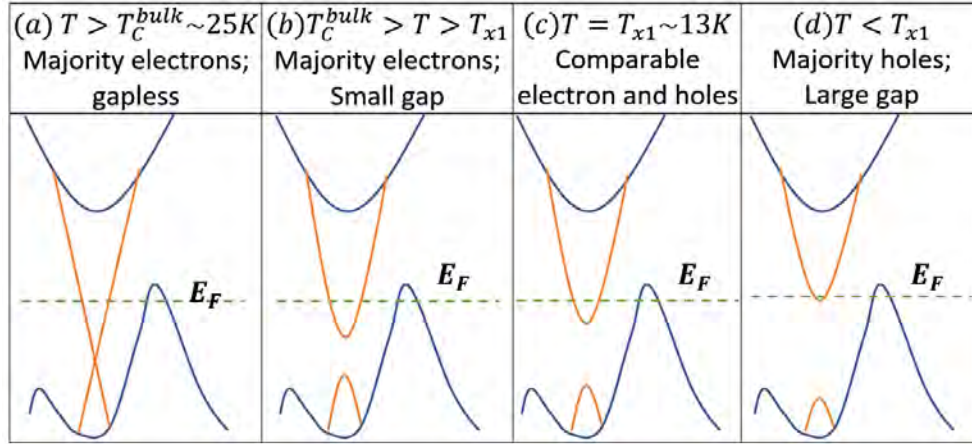


Figure 4.20: Schematic plots for the evolution of band structures for a ternary TI (3+6)-10% at different temperature regions. Here the bandstructure of the surface state is represented by red lines, and that of the gapped bulk conduction and valence bands are represented by the blue line. **(a)** $T > T_C^{bulk} \sim 25K$ where the surface state is gapless, with massless surface electrons being the majority carriers and bulk holes being the minor carriers. **(b)** $T_C^{bulk} > T > T_{x1} \sim 13 K$, where a small gap opens up so that the surface electrons become massive and bulk holes remain invariant. **(c)** $T = T_{x1}$, T_{x1} is the charge neutrality temperature where the electron and hole densities become comparable. **(d)** $T < T_{x1}$, where the bulk holes remain the majority carriers while the surface contribution decreases.

Let's first consider the (3+6)-10% ternary TI/MTI sample with a bandstructure shown in Figure 4.20. When $T > T_C^{bulk} \sim 25 K$, the surface gap is closed so that the massless surface electrons are the majority carriers while the massive bulk holes are the minority carriers. For temperatures slightly below T_C^{bulk} , a surface gap opens up due to the appearance of a finite magnetization. However, the surface gap is smaller than the indirect bulk gap, and the majority carriers are still surface electrons, although the electrons become massive. When $T = T_{x1} \sim 13 K$, the surface electron density becomes comparable to that of the bulk holes so that it is a charge neutrality point. The hysteresis loop at this temperature, therefore, looks paramagnetic. At $T = T_{x2} \sim 7 K$, the bulk holes become the majority carriers, and the surface gap becomes comparable to the indirect bulk gap. For $T < T_{x2} \sim 7 K$, the surface gap becomes larger than the indirect bulk gap so that the surface bands no longer contribute much

to the transport properties, and the bulk holes remain the majority carriers. In this limit, R_{xx} increases suddenly, and photo-induced excitations begin to affect R_{xy} .

For R_{xx} vs. B isotherms, the gapless surface electrons contribute to a V-shaped AWL behavior due to the prohibition of direct backscattering in the surface state of TIs. On the other hand, bulk hole carriers contribute to a W-shaped isotherm because of WL behavior in the low field limit and classical magnetoresistance in the high-field limit. At $T = 13$ K, both features show up in the R_{xx} vs. B curve. The competition between WL and WAL behaviors is consistent with our conjectures of two components of carriers. Thus, all experimental phenomena associated with the (3+6)-10% ternary TI/MTI sample can be consistently explained by the bandstructure shown in Figure 4.20.

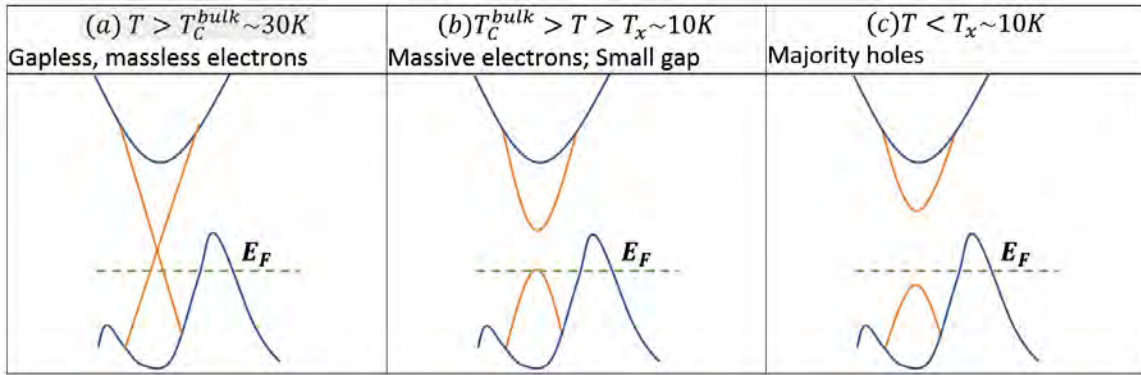


Figure 4.21: Schematic plots for the evolution of band structures for a ternary TI (1+6)-10% at different temperature regions. Here the bandstructure of the surface state is represented by red lines, and that of the gapped bulk conduction and valence bands are represented by the blue line. **(a)** $T > T_C^{bulk} \sim 30K$ where the surface state is gapless, with both surface massless holes bulk holes as carriers. **(b)** $T_C^{bulk} > T > T_x \sim 10 K$, where a small gap opens up so that the surface holes become massive and bulk holes remain invariant. **(c)** $T < T_x \sim 10K, T_{x1}$, the majority carriers are dominated by bulk holes while surface carriers diminish.

Next, we consider the (1+6)-10% ternary TI/MTI sample with a bandstructure shown in Figure 4.21. For $T > T_C^{bulk} \sim 30$ K, the surface gap is closed so that both the surface-state massless Dirac holes and bulk holes contribute to the sample conduction (Figure 4.21(a)). For $T_x \sim 10$ K $< T < T_C^{bulk}$, a small gap opens up in the surface state, and the corresponding carriers include both the surface-state massive Dirac holes and bulk holes (Figure 4.21(b)).

The coercive fields are very small due to small ferromagnetic domains, and even become slightly negative for $12\text{ K} < T \leq 15\text{ K}$, which may be attributed to the Rashba effect. Below $T_x \sim 10\text{ K}$, the surface gap becomes sufficiently large so that the dominant carriers are bulk holes (Figure 4.21(c)). The bulk ferromagnetism is well stabilized with large ferromagnetic domains so that the coercive fields increase rapidly with decreasing temperature. Moreover, for all temperatures, the carriers remain the same sign so that $d/R_{xy}/d/B/$ in the R_{xy} vs. B isotherms of the (1+6)-10% ternary TI/MTI sample is always positive **up to 1 T**, as shown in Figure 4.7, which is in contrast to the sign-changing behavior found in the (3+6)-10% ternary TI/MTI sample.

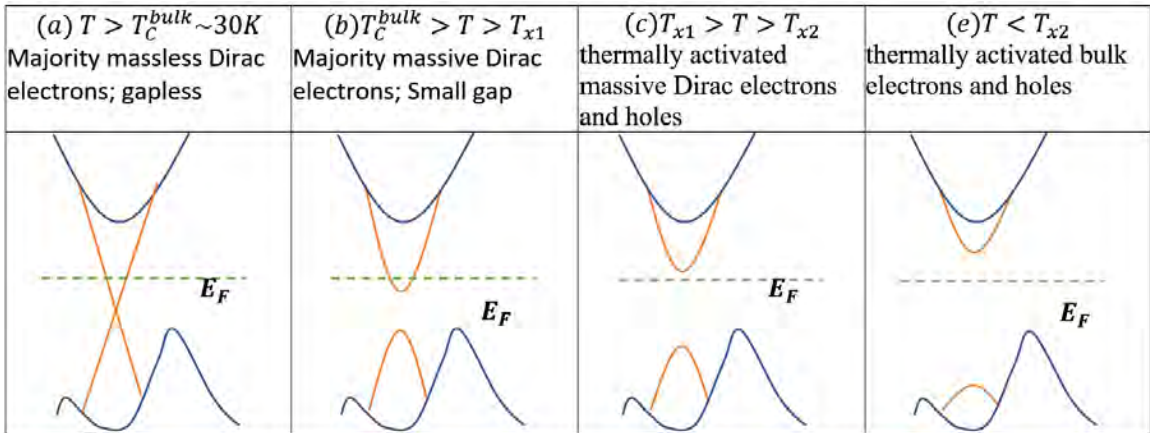


Figure 4.22: Schematic plots for the evolution of band structures for a binary TI (1+6)-10% at different temperature regions. Here the bandstructure of the surface state is represented by red lines, and that of the gapped bulk conduction and valence bands are represented by the blue line. **(a)** $T > T_C^{bulk} \sim 30\text{K}$ where the surface state is gapless, the majority carriers are massless Dirac electrons. **(b)** $T_C^{bulk} > T > T_{x1}$, where a small gap opens up so that the surface electrons become massive but still majority carriers **(c)** $T_{x1} > T > T_{x2}$, the Fermi level is within the surface gap. Majority carriers are from thermally activated surface states. **(d)** $T < T_{x2}$, the surface gap is greater than the indirect bulk gap. Majority carriers are from thermally activated bulk states.

The aforementioned discussions suggest that by accounting for the slight bandstructure variations in the ternary MTI systems as shown in Figure 4.20 and Figure 4.21, we are able to consistently explain varying experimental findings in both the (1+6)-10% ternary TI/MTI and the (3+6)-10% ternary TI/MTI samples. In this context, it is worth considering whether the bandstructure of binary MTIs may be responsible for the complete absence of hysteresis

loops in the R_{xy} -vs.- B and R_{xx} -vs.- B isotherms at $T < T_C^{bulk}$. As shown in Figure 4.22(a), the Dirac point of the surface state in Bi_2Se_3 is significantly far from all bulk conduction and valence bands, which is in contrast to the bandstructure of ternary MTIs. Therefore, for $T > T_C^{bulk} \sim 30$ K and the Fermi level slightly above the Dirac point, the surface state is gapless, and the dominant carriers are surface-state massless Dirac electrons. For $T < T_C^{bulk}$, a surface gap opens up and the majority carriers are massive Dirac electrons when the surface gap is small so that the Fermi level still intersects the top surface state (Figure 4.22(b)), thermally activated massive Dirac electrons and holes when the surface gap becomes sufficiently large so that the Fermi level falls within the surface gap (Figure 4.22(c)), and thermally activated bulk electrons and holes when the surface gap becomes larger than the indirect bulk gap (Figure 4.22(d)). The surface gap evolution depicted from Figures 4.22(b) to 4.22(d) at $T < T_C^{bulk}$ can be realized by either decreasing the temperature in a constant field or by increasing the magnetic field at a constant temperature, and in the latter case the gapped surface state naturally leads to WL behavior in the R_{xx} -vs.- B isotherms for small fields, as shown in Figure 4.4. Overall, we conjecture that the absence of intrinsic bulk carriers in the ferromagnetic state of the binary MTI cannot support sufficiently large magnetic domains to yield discernible coercive fields below T_C^{bulk} so that no hysteresis loops could be resolved in either R_{xy} -vs.- B or R_{xx} -vs.- B isotherms. Thus, details of the bandstructure and the Fermi level location in the MTIs appear to play critical roles in determining the electrical transport properties of the MTIs.

In conclusion, our electrical transport studies of bilayer TI/MTI samples have revealed many interesting properties associated with the interplay of magnetism with the surface and bulk states of these topological materials. In particular, we note that the appearance of QAHE in ternary MTIs only at extremely low temperature (~ 30 mK) and the rapid decrease of the AHE with increasing temperature may be attributed to the finite contributions from bulk states because of the bandstructure effects (Figures 4.20 and 4.21) [93]. Promising enhancement of the AHE induced by circularly polarized light has also been observed. Further exploration of photo-induced effects on controlling the magnetism of MTIs based on the findings derived from this work will likely yield exciting new results.

Chapter 5

GRAPHENE AND INTER-LAYER INTERACTION

Graphene, an allotrope of carbon in the form of a single layer of atoms in a two-dimensional hexagonal lattice, has been deemed as a wonder material for both scientific research and technological applications. It is the basic structural element of other allotropes, including graphite, charcoal, carbon nanotubes, graphene nano-ribbons, and fullerenes. It conducts heat and electricity very efficiently and is nearly transparent. However, by mixing different aspect ratios of graphene nanoribbons, we can also produce the darkest materials with nearly perfect optical absorption.

With a single-atom thickness, graphene is an ideal 2D material with a large surface to volume ratio, which has been shown to be suitable for applications to energy storage such as in supercapacitors[94-97] and lithium-ion batteries[98, 99]. The mechanical strength of a single layer of graphene is 200 times stronger than that of steel due to its stronger-than-diamond sp^2 bond[100-103]. Nevertheless, it is also a perfect two-dimensional (2D) van der Waal material with bond-free interactions between layers of graphene, which implies that graphene can be stacked with other van der Waal materials at arbitrary angles relative to its adjacent layers regardless of the lattice constants of other van der Waals materials. Interestingly, even the stacking of just two layers of graphene at a twist angle can lead to interesting properties such as structural superlubricity[104-107] at the zigzag or incommensurate angles or superconductivity near the magic angle ($\sim 1.05^\circ$)[17-19]. The weak interlayer van der Waals interaction, strong intra-layer sp^2 bonding, and small lattice constants of graphene also make graphene an ideal material for surface passivation of highly reactive materials[108].

Similar to the surface states of topological insulators (TIs), the energy dispersion relation of graphene exhibits a Dirac spectrum at the K and K' points of the first Brillouin zone. On

the other hand, the surface state of graphene contains four-fold degeneracy per band relative to that of TIs. The excess degrees of degeneracy can be lifted by either breaking the inversion symmetry to lift the valley (pseudo-spin) degeneracy or breaking the time-reversal symmetry to lift the spin degeneracy. Our group has been developing valleytronic devices based on nanoscale strain-engineered monolayer graphene [14, 16] to investigate various topological and correlated electronic phenomena associated with the broken symmetry states.

The primary challenge for technological applications of graphene lies in its scalable production and transfer. Our group has strived to achieve scalable and reproducible synthesis techniques to produce high-quality large-area monolayer graphene sheets, quasi-one-dimensional graphene nanostripes, and bilayer graphene samples with controlled twist angles, as detailed in the Ph.D. thesis of Chen-Chih Hsu [14]. This chapter describes the author's contributions to characterizing the quality of various graphene samples synthesized by other group members and providing simulations for the growth results. Additionally, DFT simulations for demonstrating superlubricity between bilayer graphene are carried out and compared with experimental findings.

In the following, we shall begin with a brief introduction of important properties of graphene, which will be followed by descriptions of various graphene-related projects that the author has collaborated with other group members, with emphasis on the specific contributions by the author.

5.1 introduction

Monolayer graphene consists of carbon atoms arranged in a two-dimensional honeycomb crystalline structure, as shown in figure 5.1(a). The unit cell is a hexagonal Bravais lattice with a basis of two atoms A and B at each lattice point. [109]

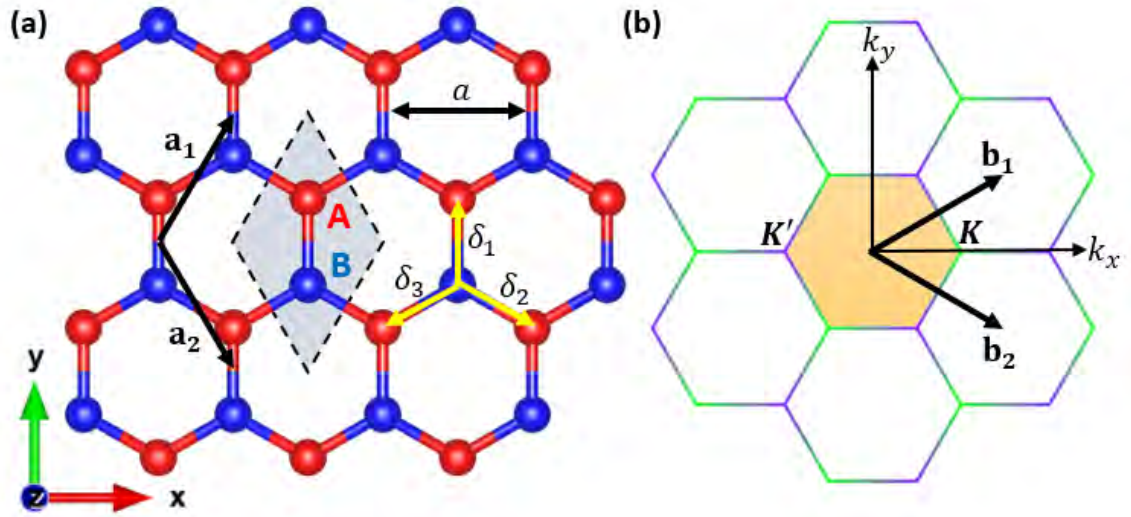


Figure 5.1: (a) Graphene honeycomb crystal consists of a hexagonal Bravais lattice with a basis of two atoms labeled as A and B. The primitive lattice vectors are \mathbf{a}_1 and \mathbf{a}_2 . The lattice constant is $a = 2.46\text{\AA}$. δ_1, δ_2 and δ_3 are the nearest-neighbor vectors. (b) The corresponding reciprocal lattice and Brillouin zone. The shaded region is the first Brillouin zone. \mathbf{b}_1 and \mathbf{b}_2 are the reciprocal primitive lattice vectors. \mathbf{K} and \mathbf{K}' are the Dirac point.

We can choose the primitive lattice vectors, for example in Figure 5.1(a), as \mathbf{a}_1 and \mathbf{a}_2 .

$$\mathbf{a}_1 = \left(\frac{a}{2}, \frac{\sqrt{3}a}{2} \right), \quad \mathbf{a}_2 = \left(\frac{a}{2}, -\frac{\sqrt{3}a}{2} \right), \quad (5.1)$$

where $a = |\mathbf{a}_1| = |\mathbf{a}_2| = 2.46\text{\AA}$ is the lattice constant of graphene and the distance between unit cells. The distance between carbon atoms is the carbon-carbon bond length $a_{CC} = a/\sqrt{3} = 1.42\text{\AA}$. A and B atoms cannot be connected through the lattice vectors, and so each of the atoms forms a sublattice.

The reciprocal lattice vectors \mathbf{b}_1 and \mathbf{b}_2 are given by

$$\mathbf{b}_1 = \left(\frac{2\pi}{a}, \frac{2\pi}{\sqrt{3}a} \right), \quad \mathbf{b}_2 = \left(\frac{2\pi}{a}, -\frac{2\pi}{\sqrt{3}a} \right). \quad (5.2)$$

The resulting reciprocal lattice is shown in Figure 5.1(b). The first Brillouin zone and second Brillouin zones are shown, and the first Brillouin zone is indicated by the shaded hexagonal region. The corners of the hexagon have two inequivalent high symmetry points K_+ and K_- . These points are associated with two inequivalent valleys from the bandstructure calculations described below. The corners belonging to the same valley can be connected through the reciprocal vectors. Therefore, K_+ and K_- may be conveniently given by

$$K_{\pm} = \left(\pm \frac{4\pi}{3a}, 0 \right). \quad (5.3)$$

5.1.1 The tight-binding model of monolayer graphene

We may express the positional (\mathbf{r}) and momentum (\mathbf{k}) dependent electronic wave function Ψ in graphene by the linear combination of atomic orbital functions ϕ_A and ϕ_B associated with the A and B-site atoms as follows:

$$\Psi(\mathbf{k}, \mathbf{r}) = c_A(\mathbf{k})\phi_A(\mathbf{k}, \mathbf{r}) + c_B(\mathbf{k})\phi_B(\mathbf{k}, \mathbf{r}) = \sum_{l=A}^B c_l \phi_l(\mathbf{k}, \mathbf{r}), \quad (5.4)$$

where c_A and c_B are coefficients, and the Bloch function is given by

$$\Phi_A(\mathbf{k}, \mathbf{r}) = \frac{1}{\sqrt{N}} \sum_{i=1}^N e^{i\mathbf{k} \cdot \mathbf{R}_{Ai}} \phi_A(\mathbf{r} - \mathbf{R}_{Ai}). \quad (5.5)$$

The energy dispersion relation can be obtained by the following relation:

$$E(\mathbf{k}) = \frac{\langle \Psi | H | \Psi \rangle}{\langle \Psi | \Psi \rangle} = \frac{\sum_{j,l=A}^B c_j^* c_l \langle \Phi_j | H | \Phi_l \rangle}{\sum_{j,l=A}^B c_j^* c_l \langle \Phi_j | \Phi_l \rangle} = \frac{\sum_{j,l=A}^B H_{jl} c_j^* c_l}{\sum_{j,l=A}^B S_{jl} c_j^* c_l}, \quad (5.6)$$

where $H_{jl} = \langle \Phi_j | H | \Phi_l \rangle$ represents the transfer integral matrix, $S_{jl} = \langle \Phi_j | \Phi_l \rangle$ is the overlap integral matrix, and H is Hamiltonian. To find the minimum the energy of the band, we need to differentiate $E(\mathbf{k})$ with c_l . In the end, we have to solve this equation:

$$\begin{pmatrix} H_{AA} & H_{AB} \\ H_{BA} & H_{BB} \end{pmatrix} \begin{pmatrix} c_A \\ c_B \end{pmatrix} = E \begin{pmatrix} S_{AA} & S_{AB} \\ S_{BA} & S_{BB} \end{pmatrix} \begin{pmatrix} c_A \\ c_B \end{pmatrix}. \quad (5.7)$$

Let us consider the diagonal terms first:

$$\begin{aligned} H_{AA} &= \frac{1}{N} \sum_{i=1}^N \sum_{j=1}^N e^{i\mathbf{k} \cdot (\mathbf{R}_{Aj} - \mathbf{R}_{Ai})} \langle \phi_A(\mathbf{r} - \mathbf{R}_{Ai}) | H | \phi_A(\mathbf{r} - \mathbf{R}_{Aj}) \rangle \\ &\approx \frac{1}{N} \sum_{i=1}^N \langle \phi_A(\mathbf{r} - \mathbf{R}_{Ai}) | H | \phi_A(\mathbf{r} - \mathbf{R}_{Ai}) \rangle \equiv \epsilon_{2p} = H_{BB}. \end{aligned} \quad (5.8)$$

In Eq. (5.8) we have used the fact that the dominant terms are from $j = i$. ϵ_{2p} is the energy of $2p_z$ orbital and can be set to zero as our reference point. For the overlap integral matrix,

$$\begin{aligned} S_{AA} &= \frac{1}{N} \sum_{i=1}^N \sum_{j=1}^N e^{i\mathbf{k} \cdot (\mathbf{R}_{Aj} - \mathbf{R}_{Ai})} \langle \phi_A(\mathbf{r} - \mathbf{R}_{Ai}) | \phi_A(\mathbf{r} - \mathbf{R}_{Aj}) \rangle \\ &= \langle \phi_A(\mathbf{r} - \mathbf{R}_{Ai}) | \phi_A(\mathbf{r} - \mathbf{R}_{Ai}) \rangle = 1 = S_{BB}. \end{aligned} \quad (5.9)$$

For off-diagonal matrix elements, the dominant term will be from the nearest neighbor

$$\begin{aligned} H_{AB} &= \frac{1}{N} \sum_{i=1}^N \sum_{j=1}^N e^{i\mathbf{k} \cdot (\mathbf{R}_{Bj} - \mathbf{R}_{Ai})} \langle \phi_A(\mathbf{r} - \mathbf{R}_{Ai}) | H | \phi_B(\mathbf{r} - \mathbf{R}_{Bj}) \rangle \\ &\approx -\frac{1}{N} \sum_{i=1}^N \sum_{j=1}^3 e^{i\mathbf{k} \cdot (\mathbf{R}_{Bj} - \mathbf{R}_{Ai})} \gamma_0 = -\gamma_0 \sum_{j=1}^3 e^{i\mathbf{k} \cdot \delta_j} \equiv -\gamma_0 f(\mathbf{k}). \end{aligned} \quad (5.10)$$

δ_j is the nearest-neighbor vector, as shown in Figure 5.1(a).

$$\delta_1 = \left(0, \frac{a}{\sqrt{3}}\right), \quad \delta_2 = \left(\frac{a}{2}, -\frac{a}{2\sqrt{3}}\right), \quad \delta_3 = \left(-\frac{a}{2}, -\frac{a}{2\sqrt{3}}\right) \quad (5.11)$$

$$f(\mathbf{k}) = \sum_{j=1}^3 e^{i\mathbf{k}\cdot\delta_j} = e^{\frac{ik_y a}{\sqrt{3}}} + 2e^{-\frac{ik_y a}{2\sqrt{3}}} \cos\left(\frac{k_x a}{2}\right). \quad (5.12)$$

For the off-diagonal overlap matrix,

$$\begin{aligned} S_{AB} &= \frac{1}{N} \sum_{i=1}^N \sum_{j=1}^N e^{i\mathbf{k}\cdot(\mathbf{R}_{Bj}-\mathbf{R}_{Ai})} \langle \phi_A(\mathbf{r}-\mathbf{R}_{Ai}) | \phi_B(\mathbf{r}-\mathbf{R}_{Bj}) \rangle \\ &\approx \frac{1}{N} \sum_{i=1}^N \sum_{j=1}^3 e^{i\mathbf{k}\cdot(\mathbf{R}_{Bj}-\mathbf{R}_{Ai})} s_0 = s_0 f(\mathbf{k}). \end{aligned} \quad (5.13)$$

Therefore for monolayer graphene,

$$H_1 = \begin{pmatrix} \epsilon_{2p} & -\gamma_0 f(\mathbf{k}) \\ -\gamma_0 f^*(\mathbf{k}) & \epsilon_{2p} \end{pmatrix}, \quad S_1 = \begin{pmatrix} 1 & -s_0 f(\mathbf{k}) \\ s_0 f^*(\mathbf{k}) & 1 \end{pmatrix}. \quad (5.14)$$

Solving the Eigen equation, we obtain the energy dispersion relations

$$E_{\pm} = \frac{\epsilon_{2p} \pm \gamma_0 |f(\mathbf{k})|}{1 \mp s_0 |f(\mathbf{k})|} = \frac{\pm \gamma_0 |f(\mathbf{k})|}{1 \mp s_0 |f(\mathbf{k})|}. \quad (5.15)$$

Here $\gamma_0 = 3.033 \text{ eV}$, $s_0 = 0.129$, $\epsilon_{2p} = 0$. Here E_+ is the conduction band energy and E_- is the valence band energy.

The band structure of monolayer graphene is illustrated in Figure 5.2 (a). We note that at the Dirac points, $f(\mathbf{K}_{\pm}) = 0$. If we introduce the momentum $\mathbf{p} = \hbar\mathbf{k} - \hbar\mathbf{K}_{\pm}$ that is measured from the center of the $\mathbf{K}_{\pm} = \mathbf{K}_{\xi}$ point, the transfer integral matrix becomes

$$H_{1\xi} = v \begin{pmatrix} 0 & \xi p_x - ip_y \\ \xi p_x + ip_y & 0 \end{pmatrix} = v(\xi \sigma_x p_x + \sigma_y p_y) = vp\boldsymbol{\sigma} \cdot \hat{\mathbf{n}}_1, \quad (5.16)$$

where $v = \sqrt{3}a\gamma_0/(2\hbar)$, $\hat{\mathbf{n}}_1 = (\xi \cos \varphi, \sin \varphi, 0)$, and $\boldsymbol{\sigma}$ is the pseudospin vector with components of the corresponding Pauli matrix. Equation (5.7) reduces into $H_1\psi = E\psi$.

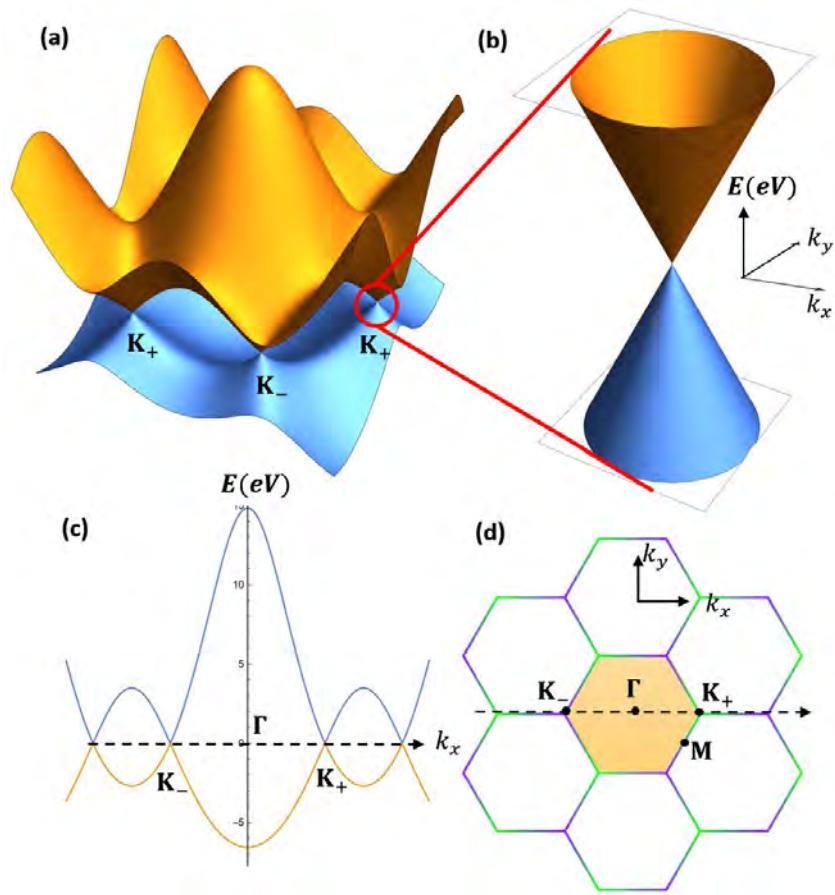


Figure 5.2: (a) Band structure of monolayer graphene in reciprocal space according to the tight binding model equation (5.15). (b) Enlarged energy dispersion relation around one of the Dirac points, showing a perfect Dirac cone for momentum k near K_{\pm} with dispersion according to equation (5.17) (c) Band structure along the dashed line cut in the reciprocal space (d).

Their eigenvalue and eigenvector is given by

$$E_{\pm} = \pm v p, \quad \psi_{\pm} = \frac{1}{\sqrt{2}} \begin{pmatrix} 1 \\ \pm \xi e^{i\xi\varphi} \end{pmatrix} e^{i\mathbf{p}\cdot\mathbf{r}/\hbar}. \quad (5.17)$$

The energy dispersion is linear around the Dirac Valley points, as shown in Figure 5.2 (b). The wave functions ψ_{\pm} look like the spinor pointing to the $(\xi \cos \varphi, \sin \varphi, 0)$ in spin $\frac{1}{2}$ system. However, the component of ψ_{\pm} is the relative amplitude of the sublattice A and B Bloch functions. Therefore, this degree of freedom is called **pseudospin**. The direction of pseudospin is parallel or anti-parallel to the electronic momentum \mathbf{p} depending on the band

and the valley as if the electron has chirality on its pseudospin. That is, the pseudospin of electron locks with its momentum, just like the spin-momentum locking in topological insulators (TIs). Hence, due to the chiral nature of low energy electrons, their backscattering is constrained like TIs. Assuming an electron goes in $\varphi = 0$ direction and is scattered by A-B symmetry preserved potential to the angle φ , the scattering factor can be calculated as $w(\varphi) = |\langle \psi_{\pm}(\varphi) | \psi_{\pm}(0) \rangle|^2 = \cos^2\left(\frac{\varphi}{2}\right)$. The direct backscattering of opposite momentum is prohibited due to the conservation of the pseudospin.

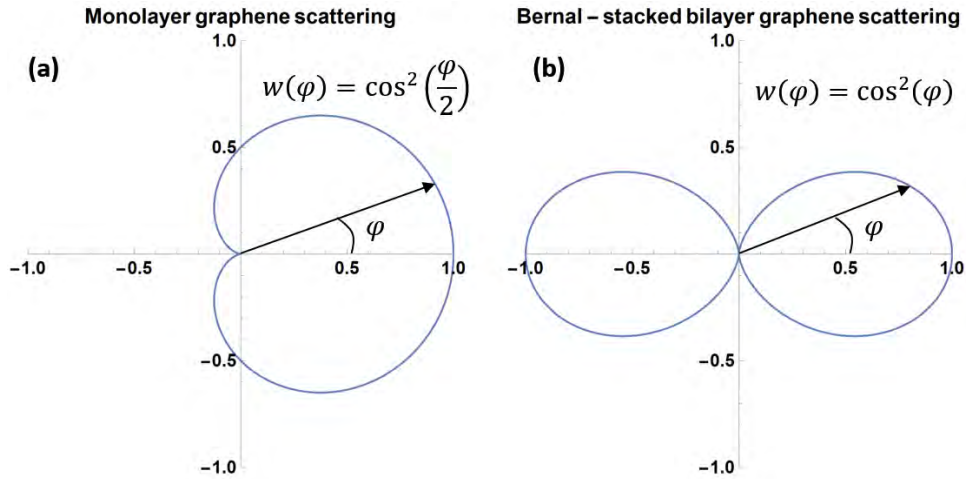


Figure 5.3: Anisotropic scattering of chiral electrons in graphene. (a) Angular dependence of $w(\varphi) = \cos^2\left(\frac{\varphi}{2}\right)$ of scattering probability off an A-B symmetric potential in monolayer graphene and (b) $w(\varphi) = \cos^2(\varphi)$ for bilayer graphene.

5.1.2 Tight-binding model of bilayer graphene

For Bernal-stacked or AB-stacked bilayer graphene, it consists of two parallel layers of graphene with a honeycomb lattice (Figure 5.4). The unit cell has 4 atoms with a pair A1, B1, from the lower layer, and a pair A2, B2 from the upper layer. For AB-stacking, one atom from each layer (B1, A2) is directly below or above each other, while other atoms (A1, B2) are below or above the center of a honeycomb lattice of next layers. The unit cell

has the same area as monolayer graphene, and therefore, the reciprocal lattice and first Brillouin zone are the same.

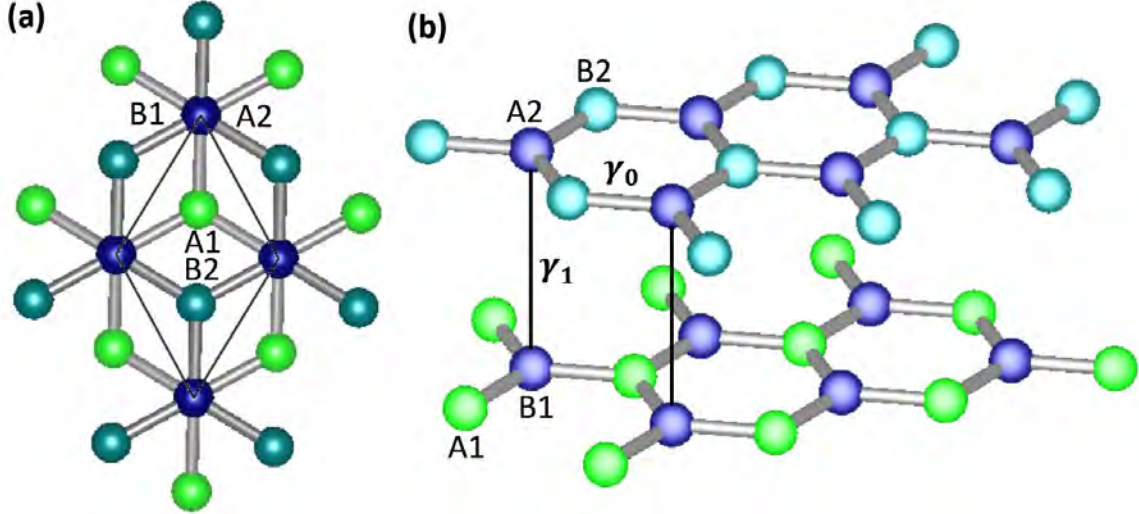


Figure 5.4: Crystalline structure of AB-stacked bilayer graphene. **(a)** Top view of the unit cell. Each unit cell has 4 atoms: A2 and B2 are atoms in the top layer, whereas A1 and B1 are atoms in the bottom layer. **(b)** Side view of the AB-stacked bilayer graphene, showing that A2 atom is directly above the B1 atom. Therefore, besides the intralayer nearest-neighbor interaction γ_0 , there is an interlayer nearest-neighbor interaction γ_1

In the tight-binding approximation, besides the intralayer nearest-neighbor coupling γ_0 between A1 and B1, A2 and B2 on each layer, there is a nearest-neighbor interlayer coupling γ_1 between B1 and A2 atoms that are directly below or above each other,

$$\gamma_1 = \langle \phi_{A2}(\mathbf{r} - \mathbf{R}_{A2}) | H | \phi_{B1}(\mathbf{r} - \mathbf{R}_{B1}) \rangle = 0.39 \text{ eV}. \quad (5.18)$$

Taking the amplitudes of A1, B1, A2, B2 wave functions as the basis, we obtain the transfer integral matrix:

$$H = \begin{pmatrix} \epsilon_{2p} & -\gamma_0 f(\mathbf{k}) & 0 & 0 \\ -\gamma_0 f^*(\mathbf{k}) & \epsilon_{2p} & \gamma_1 & 0 \\ 0 & \gamma_1 & \epsilon_{2p} & -\gamma_0 f(\mathbf{k}) \\ 0 & 0 & -\gamma_0 f^*(\mathbf{k}) & \epsilon_{2p} \end{pmatrix}. \quad (5.19)$$

The eigenvalues of the Hamiltonian are given by

$$E_{\pm}^{(\alpha)} = \pm \frac{\gamma_1}{2} \left(\sqrt{1 + \frac{4\gamma_0^2 |f(\mathbf{k})|^2}{\gamma_1^2}} + \alpha \right), \quad \alpha = \pm 1. \quad (5.20)$$

Over most of the Brillouin zone, $4\gamma_0^2 |f(\mathbf{k})|^2 \gg \gamma_1^2$, $E_{\pm}^{(\alpha)} \approx \pm \left(\gamma_0 |f(\mathbf{k})| + \frac{\alpha\gamma_1}{2} \right)$. This means both bands are similar to monolayer band with energy split by the interlayer coupling γ_1 (Figure 5.5 (a)). Near the K_{\pm} point, we replace the factor $\gamma_0 |f(\mathbf{k})|$ by vp and for $\alpha = -1$:

$$E_{\pm}^{(-1)} = \pm \frac{\gamma_1}{2} \left(\sqrt{1 + \frac{4v^2 p^2}{\gamma_1^2}} - 1 \right) \approx \pm \frac{v^2 p^2}{\gamma_1} = \pm \frac{p^2}{2m}. \quad (5.21)$$

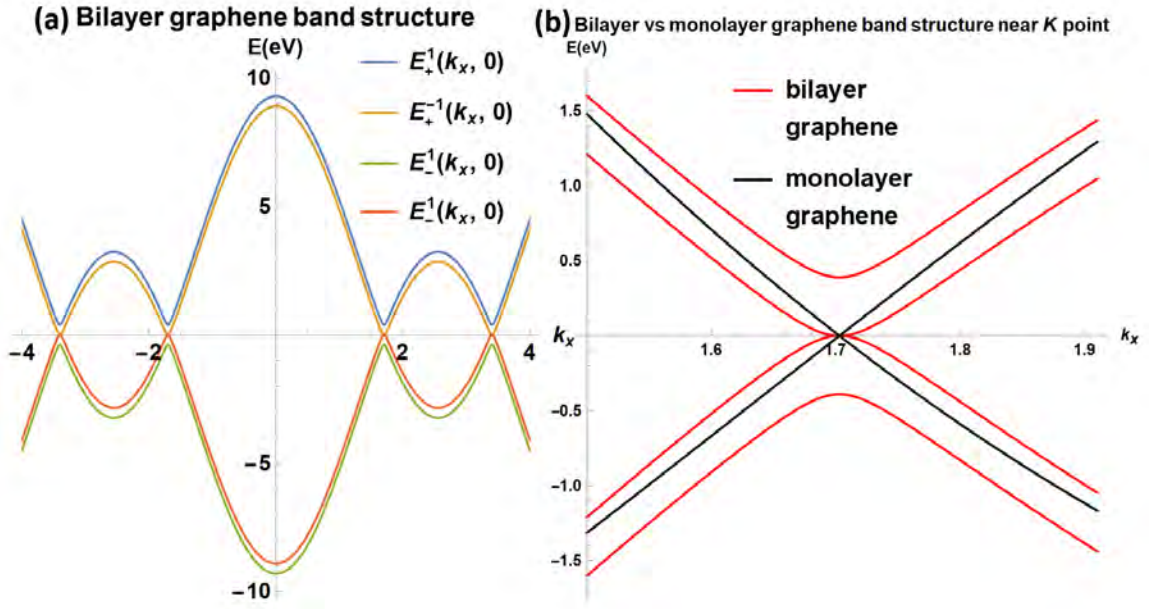


Figure 5.5: (a) Band structure of bilayer graphene along the cut line, same as Figure 5.2(d). For k sufficiently far from the K point, we note that the dispersion relation is similar to that of monolayer graphene. (b) Bilayer graphene band structure near the K point, showing quadratic dispersion rather than linear dispersion so that bilayer graphene carriers are no longer massless Dirac fermions as in the case of monolayer graphene.

The band is not linear near the K point. Instead, it is a quadratic dispersion (Figure 5.5 (b)). The surface carriers are no longer massless Dirac fermions like those in monolayer graphene. Rather, they have become massive.

The eigenstates are

$$\psi_{\pm} = \frac{1}{\sqrt{2}} \begin{pmatrix} 1 \\ \mp e^{i2\xi\varphi} \end{pmatrix} e^{i\frac{\mathbf{p}\cdot\mathbf{r}}{\hbar}}. \quad (5.22)$$

The scaling factor is $w(\varphi) = |\langle \psi_{\pm}(\varphi) | \psi_{\pm}(0) \rangle|^2 = \cos^2(\varphi)$. From Figure 5.3 (b) for $w(\varphi)$ of bilayer graphene, we can see that direct backscattering is allowed.

5.1.3 Twist bilayer graphene and the corresponding Moiré pattern

Since graphene is a 2D van der Waals material, graphene layers can be stacked with any twist angles. For any twist angles except for 0 degrees, the twist generates superstructures known as the Moiré patterns (Figure 5.6(a)), which are readily seen in STM topography. Strictly speaking, these superlattices do not have exact lattice symmetry because atoms in one superlattice cell do not match atoms in another superlattice cell, despite the same superlattice constant. The size of the superlattice depends on the twist angle, and it can be hundreds of times larger than the lattice constant of graphene at a very tiny twist angle. The relation between twist angle and superlattice constant is easier to derive in the reciprocal lattice, and we note that the larger the superlattice is, the smaller the reciprocal lattice is (Figure 5.6 (b)).

When one layer of graphene rotates against the other, so does the reciprocal lattice of each layer of graphene. The Bragg spots of the two layers separate by a displacement ΔK . Since the distance between K and the Γ point is $2\pi/a = b$:

$$\Delta K = 2b \sin\left(\frac{\theta}{2}\right) = \frac{2\pi}{a} 2 \sin\left(\frac{\theta}{2}\right) = \frac{2\pi}{L}. \quad (5.23)$$

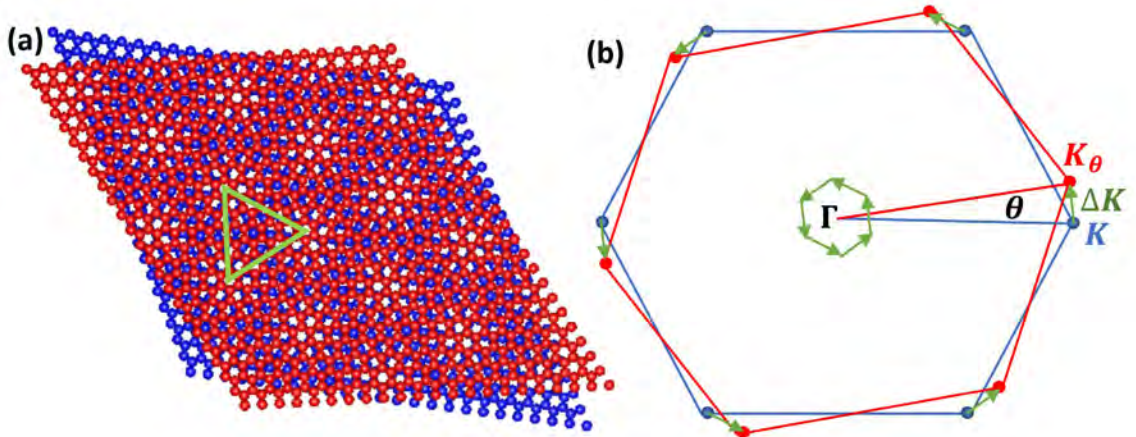


Figure 5.6: (a) Moiré pattern of twisted bilayer graphene. The superlattice structure with a much bigger lattice constant can be seen as shown by a green triangle. (b) The reciprocal lattice of the twisted bilayer graphene with a twist angle θ . The superlattice Bragg spots are from the difference between the reciprocal lattice of each layer. Since the size of the reciprocal lattice is inversely proportional to the size of the spatial lattice, the reciprocal superlattice is small. It forms an inner hexagon with an angle of θ rotation relative to the outer hexagon.

Therefore, the period of Moiré pattern L given by

$$L = \frac{a}{2 \sin\left(\frac{\theta}{2}\right)}. \quad (5.24)$$

The band structure of the twisted bilayer graphene needs to be calculated by DFT. Recently, it's discovered that for twist angles of about 1.1° , the so-called ‘magic angle,’ the electronic band structure of this ‘twisted bilayer graphene’ exhibits flat bands near-zero Fermi energy, resulting in correlated insulating states at half-filling just like a Mott insulator. With some doping, twisted bilayer graphene can become superconducting. [17-19, 110]

This discovery of superconductivity in “magic-angle” twisted bilayer graphene has stimulated intense research activities. Nevertheless, typical approaches of preparing the twist bilayer graphene by mechanical exfoliation of monolayer graphene flakes and then manually stacking two layers at a twist angle are very difficult. Our group developed a

method to synthesize bilayer graphene of different twist angles directly, which is briefly described in the following subsections. The author notes that methods of graphene synthesis in our group have been developed by other group members. The role of the author was to conduct STM studies and carried out simulations on graphene samples synthesized by others.

5.2 Single-step Growth of Graphene by Plasma-enhanced Chemical Vapor Deposition

A small flake of graphene can be obtained by simply peeling it off from graphite. However, to make graphene commercialized for applications, single domain, large area, high-quality graphene with speedy, reliable, scalable, and low-cost growth and secure transfer is necessary.

To date, several methods have been developed for the mass-production of graphene, which includes liquid-phase exfoliation of graphite[111-144], synthesis on SiC[145-165], thermal chemical vapor deposition (T-CVD)[166-189], and Plasma enhanced chemical vapor deposition (PECVD)[190-207]. PECVD has proven to be a versatile approach that offers several advantages. PECVD has been widely used for synthesizing many carbon-based materials, such as diamonds, graphene, vertically oriented graphene nano-walls and nano-sheets, and carbon nanotubes (CNTs). Additionally, PECVD techniques can be employed for fast and large-scale functionalization of graphene and related materials, which is a versatile approach that further broadens the scope of graphene-based applications. These advantages make PECVD growth of graphene and graphene-related nanostructures highly attractive and have been considered as a promising technique to improve the compatibility of graphene growth with semiconducting manufacturing processes.

We developed a new growth method based on microwave (MW) PECVD. By properly controlling the gas environment of the plasma, it is found that no active heating is necessary for the PECVD growth processes and that high-yield graphene growth can take place in a

single step on a variety of surfaces. Please refer to our paper and Chen-Chih's thesis for details [14, 207].

In the following subsections, the microwave PECVD method developed by other group members will be briefly introduced, which is followed by characterizations of the sample quality. Finally, theoretical simulations of the Moiré patterns and their comparison with experimental STM images are discussed.

5.2.1 Single-step deposition of high-mobility graphene at reduced temperatures

We have developed a new growth method based on MW-PECVD under no active heating to the substrates. This new method has been shown to reproducibly achieve, in one step, high-mobility large-sheet graphene samples that are nearly strain-free[207].

The PECVD setup is shown in Figure 5.7 (a). The growth substrates were polycrystalline copper (Cu) sheets and single crystals. The copper substrate was placed inside a quartz tube within a plasma cavity. Hydrogen-methane plasma was generated and passed through the plasma cavity. Cyano radicals in the plasma first removed the native Cu oxide on the surface of Cu. After Cu is smoothly etched, graphene growth was found to nucleate from arrays of well-aligned hexagonal domains and eventually coalesced into a large sheet of $\sim 1 \text{ cm}^2$, as schematically shown in the top right plot of Figure 5.7 (a) and further exemplified by the SEM images shown in Figure 5.7 (b).

To investigate the quality of the samples, we performed Raman spectroscopic studies on the PECVD-grown graphene, which revealed spectral characteristics of high-quality single-layer graphene (SLG). The magnitude of strain could also be estimated from both Raman spectroscopy and scanning tunneling microscopy (STM). The biaxial strain in the PECVD-graphene on Cu foil was determined by the Raman frequency shifts, which indicated that our PECVD-grown SLG samples were nearly strain-free with an average of 0.07% strain. This finding was in sharp contrast to the significant strain found in thermal CVD-grown graphene. Thermal CVD methods required growth of graphene at $\sim 1000 \text{ }^\circ\text{C}$

and then cooled down to room temperature. The cooling process caused the copper substrate to shrink while the CVD-grown graphene sheet to expand due to the negative thermal contraction coefficient of graphene, leading to lots of wrinkles on graphene and therefore, significant strain. In contrast, our PECVD grown graphene was formed at nearly room temperature, and so could prevent the problem of thermal contraction of the substrate, thus resulting in nearly strain-free samples with very high quality.

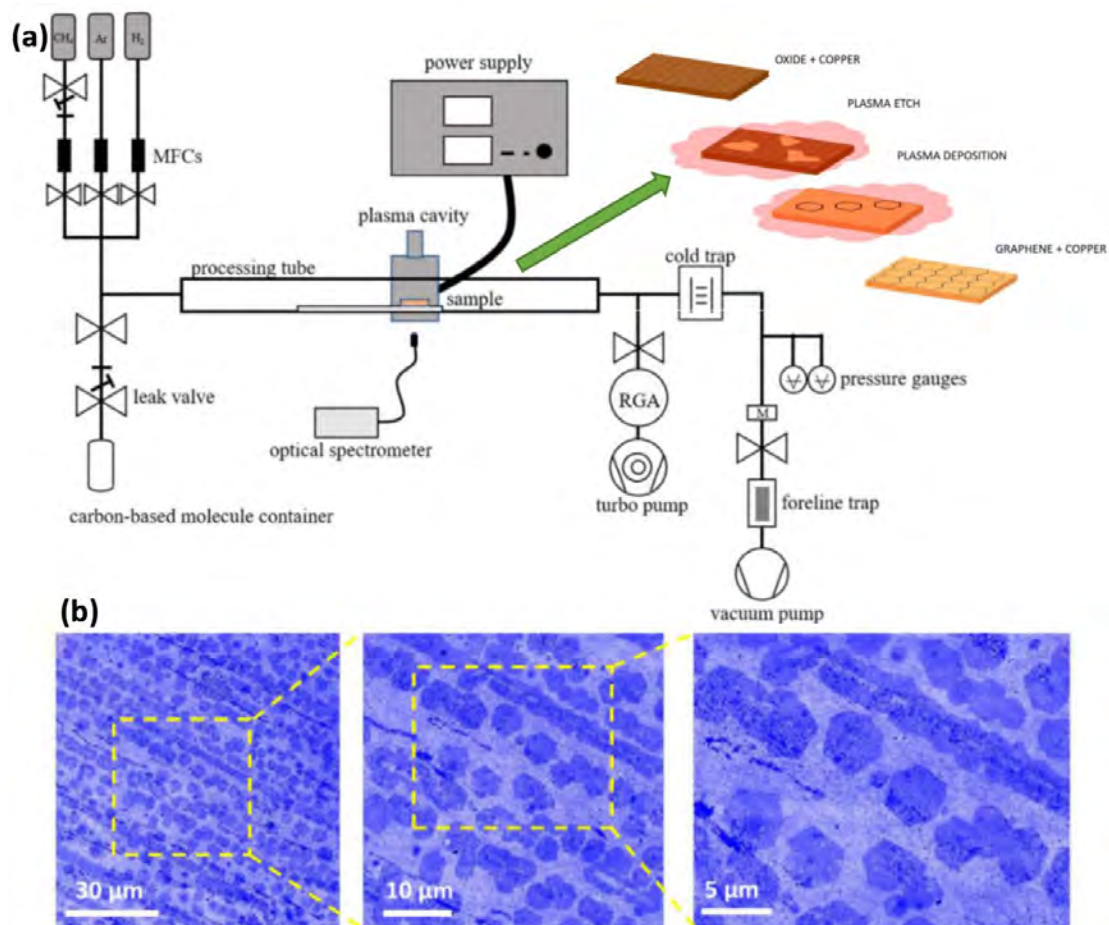


Figure 5.7: (a) A schematic of the PECVD setup for the synthesis of graphene sheets without active heating. The top right plot shows how the graphene is grown. (b) False-color SEM images of graphene grown for excessive time and transferred to single-crystalline sapphire, with increasing magnification from left to right, showing well-aligned, hexagonal adlayer graphene domains (dark) on the bottom SLG (light), which illustrate how the hexagonal grains nucleated along parallel lines of the copper foil coalesce into a single sheet of graphene. [14, 207]

5.2.2 STM imaging of PECVD grown graphene

STM imaging provides a direct way to examine the quality of PECVD grown graphene with atomic resolution. If a multilayer graphene flake appears, it will show up through stepwise jumps on the height profile. We can even compare the positions of each atom with the ideal honeycomb lattice of graphene and calculate the strain down to the atomic scale. As shown in Figure 5.8, PECVD grown graphene was nearly strain-free compared to the thermal CVD grown graphene. This result was consistent with the result of Raman spectroscopy. However, due to the far better lateral resolution of STM, it revealed that the strain was significant, narrow, and directional. In contrast, Raman spectroscopic studies averaged over a much larger area ($\sim 1 \mu\text{m}^2$) and so could not provide localized details.

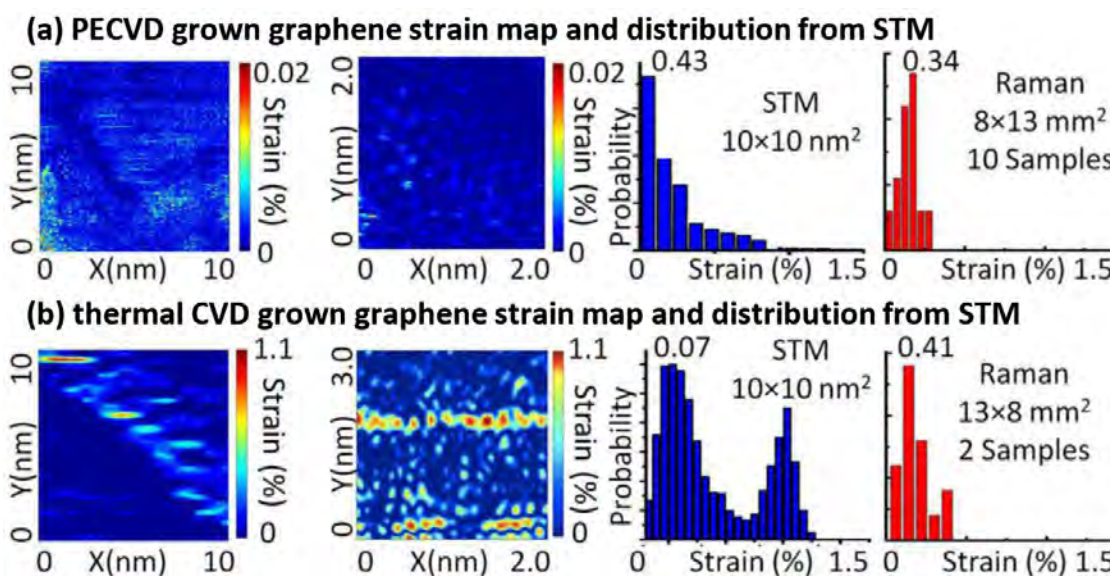


Figure 5.8: Comparison of strain-induced in graphene grown by PECVD and thermal CVD methods. From left to right, strain maps over (10 nm × 10 nm) and (2 nm × 2 nm) areas taken with STM at 77 K, strain histogram derived from the (10 nm × 10 nm) strain map and strain histogram derived from 1 cm² Raman spectroscopy for (a) PECVD-grown graphene and (b) thermal CVD-grown graphene. [14, 207]

The large-area high-quality graphene samples grown with the PECVD method were found to be monolayer without any defects for the entire region of our spectral investigation. If such high-quality single-domain graphene was grown onto another single-domain lattice

substrate like Cu single crystals Moiré pattern should show up. Even if the real-space superlattice size was too big or too vague to observe under STM studies, it would show up readily in the Fourier space.

Our graphene was grown on the different Cu substrates, which included Cu foil, single-crystalline Cu with (100) surface, and single-crystalline Cu with (111) surface. The surface of Cu (100) is a square lattice, while that of Cu (111) was a triangular lattice. Therefore, we expect no Moiré pattern appears on the STM image for graphene grown on Cu foils. At the same time, for graphene grown on Cu (100) and Cu (111), Moiré patterns of different superlattices should show up if we have a large area of high-quality graphene.

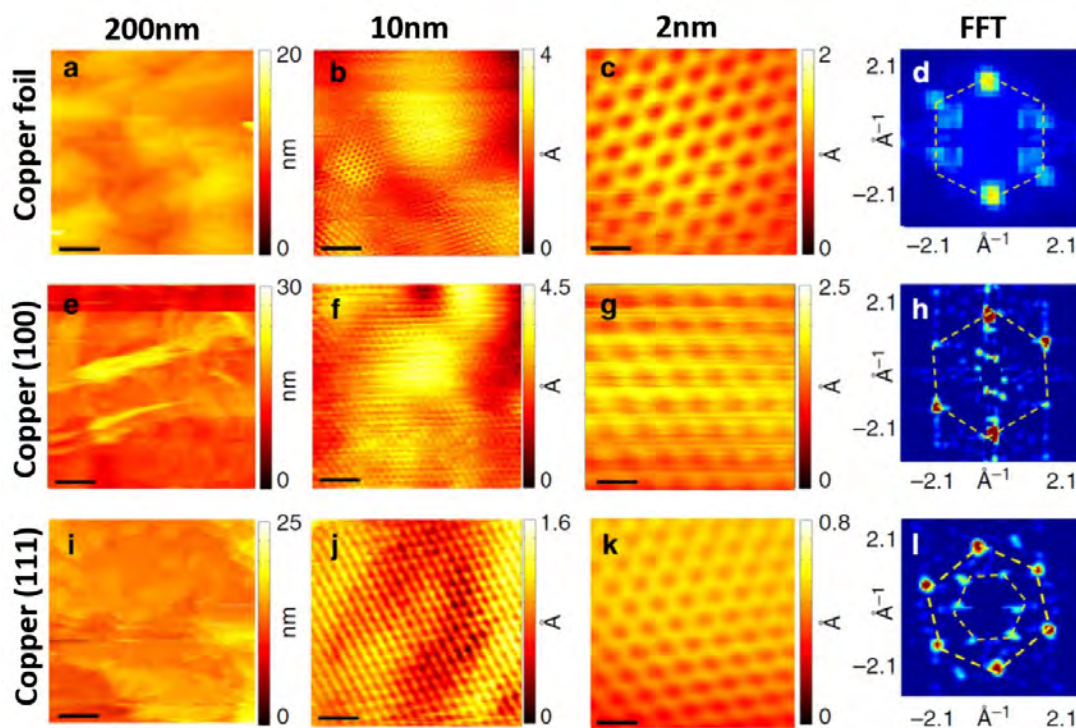


Figure 5.9: Topographies of PECVD-graphene on copper. STM topographies of PECVD graphene were taken at 77 K over ($200 \text{ nm} \times 200 \text{ nm}$), ($10 \text{ nm} \times 10 \text{ nm}$) and ($2 \text{ nm} \times 2 \text{ nm}$) areas (first three columns) and the corresponding Fast Fourier transformation (FFT) of large-area topography (fourth column) for samples grown on (a–d) Cu foil; (e–h) Cu (100); and (i–l) Cu (111). [14, 207]

Several STM topographic images were taken for our PECVD grown graphene samples, as shown in Figure 5.9. While local in spatial dimensions, they all exhibited a perfect honeycomb lattice, as shown in the Fast Fourier Transform (FFT) images. On the other hand, Moiré patterns appeared for both Cu (100) and Cu (111) substrates, yet it was absent for Cu foil substrates. However, notably in the large area map of topography, we did not see distinct real-space Moiré patterns in the graphene samples grown on both single crystalline copper substrates. To make sure that the FFT images we obtained were accurate representations of the graphene samples on different substrates, we need to simulate the Moiré patterns of graphene on single crystal Cu and their FFT. That is, we need to simulate the STM topographic images pixel by pixel and perform FFT to ensure that similar results as experiments could be achieved from simulations.

5.2.3 Simulations for the topography and FFT of 2D single-crystalline graphene on copper substrates

To simulate the FFT of the topography image, we need to first simulate the topography image pixel by pixel in order to find the corresponding functions that can generate the lattice structure that we would like to have.

Triangular lattice:

To generate lattice structures for one dimension is straightforward. We can use a periodic function like sinusoidal function like $\cos(kx)$. For 2D, the sinusoidal function becomes a plane wave. To create a 2D lattice, we need two plane waves (Figure 5.10 (a)), so that intuitively we would choose the function:

$$Tri(x, y) = \cos(\vec{K}_1 \cdot \vec{r}) \cos(\vec{K}_2 \cdot \vec{r}). \quad (5.25)$$

\vec{K}_1 and \vec{K}_2 are reciprocal lattice constants.

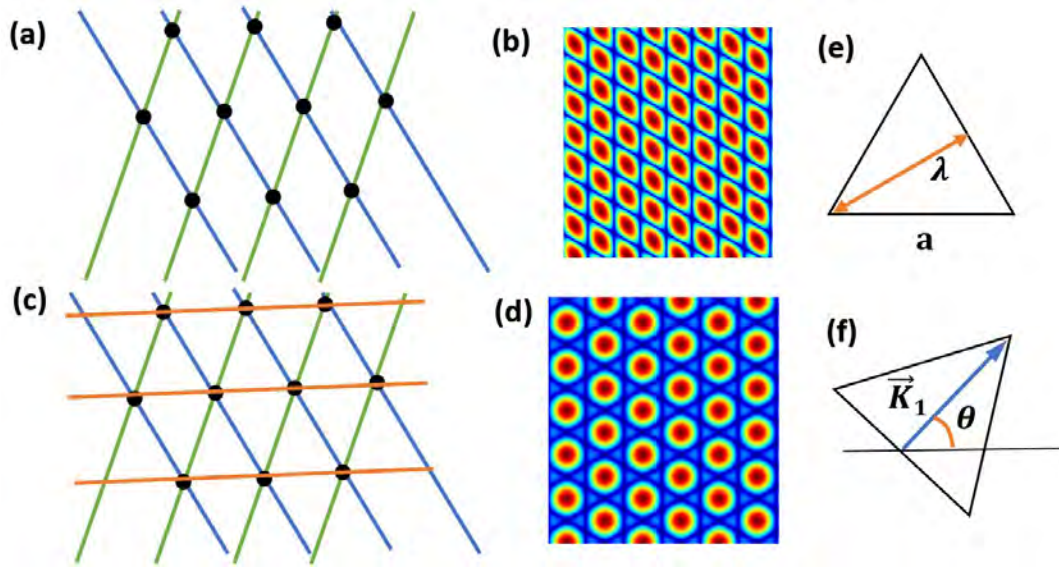


Figure 5.10: (a) Attempt to use two plane waves to create a triangular lattice leads to the structure shown in (b) that lost the C_3 symmetry. (c) Using three plane waves to create a triangular lattice shown in (d) leads to a structure satisfying the C_3 symmetric. (e) Relationship between the lattice constant a and wavelength of plane wave λ . (f) the orientation of lattice can be controlled by the orientation of the wave vector.

Unfortunately, the lattice thus created did not have the C_3 symmetry as it should be for a triangular lattice. As it turns out, we need three plane waves (Figure 5.10 (c)).

$$Tri(x, y) = Tri(\vec{r}) = \cos^2(\vec{K}_1 \cdot \vec{r}) \cos^2(\vec{K}_2 \cdot \vec{r}) \cos^2((\vec{K}_1 - \vec{K}_2) \cdot \vec{r}). \quad (5.26)$$

The lattice generated from Eq. (5.26) indeed revealed the C_3 symmetry (Figure 5.10 (d)). Here the cosine square makes sure that the function value is between 0 and 1. The wavelength will become half of the original value. This will make controlling the size of atoms accessible by taking different order of root. The relationship between the wavelength of plane waves and the lattice constant a is

$$\frac{\lambda}{2} = \lambda' = \frac{\sqrt{3}}{2} a = \frac{2\pi}{2K} \Rightarrow K = \frac{2\pi}{\sqrt{3}a}. \quad (5.27)$$

Therefore, to control the rotation of the lattice, we can simply assign \vec{K} as

$$\begin{cases} \vec{K}_1(\theta) = \frac{2\pi}{\sqrt{3}a}(\cos \theta, \sin \theta) \\ \vec{K}_2(\theta) = \frac{2\pi}{\sqrt{3}a}(\cos(\theta + 60^\circ), \sin(\theta + 60^\circ)). \end{cases} \quad (5.28)$$

The location of the lattice can simply be controlled by shifting the \vec{r} by \vec{R}

$$Tri(\vec{r} - \vec{R}, \vec{K}_1(\theta), \vec{K}_2(\theta)). \quad (5.29)$$

This is the general formula for triangular lattice for any rotation θ , displacement \vec{R} , and lattice constant a .

The size of the triangular lattice (can be deemed as half-height width) can be controlled by taking different order of root of the triangular lattice functions

$$Tri(x, y)^n. \quad (5.30)$$

Because the triangular lattice function is between 0 and 1, for $n > 1$, atoms displayed in the lattice will become smaller or sharper with increasing n . On the other hand, for $0 < n < 1$, atoms displayed will become larger with decreasing n . However, as shown in Figure 5.11, larger order of root of function hugely amplifies the small value of the function and thus amplifies the small feature we do not want to see. In Figure 5.11, the only function with $n = 1/2$ shows a perfect triangular FFT. For $n = 1/6$, the FFT becomes hexagons mixed with triangles. For $n = 1/16$, the lattice points along the three straight lines are amplified.

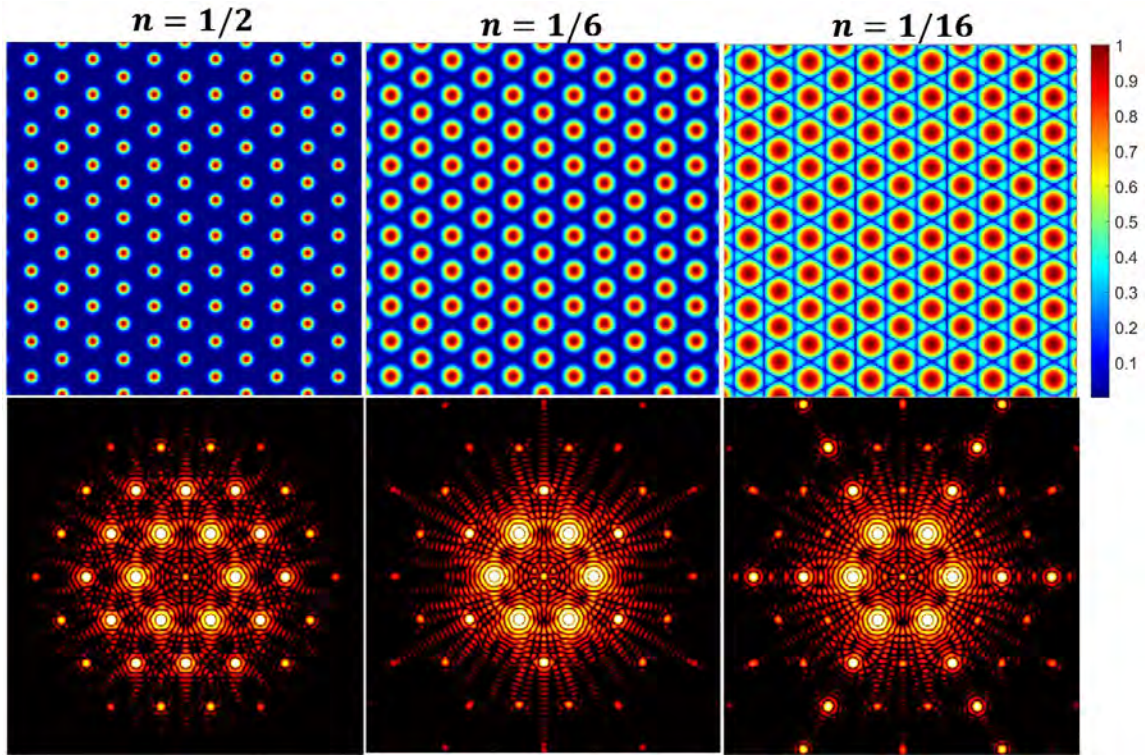


Figure 5.11: Triangular lattices and the corresponding FFTs generated from the functions shown in Eqs. (5.28) – (5.30). First row: triangular function with different exponent n . For $n > 0$, if n is smaller, the size of the lattice point is bigger. This helps us control the size of the atoms. Second row: The corresponding FFTs for the lattice structures shown in the first row.

With the approach outlined above, no matter how big the atoms may be, they will never touch each other. However, to form bonding between atoms like atomically resolved images of STM, we need to make atoms overlap. To do this, we can combine different triangular lattices to form a denser triangular lattice. Given that the size of a real lattice is constant, a denser simulated lattice will correspond to an effectively larger size when we scale the denser lattice back to the real lattice constant, as shown in Figure 5.12. This construction is effectively like putting more atoms into the basis of a unit cell. For a doubly dense lattice, we have put 3 more lattices inside the original lattice. Assume the basis primitive vector \mathbf{d}

$$\mathbf{d}_1 = \frac{\mathbf{a}}{2}(-\sin \theta, \cos \theta) \quad \mathbf{d}_2 = \frac{\mathbf{a}}{2}(\cos(\theta + 30^\circ), \sin(\theta + 30^\circ)). \quad (5.31)$$

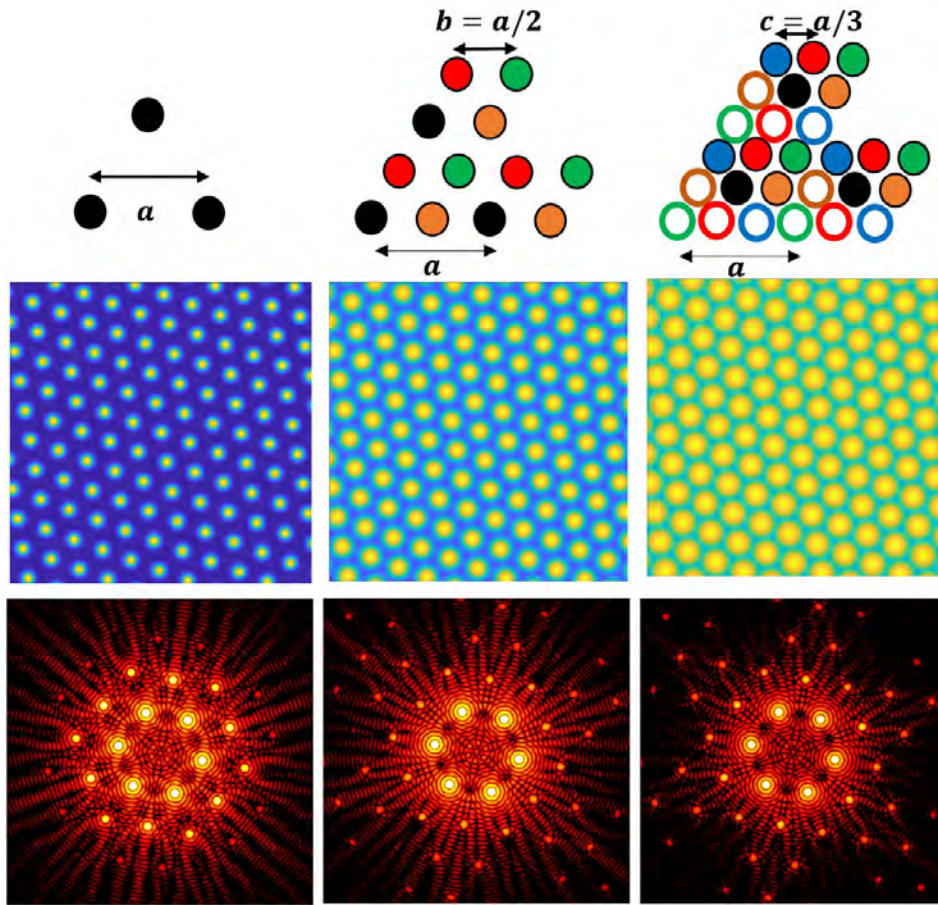


Figure 5.12: Illustration of the scheme to enlarge the size of atoms in a triangular lattice by making the effective lattice denser. **First row** from left to right: single lattice, doubly dense lattice, triply dense lattice. For doubly dense lattice, the lattice constant $b = a/2$; for triply dense lattice, the lattice constant $c = a/3$. **Second row:** Effective lattice images by scaling b and c back to a . The size of atoms is enlarged and begins to overlap to nearby atoms. **Third row:** The FFTs corresponding to the lattices shown in the second row. Even though doubly dense and triply dense lattice shows some large scale patterns, triangular lattice points remain dominant.

The doubly dense function becomes

$$Tri_2(\theta) = \text{Max} \left(\text{Tri}(\vec{r}, \theta), \text{Tri}(\vec{r} - \vec{d}_1, \theta), \text{Tri}(\vec{r} - \vec{d}_2, \theta), \text{Tri}(\vec{r} - \vec{d}_1 - \vec{d}_2, \theta) \right). \quad (5.32)$$

Notice that we choose the max of all four functions rather than adding them together. This helps us eliminate unwanted small value features and makes the FFT image look clean.

Square lattice:

A square lattice structure is easier to construct. We just need a product of two sinusoidal functions with two perpendicular wave vectors.

$$Squ(x, y) = Squ(\vec{r}) = \cos^4(\vec{K}_1 \cdot \vec{r}) \cos^4(\vec{K}_2 \cdot \vec{r}). \quad (5.33)$$

Here we use the fourth-order power to enhance the lattice points.

$$\begin{cases} \vec{K}_1(\theta) = \frac{\pi}{a} (\cos \theta, \sin \theta) \\ \vec{K}_2(\theta) = \frac{\pi}{a} (\cos(\theta + 90^\circ), \sin(\theta + 90^\circ)) \\ \quad = \frac{\pi}{a} (-\sin \theta, \cos \theta). \end{cases} \quad (5.34)$$

The size of atoms is also controlled by $Squ(x, y)^n$. Again, even though we can make lattice points bigger, its size never exceeds the lattice constant. Therefore, to create overlaps between neighboring atoms, we have to add two square lattices together to make it denser. The simplest choice is to put the lattice point into the center of the original lattice by choose basis primitive vector \mathbf{d}_1

$$\mathbf{d}_1 = \frac{a}{2} (\cos \theta - \sin \theta, \sin \theta + \cos \theta). \quad (5.35)$$

This will generate a doubly dense square lattice or simply an FCC lattice. This choice is convenient because we can simply use the Cu FCC lattice constant directly without changing the formula (Figure 5.13). The doubly dense square lattice function becomes

$$Squ_2(\theta) = Max(Squ(\vec{r}, \theta), Squ(\vec{r} - \vec{d}_1, \theta)). \quad (5.36)$$

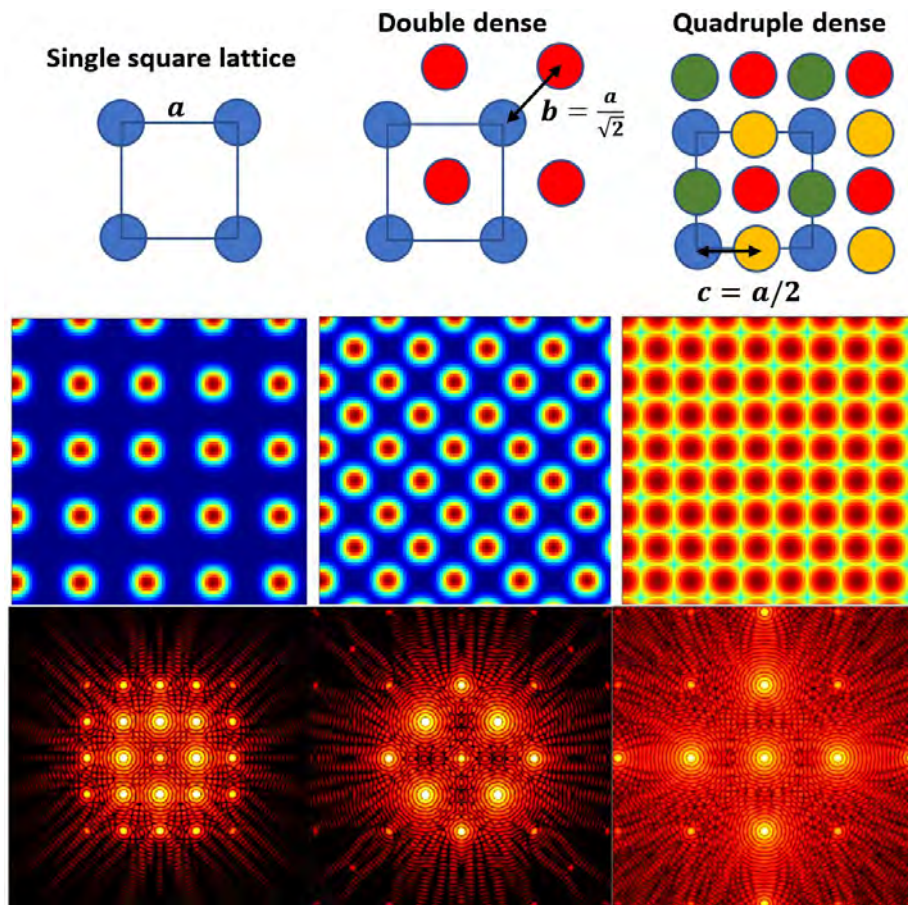


Figure 5.13: Illustration of the scheme to enlarge the size of atoms in a square lattice by making the effective lattice denser. **First row** from left to right: single square lattice, doubly dense lattice, quadruple dense lattice. For doubly dense lattice, the lattice constant $b = a/\sqrt{2}$; for quadruple dense lattice, the lattice constant $c = a/2$. **Second row:** Effective lattice images by scaling b and c back to a . **Third row:** The FFTs corresponding to the lattices shown in the second row. The reciprocal lattice size is bigger when the spatial lattice is denser.

From simulations of the triangular lattices and square lattices, we found that lattice points only contribute to the FFT when the size of lattice points is small. If the lattice points overlap to each other too much, the minimum between lattice points will contribute more to the FFT signals. That is, the lattice points themselves become a background.

Hexagonal lattice:

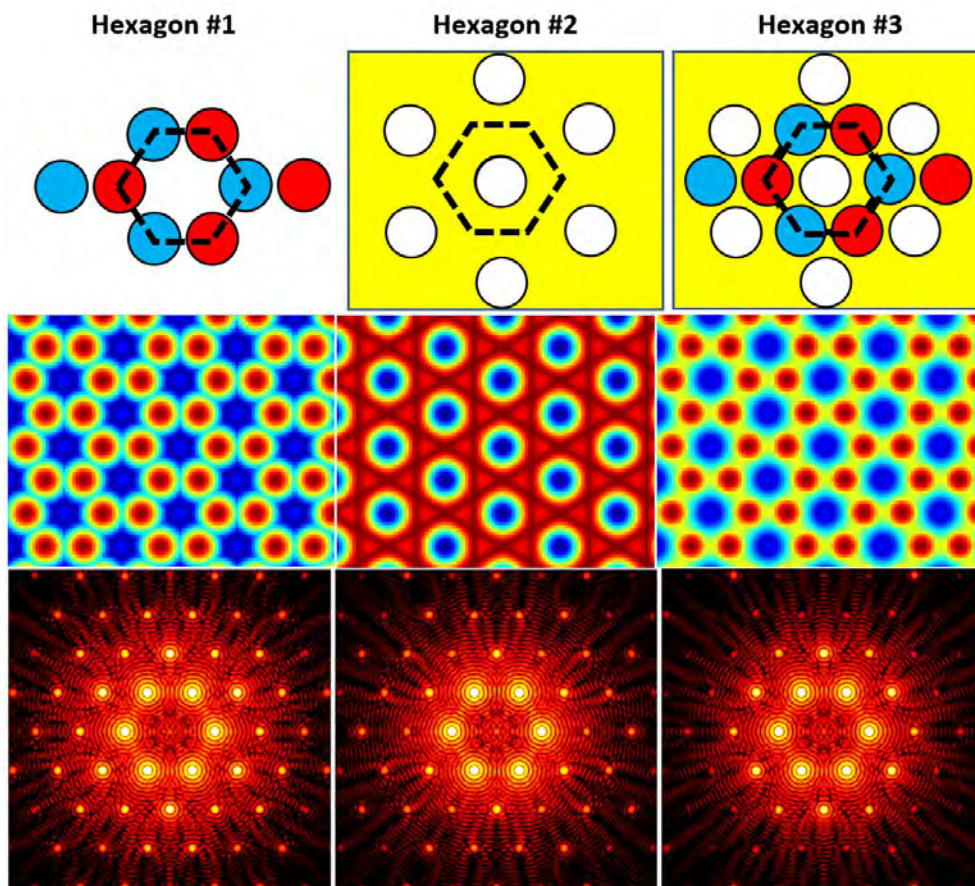


Figure 5.14: Illustration of different approaches to construct a hexagonal lattice. **First row:** a schematic explanation for the method used to generate hexagon #1, hexagon #2, and hexagon #3. Hexagon #1 combines two triangular lattices. Hexagon #2 uses a constant background with the deduction of a triangular lattice. Hexagon #3 combines hexagons #1 and #2, so it has both bond-like and atom-like hexagonal structures. **Second row:** Lattice images based on the methods of construction shown in the first row. **Third row:** FFTs of the lattice images shown in the second row.

There are two ways to construct a hexagonal lattice. The first is to combine two triangular lattices together, which gives rise to the atom-like hexagonal lattice (hexagon #1 in Figure 5.14). The second is to use a constant background minus triangular lattice, which results in a bond-like hexagonal lattice (hexagon #2 in Figure 5.14). Alternatively, we can simply combine both methods to produce hexagons shown as hexagon #3 in Figure 5.14. Although using a triangular lattice minus another triangular lattice with greater lattice constant can

also generate a hexagonal lattice, this approach will make lattice points more dilute and deviate from the real situation. In the end, hexagon #3 is closer to the real STM topography of graphene, so we will use it for our simulations.

5.2.4 Simulations for graphene on single crystalline copper substrate

To simulate STM images of graphene on single-crystalline copper substrates, we need to consider two important factors. First, we need to know the crystalline structures and lattice constants of both graphene and copper. Second, we cannot simply add the structural contributions from graphene and copper together. Rather, we must take into consideration the STM tunneling effect.

Graphene, as introduced at the beginning of Chapter 5, has a lattice constant 246.4 pm.

Copper is face-center-cubic (FCC), with a lattice constant $a = 361.49$ pm. [208] Along the (111) surface, it shows a triangular lattice structure with a lattice constant $c = \frac{a}{\sqrt{2}} = 255.61$ pm. Along the (100) surface, it shows a square lattice structure with a lattice constant $b = \frac{a}{\sqrt{2}} = 255.61$ pm. (Figure 5.15)

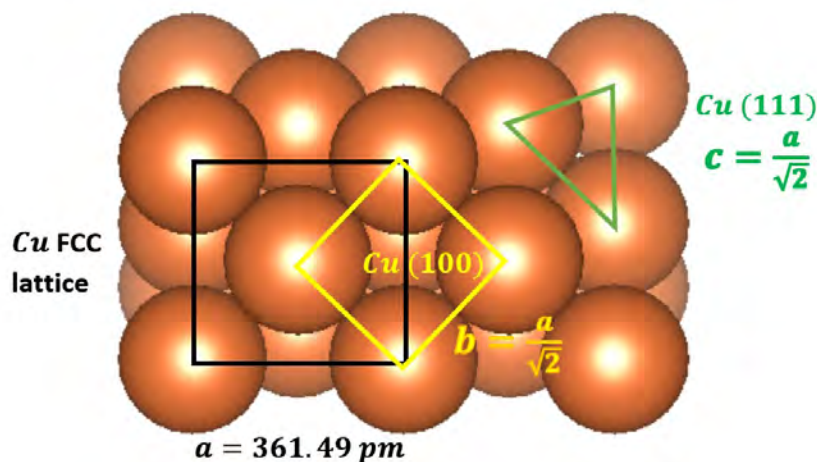


Figure 5.15: Lattice structure of Cu. Along the (111) direction, the surface reveals a triangular lattice structure with a lattice constant $c = a/\sqrt{2}$. Along the (100) direction, the surface exhibits a square lattice structure with a lattice constant $c = a/\sqrt{2}$ or an FCC lattice with a lattice constant a .

Single crystalline Cu (111) surface is a triangular lattice with a lattice constant quite close to that of graphene, and it is deemed as a perfect substrate to grow graphene. On the other hand, the mismatch between Cu (100) surface and graphene is more significant, let alone the copper foil. However, it is clear that all of the aforementioned Cu substrates can grow graphene, which is not surprising considering that graphene is a van der Waal material. If there may be any discernible bonding effect between graphene and the Cu substrate, we should be able to resolve the effect from the Moiré patterns and the FFT images.

Model to incorporate the effect of the underlying layer

Although simply overlapping two layers of different lattices together can provide an accurate account for the size of the Moiré superlattices, such a linear superposition is not what the STM images reveal. This is because the tunneling current from the STM tip decays with the distance exponentially, and so the contribution from the bottom layer is always less than the top layer. Mathematically speaking, if a layer of a lattice superposes to another layer, the FFT of the combined lattice is also the superposition of the FFTs of both lattices. The bottom layer must interfere with the top layer rather than behaves independently. Otherwise, no new interference pattern appears in the experimental FFT. There are two ways to construct a realistic Moiré superlattice. The first approach is a “filling-the-hole” mode:

$$\text{Moire1} = \text{Max}(Z_{top}, A \times Z_{bottom}), 0 \leq A \leq 1. \quad (5.37)$$

Here Z_{top} denotes the topography (height of atom) of the top layer and Z_{bottom} is the topography of the bottom layer. This model implies that we can see the feature of the bottom layer through the hole at the center of the graphene lattice.

The second approach is the STM decay mode:

$$\text{Moire2} = Z_{top} + A \times \exp(-C \times Z_{top}) \times Z_{bottom}. \quad (5.38)$$

The idea is that tunneling current decays exponentially with the distance from the STM tip. Therefore, the contribution from the bottom layer is inversely exponentially proportional to the separation distance of the top layer so that the effect of the top layer is amplified. We can combine both ways too. After some trial and error, Moire2 appears to be a better method to amplify the features of the superlattice.

5.2.5 Graphene on copper (111) surface

To simulate graphene on Cu (111) surface, we use hexagon #3 (Figure 5.14) with a lattice constant 246.4 pm for graphene and a doubly dense triangular lattice with a lattice constant 255.61 pm for Cu (111). Next, we must figure out how to place the graphene layer on top of the Cu (111) surface.

If we assume that the graphene forms bonding with the underlying Cu through epitaxial growth, then the bond lengths between carbon atoms in graphene may become approximately the same as the lattice constant of Cu to match the Cu lattice. In this case, some carbon atoms of graphene would be sitting right above some of the copper atoms. On the other hand, if we assume that graphene will maintain its lattice constant and will only have van der Waals interaction with copper, then the resulting Moiré pattern will be more random. Since we only have limited STM imaging studies for graphene on Cu (111), we may not be able to differentiate the two scenarios. Nonetheless, it is still worth doing simulations so that the results can be compared with experimental data.

Assuming graphene grows on copper through bonding with Cu atoms and maintains the bonding effect even after growth, the lattice constant of graphene may become larger to better match the lattice constant of Cu. Hence, the structure is similar to the AB stacking of graphene, with one atom on the basis of unit cell sit right at the top of the Cu atom while another one sits in the minimum between Cu atoms (Figure 5.16 first row left). In this case, no Moiré pattern appears, and the FFT image reveals clean hexagons without additional features within the hexagons (Figure 5.16 third row left).

Alternatively, if graphene tends to grow on the local minimum between Cu atoms, we will see the effect of the same lattice constant of graphene and Cu too. In contrast, all the atoms of graphene are located in the minimum between Cu atoms, or Cu atoms are under the holes of the hexagons of graphene. No Moiré pattern shows up, but lattice points in the FFT is weaker (Figure 5.16 third row right).

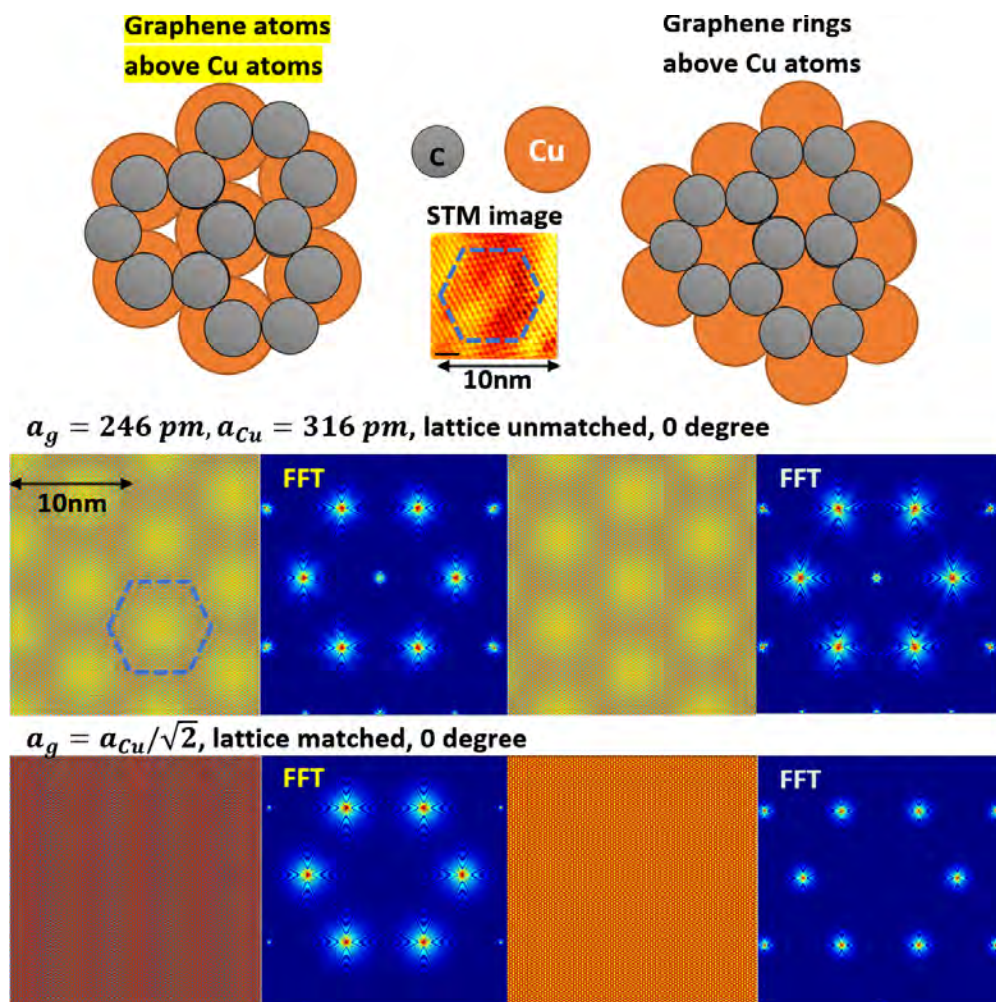


Figure 5.16: Moiré patterns of graphene on copper (111) with different stacking. Left side: on-site stacking. Right side: off-site stacking. Combined lattices over a (20 nm × 20 nm) area and their FFTs are simulated for mismatched lattice (2nd row) and matched lattice (3rd row) with no rotation. Moiré patterns appear in the mismatch lattices while disappearing in the matched lattices.

Since the sp^2 bond of graphene is very strong, it is generally difficult to stretch the honeycomb cell of graphene to match the underlying substrate. If the lattice constant of graphene does not match that of Cu (111), Moiré superlattices are expected to show up at any angle θ between the graphene and Cu layers. In the case of $\theta = 0$, we should have the largest superlattice size in real space and the smallest hexagon in the center of the big hexagon in the FFT. With increasing twist angle θ , the size of Moiré superlattices decreases whereas that of the inner hexagon in the FFT increases and also rotates relative to the outer hexagon. On the other hand, the specific local stacking of graphene on Cu (111) does not affect the Moiré superlattices because varying stacking can be found at different locations. As shown in the second row of Figure 5.16, different stacking simply leads to linear translations of the same superlattices without changing either the size or the symmetry.

Next, we want to investigate the feasibility of generating images similar to empirical STM results from simulations. Based on what we have outlined above for the simulation, two issues are noteworthy: First, since the size of Cu atoms is much bigger than that of carbon atoms, Moiré patterns would not be apparent without increasing the color contrast of the superlattice structure. Therefore, under realistic STM scans, we probably can only resolve the graphene honeycomb lattice rather than some superlattice patterns in real space. Second, Bragg spots associated with the superlattice structure can appear in the FFT inside the hexagon reciprocal lattice of graphene because FFT is obtained by summing the signals over a large spatial area. So studies of the FFT are a powerful way to verify the existence of Moiré superlattices.

Therefore, we can vary the twist angle between graphene and Cu in our simulations and compare their resulting FFTs with what we obtained from the STM study. If a similar pattern appears, it may explain the origin of the Moiré pattern observed in the FFT image of the STM study. In Figure 5.17, the Moiré patterns and corresponding FFT images are shown for different twist angles, stacking, and lattice constants. Due to the 6-fold symmetry of the triangular lattice, we only have to investigate the twist angles θ between 0 and 30° . The resolution is 512 pixels, consistent with our STM images.

From Figure 5.17, the only discernible lattice mismatch effect only occurs at $\theta = 0$ for both the real space and FFT images. For mismatched lattice constant, stacking is not important because we found the same FFT images and the same size of the Moiré superlattice for a given twist angle θ .

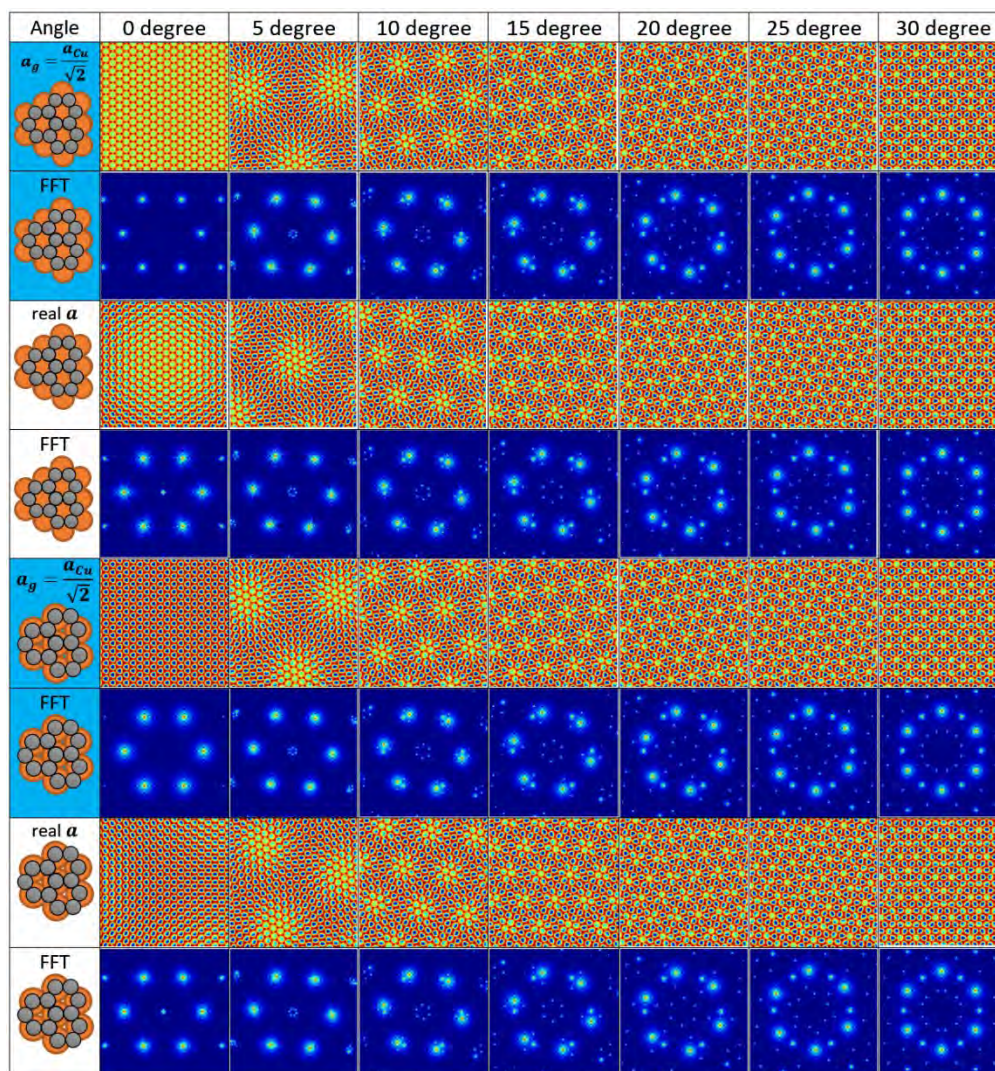


Figure 5.17: Comparison of real-space Moiré patterns and the corresponding FFT images from simulations for different twist angles, stacking, and lattice constants. The size of all topographic images is (4 nm × 4 nm). Here the graphene lattice constant is given by either the realistic value or the lattice-match assumption $a_g = a_{Cu}/\sqrt{2}$.

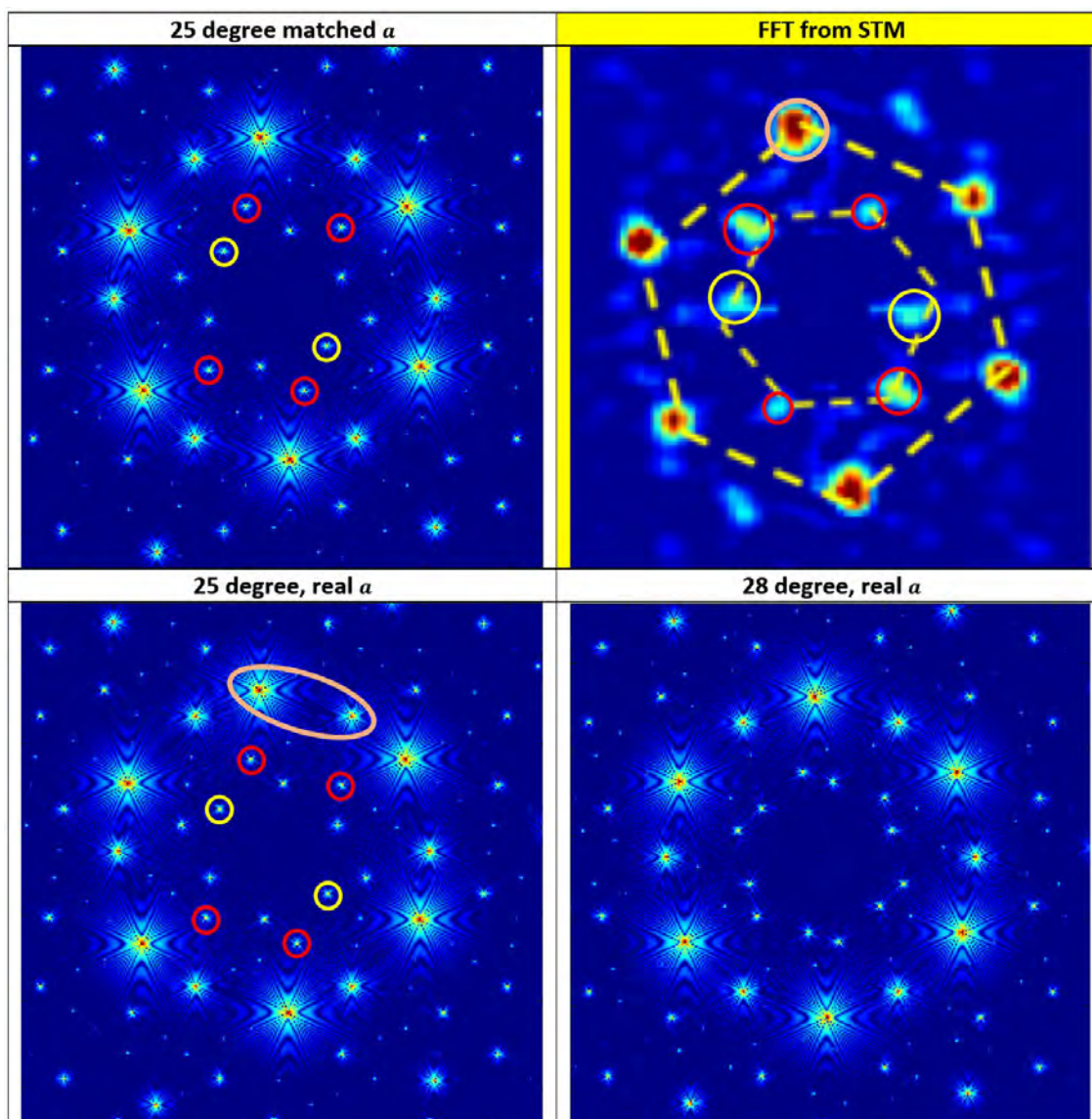


Figure 5.18: FFT simulation results for candidate models of graphene on Cu (111) that account for the real FFT from STM studies. The yellow circles reveal the critical differences between the assumption of a matched lattice constant to copper and the real lattice constant of graphene. Simulations using the real lattice constant of graphene are more consistent with the experimental STM data than that using a matched lattice constant. The center of the orange oval for the 25 degrees image is also consistent with the real STM image

Comparing with the FFT image from STM studies, we found that the FFT of graphene on Cu (111) with a twist angle of $\theta = 25^\circ$ appears to exhibit consistent features. In general, the simulated results contain more detailed features than the experimental FFT image due to

limited experimental resolution. These comparisons reveal that the critical differences appear between the FFT obtained by using a matched lattice constant to copper and that obtained by using a real graphene lattice constant, as shown by the yellow circles in Figure 5.18. Specifically, the yellow circles in the FFT obtained by using a real graphene lattice constant are consistent with the FFT of STM image, while those in the FFT obtained by using the matched lattice to copper do not agree with experimental results. This finding suggests that graphene grown on Cu (111) still maintains its bond length and that the interaction between graphene and copper substrate is consistent with the van der Waals force.

Despite the reasonable agreement between simulations and experimental data, one unresolved issue is that there are always two sets of Bragg spots forming the outer hexagon found in the simulation, while in the FFT of STM data, only one set of Bragg spots is found in the formation of the outer hexagon. One possible explanation may be due to the fact that, in our simulation function, we have only added two functions of the atomic layers together without trying to constrain them by a specific relationship. With an additional constraint, the two sets of Bragg spots forming the outer hexagon may become merged into one set of Bragg spots for the outer hexagon. In this context, it is interesting to note that the center location of the orange oval in the FFT simulation with $\theta = 25^\circ$ is actually consistent with the orange circle in the FFT of STM data.

Another worth noting point is that the FFT simulation with $\theta = 28^\circ$ reveals a perfect inner hexagon, which at first glance seems to be in better agreement with the FFT of STM data. However, closer inspection of the STM data indicates that the Bragg spots inside the outer hexagon do not agree with a perfect inner hexagon. Instead, they are consistent with the features shown by the FFT simulation with $\theta = 25^\circ$ and the real graphene lattice constant. Therefore, we believe that the correct twist angle between graphene and Cu (111) is 25° .

Summary of the simulations of graphene on Cu (111) surface

Through the simulations outlined above, we have successfully identified the twist angle between the monolayer graphene and its copper (111) substrate after comparing it to the simulation results with the FFT from STM studies. Additionally, we have concluded that the lattice constants of graphene and copper do not change under the PECVD growth process.

We further note that the appearance of a well-defined twist angle between the graphene and Cu (111) surface suggests that graphene has a preferred growth orientation relative to the substrate. A Moiré pattern with $\theta = 25^\circ$ corresponds to a small superlattice constant, which seems to imply that the PECVD graphene growth on copper prefers a smaller size of Moiré superlattices. Further investigations of the correlation between the preferred growth orientation and the PECVD growth conditions/substrates may be an interesting subject to pursue if more STM studies can be taken on different graphene samples and compared with simulations.

5.2.6 Graphene on copper (100) surface

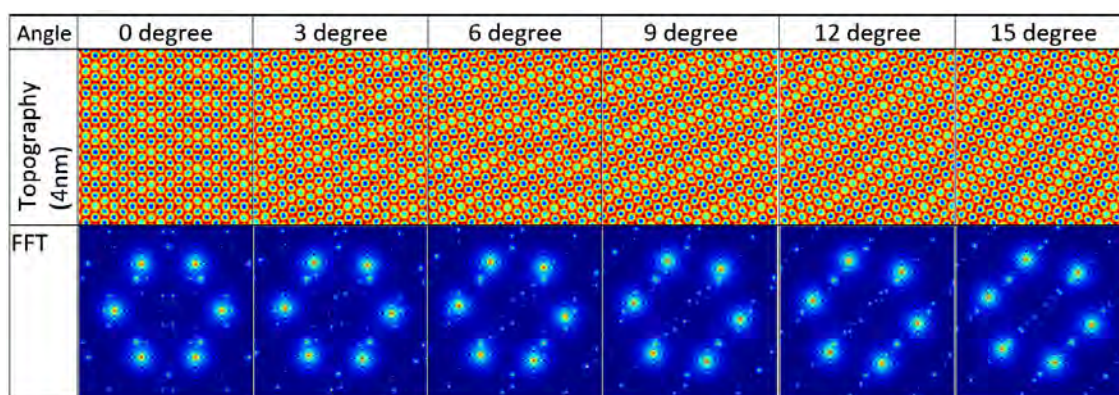


Figure 5.19: Real-space Moiré patterns and the corresponding FFTs of graphene on a Cu (100) surface with a twist angle from $\theta = 0$ to 15° .

Graphene grown on copper (100) is relatively easier to simulate. Given that Cu (100) surface corresponds to a square lattice, it does not match the honeycomb lattice of graphene

at any lattice constant. We can treat graphene on Cu (100) substrate as a simple 2D van der Waals material with any stacking on copper and expect to get the same FFT. Additionally, we only have to simulate the angular range of $\frac{90-60}{2} = 15$ degrees to cover all of the possible patterns, as exemplified in Figure 5.19.

For graphene on Cu (100), the Moiré pattern is generally more challenging to recognize. At $\theta = 0$, the Moiré pattern still looks like a lattice. On the other hand, for $\theta = 15^\circ$, the Moiré pattern becomes parallel lines. If we compare them with the FFT from STM, we find some similarities for $\theta = 3^\circ \sim 5^\circ$. As shown in Figure 5.20, at a twist angle of $\theta = 4^\circ$, the simulation shows similar features inside the outer hexagon as those found in the FFT of the STM image (*e.g.*, features indicated by the yellow circles in both images of Figure 5.20). However, some other features are not consistent between the simulations and the real FFT image. For instance, the real FFT image is not consistent with a perfect 6-fold symmetry for graphene because two of the Bragg spots forming the outer hexagon exhibit weaker intensities than the other four. Moreover, the four bright Bragg spots do not exhibit the 4-fold symmetry of Cu (100) either.

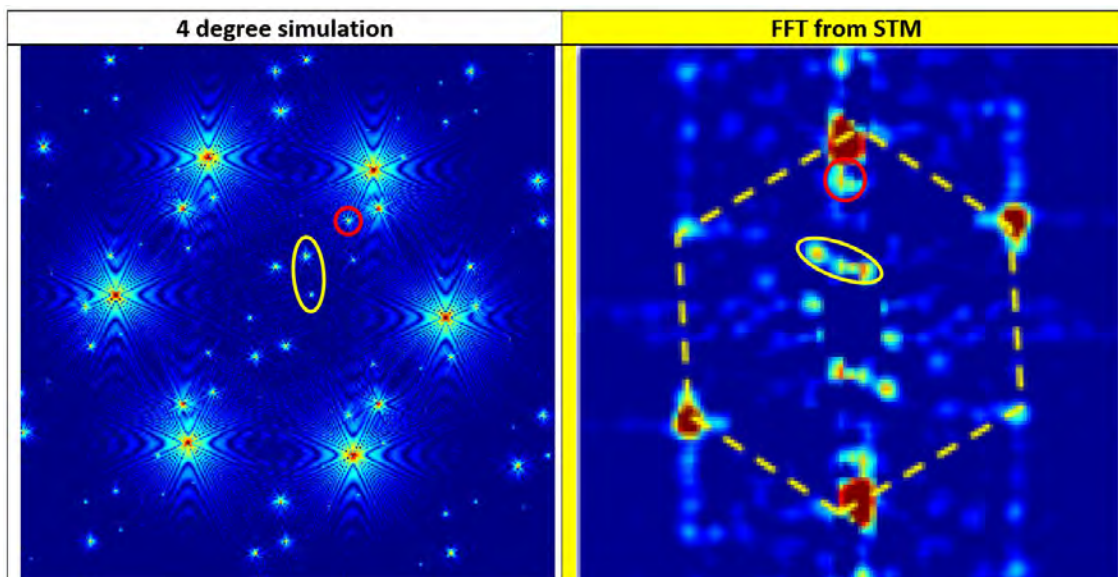


Figure 5.20: Simulations of the FFT of graphene on Cu (100) at a twist angle of $\theta = 4^\circ$ vs. the FFT obtained from STM studies of graphene on Cu (100).

5.2.7 Summary of PECVD graphene growth on Cu substrates

For graphene grown on single crystalline copper substrates, Moiré patterns are expected to appear. However, from STM topographic studies, we find that signals of the real space Moiré patterns are generally too weak to detect. On the other hand, FFTs of the real space topographic images are shown to reveal clear Moiré superlattices in the reciprocal space in addition to the graphene reciprocal lattice. The appearance of Moiré patterns in our STM studies is also a testament to the high quality of our PECVD-grown monolayer graphene.

In our simulations of the Moiré patterns in the reciprocal space, a critical task is to construct the spectral features inside the outer hexagon to be consistent with those found in the real FFT. By creating functions to represent triangular and square lattices and by adding them together with proper spectral weights due to the tunneling effect, we have been able to successfully construct reciprocal space Moiré superlattices that are largely consistent with the experimental FFT images.

Despite the overall agreement, we note that our simulations generally produce more features in the FFTs than the experimental FFT images from STM measurements. There are two factors that contribute to such discrepancy in addition to limited experimental resolution. First, the lattices generated from our simulations are not precisely the same as the real lattices. Second, we have oversimplified the contributions to the tunneling current from the bottom layers. However, even with our relatively simple model, we have been able to derive an in-depth understanding of the interfacial properties of graphene on Cu single crystals. Specifically, we find that the graphene lattice constant remains invariant after PECVD growth, and the interaction between graphene and its underlying Cu substrate is consistent with the van der Waals force. Additionally, preferred growth orientations are found for different single crystalline copper surfaces. Overall, the apparent Moiré patterns in the FFTs of our monolayer graphene samples on copper indicate atomic flatness and long-range order of the PECVD-grown graphene.

5.3 Direct growth of mm-size twisted bilayer graphene by plasma-enhanced chemical vapor deposition

Our room temperature PECVD growth techniques are not restricted to the synthesis of high-quality large-area monolayer graphene sheets on copper. By tuning the growth parameters, our research group has shown successful growth of quasi-one-dimensional graphene nanostripes as well as selective growth of multilayer graphene on metallic nanostructures and dielectric substrates.[107, 192, 207, 209]

The recent discovery of unconventional superconductivity in twisted bilayer graphene at a “magic angle” has attracted much attention and stimulated intense research. The most common approach to prepare bilayer graphene with a certain twist angle involves manual alignments of two mechanically exfoliated monolayer graphene flakes. This approach has numerous difficulties: First, the process is neither scalable nor reproducible and is extremely low-yield. Second, the process of transferring one monolayer of graphene to the other monolayer could introduce contaminants and damages to the graphene layer, thereby altering the properties. Third, the twist angle cannot be reproduced easily with precision.

Given all the aforementioned challenges, it would be highly desirable to develop alternative scalable and reproducible approaches to synthesize twisted bilayer graphene with controlled twist angles. Indeed, Yen-Chun Chen in our group took upon the task and successfully developed a new PECVD method to grow single-crystalline hexagonal bilayer graphene (BLG) flakes and mm-size BLG films with the interlayer twist angle controlled by the growth parameters. [206] These samples have been characterized by Raman spectroscopy, scanning electron microscopy (SEM), Kelvin probe force microscopy (KPFM), x-ray photoelectron spectroscopy (XPS), ultraviolet photoelectron spectroscopy (UPS), and STM. The STM characterization of the BLG was carried out by the author.

In the following subsection, a brief description of the PECVD growth setup and conditions is given, which is followed by detailed studies of the STM measurements and simulations

of Moiré patterns from twisted bilayer graphene. More details of the bilayer graphene synthesis can be found in Reference [206].

5.3.1 Experimental setup and growth conditions

The PECVD system consists of a microwave plasma source, a growth chamber, and a gas delivery system. The plasma source (Ophos Instruments Inc.) includes an Evenson cavity and a power supply (MPG-4) that provides an excitation frequency of 2450 MHz. The Evenson cavity matches the size of the growth chamber, which primarily consists of a 1/2-inch quartz tube (with the inner and outer diameters being 10.0 mm and 12.5 mm, respectively) and components for vacuum control. The reactant gas delivery system consists of four mass flow controllers (MFCs) for CH₄, Ar, H₂, and O₂. An extra variable leak valve is placed before the CH₄-MFC for precise control of the partial pressure of CH₄. During the growth process, the pressure of the system is maintained at ~ 25 mTorr. For the PECVD growth substrates, we use 25 μm-thick Cu-foils (Alfa Aesar with purity = 99.9996%). Prior to the graphene synthesis, the Cu-foils are always sonicated in ACE and IPA for 5 minutes then dried by nitrogen gas before inserted into the growth chamber. Several pieces of (1.5 × 0.8) cm² Cu-foils may be first placed on a quartz boat and then introduced into the growth chamber.

Table 5.1 the growth condition for monolayer, bilayer graphene, and twist bilayer graphene. Adapt from supplementary of [206]

Table 5.1	Plasma (W)	P _{CH₄} (torr)	P _{H₂} (torr)	P _{CH₄} / P _{H₂}	Growth Time
MLG	40	1×10 ⁻⁶	1.2×10 ⁻⁵ (~ 2 sccm)	0.1	3 mins
BLG (random)	40	7×10 ⁻⁷	1.6×10 ⁻⁵ (~ 2.5 sccm)	0.04	3 mins
BLG (small-angle distributions)	40	9×10 ⁻⁷	1.75×10 ⁻⁵ (~ 2.7 sccm)	0.05	3 mins

MLG: monolayer graphene BLG: bilayer graphene

The growing parameter is summarized in Table 5.1. By controlling the supply of CH₄ and H₂, we can grow monolayer, AB-stacking bilayer, or twist bilayer graphene, as exemplified by the optical images shown in Figure 5.21.

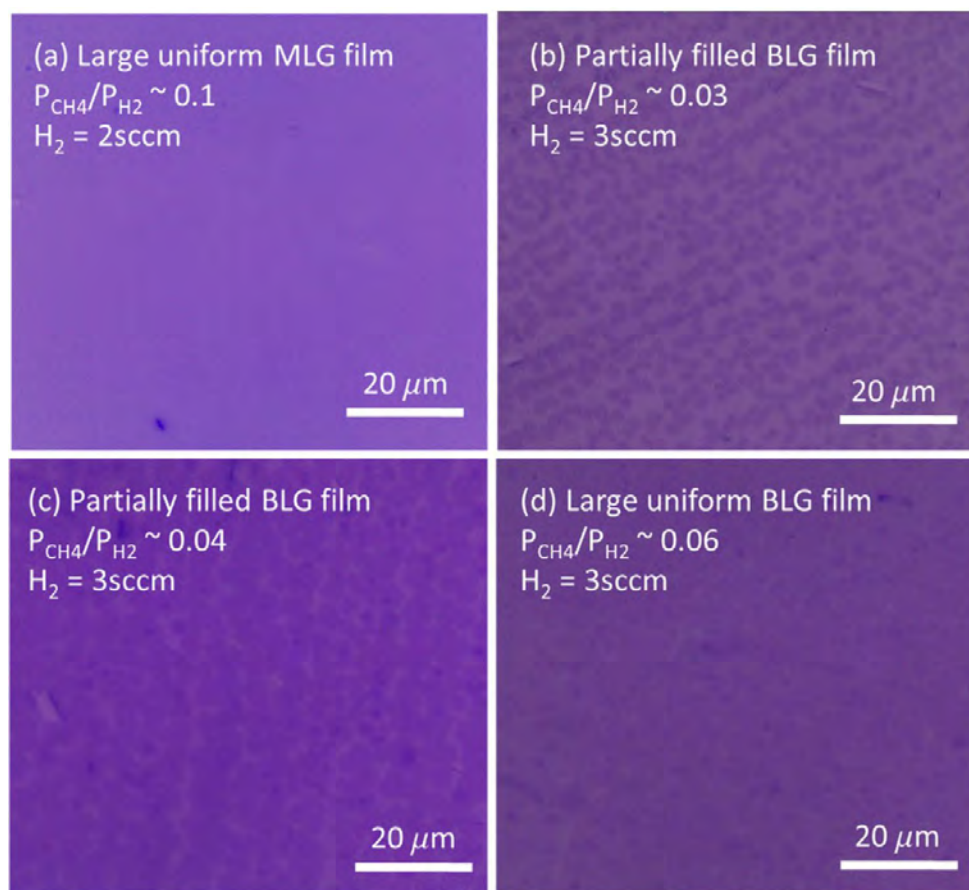


Figure 5.21: Optical images of large monolayer graphene (MLG) and bilayer graphene (BLG) films transferred onto 285 nm-thick SiO₂/Si substrates and grown under different (P_{CH4}/P_{H2}) ratios over the same growth time: **(a)** a large MLG film, **(b)** a partially filled BLG film with smaller coverage under a large MLG, **(c)** a partially filled BLG film with higher coverage under a large MLG, and **(d)** a large uniform BLG film. [206]

5.3.2 STM images for PECVD-grown twisted bilayer graphene

Scanning tunneling microscope is a powerful tool to determine the twist angle of bilayer graphene. From Section 5.2, we have shown that the FFTs of monolayer graphene on polycrystalline copper foils exhibit a perfect hexagon. Therefore, when we consider the FFT of bilayer graphene grown on Cu foils, there is no need to consider the influence from the substrate. Therefore, in this subsection we focus on the consideration of Moiré patterns associated with different twist angles of bilayer graphene.

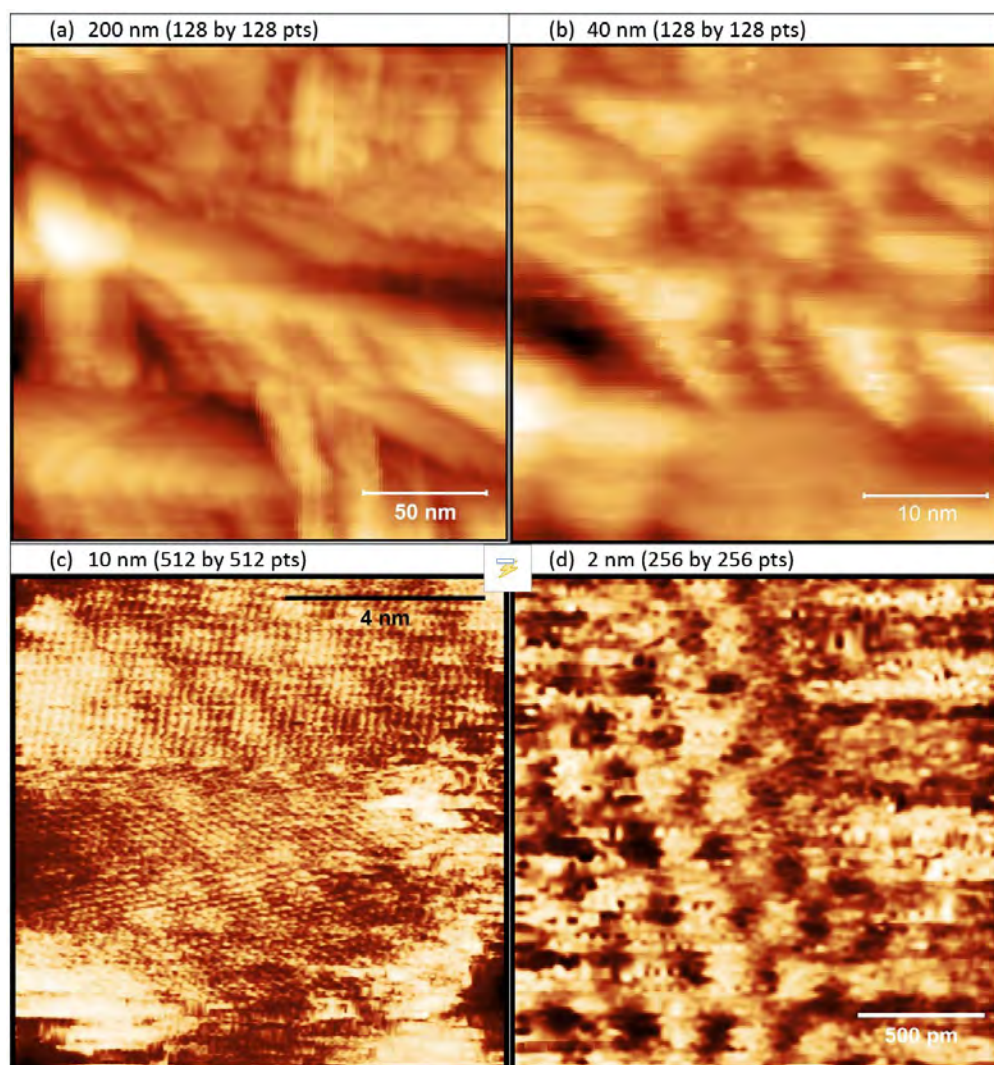


Figure 5.22: STM topographic images of PECVD-grown twisted bilayer graphene for different sizes of areas and spatial resolutions.

Figure 5.22 shows the STM topographic images of a PECVD-grown twisted bilayer graphene sample over different sizes of areas and with different spatial resolutions. For a large-area scan as shown in Figure 5.22 (a) over an area of (200 nm \times 200 nm), the image reveals that the copper substrate was not atomically flat, which made it difficult to resolve large-size Moiré lattices. For an intermediate-size scan as shown in Figure 5.22 (b) over an area of (40 nm \times 40 nm), possible Moiré patterns began to emerge even without atomic resolution. For a small-area (10 nm \times 10 nm) scan as shown in Figure 5.22 (c), Moiré

patterns with atomic resolution appeared. For a high-resolution scan as shown in Figure 5.22 (d), individual carbon atoms were clearly visible. In contrast to the honeycomb structure of monolayer graphene, the arrangements of carbon atoms appeared to form a triangular lattice, indicating that the sample was bilayer graphene with either AB-stacking or a very small twist angle.

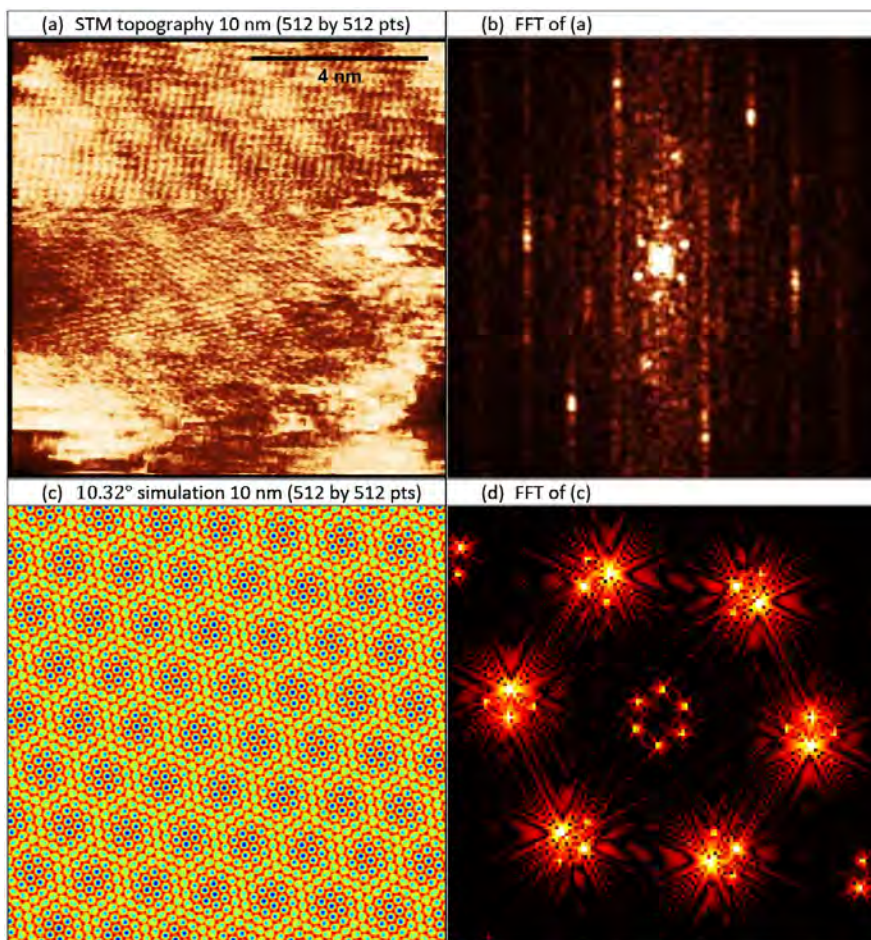


Figure 5.23: (a) STM image with atomic resolution and Moiré patterns over a (10 nm × 10 nm) area. (b) FFT of the image taken in Part (a). (c) Real-space Moiré patterns simulated for a (10 nm × 10 nm) area with a twist angle $\theta = 10.32^\circ$. (d) FFT of the real-space Moiré patterns shown in Part (c).

The lattice constant of the Moiré superlattices can be determined from either the periodicity on the topographic image or from the inner lattice size of the FFT image, although in general FFTs can provide better precision (Figure 5.23). Recall the formula:

$$\Delta K = 2b \sin\left(\frac{\theta}{2}\right) = \frac{2\pi}{a} 2 \sin\left(\frac{\theta}{2}\right) = \frac{2\pi}{L}. \quad (5.23)$$

We note that the value of $\frac{\Delta K}{b}$ in Eq. (5.23) can be measured precisely from the FFT. For example, from Figure 5.23 we find that

$$\frac{\Delta K}{b} = 0.18 = 2 \sin\left(\frac{\theta}{2}\right) \Rightarrow \theta = 10.32^\circ$$

$$L = \frac{a}{2 \sin\left(\frac{\theta}{2}\right)} = \frac{246.4 \text{ pm}}{0.18} = 1.37 \text{ nm}.$$

In Figure 5.23 (a), the 4 nm scale bar corresponds to approximately three lattice constants, and so the size of the superlattice is consistent with our calculation from the FFT. Although the size of the superlattice can be measured directly from the topographic image, the boundary of the superlattice is generally difficult to resolve. Therefore, to reduce the errors in the estimation, a topographic image would need to include several superlattices along each dimension. Using the simulations outlined in Section 5.2, we obtained a topographic image with a similar superlattice size and the corresponding FFT (Figures 5.23 (c) and (d)). Nevertheless, the superlattice structure looks different from the STM image, suggesting that our algorithm is still not accurate enough to fully account for the real STM image.

Although the topographic image with Moiré patterns and atomic resolution can provide accurate measurements of the twist angle, for very small twist angles with large-size superlattices, STM studies become impractical.

Figure 5.24 shows the size of the Moire superlattices vs. the twist angle. The size of the Moiré superlattice reaches infinity as the twist angle approaches 0° . We further note that there are two curves in Figure 5.24 because there are two ΔK values from one reciprocal lattice point in one layer to two nearest reciprocal lattice points in the other layer. From Figure 5.24, we note that the superlattice size at the magic angle is about 13 ~ 14 nm.

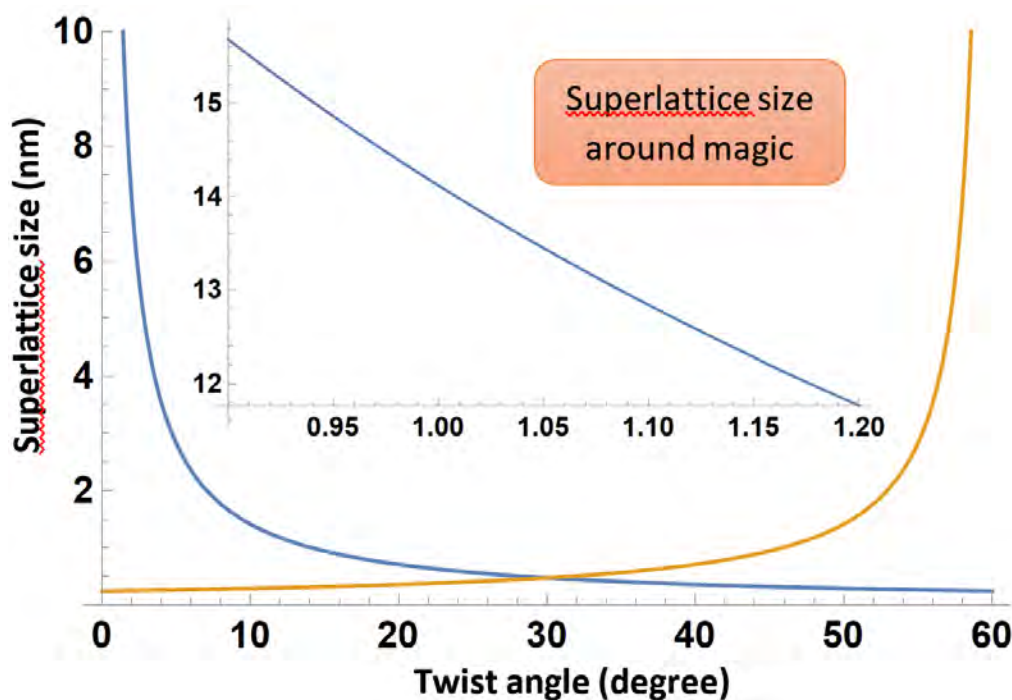


Figure 5.24: Size of the Moiré superlattice vs. twist angle. The inset shows the enlarged details for twist angles around the magic angle ($\sim 1.05^\circ$)

There is no problem for STM to resolve the Moiré patterns of any size even without atomic resolution. On the other hand, to obtain Moiré patterns in the reciprocal space via the FFTs, long-range periodicity is necessary. For instance, to resolve the Moiré patterns of twist bilayer graphene at the magic angle, a ($50 \text{ nm} \times 50 \text{ nm}$) topographic map will be necessary to achieve sufficiently clean signals in the corresponding FFT. On the other hand, to observe the outer hexagon of graphene in FFTs, topographic images with atomic resolution are required. Therefore, to reveal both inner and outer hexagons in the FFTs, super high-resolution of large-area topographic maps are necessary.

In our studies of the bilayer graphene on Cu foil, the uneven substrate with features around 10 nm also made it challenging to resolve the Moiré patterns of bilayer graphene. Therefore, it is useful to carry out simulations to verify our understanding of the STM studies.

5.3.3 Simulations for the Moiré pattern and FFT of twist bilayer graphene

Moiré pattern simulation is a handy tool not only for better understanding of the STM images but also for optimizing the scan parameters to obtain best images of topographic images and the resulting FFTs.

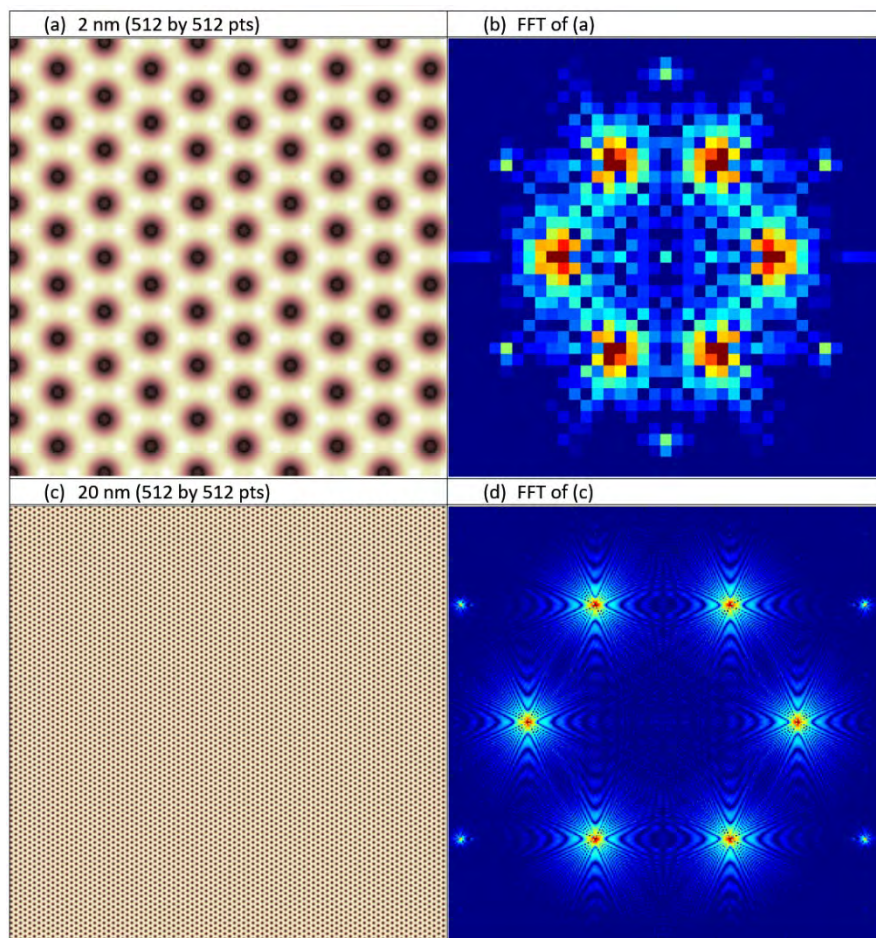


Figure 5.25: Simulations of graphene topography and FFT. **(a)** Real-space simulation over a ($2 \text{ nm} \times 2 \text{ nm}$) area. **(b)** FFT of Part (a). **(c)** Real-space simulation over a ($20 \text{ nm} \times 20 \text{ nm}$) area. **(d)** FFT of Part (c).

For example, Figure 5.25 shows the simulation of graphene topography for ($2 \text{ nm} \times 2 \text{ nm}$) and ($20 \text{ nm} \times 20 \text{ nm}$) areas. The ($2 \text{ nm} \times 2 \text{ nm}$) image includes about 8 lattices from side to side, while the ($20 \text{ nm} \times 20 \text{ nm}$) image includes about 80 lattices. The FFT of the ($2 \text{ nm} \times 2 \text{ nm}$) topography is much rougher than that of the ($20 \text{ nm} \times 20 \text{ nm}$). However, the

reciprocal lattice points are still recognizable. We will treat 8 Moiré superlattices side to side as the minimum requirement to observe a clear Moiré reciprocal lattice in the FFT image. The STM image in Figure 5.23 (c) happens to have 8 Moiré superlattices from side to side, and therefore we can see a clear Moiré reciprocal lattice.

To achieve atomic resolution, 4 pixels per atom is the minimum requirement. Consequently, we set 50 pm/pixel as the minimum requirement to resolve atoms. For a twist angle near the magic angle, the size of the Moiré superlattices is about 12 to 15 nm. Therefore, a (100 nm \times 100 nm) topographic map is required to observe clear a Moiré reciprocal lattice while (2000 \times 2000) pixels are necessary to obtain atomic resolution and, therefore, the outer hexagon associated with graphene in FFTs. STM images with a large number of pixels generally take a long time to acquire, and thermal shifts during the long scan could distort the resulting image. Therefore, taking one larger area and another smaller area scan of topography and combine their FFTs may be a good compromise to provide good estimates of the twist angle.

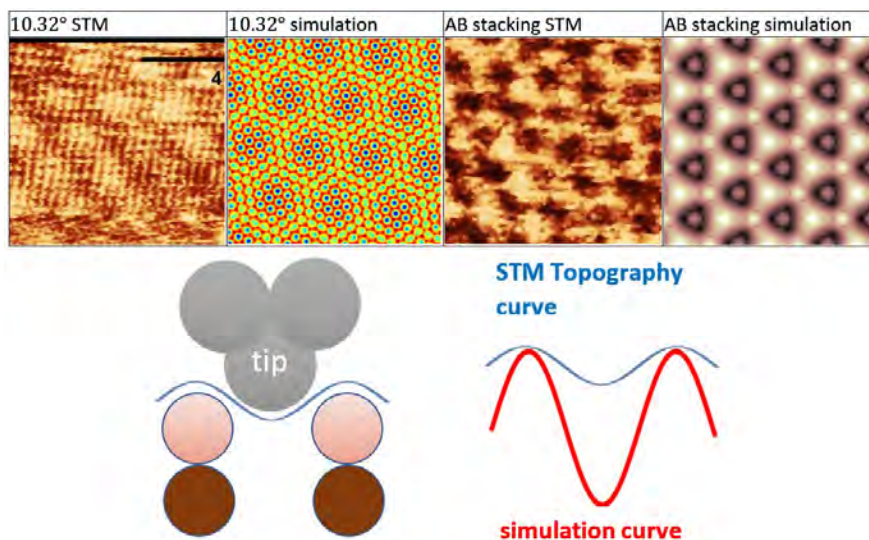


Figure 5.26: Simulation of twist bilayer graphene. The first row shows a comparison between real STM topography and a simulated topography at 10.32° and AB stacking (0°). The second row explains the deviation of simulations from the real image when the bottom lattice has holes.

Simulations can help us optimize the choice of scan parameters. From Figure 5.23, we can see that the Moiré pattern simulation used in Section 5.2 gives us an accurate measurement of the Moiré superlattices in topography and FFT. However, closer inspection of the topography of simulation is not perfectly the same as the STM image (Figure 5.26, first row).

This problem arises from how my code deals with a hole in the middle of the hexagonal lattice: When the hole of a hexagon is on top of the hole of another hexagon at the bottom, our simulation function creates an artificially deeper hole. This is because, for an STM tip scanning over the surface of graphene, the effective hole to the STM tip is only a little lower than the nearby atoms because of the finite size of the atom on the STM tip. Generally speaking, the simulated pattern for atoms or lattices is still correct with height, although in the case of holes associated with the top layer, they would appear more in-depth than the real situation.

On the other hand, if the atoms at the bottom can fill the void of the top lattice, the simulated topography is accurate. For example, AB stacking bilayer graphene in Figure 5.26 is nearly the same as what we observe from STM topography. The simulation of graphene on a copper substrate is also accurate because of no holes in the copper substrate as well as the bigger size of copper atoms.

Deeper holes usually introduce more reciprocal lattice points in the FFT, but they will not remove correct features from the lattice points. As we have seen in Section 5.2, the FFTs of our simulation always provide more points than the FFTs of real STM images. Hence, we need to be careful in order to recognize the correct reciprocal lattice points in the FFTs from simulations.

Simulation for Moiré pattern and FFT of twist bilayer graphene at the magic angle

In Figure 5.27, simulations of the Moiré pattern and its FFT for the magic angle are done for different sizes, (100 nm × 100 nm) and (30 nm × 30 nm), and with different pixels, (256 × 256), (512 × 512) and (2048 × 2048), from side to side. The (100 nm × 100 nm)

topography includes around 8 superlattices. The Moiré pattern is clear despite of the limited resolution. Therefore, the inner hexagon in FFT images is clear for all resolution. The outer hexagon is still complete for (512×512) and (2048×2048) pixels. However, for (256×256) pixels, the outer hexagon disappears. If we look at the topography for (256×256) pixels and $(100 \text{ nm} \times 100 \text{ nm})$, stripe features appear due to poor resolution. Quantitatively, for the 100-nm/256-pixel topography, each pixel spans 0.4 nm, which is larger than the size of a graphene atom. Therefore, it is not surprising that the outer hexagon disappears in the FFT.

For the $(30 \text{ nm} \times 30 \text{ nm})$ topography, it spans about 3 superlattices from side to side. Surprisingly, even at (256×256) pixels, both the inner and outer hexagons can already be resolved. However, the Bragg spots of the inner hexagon are much larger than those in the FFT of the $(100 \text{ nm} \times 100 \text{ nm})$ topography. On the other hand, the outer hexagon is much clearer due to higher resolution.

From the simulation, we know that Bragg spots of Moiré superlattices can be resolved in FFTs even without real-space atomic resolution. Therefore, properly calibrated STM topography can provide the size of Moiré superlattices either in topography or in FFT space, thereby giving us a good estimate of the twist angle. Additionally, simulations can provide a good idea about what the shape of the Moiré pattern should look like, thereby helping us identify from STM measurements the real Moiré patterns associated with the sample and excluding the substrate features.

Since the STM calibration conditions can vary easily with the environment, temperature, time, and various other factors, the topography of Moiré patterns with atomic resolutions can provide self-calibration and help us estimate the twist angle more accurately. From our simulations, we have found that topography with a size of 4 superlattice constants and with atomic resolution will be sufficient to reveal a complete outer hexagon and an inner hexagon in the FFT. Therefore, simulations help set a lower limit on the spatial size and the number of pixels, thereby enabling more efficient STM data acquisition.

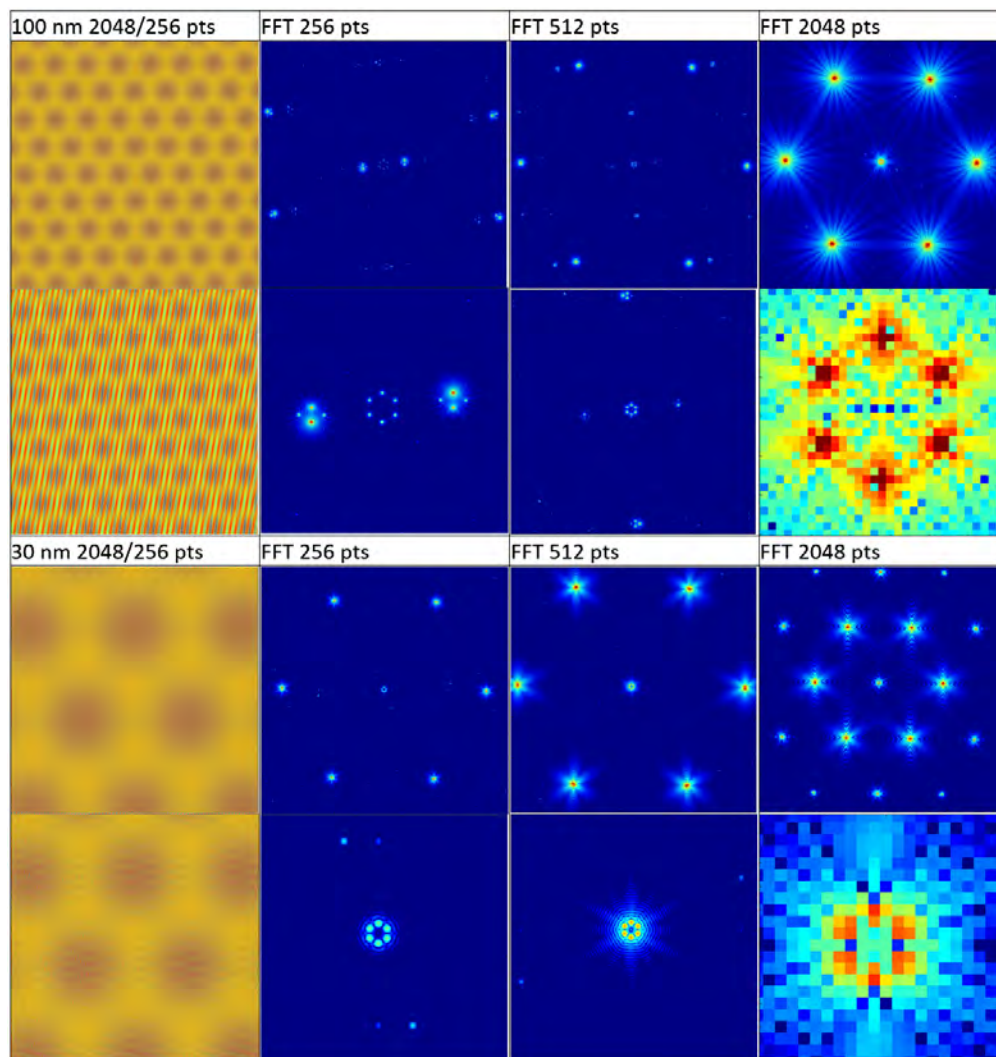


Figure 5.27: Simulation of the Moiré pattern and its FFT near the magic-angle $\theta = 1.1^\circ$ for different sizes of areas and resolutions. For topography, the top image has (2048×2048) pixels, while the bottom image has (256×256) pixels. For FFT, the top image is around the first Brillouin zone, and the bottom image is a zoom-in of the top image.

5.3.4 Summary

PECVD-grown bilayer graphene under proper growth conditions can result in controlled twist angles. Under STM studies, different Moiré patterns can be revealed as a function of the twist angle of the bilayer graphene. A larger twist angle with a smaller size of Moiré superlattices is easier to observe by STM to determine the twist angle. For a small twist

angle around the magic angle 1.1° , we employ simulations to predict the topography and FFT images, which help optimize the parameters for future STM measurements. For Moiré patterns associated with small twist angles, a large area scan is required. However, uneven substrate surfaces may hinder our ability to resolve the real Moiré pattern from the substrate contributions. Additionally, spatial variations in the twist angle distribution will pose significant challenges to identifying the local twist angle if the domain of each twist angle is smaller than the size of the corresponding superlattice.

All in all, the demonstration of direct growth of twisted bilayer graphene by PECVD is an important advancement. If the twist angle can be further controlled to high precision, it will become feasible to develop practical devices based on twisted bilayer graphene for technological applications.

5.4 Investigation of the interlayer interaction of bilayer graphene by density functional theory (DFT)

Graphite has been well known as a solid lubricant long before the discovery of superconductivity in magic-angle twisted bilayer graphene. When two atomically flat graphene layers slide against each other, the friction is generally very low except along the armchair directions where both layers become strongly locked. With properly controlled conditions, the frictional coefficient can fall below 0.01, reaching the limit of structural superlubricity [210, 211]. Generally speaking, superlubricity arises from incommensurability between rotated graphite layers. Under incommensurability, the stacking of carbon atoms is different at different locations for twist angles other than 0 and 30° . Alternatively, we may say that twist bilayer graphene with Moiré patterns would exhibit low friction when one layer slides against the other.

However, stacking is static, whereas sliding is dynamic. To fully understand how friction arises from the relative motion of the layers in bilayer graphene, we need to investigate the

interaction between the layers. In the following, we will employ density functional theory (DFT) to calculate the interaction between two atomically flat graphene layers.

5.4.1 introduction of the density function theory

Density-functional theory (DFT) is a computational quantum mechanical modeling method for *ab initio* calculation and prediction. It is conceptually based on the Schrodinger equation. For N-electron states, the Schrodinger equation is given by

$$\hat{H}\Psi = [\hat{T} + \hat{V} + \hat{U}]\Psi = \left[\sum_i^N \left(-\frac{\hbar^2}{2m_i} \nabla_i^2 \right) + \sum_i^N V(\vec{r}_i) + \sum_i^N U(\vec{r}_i, \vec{r}_j) \right] \Psi = E\Psi. \quad (5.39)$$

Instead of solving for the wave function Ψ , DFT solves for the electron density $n(\vec{r})$

$$n(\vec{r}) = N \int d^3r_2 \dots \int d^3r_N \Psi^*(\vec{r}_1, \vec{r}_2, \dots, \vec{r}_N) \Psi(\vec{r}_1, \vec{r}_2, \dots, \vec{r}_N). \quad (5.40)$$

It can be proved that both the energy and wave function of the system are unique functionals of n . For ground-state electron density n_0

$$E_0 = E[n_0]. \quad (5.41)$$

The potential energy can be expressed explicitly by n :

$$V[n] = \int V(\vec{r})n(\vec{r})d^3r. \quad (5.42)$$

The total energy is therefore given by

$$E(n) = T[n] + U[n] + V[n]. \quad (5.43)$$

By using the variational principle to minimize energy, we can obtain the ground state and ground-state electron density n_0 . Other properties can be calculated accordingly with n_0 .

Practically speaking, interaction potential $U[n]$ is hard to solve. Several approximations and pseudopotential techniques have been developed to help computation. The software we used to do DFT calculations is the Vienna Ab initio Simulation Package (VASP).

Here I would like to express my gratitude to Professor Bill Goddard for providing us with the license of VASP and their computing power of a supercomputer. I also thank Anqi for his help and instruction with the DFT calculations.

5.4.2 Optimization of graphite and bilayer graphene

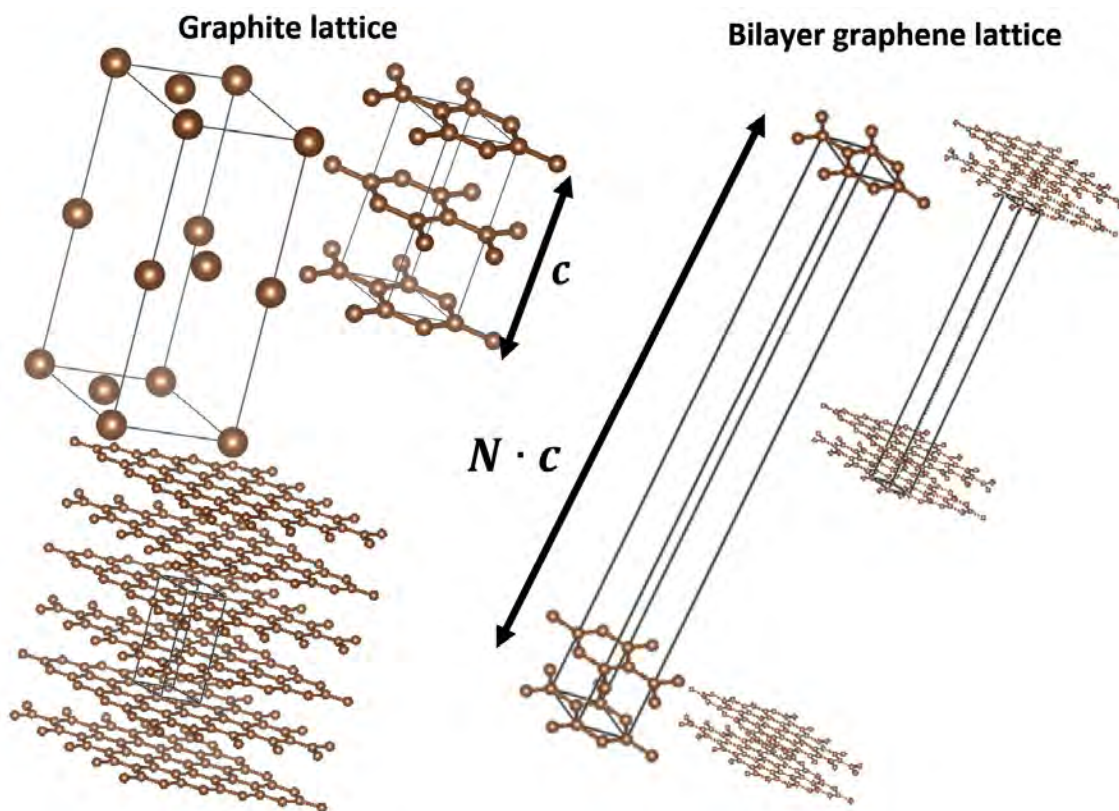


Figure 5.28: Cell of graphite lattice and bilayer graphene lattice. Graphite lattice cell has 4 atoms. To calculate the bilayer graphene, we simply increase the size of the cell for graphite while maintaining the distance between the graphene sheets. As the distance increases, the interaction between different bilayer graphene becomes negligible.

To simulate the situation of two graphene layers sliding against each other, we must first optimize the lattice structure for graphite. Since the properties of graphite are well-known,

this procedure can help verify the effectiveness of the DFT calculation for the parameter and pseudopotential we choose. VASP assumes a periodic boundary condition (PBC) for the cell it calculates. For graphite, each cell has 4 atoms. Therefore, the simulation of graphite only needs to calculate 4 atoms (Figure 5.28). To optimize the structure of graphite, we use the pseudopotential of a carbon atom and let all atoms in the cell be free to relax in all the directions. After optimization, the optimized cell is obtained and will be fixed and used for all other simulations.

To simulate bilayer graphene, simply putting two layers of graphene in the cell is not enough. Due to the PBC in the z -direction, this approach with an optimized structure will be for graphite rather than for bilayer graphene. A simple trick to resolve this issue is to increase the size of the cell while maintaining the distance between layers of graphene, as shown in Figure 5.28. In this case, the simulation implies that the bilayer graphene cells are separated by a large distance. Under this circumstance, the interaction between different bilayer graphene cells becomes negligible. Thus, the structure that we calculate would be equivalent to that of a single cell of bilayer graphene.

5.4.3 Optimization of bilayer graphene for mixed stacking

The next step is to simulate the bilayer graphene with different stacking. For graphite, the structure is AB stacking, and so is bilayer graphene after expanding the unit cell. If we shift the top lattice against the bottom lattice, it's equal to different stacking without rotation. With rotation, it will generate a Moiré pattern with a large size of superlattices so that the unit cell must expand to include many more atoms as shown in Figure 5.30 (a), which will require computer power far beyond what is available. We would also like to optimize the lattice with different stacking so we can compare the simulated results with known data. For this purpose, considering different stacking without rotation should be sufficient.

For simulations of different stacking, the x and y coordinates of atoms for both layers are fixed, and only the z coordinate is relaxed. If x and y coordinates are not fixed, both sheets will relax back to the AB-stacking so that no new information can be obtained.

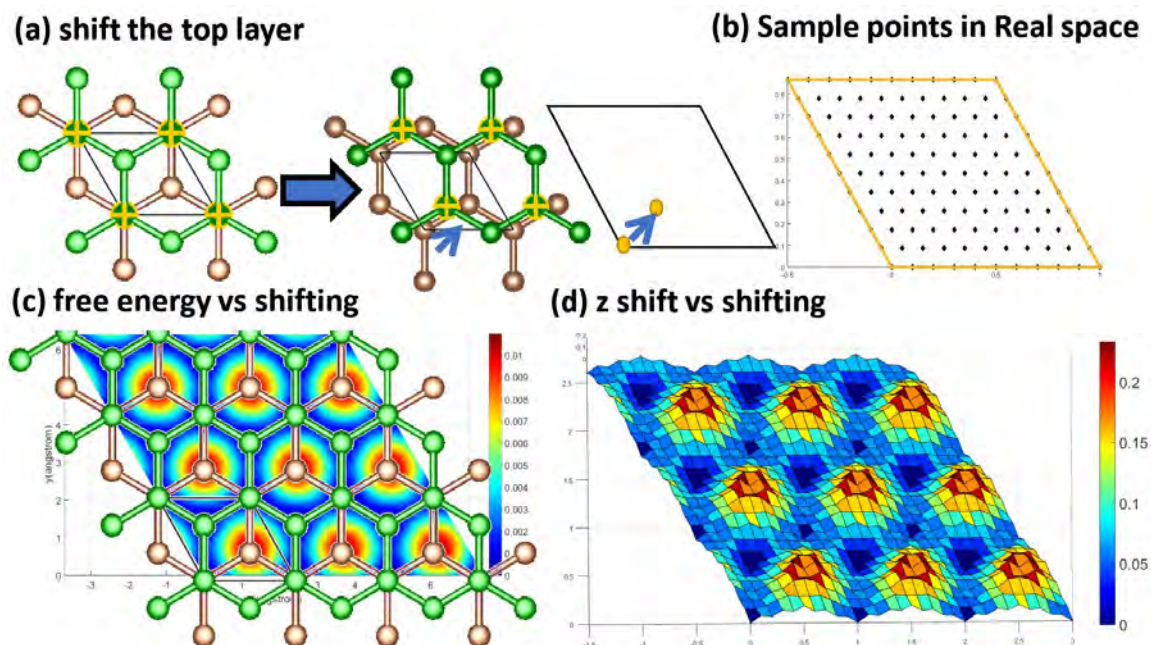


Figure 5.29: DFT simulations for graphene of different stacking without rotation. **(a)** Here we use the coordinates of atoms indicated by the yellow crosses in the top layer (green) to represent the shift. **(b)** The sample points of the top layer that we took for the simulation. **(c)** Free energy (eV) vs. shift (in unit of the lattice constant a) of the top layer (green) relative to the bottom layer (brown). Here the lattice structure is superposed for easy comparison, where we assume that the bottom layer is fixed and the top layer is moving. **(d)** The positional variations in the z -direction of the top layer vs. shift.

Figure 5.29 shows how the shift of the top layer horizontally relative to the bottom layer is achieved. We took 11 by 11 points within the cell for simulation. In each simulation, we will obtain the free energy and the new z -coordinates of carbon atoms after relaxing. The free energy map in Figure 5.29 (c) shows that the free energy is maximum for AA stacking, where all atoms in the top layers are right on the top of all atoms of the bottom layer. AB stacking indeed shows minimum free energy as expected. However, if we check the blue color (locations with minimum energy) around the red color (locations with maximum energy), all the blue regions are connected. This observation suggests that the graphene layers can move along the paths of connected blue regions freely without much resistance. Similarly, the map of z -position vs. shift in Figure 5.29 (d) shows that the top layer is

highest around the AA stacking. However, right at AA stacking, there might be some bonding effect so that the z shift is not maximum there.

5.4.4 Top layer moving in any direction relative to the bottom layer

To simulate friction between two graphene layers, relative motion between the layers of bilayer graphene is necessary. Therefore, we investigate the motion of the top layer along an arbitrary direction relative to the bottom layer without changing the orientation and calculate the free energy variations (figure 5.30).

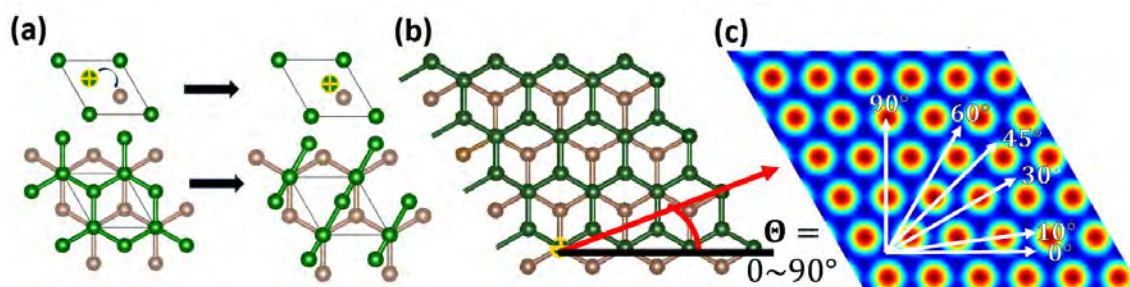


Figure 5.30: (a) Problems encountered in the DFT simulations for changing the relative orientation of the top layer: The top layer can no longer share the same unit cell and lattice vectors as the bottom layer. (b) Moving the top layer against the bottom layer along an arbitrary direction relative to a zigzag axis of the bottom layer. (c) The resulting free energy vs. shift in any arbitrary direction can be obtained along the crossline drawn on the free energy map vs. shift.

The motion speed of the top layer is set to be a constant rather than the force on the top layer. This constraint ensures that the motion of the top layer only follows a straight line without possible zigzag motion. The speed is set between 100 m/s and 200 m/s. For these values of speed, no dependence of the free energy and force maps on the speed is observed. Unlike molecules dynamics simulations, our DFT simulations for the relative motion along arbitrary direction will be similar to results derived from the crosslines on the map of free energy vs. shift. However, such motion simulations can provide much higher resolution (3000 points) on the free energy map in a short time, which can help a more detailed analysis to be discussed later.

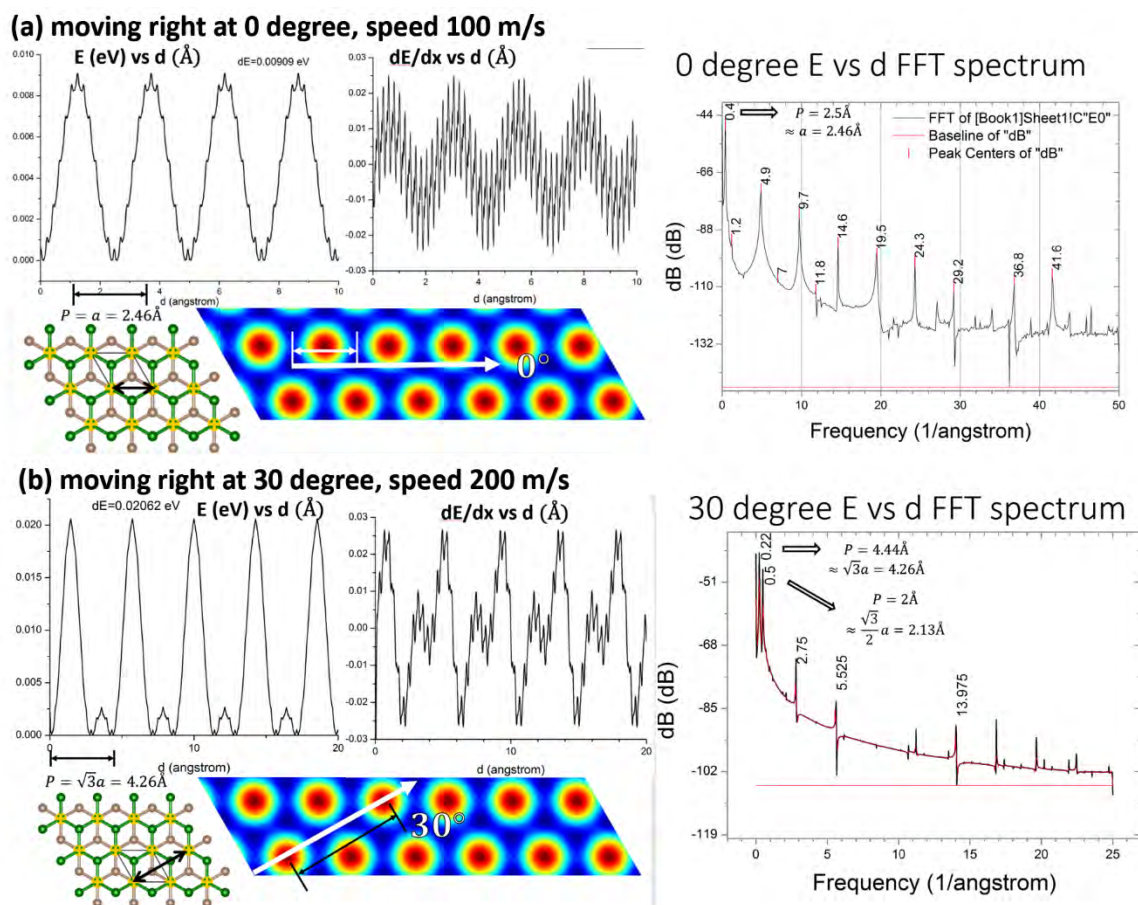


Figure 5.31: Simulation of the relative motion of two graphene layers in bilayer graphene at (a) $\theta = 0$ with speed = 100 m/s, and (b) $\theta = 30^\circ$ with speed = 200 m/s. At each angle, energy (E) vs. shift distance (d), dE/dx -vs.- d , and the FFT of E -vs.- d are provided. E -vs.- d matches the crossline over the E map as expected.

Figure 5.31 shows the free energy (E) profile vs. top layer moving distance (d) for different moving directions. The E -vs.- d curve matches the crossline of the energy map in Figure 5.30. In the FFT of E -vs.- d , peaks associated with the periodicity of the crosslines can be identified. However, the E -vs.- d curves reveal not only the expected sinusoidal behavior but also additional modulations, which are also present in the FFTs of E -vs.- d curves. The physical origin of the modulations is currently unknown.

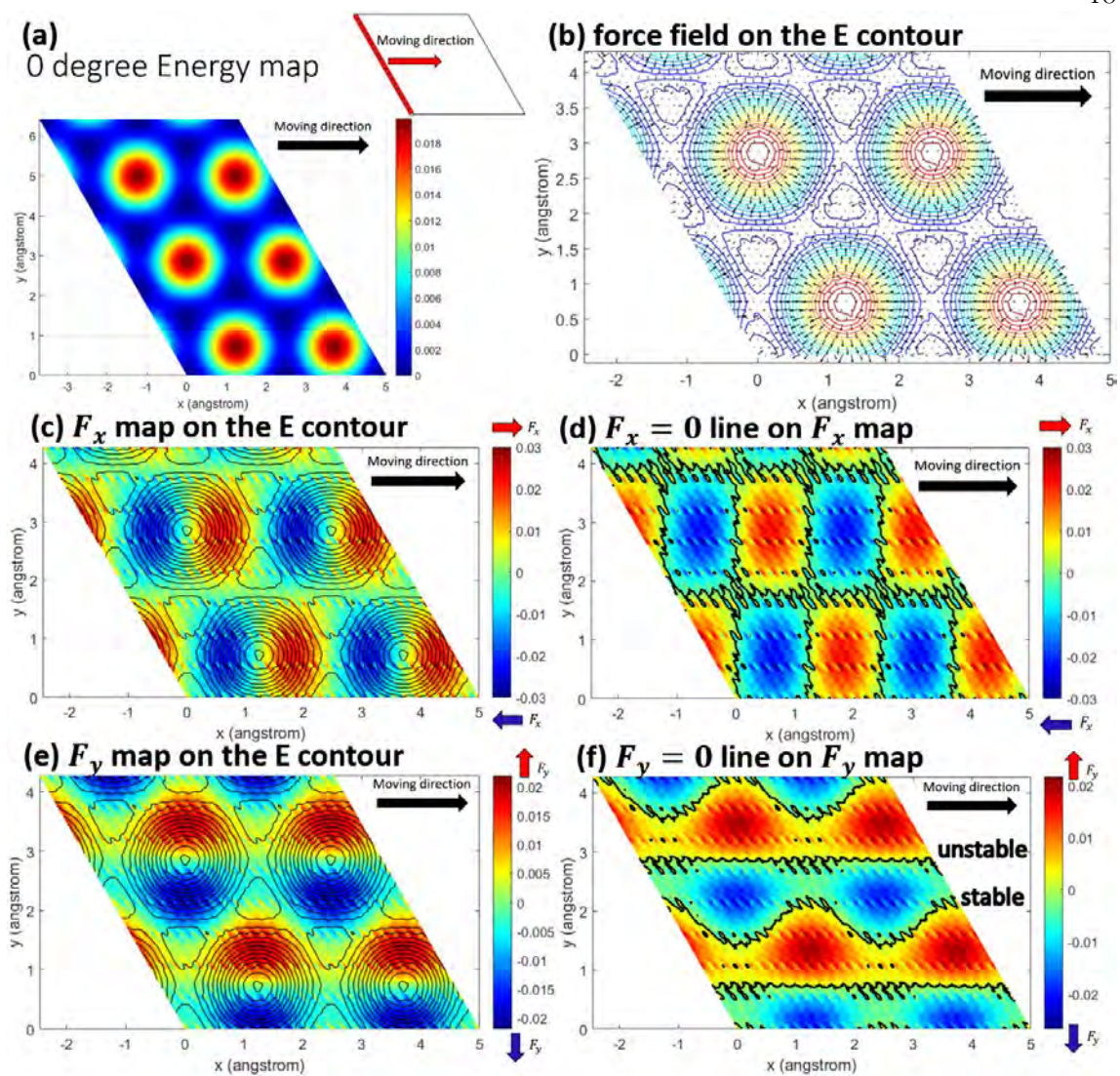


Figure 5.32: Force field analysis for the top layer of bilayer graphene moving along the direction with $\theta = 0$. (a) Energy map generated by several simulations by shifting the initial location along the boundary of the cell. (b) Force field vector map on the energy contour, where the force field is obtained from the gradient of the energy map. (c) x -component force field (F_x) map on the energy (E) contour. (d) F_x map with $F_x = 0$ lines on it. (e) y -component force field (F_y) map on E contour. (f) F_y map with $F_y = 0$ lines on it. There are stable and unstable $F_y = 0$ lines.

The force curve that we obtained for moving along some direction does not represent all the results for that direction because it only represents the profile curve for one initial stacking. On the other hand, if we perform simulations of the same speed and direction along the boundary of the cell, the moving path would cover all cells so that we can obtain a high-resolution free energy map.

5.4.5 Analysis of the free energy map

We can obtain a high-resolution free energy map by taking several DFT simulations for motion along a specific direction with a different initial shift to cover all the areas of the unit cell. Figure 5.32 shows the free energy map for moving along $\theta = 0$. From the free energy map, the force field can be calculated through a gradient of energy vs. xy coordinate.

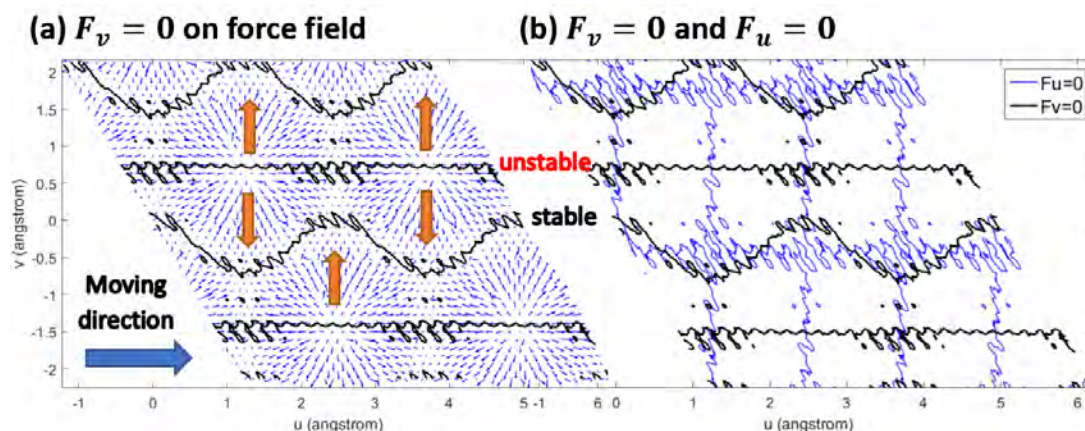


Figure 5.33: Top layer motion at $\theta = 0$, showing (a) the $F_{vertical}(F_v) = 0$ curves in the force field map and (b) the $F_{parallel}(F_u) = 0$ curves in the force field map.

For generalization to all moving angles, we define the direction parallel to the motion as the u -coordinate and the direction vertical to the moving direction as v -coordinate, so that (u, v) is referred to as the moving coordinate. At $\theta = 0$, (u, v) is equal to the x and y coordinates. From the force field map in Figure 5.32 (b), the force is most significant around the AA stacking. This is not surprising due to the highest free energy there.

Parallel force and vertical force maps are shown in Figures 5.32 (c)(d)(e)(f) and Figure 5.33, respectively. In Figure 5.33 (a), The $F_v = 0$ lines are added onto the force field map. It's clear from the plot that one set of curves is stable, and the other is unstable. That is, when we put the top layer along with the bottom layer of graphene, the top layer will move into the stable $F_v = 0$ curve quickly. If we overlap with $F_u = 0$ lines, we found one of $F_u =$

0 lines are parallel to the $F_v = 0$. $F_u = 0$ is expected to be the trajectory along which the top layer will move if we apply a small force.

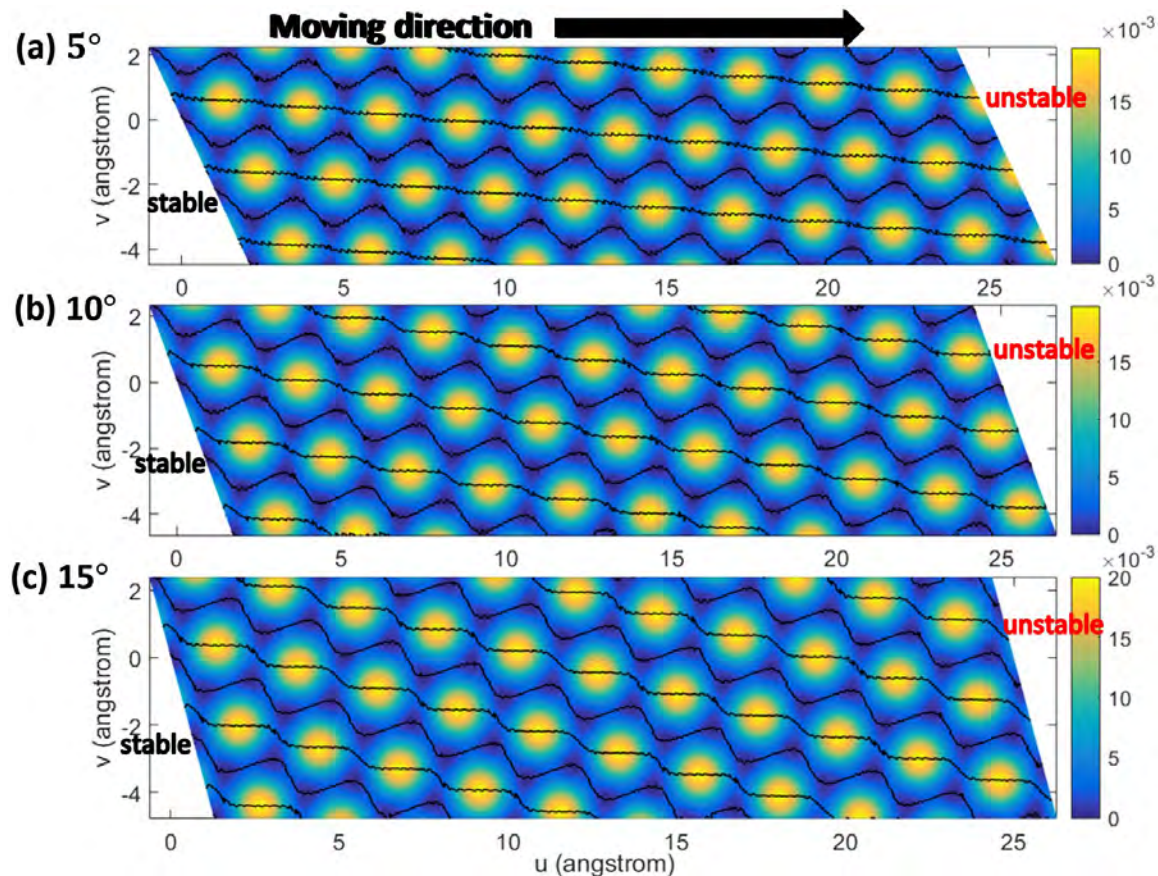


Figure 5.34: $F_v = 0$ lines on the free energy map for the top layer moving along $\theta =$ (a) 5° , (b) 10° and (c) 15° .

A similar analysis can be done for other angles. Figure 5.34 shows the $F_v = 0$ lines for moving angle at 5° , 10° , and 15° . Both stable and unstable lines are continuous. The stable line is not totally vertical to the moving direction, so it will keep pushing the astray graphene layer back to the $F_v = 0$ stable line. On the other hand, the $F_v = 0$ lines are not parallel to the moving direction. The top layer will keep moving along the zigzag path with small frictions. It is also conceivable that sudden jumps of the top layer can occur from one stable line to another stable line in order to maintain the moving direction. In the experiment done by frictional force microscopy (FFM) on graphene, the tip would undergo

“stick-slip” motion where the tip would jump discontinuously over single lattice spacing [210]. The findings from our simulation may have provided an explanation for the empirical observation.

5.4.6 Lock-in effect for motion along the armchair direction with $\theta = 30^\circ$

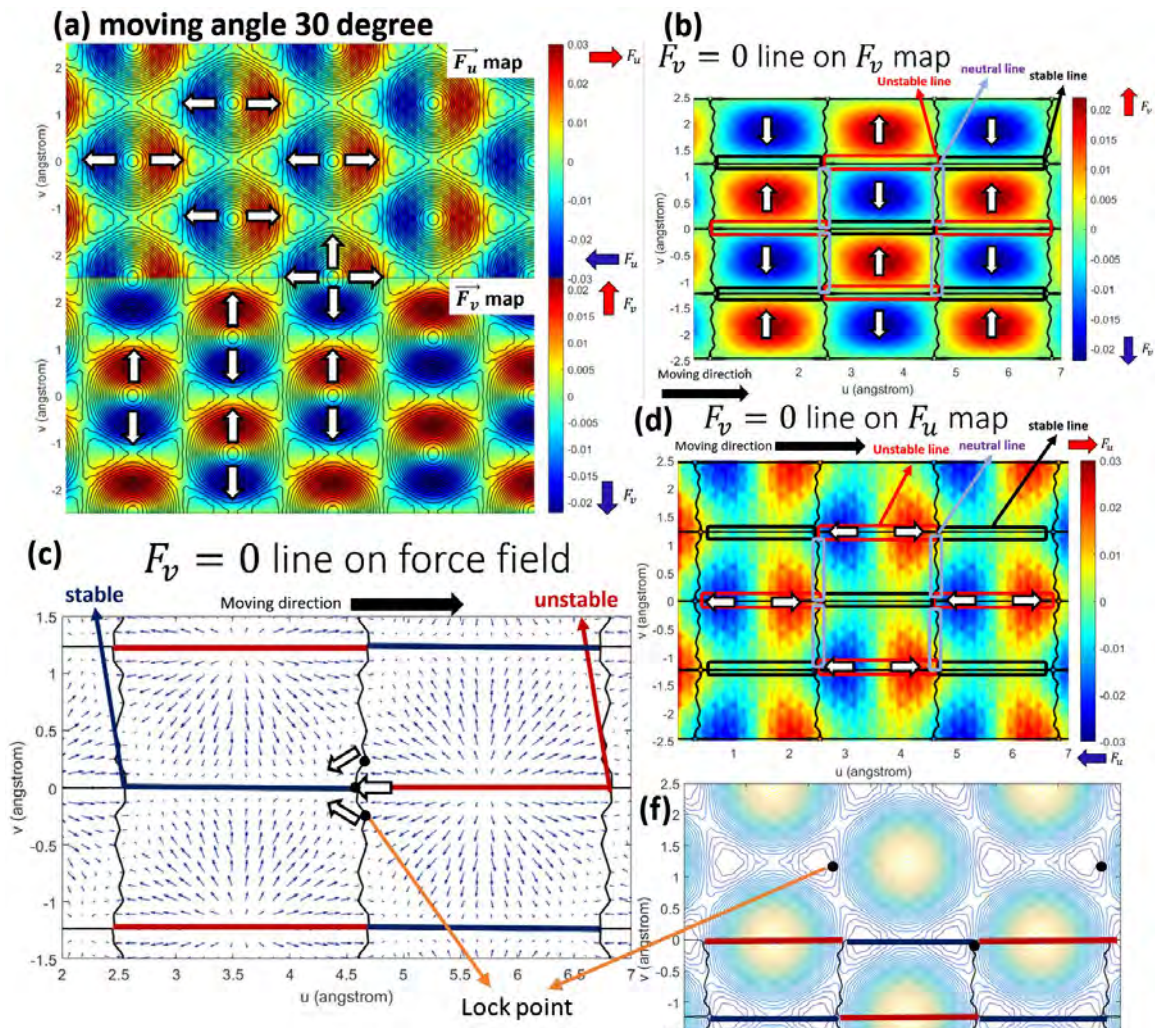


Figure 5.35: Force field analysis for motion direction along $\theta = 30^\circ$. (a) F_u and F_v maps. (b) $F_v = 0$ lines on the force field F_v map, showing both stable and unstable lines. (c) Force vector field map with stable and unstable $F_v = 0$ lines. (d) $F_v = 0$ lines on the force field F_u map, showing both stable and unstable lines. (e) $F_v = 0$ lines on the energy map, (f) Energy map.

At the moving angle $\theta = 30^\circ$, which is along the armchair direction of the bottom layer, something interesting happened. The $F_v = 0$ lines in Figure 5.35 (b) show horizontal and vertical lines. However, stable lines and unstable lines are connected alternatively on the horizontal $F_v = 0$ line. As $F_v = 0$ line overlapped with horizontal force map (Figure 5.35 (d)), the end of the stable line shows strong negative force already. Since it is still in the stable line region, the graphene will be stuck here, as illustrated by the force map in Figure 5.35 (c).

The appearance of a nearly vertical line is interesting. In theory, $F_v = 0$ can never be fully vertical. Indeed, although they are referred to as neutral lines, these vertical lines show zigzag sections composed of a series of stable and unstable lines. To keep a constant motion of the top graphene layer along one direction, it will require a force to counter the friction, and this force will also prevent the back motion of graphene. The appearance of the zigzag lines implies that graphene will be stuck at the local right most point along the zigzag line, as elaborated in Figure 5.36.

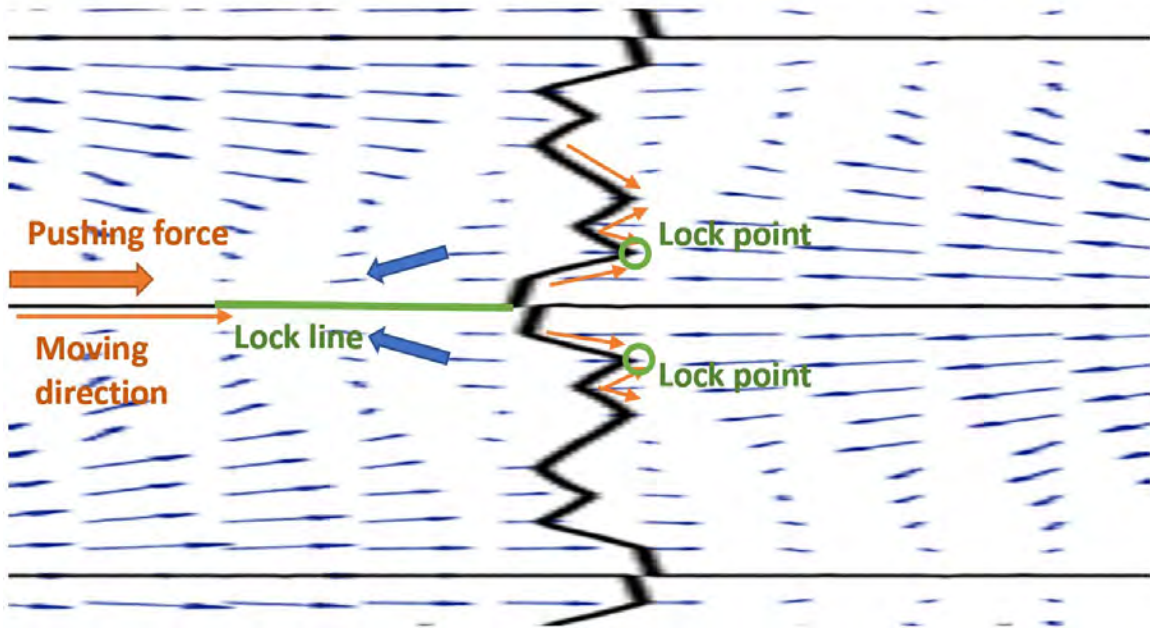


Figure 5.36: Zoom in view of near $F_v = 0$ lines on the force field map around the vertical line region.

In conclusion, if we push the top graphene layer at the angle $\theta = 30^\circ$, the graphene layer will be stuck along the lock lines in Figure 5.36 for small enough force. If the force is high enough, the graphene will move up and down a little. At the maximum force, the graphene will be stuck at the lock point. A force stronger than the maximum force will allow graphene to overcome the barrier and keep moving. On the other hand, if the force is removed, graphene will retract back to the minimum energy point.

5.4.7 Summary

The origin of the ultralow friction in graphite was deemed to be incommensurability between rotated graphene layers. However, even with commensurability so that there are no Moiré patterns or superlattice structures, our simulations reveal that the friction from the relative motion of graphene layers still depends on the moving angles. The free energy calculated by DFT for different stacking shows hexagonal low energy regions. Moving along the zigzag direction shows small to little resistance while moving along the armchair direction leads to strong resistance and ultimately locked motion. Because armchair direction appears every 60° , we will see a lock-in effect when we change the moving angle every 60° . This finding is consistent with experimental observation. Additionally, our simulation can explain other empirical phenomena such as self-retraction and stick-slip movement. [104, 212-215]

For stacking with a different orientation, DFT simulations using the VASP will be much more challenging because of its implementation of periodic boundary conditions. The only way to get around the problem is to include lots of atoms in a cell. Unfortunately, this approach becomes untenable because of the demand for considerable computation time. On the other hand, we may consider applying the free energy map derived from the DFT simulations to molecule dynamic (MD) simulations because MD simulations can handle more atoms in a short time. However, both methods are quite challenging to be applied to twist bilayer graphene.

Despite substantial simplifications employed in our DFT calculations, various findings that are consistent with experimental observation have been successfully derived, which provide useful insights into understanding the microscopic origin for the occurrence of structural superlubricity in graphite.

Chapter 6

CONCLUSION AND FUTURE PROJECT

Table 6.1 Summary of studies on the bilayer topological insulators

Bilayer Topological insulator TI/MTI		
<ul style="list-style-type: none"> ▪ Surface gap opens around 200K, inhomogeneous (STM) ▪ AHE occurs around 25~30K (transport) 		
Binary TI/MTI	Ternary TI/MTI	
<ul style="list-style-type: none"> ○ Negligible hysteresis ○ Weak localization ○ small magnetic domains ○ Impurity resonance at the boundary of gapped and gapless regions 	<ul style="list-style-type: none"> □ Hysteresis below AHE T_C^{bulk} □ Negative coercive field at 13K $\sim T_C^{bulk}$ □ Competition between WL and WAL □ No impurity resonance, larger domains 	
	(1+6)-10% ternary	(3+6)-10% ternary
	<ul style="list-style-type: none"> • WL at low temperature 	<ul style="list-style-type: none"> • WAL for all T • WL below 13K

As summarized in Table 6.1, we have used scanning tunneling microscopy and spectroscopy (STM/STS) to investigate proximity-induced magnetic effects on the surface Dirac spectra of both binary (Bi_2Se_3) and ternary ($(Bi,Sb)_2Te_3$) topological insulator (TI) / magnetic topological insulator (MTI) bilayer structures. With STS measurements at different temperatures, we found spatial inhomogeneity in the tunneling spectra, and the majority spectra change gradually from the V-shaped Dirac spectrum to U-shaped gapped spectrum. A spatially inhomogeneous surface spectral gap Δ opens up below a two-dimensional (2D) Curie temperature around 240 K, which is much higher than the bulk Curie temperature determined from the anomalous Hall resistance. For both the binary and ternary TI/MTI systems, the spatial homogeneity of the gap generally increases with increasing c -axis magnetic field and increasing Cr doping level, suggesting that the physical origin of this surface gap is associated with proximity-induced c -axis

ferromagnetism. The range of proximity effect is about 5 QL from investigating TI/MTI bilayer structures with different thicknesses of the top TI layer.

Comparative spectral studies of ternary and binary TI/MTI structures further reveal excess spectral contributions from the bulk bands and more spatial homogeneity in the STS of ternary TI/MTI samples. These results from the STS studies can account for the differences in the electrical transport properties of ternary and binary TI/MTI samples.

In addition to the observed proximity magnetism from majority spectra, spatially localized sharp resonant spectra are found along the boundaries of gapped and gapless regions in binary TI/MTI samples. These spectral resonances are long-lived in zero magnetic fields, with their occurrences being most prominent near the 2D Curie temperature and becoming suppressed under strong *c*-axis magnetic fields. We attribute these phenomena to the resonant responses of isolated magnetic impurities to the topological magnetoelectric (TME) effect, which are topologically protected by the surface states. In contrast, the absence of magnetic impurity resonances in ternary TI/MTI structures is consistent with the persistent presence of bulk band contributions and the long-range ferromagnetism.

Detailed investigations of the electrical transport properties of both ternary and binary TI/MTI samples as functions of temperature and magnetic field have been carried out using a Physical Property Measurement System (PPMS). The bulk Curie temperature determined from the onset of the anomalous Hall effect (AHE) is ~ 30 K for all TI/MTI samples. On the other hand, only the ternary TI/MTI samples exhibit apparent long-range ferromagnetism below the bulk Curie temperature, as manifested by the hysteretic behavior as a function of the magnetic field in the longitudinal and Hall resistance. Additionally, at low temperatures, the binary TI/MTI samples exhibit weak localization (WL) behavior, whereas the ternary TI/MTI samples reveal weak anti-localization (WAL) behavior. We attribute the different electrical transport properties between the ternary and binary TI/MTI samples to the differences in their band structures and their Fermi level position relative to the Dirac point.

Circularly polarized light on the ternary TI/MTI system is found to enhance the anomalous Hall resistance below 8 K. However, the Hall resistance is only changed under a specific orientation of the magnetic field, which may be due to the Rashba effect associated with the asymmetric interfaces in the TI/MTI system. Further exploration of photo-induced effects on controlling the magnetism of MTIs based on the findings derived from this work will likely yield exciting new results.

Simulations have been carried out to account for various Moiré patterns and high contrast fast Fourier transform (FFT) of graphene on Cu (111) and Cu (110) surfaces, and of twisted bilayer graphene. These results are compared with STM topographic images and FFT and found favorable agreement. The simulations of both topographic images and FFT have been applied to optimizing the experimental parameters chosen for STM studies to save the scan time while still obtaining useful images.

Density functional theory (DFT) simulations of the interaction between bilayer graphene are developed, which successfully account for experimental observation of structural superlubricity for graphene motion along the zigzag and incommensurate direction, and the lock-in effect along the armchair direction.

6.1 Future project

With the installation of optical capabilities to the PPMS and STM systems, we will be able to explore interesting optical effects on various quantum materials, including topological insulators and van der Waals materials.

The upcoming custom-made STM/AFM system will enable STM and AFM scans simultaneously. Such new capabilities will not only provide versatile imaging tools for a wide range of materials but also enable studies of the electronic properties of semiconductors and insulators as well as phase transitions between poorly conducting and highly conducting states (*e.g.*, metal-insulator transitions). The commercial STM will be more user-friendly, more stable, and more reliable, especially in cryogenic use. The atomic

resolution will be easily achieved and enable us to study the impurity resonances in TIs more easily. Combining with the recent upgrade to the commercial glove box, handling and loading of air-sensitive samples will be much easier and faster.

Finally, as the extension of this thesis work, several physics topics are worth further exploration. First, the WL and WAL behavior found in the binary and ternary TI/MTI systems may be investigated at higher temperatures. Second, the field history-dependent study of TI/MTI systems may be studied by STM/STS. Third, optical effects on TIs and MTIs may be further investigated by STM/STS and electrical transport measurements. Finally, spectroscopic and transport studies of pure MTI samples and MTI/AFM samples may be carried out and compared with the studies of TI/MTI systems presented in this thesis. These proposed future projects are summarized in Table 6.2.

Table 6.2 Summary of proposed future projects

PPMS	Old STM	KNI STM with light	New STM/AFM/MFM
<ul style="list-style-type: none"> • Optical effect • R vs. B at higher T • Field history dependent study 	<ul style="list-style-type: none"> • Field effect at 4.2K • MTI sample • MTI/AFM sample • Iron-based superconductors • Cuprate superconductors 	<ul style="list-style-type: none"> • Optical effect for binary and ternary TI by STM 	<ul style="list-style-type: none"> • Magnetic domain study • STM/AFM simultaneous study • Impurity resonance study • Field history dependent study

BIBLIOGRAPHY

1. Tokura, Y., K. Yasuda, and A. Tsukazaki, *Magnetic topological insulators*. Nature Reviews Physics, 2019. **1**(2): p. 126-143.
2. He, L., X. Kou, and K.L. Wang, *Review of 3D topological insulator thin-film growth by molecular beam epitaxy and potential applications*. physica status solidi (RRL)—Rapid Research Letters, 2013. **7**(1-2): p. 50-63.
3. He, K., Y. Wang, and Q.-K. Xue, *Topological Materials: Quantum Anomalous Hall System*. Annual Review of Condensed Matter Physics, 2018. **9**(1): p. 329-344.
4. Hasan, M.Z. and C.L. Kane, *Colloquium: Topological insulators*. Reviews of Modern Physics, 2010. **82**(4): p. 3045-3067.
5. Nagaosa, N., et al., *Anomalous Hall effect*. Reviews of Modern Physics, 2010. **82**(2): p. 1539-1592.
6. Zhang, J., *Quantum Anomalous Hall Effect*, in *Transport Studies of the Electrical, Magnetic and Thermoelectric properties of Topological Insulator Thin Films*. 2016. p. 87-98.
7. Castro Neto, A.H., et al., *The electronic properties of graphene*. RvMP, 2009. **81**(1): p. 109-162.
8. McCann, E. and M. Koshino, *The electronic properties of bilayer graphene*. Reports on Progress in Physics, 2013. **76**(5): p. 056503.
9. Lee, X.J., et al., *Review on graphene and its derivatives: Synthesis methods and potential industrial implementation*. Journal of the Taiwan Institute of Chemical Engineers, 2019. **98**: p. 163-180.
10. Lang, M., et al., *Competing weak localization and weak antilocalization in ultrathin topological insulators*. Nano Lett, 2013. **13**(1): p. 48-53.
11. Liu, W.E., E.M. Hankiewicz, and D. Culcer, *Weak Localization and Antilocalization in Topological Materials with Impurity Spin-Orbit Interactions*. Materials, 2017. **10**(7): p. 807.
12. Lu, H.-Z. and S.-Q. Shen, *Weak localization and weak anti-localization in topological insulators*. Proceedings of SPIE - The International Society for Optical Engineering, 2014. **9167**.
13. He, K., *The Quantum Hall Effect Gets More Practical*. Physics, 2015. **8**.
14. Hsu, C.-C., *Physics and Applications of Graphene-based Nanostructures and Nano-meta Materials*, in *Physics*. 2020, California Institute of Technology.
15. Chen, C.C., et al., *Magnetism-induced massive Dirac spectra and topological defects in the surface state of Cr-doped Bi₂Se₃-bilayer topological insulators*. New Journal of Physics, 2015. **17**(11): p. 113042.
16. Hsu, C.-C., et al., *Nanoscale strain engineering of giant pseudo-magnetic fields, valley polarization, and topological channels in graphene*. Science Advances, 2020. **6**(19): p. eaat9488.
17. Cao, Y., et al., *Unconventional superconductivity in magic-angle graphene superlattices*. Nature, 2018. **556**(7699): p. 43-50.
18. Kim, K., et al., *Tunable moire bands and strong correlations in small-twist-angle bilayer graphene*. Proc Natl Acad Sci U S A, 2017. **114**(13): p. 3364-3369.
19. Bistritzer, R. and A.H. MacDonald, *Moire bands in twisted double-layer graphene*. Proc Natl Acad Sci U S A, 2011. **108**(30): p. 12233-7.
20. Chang, C.Z., et al., *Experimental observation of the quantum anomalous Hall effect in a magnetic topological insulator*. Science, 2013. **340**(6129): p. 167-70.

21. Yu, R., et al., *Quantized anomalous Hall effect in magnetic topological insulators*. Science, 2010. **329**(5987): p. 61-4.
22. Nomura, K. and N. Nagaosa, *Surface-quantized anomalous Hall current and the magnetoelectric effect in magnetically disordered topological insulators*. Physical review letters, 2011. **106**(16): p. 166802.
23. Garate, I. and M. Franz, *Inverse spin-galvanic effect in the interface between a topological insulator and a ferromagnet*. Physical review letters, 2010. **104**(14): p. 146802.
24. Wei, P., et al., *Exchange-coupling-induced symmetry breaking in topological insulators*. Physical review letters, 2013. **110**(18): p. 186807.
25. Qi, X.-L., et al., *Inducing a magnetic monopole with topological surface states*. Science, 2009. **323**(5918): p. 1184-1187.
26. Morimoto, T., A. Furusaki, and N. Nagaosa, *Topological magnetoelectric effects in thin films of topological insulators*. Physical Review B, 2015. **92**(8): p. 085113.
27. Chen, X., et al., *Molecular beam epitaxial growth of topological insulators*. Advanced Materials, 2011. **23**(9): p. 1162-1165.
28. Chang, C.-Z., et al. *Growth of quantum well films of topological insulator Bi₂Se₃ on insulating substrate*. in *Spin*. 2011. World Scientific.
29. Kou, X., et al., *Scale-Invariant Quantum Anomalous Hall Effect in Magnetic Topological Insulators beyond the Two-Dimensional Limit*. Physical Review Letters, 2014. **113**(13): p. 137201.
30. Tang, J., et al., *Electrical Detection of Spin-Polarized Surface States Conduction in (Bi_{0.53}Sb_{0.47})₂Te₃ Topological Insulator*. Nano Letters, 2014. **14**(9): p. 5423-5429.
31. Fan, Y., et al., *Magnetization switching through giant spin-orbit torque in a magnetically doped topological insulator heterostructure*. Nature Materials, 2014. **13**(7): p. 699-704.
32. Bardeen, J., *Tunnelling from a Many-Particle Point of View*. Physical Review Letters, 1961. **6**(2): p. 57-59.
33. Chen, C.-T., *Scanning Tunneling Spectroscopy Studies of High-Temperature Cuprate Superconductors*. 2006, California Institute of Technology.
34. Robbins, A.B., *Exploring Microscopic Thermal Transport Properties of Molecular Crystals with Simulations and Experiments*. 2019, California Institute of Technology.
35. Teague, M.L., *Scanning Tunneling Spectroscopic Studies on High-Temperature Superconductors and Dirac Materials*. 2013, California Institute of Technology.
36. Hasan, M.Z. and C.L. Kane, *Colloquium: topological insulators*. Reviews of modern physics, 2010. **82**(4): p. 3045.
37. Michiardi, M., et al., *Bulk band structure of Bi₂Te₃*. Physical Review B, 2014. **90**(7).
38. Yazyev, O., J. Moore, and S. Louie, *Spin Polarization and Transport of Surface States in the Topological Insulators Bi₂Se₃ and Bi₂Te₃ from First Principles*. Physical review letters, 2010. **105**: p. 266806.
39. Ryu, B., et al., *Prediction of the band structures of Bi₂Te₃-related binary and Sb/Se-doped ternary thermoelectric materials*. Journal of the Korean Physical Society, 2016. **68**(1): p. 115-120.
40. Zhang, H., et al., *Topological insulators in Bi₂Se₃, Bi₂Te₃ and Sb₂Te₃ with a single Dirac cone on the surface*. Nature physics, 2009. **5**(6): p. 438-442.
41. Culcer, D., *Transport in three-dimensional topological insulators: Theory and experiment*. Physica E: Low-dimensional Systems and Nanostructures, 2012. **44**(5): p. 860-884.
42. Ghaemi, P., R.S. Mong, and J.E. Moore, *In-plane transport and enhanced thermoelectric performance in thin films of the topological insulators Bi₂Te₃ and Bi₂Se₃*. Physical review letters, 2010. **105**(16): p. 166603.

43. Checkelsky, J.G., et al., *Bulk band gap and surface state conduction observed in voltage-tuned crystals of the topological insulator Bi₂Se₃*. Phys Rev Lett, 2011. **106**(19): p. 196801.
44. Chen, J., et al., *Gate-voltage control of chemical potential and weak antilocalization in Bi(2)Se(3)*. Phys Rev Lett, 2010. **105**(17): p. 176602.
45. Chiatti, O., et al., *2D layered transport properties from topological insulator Bi₂Se₃ single crystals and micro flakes*. Sci Rep, 2016. **6**: p. 27483.
46. He, L., et al., *Surface-dominated conduction in a 6 nm thick Bi₂Se₃ thin film*. Nano Lett, 2012. **12**(3): p. 1486-90.
47. Jauregui, L.A., et al., *Gate tunable relativistic mass and Berry's phase in topological insulator nanoribbon field effect devices*. Sci Rep, 2015. **5**: p. 8452.
48. Steinberg, H., et al., *Surface state transport and ambipolar electric field effect in Bi(2)Se(3) nanodevices*. Nano Lett, 2010. **10**(12): p. 5032-6.
49. Tang, J., et al., *Electrical detection of spin-polarized surface states conduction in (Bi(0.53)Sb(0.47))₂Te₃ topological insulator*. Nano Lett, 2014. **14**(9): p. 5423-9.
50. Wang, Y., et al., *Gate-controlled surface conduction in Na-doped Bi₂Te₃ topological insulator nanoplates*. Nano Lett, 2012. **12**(3): p. 1170-5.
51. Hajlaoui, M., et al., *Time resolved ultrafast ARPES for the study of topological insulators: The case of Bi₂Te₃*. The European Physical Journal Special Topics, 2013. **222**(5): p. 1271-1275.
52. Kordyuk, A., *ARPES experiment in fermiology of quasi-2D metals*. Low Temperature Physics, 2014. **40**(4): p. 286-296.
53. Wang, J., et al., *Evidence for electron-electron interaction in topological insulator thin films*. Physical Review B, 2011. **83**(24): p. 245438.
54. Hsieh, D., et al., *Observation of unconventional quantum spin textures in topological insulators*. Science, 2009. **323**(5916): p. 919-922.
55. Crepaldi, A., et al., *Evidence of reduced surface electron-phonon scattering in the conduction band of Bi₂Se₃ by nonequilibrium ARPES*. Physical Review B, 2013. **88**(12): p. 121404.
56. Chen, Y., et al., *Experimental realization of a three-dimensional topological insulator, Bi₂Te₃*. science, 2009. **325**(5937): p. 178-181.
57. Xu, N., et al., *Exotic Kondo crossover in a wide temperature region in the topological Kondo insulator SmB₆ revealed by high-resolution ARPES*. Physical Review B, 2014. **90**(8): p. 085148.
58. Teague, M.L., et al., *Observation of Fermi-energy dependent unitary impurity resonances in a strong topological insulator Bi₂Se₃ with scanning tunneling spectroscopy*. Solid State Communications, 2012. **152**(9): p. 747-751.
59. Zhong, M., et al., *Effect of impurity resonant states on optical and thermoelectric properties on the surface of a topological insulator*. Scientific Reports, 2017. **7**(1): p. 1-10.
60. Fu, L. and C.L. Kane, *Superconducting proximity effect and Majorana fermions at the surface of a topological insulator*. Physical review letters, 2008. **100**(9): p. 096407.
61. Liu, Z., et al., *Interacting Majorana chain: Transport properties and signatures of an emergent two-dimensional weak topological phase*. Physical Review B, 2017. **96**(20).
62. Lutchyn, R.M., J.D. Sau, and S. Das Sarma, *Majorana fermions and a topological phase transition in semiconductor-superconductor heterostructures*. Phys Rev Lett, 2010. **105**(7): p. 077001.
63. Meidan, D., A. Romito, and P.W. Brouwer, *Transport signatures of interacting fermions in quasi-one-dimensional topological superconductors*. Physical Review B, 2016. **93**(12).
64. Akhmerov, A., J. Nilsson, and C. Beenakker, *Electrically detected interferometry of Majorana fermions in a topological insulator*. Physical review letters, 2009. **102**(21): p. 216404.

65. Cook, A. and M. Franz, *Majorana fermions in a topological-insulator nanowire proximity-coupled to an s-wave superconductor*. Physical Review B, 2011. **84**(20): p. 201105.
66. Tanaka, Y., T. Yokoyama, and N. Nagaosa, *Manipulation of the Majorana fermion, Andreev reflection, and Josephson current on topological insulators*. Physical review letters, 2009. **103**(10): p. 107002.
67. Xu, J.-P., et al., *Experimental detection of a Majorana mode in the core of a magnetic vortex inside a topological insulator-superconductor Bi₂Te₃/NbSe₂ heterostructure*. Physical review letters, 2015. **114**(1): p. 017001.
68. Cook, A., M. Vazifeh, and M. Franz, *Stability of Majorana fermions in proximity-coupled topological insulator nanowires*. Physical Review B, 2012. **86**(15): p. 155431.
69. Law, K.T., P.A. Lee, and T.K. Ng, *Majorana fermion induced resonant Andreev reflection*. Physical review letters, 2009. **103**(23): p. 237001.
70. Ioselevich, P. and M. Feigel'man, *Anomalous Josephson current via Majorana bound states in topological insulators*. Physical Review Letters, 2011. **106**(7): p. 077003.
71. Shan, W.-Y., H.-Z. Lu, and S.-Q. Shen, *Effective continuous model for surface states and thin films of three-dimensional topological insulators*. New Journal of Physics, 2010. **12**(4): p. 043048.
72. Zhang, Y., et al., *Crossover of the three-dimensional topological insulator Bi₂Se₃ to the two-dimensional limit*. Nature Physics, 2010. **6**(8): p. 584-588.
73. <Anomalies in the electronic structure of Bi₂Se₃.pdf>.
74. Zhang, H., et al., *Topological insulators in Bi₂Se₃, Bi₂Te₃ and Sb₂Te₃ with a single Dirac cone on the surface*. Nature Physics, 2009. **5**(6): p. 438-442.
75. *Band structure of the topological insulators*
Available from:
https://www.researchgate.net/post/Why_in_Topological_Insulators_TIs_bands_are_not_parabolic_type.
76. Zhu, S., et al., *Ultrafast electron dynamics at the Dirac node of the topological insulator Sb₂Te₃*. Sci Rep, 2015. **5**: p. 13213.
77. <Prediction of the Band Structures of Bi₂Te₃-related Binary.pdf>.
78. He, X., et al., *Substitution-induced spin-split surface states in topological insulator (Bi_{1-x}Sb_x)₂Te₃*. Sci Rep, 2015. **5**: p. 8830.
79. Lang, M., et al., *Competing Weak Localization and Weak Antilocalization in Ultrathin Topological Insulators*. Nano Letters, 2013. **13**(1): p. 48-53.
80. Chang, C.-Z., et al., *Chemical-Potential-Dependent Gap Opening at the Dirac Surface States of Bi₂Se₃ Induced by Aggregated Substitutional Cr Atoms*. Physical Review Letters, 2014. **112**(5): p. 056801.
81. Biswas, D. and K. Maiti, *Anomalies in the electronic structure of Bi₂Se₃*. arXiv preprint arXiv:1502.03631, 2015.
82. Liu, W., et al., *Enhancing magnetic ordering in Cr-doped Bi₂Se₃ using high-TC ferrimagnetic insulator*. Nano Lett, 2015. **15**(1): p. 764-9.
83. Collins-McIntyre, L., et al., *Magnetic ordering in Cr-doped Bi₂Se₃ thin films*. EPL (Europhysics Letters), 2014. **107**(5): p. 57009.
84. Lee, I., et al., *Imaging Dirac-mass disorder from magnetic dopant atoms in the ferromagnetic topological insulator Cr_x(Bi_{0.1}Sb_{0.9})_{2-x}Te₃*. Proceedings of the National Academy of Sciences of the United States of America, 2015. **112**(5): p. 1316-1321.
85. <Weak localization and weak anti-localization in topological insulators.pdf>.

86. <Competing Weak Localization and Weak Antilocalization in Ultrathin Topological Insulators SI.pdf>.
87. Shan, W.-Y., H.-Z. Lu, and S.-Q. Shen, *Effective continuous model for surface states and thin films of three-dimensional topological insulators*. New Journal of Physics, 2010. **12**(4).
88. He, Q.L., et al., *Tailoring exchange couplings in magnetic topological-insulator/antiferromagnet heterostructures*. Nat Mater, 2017. **16**(1): p. 94-100.
89. Pan, Y., et al., *Helicity dependent photocurrent in electrically gated $(Bi_{1-x}Sb_x)_2Te_3$ thin films*. Nat Commun, 2017. **8**(1): p. 1037.
90. McIver, J.W., et al., *Control over topological insulator photocurrents with light polarization*. Nat Nanotechnol, 2011. **7**(2): p. 96-100.
91. Qu, D.-X., et al., *Anomalous helicity-dependent photocurrent in the topological insulator $(Bi_{0.5}Sb_{0.5})_2Te_3$ on a GaAs substrate*. Physical Review B, 2018. **97**(4).
92. He, L., et al., *Epitaxial growth of Bi_2Se_3 topological insulator thin films on Si (111)*. Journal of Applied Physics, 2011. **109**(10): p. 103702.
93. Pan, L., et al., *Probing the low-temperature limit of the quantum anomalous Hall effect*. Science Advances, 2020. **6**(25): p. eaaz3595.
94. Liu, C., et al., *Graphene-based supercapacitor with an ultrahigh energy density*. Nano Lett, 2010. **10**(12): p. 4863-8.
95. Chen, S., et al., *Graphene Oxide– MnO_2 Nanocomposites for Supercapacitors*. ACS Nano, 2010. **4**(5): p. 2822-2830.
96. Wu, Z.S., et al., *Three-dimensional nitrogen and boron co-doped graphene for high-performance all-solid-state supercapacitors*. Adv Mater, 2012. **24**(37): p. 5130-5.
97. Zhu, Y., et al., *Carbon-based supercapacitors produced by activation of graphene*. Science, 2011. **332**(6037): p. 1537-41.
98. Choi, J.W. and D. Aurbach, *Promise and reality of post-lithium-ion batteries with high energy densities*. Nature Reviews Materials, 2016. **1**(4): p. 16013.
99. Ko, M., et al., *Scalable synthesis of silicon-nanolayer-embedded graphite for high-energy lithium-ion batteries*. Nature Energy, 2016. **1**(9): p. 16113.
100. Papageorgiou, D.G., I.A. Kinloch, and R.J. Young, *Mechanical properties of graphene and graphene-based nanocomposites*. Progress in Materials Science, 2017. **90**: p. 75-127.
101. Lee, C., et al., *Measurement of the Elastic Properties and Intrinsic Strength of Monolayer Graphene*. Science, 2008. **321**(5887): p. 385-388.
102. Cao, K., et al., *Elastic straining of free-standing monolayer graphene*. Nature Communications, 2020. **11**(1): p. 284.
103. Bao, W., *Electrical and Mechanical Properties of Graphene*. 2011, UC Riverside.
104. Yang, J., et al., *Observation of high-speed microscale superlubricity in graphite*. Phys Rev Lett, 2013. **110**(25): p. 255504.
105. Liu, Z., et al., *Observation of Microscale Superlubricity in Graphite*. Physical Review Letters, 2012. **108**(20): p. 205503.
106. Mandelli, D., et al., *The Princess and the Nanoscale Pea: Long-Range Penetration of Surface Distortions into Layered Materials Stacks*. ACS Nano, 2019. **13**(7): p. 7603-7609.
107. Tseng, W.S., et al., *Direct large-area growth of graphene on silicon for potential ultra-low-friction applications and silicon-based technologies*. Nanotechnology, 2020. **31**(33): p. 335602.

108. Tseng, W.-S., et al., *Stabilization of hybrid perovskite CH₃NH₃PbI₃ thin films by graphene passivation*. *Nanoscale*, 2017. **9**(48): p. 19227-19235.
109. Murali, R., *Graphene Nanoelectronics*. 2012.
110. Velasco, J., Jr., et al., *Transport spectroscopy of symmetry-broken insulating states in bilayer graphene*. *Nat Nanotechnol*, 2012. **7**(3): p. 156-60.
111. Xu, Y., et al., *Liquid-Phase Exfoliation of Graphene: An Overview on Exfoliation Media, Techniques, and Challenges*. *Nanomaterials* (Basel, Switzerland), 2018. **8**(11): p. 942.
112. Hernandez, Y., et al., *High-yield production of graphene by liquid-phase exfoliation of graphite*. *Nat Nanotechnol*, 2008. **3**(9): p. 563-8.
113. Shen, Z., et al., *Preparation of graphene by jet cavitation*. *Nanotechnology*, 2011. **22**(36): p. 365306.
114. Parviz, D., et al., *Challenges in Liquid-Phase Exfoliation, Processing, and Assembly of Pristine Graphene*. *Adv Mater*, 2016. **28**(40): p. 8796-8818.
115. Ciesielski, A. and P. Samorì, *Graphene via sonication assisted liquid-phase exfoliation*. *Chem Soc Rev*, 2014. **43**(1): p. 381-98.
116. Khan, U., et al., *High-concentration solvent exfoliation of graphene*. *Small*, 2010. **6**(7): p. 864-71.
117. Lin, Z., et al., *Simple Technique of Exfoliation and Dispersion of Multilayer Graphene from Natural Graphite by Ozone-Assisted Sonication*. *Nanomaterials* (Basel), 2017. **7**(6).
118. Paton, K.R., et al., *Scalable production of large quantities of defect-free few-layer graphene by shear exfoliation in liquids*. *Nat Mater*, 2014. **13**(6): p. 624-30.
119. Rangappa, D., et al., *Rapid and direct conversion of graphite crystals into high-yielding, good-quality graphene by supercritical fluid exfoliation*. *Chemistry*, 2010. **16**(22): p. 6488-94.
120. Narayan, R. and S.O. Kim, *Surfactant mediated liquid phase exfoliation of graphene*. *Nano Converg*, 2015. **2**(1): p. 20.
121. Liu, W.W. and J.N. Wang, *Direct exfoliation of graphene in organic solvents with addition of NaOH*. *Chem Commun (Camb)*, 2011. **47**(24): p. 6888-90.
122. Xu, J., et al., *Liquid-phase exfoliation of graphene in organic solvents with addition of naphthalene*. *J Colloid Interface Sci*, 2014. **418**: p. 37-42.
123. Wang, X., et al., *Direct exfoliation of natural graphite into micrometre size few layers graphene sheets using ionic liquids*. *Chem Commun (Camb)*, 2010. **46**(25): p. 4487-9.
124. Ager, D., et al., *Aqueous graphene dispersions-optical properties and stimuli-responsive phase transfer*. *ACS Nano*, 2014. **8**(11): p. 11191-205.
125. Tao, H., et al., *Scalable exfoliation and dispersion of two-dimensional materials - an update*. *Phys Chem Chem Phys*, 2017. **19**(2): p. 921-960.
126. Yi, M., et al., *Water can stably disperse liquid-exfoliated graphene*. *Chem Commun (Camb)*, 2013. **49**(94): p. 11059-61.
127. Lotya, M., et al., *Liquid phase production of graphene by exfoliation of graphite in surfactant/water solutions*. *J Am Chem Soc*, 2009. **131**(10): p. 3611-20.
128. Green, A.A. and M.C. Hersam, *Solution phase production of graphene with controlled thickness via density differentiation*. *Nano Lett*, 2009. **9**(12): p. 4031-6.
129. Lotya, M., et al., *High-concentration, surfactant-stabilized graphene dispersions*. *ACS Nano*, 2010. **4**(6): p. 3155-62.
130. Buzaglo, M., et al., *Critical parameters in exfoliating graphite into graphene*. *Phys Chem Chem Phys*, 2013. **15**(12): p. 4428-35.

131. Sun, Z., et al., *Highly concentrated aqueous dispersions of graphene exfoliated by sodium taurodeoxycholate: dispersion behavior and potential application as a catalyst support for the oxygen-reduction reaction*. Chemistry, 2012. **18**(22): p. 6972-8.
132. Notley, S.M., *Highly concentrated aqueous suspensions of graphene through ultrasonic exfoliation with continuous surfactant addition*. Langmuir, 2012. **28**(40): p. 14110-3.
133. Sun, Z., et al., *High-concentration graphene dispersions with minimal stabilizer: a scaffold for enzyme immobilization for glucose oxidation*. Chemistry, 2014. **20**(19): p. 5752-61.
134. Kim, J., et al., *Direct exfoliation and dispersion of two-dimensional materials in pure water via temperature control*. Nat Commun, 2015. **6**: p. 8294.
135. Ding, J.H., H.R. Zhao, and H.B. Yu, *A water-based green approach to large-scale production of aqueous compatible graphene nanoplatelets*. Sci Rep, 2018. **8**(1): p. 5567.
136. Ma, H., et al., *Direct exfoliation of graphite in water with addition of ammonia solution*. J Colloid Interface Sci, 2017. **503**: p. 68-75.
137. Lalwani, G., W. Xing, and B. Sitharaman, *Enzymatic Degradation of Oxidized and Reduced Graphene Nanoribbons by Lignin Peroxidase*. J Mater Chem B, 2014. **2**(37): p. 6354-6362.
138. Ding, J., et al., *Ultrahigh performance heat spreader based on gas-liquid exfoliation boron nitride nanosheets*. Nanotechnology, 2017. **28**(47): p. 475602.
139. Wang, Y., Z. Shi, and J. Yin, *Facile synthesis of soluble graphene via a green reduction of graphene oxide in tea solution and its biocomposites*. ACS Appl Mater Interfaces, 2011. **3**(4): p. 1127-33.
140. Dimiev, A.M., et al., *Chemical Mass Production of Graphene Nanoplatelets in ~100% Yield*. ACS Nano, 2016. **10**(1): p. 274-9.
141. Chen, X., J.F. Dobson, and C.L. Raston, *Vortex fluidic exfoliation of graphite and boron nitride*. Chem Commun (Camb), 2012. **48**(31): p. 3703-5.
142. Dong, L., et al., *A non-dispersion strategy for large-scale production of ultra-high concentration graphene slurries in water*. Nat Commun, 2018. **9**(1): p. 76.
143. Varrla, E., et al., *Turbulence-assisted shear exfoliation of graphene using household detergent and a kitchen blender*. Nanoscale, 2014. **6**(20): p. 11810-9.
144. Wei, Y. and Z. Sun, *Liquid-phase exfoliation of graphite for mass production of pristine few-layer graphene*. Current Opinion in Colloid & Interface Science, 2015. **20**(5): p. 311-321.
145. Han, D., et al., *High-quality graphene synthesis on amorphous SiC through a rapid thermal treatment*. Carbon, 2017. **124**: p. 105-110.
146. Juang, Z.-Y., et al., *Synthesis of graphene on silicon carbide substrates at low temperature*. Carbon, 2009. **47**(8): p. 2026-2031.
147. Shtepliuk, I., V. Khranovskyy, and R. Yakimova, *Combining graphene with silicon carbide: synthesis and properties – a review*. Semiconductor Science and Technology, 2016. **31**(11): p. 113004.
148. Mishra, N., et al., *Graphene growth on silicon carbide: A review: Graphene growth on silicon carbide*. physica status solidi (a), 2016. **213**: p. 2277-2289.
149. Badami, D.V., *X-Ray studies of graphite formed by decomposing silicon carbide*. Carbon, 1965. **3**(1): p. 53-57.
150. Hass, J., W.A. de Heer, and E.H. Conrad, *The growth and morphology of epitaxial multilayer graphene*. Journal of Physics: Condensed Matter, 2008. **20**(32): p. 323202.
151. Berger, C., et al., *Ultrathin Epitaxial Graphite: 2D Electron Gas Properties and a Route toward Graphene-based Nanoelectronics*. The Journal of Physical Chemistry B, 2004. **108**(52): p. 19912-19916.

152. de Heer, W.A., et al., *Large area and structured epitaxial graphene produced by confinement controlled sublimation of silicon carbide*. Proceedings of the National Academy of Sciences, 2011. **108**(41): p. 16900-16905.
153. Emtsev, K.V., et al., *Towards wafer-size graphene layers by atmospheric pressure graphitization of silicon carbide*. Nature Materials, 2009. **8**(3): p. 203-207.
154. Yu, X.Z., et al., *New synthesis method for the growth of epitaxial graphene*. Journal of Electron Spectroscopy and Related Phenomena, 2011. **184**(3): p. 100-106.
155. Virojanadara, C., et al., *Homogeneous large-area graphene layer growth on 6H-SiC(0001)*. Physical Review B, 2008. **78**(24): p. 245403.
156. Yazdi, G.R., et al., *Growth of large area monolayer graphene on 3C-SiC and a comparison with other SiC polytypes*. Carbon, 2013. **57**: p. 477-484.
157. Tedesco, J.L., et al., *Morphology characterization of argon-mediated epitaxial graphene on C-face SiC*. Applied Physics Letters, 2010. **96**(22): p. 222103.
158. Ruan, M., et al., *Epitaxial graphene on silicon carbide: Introduction to structured graphene*. MRS Bulletin, 2012. **37**(12): p. 1138-1147.
159. Tromp, R.M. and J.B. Hannon, *Thermodynamics and Kinetics of Graphene Growth on SiC(0001)*. Physical Review Letters, 2009. **102**(10): p. 106104.
160. Emtsev, K.V., et al., *Ambipolar doping in quasifree epitaxial graphene on SiC(0001) controlled by Ge intercalation*. Physical Review B, 2011. **84**(12): p. 125423.
161. Varchon, F., et al., *Electronic Structure of Epitaxial Graphene Layers on SiC: Effect of the Substrate*. Physical Review Letters, 2007. **99**(12): p. 126805.
162. Ouerghi, A., et al., *Large-Area and High-Quality Epitaxial Graphene on Off-Axis SiC Wafers*. ACS Nano, 2012. **6**(7): p. 6075-6082.
163. Camara, N., et al., *Current status of self-organized epitaxial graphene ribbons on the C face of 6H-SiC substrates*. Journal of Physics D: Applied Physics, 2010. **43**(37): p. 374011.
164. Hibino, H., et al., *Thickness Determination of Graphene Layers Formed on SiC Using Low-Energy Electron Microscopy*. e-Journal of Surface Science and Nanotechnology, 2008. **6**: p. 107-110.
165. Yu, H., et al., *Large Energy Pulse Generation Modulated by Graphene Epitaxially Grown on Silicon Carbide*. ACS Nano, 2010. **4**(12): p. 7582-7586.
166. Kalita, G. and M. Tanemura, *Fundamentals of Chemical Vapor Deposited Graphene and Emerging Applications*. 2017.
167. Yang, X., et al., *Chemical vapour deposition of graphene: layer control, the transfer process, characterisation, and related applications*. International Reviews in Physical Chemistry, 2019. **38**(2): p. 149-199.
168. Plutnar, J., M. Pumera, and Z. Sofer, *The chemistry of CVD graphene*. Journal of Materials Chemistry C, 2018. **6**(23): p. 6082-6101.
169. Chen, X., L. Zhang, and S. Chen, *Large area CVD growth of graphene*. Synthetic Metals, 2015. **210**: p. 95-108.
170. Liu, Z., et al., *Chapter 2 - CVD Synthesis of Graphene*, in *Thermal Transport in Carbon-Based Nanomaterials*, G. Zhang, Editor. 2017, Elsevier. p. 19-56.
171. Zhang, Y., L. Zhang, and C. Zhou, *Review of Chemical Vapor Deposition of Graphene and Related Applications*. Accounts of Chemical Research, 2013. **46**(10): p. 2329-2339.
172. Faggio, G., et al., *Recent Advancements on the CVD of Graphene on Copper from Ethanol Vapor*. C — Journal of Carbon Research, 2020. **6**(1): p. 14.

173. Cai, Z., et al., *Chemical Vapor Deposition Growth and Applications of Two-Dimensional Materials and Their Heterostructures*. Chemical Reviews, 2018. **118**(13): p. 6091-6133.
174. Reina, A., et al., *Large Area, Few-Layer Graphene Films on Arbitrary Substrates by Chemical Vapor Deposition*. Nano Letters, 2009. **9**(1): p. 30-35.
175. Deokar, G., et al., *Towards high quality CVD graphene growth and transfer*. Carbon, 2015. **89**: p. 82-92.
176. Losurdo, M., et al., *Graphene CVD growth on copper and nickel: role of hydrogen in kinetics and structure*. Physical Chemistry Chemical Physics, 2011. **13**(46): p. 20836-20843.
177. Pasternak, I., et al., *Graphene growth on Ge (100)/Si (100) substrates by CVD method*. Scientific reports, 2016. **6**(1): p. 1-7.
178. Seah, C.-M., S.-P. Chai, and A.R. Mohamed, *Mechanisms of graphene growth by chemical vapour deposition on transition metals*. Carbon, 2014. **70**: p. 1-21.
179. Verguts, K., et al., *Epitaxial Al₂O₃ (0001)/Cu (111) template development for CVD graphene growth*. The Journal of Physical Chemistry C, 2016. **120**(1): p. 297-304.
180. Al-Shurman, K. and H. Naseem. *CVD Graphene growth mechanism on nickel thin films*. in *Proceedings of the 2014 COMSOL Conference in Boston*. 2014.
181. Wood, J.D., et al., *Effects of polycrystalline Cu substrate on graphene growth by chemical vapor deposition*. Nano letters, 2011. **11**(11): p. 4547-4554.
182. Zhang, Y., et al., *Comparison of graphene growth on single-crystalline and polycrystalline Ni by chemical vapor deposition*. The Journal of Physical Chemistry Letters, 2010. **1**(20): p. 3101-3107.
183. Addou, R., et al., *Monolayer graphene growth on Ni (111) by low temperature chemical vapor deposition*. Applied Physics Letters, 2012. **100**(2): p. 021601.
184. Meng, L., et al., *Molecular dynamics simulation of chemical vapor deposition graphene growth on Ni (111) surface*. The Journal of Physical Chemistry C, 2012. **116**(10): p. 6097-6102.
185. John, R., et al., *Single-and few-layer graphene growth on stainless steel substrates by direct thermal chemical vapor deposition*. Nanotechnology, 2011. **22**(16): p. 165701.
186. Liu, W., et al., *Synthesis of high-quality monolayer and bilayer graphene on copper using chemical vapor deposition*. Carbon, 2011. **49**(13): p. 4122-4130.
187. Gao, J., et al., *Formation of carbon clusters in the initial stage of chemical vapor deposition graphene growth on Ni (111) surface*. The Journal of Physical Chemistry C, 2011. **115**(36): p. 17695-17703.
188. Regmi, M., M.F. Chisholm, and G. Eres, *The effect of growth parameters on the intrinsic properties of large-area single layer graphene grown by chemical vapor deposition on Cu*. Carbon, 2012. **50**(1): p. 134-141.
189. Hesjedal, T., *Continuous roll-to-roll growth of graphene films by chemical vapor deposition*. Applied Physics Letters, 2011. **98**(13): p. 133106.
190. Woehrl, N., et al., *Plasma-enhanced chemical vapor deposition of graphene on copper substrates*. AIP Advances, 2014. **4**(4): p. 047128.
191. Kaindl, R., et al., *Synthesis of Graphene-layer Nanosheet Coatings by PECVD*. Materials Today: Proceedings, 2015. **2**(8): p. 4247-4255.
192. Yeh, N.-C., et al., *Single-step growth of graphene and graphene-based nanostructures by plasma-enhanced chemical vapor deposition*. Nanotechnology, 2019. **30**(16): p. 162001.
193. Peng, K.-J., et al., *Hydrogen-free PECVD growth of few-layer graphene on an ultra-thin nickel film at the threshold dissolution temperature*. Journal of Materials Chemistry C, 2013. **1**(24): p. 3862-3870.

194. Yang, C., et al., *Direct PECVD growth of vertically erected graphene walls on dielectric substrates as excellent multifunctional electrodes*. Journal of Materials Chemistry A, 2013. **1**(3): p. 770-775.
195. Li, M., et al., *Controllable Synthesis of Graphene by Plasma-Enhanced Chemical Vapor Deposition and Its Related Applications*. Advanced Science, 2016. **3**(11): p. 1600003.
196. Ullah, Z., et al., *A comparative study of graphene growth by APCVD, LPCVD and PECVD*. Materials Research Express, 2018. **5**(3): p. 035606.
197. Yamada, T., et al., *Low-temperature graphene synthesis using microwave plasma CVD*. Journal of Physics D: Applied Physics, 2013. **46**(6): p. 063001.
198. Kato, T. and R. Hatakeyama, *Direct growth of doping-density-controlled hexagonal graphene on SiO₂ substrate by rapid-heating plasma CVD*. ACS Nano, 2012. **6**(10): p. 8508-8515.
199. Kalita, G., K. Wakita, and M. Umeno, *Low temperature growth of graphene film by microwave assisted surface wave plasma CVD for transparent electrode application*. RSC Advances, 2012. **2**(7): p. 2815-2820.
200. Kalita, G., et al., *Low temperature deposited graphene by surface wave plasma CVD as effective oxidation resistive barrier*. Corrosion science, 2014. **78**: p. 183-187.
201. Yamada, T., et al., *A roll-to-roll microwave plasma chemical vapor deposition process for the production of 294 mm width graphene films at low temperature*. Carbon, 2012. **50**(7): p. 2615-2619.
202. Yamada, T., M. Ishihara, and M. Hasegawa, *Large area coating of graphene at low temperature using a roll-to-roll microwave plasma chemical vapor deposition*. Thin Solid Films, 2013. **532**: p. 89-93.
203. Kim, J., et al., *Low-temperature synthesis of large-area graphene-based transparent conductive films using surface wave plasma chemical vapor deposition*. Applied physics letters, 2011. **98**(9): p. 091502.
204. Terasawa, T.-o. and K. Saiki, *Growth of graphene on Cu by plasma enhanced chemical vapor deposition*. Carbon, 2012. **50**(3): p. 869-874.
205. Alrefae, M.A., et al., *Process optimization of graphene growth in a roll-to-roll plasma CVD system*. AIP Advances, 2017. **7**(11): p. 115102.
206. Chen, Y.-C., et al., *Direct growth of mm-size twisted bilayer graphene by plasma-enhanced chemical vapor deposition*. Carbon, 2020. **156**: p. 212-224.
207. Boyd, D.A., et al., *Single-step deposition of high-mobility graphene at reduced temperatures*. Nature Communications, 2015. **6**(1): p. 6620.
208. *Technical data for Copper*. [cited 2020 April 8]; Atomic dimensions and structure]. Available from: <https://periodictable.com/Elements/029/data.html>.
209. Hsu, C.-C., et al., *High-yield single-step catalytic growth of graphene nanostripes by plasma enhanced chemical vapor deposition*. Carbon, 2018. **129**: p. 527-536.
210. Dienwiebel, M., et al., *Superlubricity of graphite*. Phys Rev Lett, 2004. **92**(12): p. 126101.
211. Filleter, T., et al., *Friction and dissipation in epitaxial graphene films*. Phys Rev Lett, 2009. **102**(8): p. 086102.
212. Liu, Y., F. Grey, and Q. Zheng, *The high-speed sliding friction of graphene and novel routes to persistent superlubricity*. Sci Rep, 2014. **4**: p. 4875.
213. Balakrishna, S.G., A.S. de Wijn, and R. Bennewitz, *Preferential sliding directions on graphite*. Physical Review B, 2014. **89**(24).
214. Dienwiebel, M., et al., *Model experiments of superlubricity of graphite*. Surface Science, 2005. **576**(1-3): p. 197-211.

215. Verhoeven, G.S., M. Dienwiebel, and J.W.M. Frenken, *Model calculations of superlubricity of graphite*. Physical Review B, 2004. **70**(16).